A Comparison of Saliency Based Sensorless Control Techniques for a PM Machine

Yu Duan (BEng, MSc)

Thesis submitted to the University of Nottingham for the degree of Doctor of Philosophy

July 2012

Abstract

This thesis analyzes saliency-based sensorless control methods for AC surface mounted permanent magnet machines (PMSM), because PMSMs have features that make them attractive for use in industrial drives: small size, high efficiency, low maintenance, high dynamics, and high power density. The thesis focuses on four different HF injection sensorless methods, which utilize resistance and inductance based saliencies for position estimation: the measurement axis method, the eddy current resistance based saliency tracking method, the eddy current inductance based saliency tracking method, and the PWM switching frequency injection method. The emphasis is in the comparison of the four HF saliency tracking methods under various conditions such as steady state, load impact, speed reversal, and zero and low speed operation. The amplitude and frequency of the injection signals are also compared to choose the best HF injection signal for the four saliency tracking methods. The best sensorless control method using eddy current resistance based saliency is introduced and the experimental results confirm the expected advantages for this sensorless application.

This thesis also describes the development and enhancement of current derivative measurement for saliency tracking methods, which uses the stator current transient response to the voltage vectors contained in the fundamental PWM sequence. Due to the HF switching oscillations caused by the switching of the IGBT and parasitic capacitance, the accuracy of the current measurement is reduced and requires a minimum vector time of approximately 6μs. A signal processing algorithm is proposed which uses current samples during the high frequency current oscillations, and can potentially reduce this minimum pulse time.

Acknowledgement

Apart from the efforts of me, the success of this project depends largely on the encouragement and guidelines of many others. I take this opportunity to express my gratitude to the people who have been instrumental in the successful completion of this PhD project.

I am heartily thankful to my most sincere gratitude to my supervisor Professor Mark Sumner for his guidance and support over the course of this project. His professional attitude always makes my research problems clear and helps me out of being lost. I would like to acknowledge the Tower Innovation Scholarship for the financial support received to carry out this research work at The University of Nottingham. I would also like to thank Mrs Laura Sun for her great help and valuable assistance in The Faculty of Engineering. Dr. Edward Christopher and Dr. Alan Waston patiently helped me with the instrumentation and safety measures. Also I would like to give the thank to my best friends and colleagues, Dr. Kamel Saleh, Dr. Qiang Gao and Dr. Yahan Hua. They provided much more research information for my simulation and experimental work. I would like to thank especially Dr. Lee Empringham, Dr. Liliana de Lillo, Dr. Masoud Almaleki, and Dr. Khwan-on Sudarat for their help and friendship. I would also like to thank Mr. Colin Blackburn, Mr. Paul Moss, and Mr. Mathew Cooper, for providing such an enjoyable working environment and all their technical support during the course of this work. Also, I would express my appreciation to my examiners, Dr. Ramon Blasco-Gimenez (Technical University of Valencia) and Dr. Chris Gerada for their advice on the final corrections to this thesis.

Finally, yet importantly, this thesis should be attributed to my dear wife, Mrs. Ying Zhou for her constant support in my study life. I would like to express my heartfelt thanks to my beloved parents, Mr. Zhong-Nan Duan, Mrs. Yu-Hua Liu and parents-in-law, Mr. Pei-Wen Zhou, Mrs. Yue-Hua Zhao for their blessings, my friends/classmates for their help and wishes for the successful completion of this project.

Contents

Abstract.....i

Acknowledgement.....ii

Chapter 1: Introduction.....1

1.1 Background of the Research.....1

1.2 The Structure of the Thesis.....3

Chapter 2: Overview of sensorless control of AC machines.....5

2.1 Vector Control of a PMSM using an Encoder.....7

2.2 Sensorless Control Based on the Fundamental Mathematical Model...10

2.2.1 Observer Based Methods.....11

2.2.2 Model Reference Adaptive System.....14

2.2.3 Extended Kalman Filter.....16

2.3 Saliency Tracking in Sensorless Control of PMSM.....17

2.3.1 Saliency in PMSM.....18

2.3.2 Position Estimation Using High Frequency Signal Injection 23

2.3.2.1 The Rotating Signal Injection in the Stationary Frame 24

2.3.2.2 The Pulsating Signal Injection in the Estimated Rotor Frame....25

2.3.2.3 Eddy Current Reflected Resistance and Inductance Based Method....26

2.3.2.4 PWM Switching Frequency Injection Method....28

2.3.3 Position Estimation using Transient Current Response....29

2.3.3.1 The INFORM Method....30

2.3.3.2 Fundamental PWM Excitation....32

2.3.4 Tracking Mechanism....33

2.3.4.1 Mechanical Observer....34

2.3.4.2 A Comparison of the mechanical observer with a Phase locked loop....34

2.4 Conclusions....37

Chapter 3: Enhanced Current Derivative Measurement....40

3.1 Introduction....40

3.2 Sensorless Control using Current Derivative Measurement....41

3.2.1 Measurement of *di/dt* Signal using Sensors....41

3.2.2 Measurement of *di/dt* Signal using Current Samples....49

3.2.3 Simulation Results of Sensorless Control using *S-function*....52

3.3 Current Sampling at the Switching Caused High Frequency Oscillations....58

3.3.1 Optimization using Recursive Least Square Algorithm....59

3.3.2 Experimental Results....61

3.4 Conclusions....69

Chapter 4: Saliency tracking using high frequency Injection.....70

4.1 Introduction.....70

4.2 Measurement Axis Method.....71

4.2.1 Theory of Saliency Tracking.....72

4.2.2 Demodulation Process.....75

4.2.3 Calibration of the Position Angle Offset.....77

4.3 Eddy Current Reflected Resistance Based Saliency Tracking Method.....79

4.3.1 Theory of Saliency Tracking Method.....80

4.3.2 Demodulation Process.....85

4.3.3 Eddy Current Effects on Position Estimation.....87

4.4 Eddy Current Reflected Inductance-based Saliency Tracking Method.....89

4.4.1 Theory of Saliency Tracking Method.....89

4.4.2 Demodulation Process.....90

4.5 PWM Switching Frequency Injection Method.....92

4.5.1 Theory of Saliency Tracking Method.....92

4.5.2 Demodulation Process.....96

4.6 Conclusions.....101

Chapter 5: Experimental Rig.....102

5.1 Overall Structure of Rig.....102

5.2 Overview of the Drive System.....104

5.2.1 Machine and Control.....104

5.2.1.1 PMSM Machine and Control.....105

5.2.1.2 DC Machine and Control.....105

5.3 Measurement Circuit.....107

5.3.1 Current and Voltage Measurement.....107

5.3.2 Position Measurement Circuit.....108

5.3.3 Initial Position from the Encoder.....109

5.3.4 Current Derivative Measurement Circuit.....110

5.4 Conclusions.....112

Chapter 6: Results from the four sensorless control methods.....113

6.1 Benchmark Results for Sensored Control.....113

6.1.1 Experimental Results from Sensored Control.....114

6.1.2 Speed Control Bandwidth when using Sensorless Control.....116

6.2 Comparison of Position and Speed Estimation in the Steady State.....121

6.2.1 Position and Speed Error under Different Load Condition.....122

6.2.2 Position and Speed Error at Different Rotor Speeds.....127

6.3 Comparison of Total Harmonic Distortion in the Current.....131

6.3.1 THD Measurement under Different Load Conditions.....132

6.3.2 THD Measurement at Different Rotor Speeds.....133

6.4 Position Error for Different Load Transients.....135

6.5 Comparison of Injection Frequencies.....141

6.5.1 Signal to Noise Ratio.....142

6.5.2 Comparative Results for the Two Injected Frequencies.....143

6.5.3 Comparative Results at Speed Reversal.....144

6.5.4 Comparative Results during Load Transients.....146

6.6 Conclusions.....148

Chapter 7: Discussions and Conclusions.....149

7.1 Sensorless Control using HF Injection Saliency Tracking.....149

7.2 Signal Processing for Current Derivative Measurement.....151

7.3 Further Work.....152

Appendix A: System Control Platform

A1. Digital Signal Processor Kit (DSK).....153

A2. Field Programmable Gate Array (FPGA).....154

A3. Encoder Interface Board.....155

A4. HPI Daughter Card and Host Programme.....156

A5. Gate Drive Circuit.....158

A6. DC Link Power Circuit.....161

A7. Protection Circuit.....163

Appendix B: Schematics and Rig Photos.....166

B1. Power Circuit.....166

B2. Main Power Circuit Schematics.....167

B3. Gate Drive Circuit.....168

B4. DC machine and PMSM.....168

B5. Gate Drive Circuit Schematics.....169

Appendix C: C MEX S-Function.....170

Appendix D: Publications.....174

Bibliography.....175

List of Figures

2.1 permanent magnet machines classification.....7

2.2 transformation to α-β co-ordinates and transformation to d-q axis.....8

2.3 basic scheme of vector control for pm machine.....10

2.4 full observer with both rotor speed and stator resistance estimation.....13

2.5 configuration of a parallel model reference adaptive system.....15

2.6 the operation of Kalman filter.....17

2.7 rotor structure of PMSM.....19

2.8 heterodyne demodulation method and tracking observer.....25

2.9 the injection signal with half the PWM switching frequency.....29

2.10 mechanical observer block diagram for position/speed estimation.....34

2.11 Upper: Tracking Mechanism of using Mechanical Observer;

Lower: Tracking Mechanism of using PLL.....35

2.12 Left: root-locus method of mechanical observer (PID Controller)

Right: root-locus method of phase locked loop (PI Controller).....36

2.13 Upper: position error in sensorless control (Mechanical observer);

Lower: position error in sensorless control (PLL).....37

3.1 overall structure of sensorless control using *di/dt* sensors.....42

3.2 (left) space vectors in six sectors;

(right) voltage vector, current and di/dt. 43

3.3 equivalent circuit with u1 being applied in the star connection.....43

3.4 two active and two null vectors are presented in each sector.....48

3.5 proposed current sampling instants in sector 1.....50

3.6 proposed current sampling for di/dt calculation in phase A.....52

3.7 the flow chart of *S-Function*.....54

3.8 (a) the simulated three-phase real di/dt using sensors;

(b) the calculated three-phase di/dt using current samples;.....55

3.9 the estimated position signal $P\alpha$ and $P\beta$.....56

3.10 (a), (b), (c), (d) measured and estimated simulation results;

(e) speed error; (f) position error.....57

3.11 captured of I_c when motor is running at 100rpm with no load.....58

3.12 captured I_c when motor is running at 100rpm with 70% of load.....59

3.13 100rpm without load - red straight line is estimated signal using 30 samples;

blue straight line is the real signal which is estimated using all samples.....62

3.14 100rpm without load - red straight line is estimated signal using 60 samples;

blue straight line is the real signal which is estimated using all samples.....63

3.15 100rpm with 70% of load - red straight line is estimated signal using

30 samples; blue straight line is the real signal which is

estimated using all samples.....64

3.16 100rpm with 70% of load - red straight line is estimated signal using

60 samples; blue straight line is the real signal which is

estimated using all samples.....64

3.17 200rpm without load - red straight line is estimated signal using

30 samples; blue straight line is the real signal which is

estimated using all samples.....65

3.18 200rpm without load - red straight line is estimated signal using

60 samples; blue straight line is the real signal which is

estimated using all samples.....65

3.19 200rpm with 70% of load - red straight line is estimated signal using

30 samples; blue straight line is the real signal which is

estimated using all samples.....66

3.20 200rpm with 70% of load - red straight line is estimated signal using

60 samples; blue straight line is the real signal which is

estimated using all samples.....66

3.21 300rpm without load - red straight line is estimated signal using

30 samples; blue straight line is the real signal which is

estimated using all samples.....67

3.22 300rpm without load - red straight line is estimated signal using

60 samples; blue straight line is the real signal which is

estimated using all samples.....67

3.23 300rpm with 70% of load - red straight line is estimated signal using

30 samples; blue straight line is the real signal which is

estimated using all samples.....68

3.24 300rpm with 70% of load - red straight line is estimated signal using

60 samples; blue straight line is the real signal which is

estimated using all samples.....68

4.1 block diagram of pulsating signal injection sensorless method.....72

4.2 the measurement axis method by using HF injection.....74

4.3 structure of signal processing procedures and mechanical observer.....76

4.4 position errors before and after the phase shift

compensation (rotor speed at 160rpm).....79

4.5 PMSM with stator resistance accounting for eddy current.....84

4.6 demodulation process for position estimation based on

resistance-based saliency.....86

4.7 demodulation process for inductance-based saliency.....90

4.8 real axis, estimated axis, and measurement axis in rotor reference frame.....93

4.9 block diagram of the PMW switching frequency injection method.....94

4.10 four possible square-wave injection voltage types.....95

4.11 (a) voltage injection frequency with 2.5KHz;

(b) voltage injection frequency with 1KHz.....96

4.12 block diagram of the proposed signal processing and observer.....99

4.13 the *d-axis* voltage injection signal in two PWM periods and

the corresponding current samples.....100

5.1 overall structure of AC PMSM drive system.....104

5.2 the digital converter and external control unit.....106

5.3 measurement transducers 108

5.4 calibration and testing of current derivative sensors.....111

5.5 comparison between calculated and measured current derivatives signals.....112

6.1 sensored control for speed reversal operation.....115

6.2 load impact – increasing load from 0 to 100%.....115

6.3 load impact – decreasing load from 100% to 0.....116

6.4 root-locus design of sensored speed controller.....118

6.5 root-locus design of sensorless speed controller.....118

6.6 sensorless control for speed reversal operation.....120

6.7 enlarged speed response from Fig 6.1 and Fig 6.6.....120

6.8 Upper: speed response from sensored control during load transient;
Lower: estimated speed response from sensorless
control during load transient.....121

6.9 control structure of four sensorless methods.....122

6.10 Upper: step change in load from 0 to 100% load;
Lower: reducing the load from 100% to 0.....123

6.11 Upper: rotor speed from encoder; (rotor at 0rpm)
Lower: the estimated rotor speed using eddy current
resistance-based method.....137

6.12 position error during the load increased from 0 to 100%.....138

6.13 position error during the load increased from 0 to 100% (160rpm).....138

6.14 Upper: rotor speed from encoder; (rotor at 160rpm)
Lower: the estimated rotor speed using eddy current
resistance-based method.....139

6.15 position error during the load increased from 100%. to 0.....139

6.16 Upper: rotor speed from encoder; (rotor at 0 rpm)
Lower: the estimated rotor speed using eddy current
resistance-based method.....140

6.17 position error during the load increased from 100% to 0 (160rpm).....140

6.18 Upper: rotor speed from encoder; (rotor at 160rpm)
Lower: the estimated rotor speed using eddy current
resistance-based method.....141

6.19 (a), estimated speed and (b), position error with no load.....145

6.20 (a), estimated speed and (b), position error with 100% of load.....146

6.21 comparison of (a), position error, and (b), recovery time with 1KHz and
2.5KHz HF injection frequencies during load transient.....147

A1 TMSC6713 DSP starter kit.....154

A2 FPGA data acquisition system.....155

A3 encoder interface board.....156

A4 HPI daughter interface card.....157

A5 gate drive circuit for dual IGBT switches.....160

A6 structure of DC link capacitors.....162

A7 DC link circuit of the test rig.....163

A8 snubber capacitors for circuit protection.....165

B1 the inverter test bed.....166

B2 main power circuit schematics.....167

B3 the photo of gate drive circuit board.....168

B4 the DC machine and the PMSM.....168

B5 the circuit schematics of the IGBT gate driver.....169

C1 sensorless control simulation of PM machine using current measurement.....173

List of Tables

3.1 definition of voltage space vectors.....42

3.2 position Scalars for estimation in different sectors.....46

3.3 reforming the new position scalars in the star connected machine.....48

3.4 related time or frequency in simulation.....54

3.5 estimation errors using the different number of samples.....69

4.1 a look-up table for phase shift compensation.....78

5.1 parameters of surface mounted PMSM.....105

6.1 estimation using measurement axis method.....124

6.2 estimation using eddy current resistance-based method.....124

6.3 estimation using eddy current inductance-based method.....124

6.4 estimation using PWM switching frequency injection method.....124

6.5 estimation with no load using measurement axis method.....127

6.6 estimation with no load using eddy current resistance-based method.....127

6.7 estimation with no load using eddy current inductance-based method.....127

6.8 estimation with no load using PWM
switching frequency injection method.....127

6.9 estimation with 100% load using measurement axis method.....128

6.10 estimation with 100% load using eddy current resistance-based method.....128

6.11 estimation with 100% load using eddy current inductance-based method.....129

6.12 estimation with 100% load using PWM
switching frequency injection method.....129

6.13 estimation using measurement axis method.....129

6.14 estimation using eddy current resistance-based method.....130

6.15 estimation using eddy current inductance-based method.....130

6.16 estimation using PWM switching frequency injection method.....130

6.17 measurement axis method under load condition.....132

6.18 eddy current resistance based method under load condition.....132

6.19 eddy current inductance based method under load condition.....132

6.20 PWM frequency injection method under load condition.....132

6.21 estimation with no load using measurement axis method.....133

6.22 estimation with no load using eddy current resistance-based method.....133

6.23 estimation with no load using eddy current inductance-based method.....133

6.24 estimation with no load using PWM
switching frequency injection method.....133

6.25 estimation with 100% load using measurement axis method.....134

6.26 estimation with 100% load using eddy current resistance-based method.....134

6.27 estimation with 100% load using eddy current inductance-based method.....134

6.28 estimation with 100% load using PWM
switching frequency injection method.....134

6.29 position error using measurement axis method.....135

6.30 position error using eddy current resistance based method.....135

6.31 position error using eddy current inductance based method.....136

6.32 position error using PWM frequency injection method.....136

6.33 comparative results under the different load condition at standstill.....143

6.34 comparative results of position error, speed error, and THD of I_{abc}.....144

6.35 peak position error and length of recovery time during load transient.....147

A1 the used components of gate drive circuits.....161

C1 translations of *S-function* routine.....171

Chapter 1

Introduction

1.1 Background of the Research

The permanent magnet AC machine attracts attention in many industrial, commercial and transportation applications due to its high efficiency, low torque ripple, simplicity, and robustness. The permanent magnet machine is classified into two groups: brushless DC machines and permanent magnet synchronous machines. They have a similar structure but they have totally different applications. They differ according to the shape of the back-EMF voltage induced in the stator windings. The theory of field oriented (vector) control for AC machines was introduced in 1969 [1, 90]. The development of fast switching power devices as well as digital controllers with rapid computing capabilities have all enabled high performance field oriented control for Permanent Magnet Synchronous Motor (PMSM) drives and these are now a competitor for other industrial drives. The field oriented control of an AC machine (See Chapter 2 for more details) needs the stator flux or rotor flux position for the speed feedback, the speed control and the frame transformation [1]. For the machine control, the brush DC machine uses the DC trapezoidal type excitation signal and PMSM uses AC sinusoidal type excitation signal. PMSM produces smoother torque than brushless DC machines due to the PMSM's sinusoidal distribution of the windings. The shape of the back-EMF also allows the operation of the PMSM from the standard AC inverters. The PMSM is suitable for a wider range of applications than the DC machine especially over a wider power range. Hence, the vector controlled PMSM drives are now being considered as a serious replacement for DC drives in many applications.

The measurement of the rotor position required for vector control is usually made using an optical encoder or resolver and signal transmission cables, which increases the system cost, especially for low and medium power drives. In the last 20 years, methods have been researched for PMSM control without a position sensor. This advanced technique is called "sensorless", "self-sensing", or "encoderless" PMSM control. Some commercial products have appeared in the industrial market as a result of the research efforts. The sensorless control of AC machines is becoming an attractive function for many industrial applications.

Model based sensorless control has been widely used in commercial sensorless induction motor control systems for many years with all major drives manufacturers providing a sensorless option for medium and high speed use. These schemes feed measured currents and voltage references into a mathematical model of the motor to estimate its speed [5, 12, 15, 21, 24, 70]. The performance of these schemes is accepted as being stable but inaccurate at low speed and the inaccuracies of model parameters and non-linearities of the power converter used become influential. However many drives applications do not require precise speed control at low speed and this performance is acceptable.

Model based sensorless control of PM machines can also now be found in applications such as electric-hydraulic power steering in cars. However, as PM machines are significantly more expensive than induction motors, good performance sensorless control is required at low speeds and zero speed as well. For this reason saliency tracking techniques have been researched. These techniques aim to detect a saliency in the machine cause either by its construction (geometric) or by local saturation and this is usually detected as a variation of leakage inductance with rotor position. This variation is usually detected either by

1. Injecting a high frequency current/voltage onto the motor: the saliency is encoded into the induced voltage/current response [6, 7, 8, 9, 11, 72]:
2. Looking at the current transient caused by the switching of an IGBT in the inverter [4, 5, 6].

There are many schemes proposed for the methods of (1), and these will be discussed in chapter 2. The first aim of this thesis is to compare and contrast the transient and steady state performance of four of these schemes in order to determine which is the most suitable for industrial PM drives.

Two significant problems exist with the methods of (2). Firstly, the stator current transient (di/dt) must be measured in response to IGBT switching events and this usually required additional di/dt sensors e.g. Rogowski Coil [93], which add cost and complexity. The second arises from the high frequency parasitic capacitances found in a drive eg IGBT to heat sink, cable to shield and inter-winding in the motor itself. The switching of a device excites a high frequency oscillation in these parasitic circuits and these must die down before di/dt can be measured. This takes several microseconds and this therefore imposes a minimum pulse width on the PWM scheme, which then introduces distortion into the stator current waveform. Therefore research is presented in this thesis which aims to demonstrate the viability of using current sensors rather than current derivative sensors, and also using signal processing schemes to determine the underlying current derivative in the presence of the HF oscillations, to reduce the minimum pulse time.

1.2 The Structure of the Thesis

The research presented in this thesis covers the four HF d-axis injection methods and the PWM voltage vector excitation saliency tracking method. Research is undertaken with the aim of achieving both investigated comparison of the four HF injection methods and enhanced current derivative measurement using signal processing methods. For the comparison of the four HF injection methods, the thesis gives more theoretical information for each method, especially the information of modulation process. The four methods are compared using the experimental results. For the measurement of current derivatives, the obtained results are processed offline using Matlab software programming to sample the current derivatives. All experiments are undertaken with a 3.82 kW surface mounted PMSM and simulation of the current derivative method is undertaken using Simulink.

Chapter 2 starts with the literature review for both AC machines and their sensorless vector control. The model and non-model based methods are also reviewed. For the model based method, MRAS, EKF, and observer based method are introduced. For the non-model based method, the saliency in the PMSM and different HF injection saliency tracking methods are also reviewed. Finally, in this chapter, the design of the different tracking mechanisms are introduced and compared.

Chapter 3 deals with the review of the PWM voltage vector excitation saliency tracking method for position estimation. Simulation results are presented and discussed using this estimation method. The advanced signal processing technique is based on the recursive least square algorithms (RLS). The experimental results with various conditions show the potential for improved measurement of the current derivatives.

Chapter 4 describes the implementation of the sensorless speed control of the PMSM using HF injection in the d-axis of the machine. The four HF injection methods are described in their principles. When comparing the four methods, the demodulation process is the only part, which changes for each of methods.

Chapter 5 reviews the experimental rig, which is used for this research.

Chapter 6 details the experimental results using the four HF injection sensorless speed control schemes on a surface mounted PM synchronous motor. The discussions and comparisons are carried out to obtain the best HF injection tracking method. The comparison of the experimental results using two different injection frequencies is also described.

Chapter 7 finally concludes the thesis and gives the recommendations for future research.

Chapter 2

Overview of Sensorless Control of AC Machines

PMSMs have attracted attention for many industrial applications. They have many advantages such as high power density, high-precision positioning, high torque to inertia ratio and high efficiency [3]. They are also high cost due to the rising price of Rare-earth materials. The sources of excitation are the field of the permanent magnet situated on the rotor and the field generated by the stator winding. The PMSM have no electrical connections in the rotor. The rotor field is produced by the permanent magnet and there is no need to consider copper losses, brushes, and slip rings in the rotor [3]. PM machines can be classified as shown in Fig 2.1 [3]. According to the differences in the stator winding, PM machines are classified as PM with D.C. excitation (PMDC) or PM with A.C. excitation (PMAC). PMAC machines can be classified as trapezoidal-type PMAC machines or sinusoidal type PMAC machines, which depend on the type of back-EMF voltage induced in the stator winding [3]. According to the positioning of the magnet in the rotor of the PM machine, the PMSM can be classified as having its magnet on the surface of the rotor (SPMSM) and the magnet inside of the rotor (IPMSM).

The first concept of vector control was proposed by Felix Blaschke in 1996 [1]. Vector control is also called field oriented control, and uses a rotating frame *dq-axis* aligned to the rotor flux to control the torque and field independently through rotor flux orientation. Vector control has been used on AC machines such as induction motors and permanent magnet motors. Vector control utilizes the motor shaft mounted encoder to obtain the flux position for field orientation and closed-loop motor control. However, the encoders in many industrial applications have several

disadvantages. They increase cost, reduce reliability, increase machine size, require signal cables, need installation, and are susceptible to noise interference. Therefore, the control of the rotor speed or position without using an encoder has attracted considerable research over recent years. The first sensorless control of an induction motor was proposed by Joetten and Maeder in 1983 [4]. The rotor frequency estimator forms an inner control loop, as part of the drive control system [5]. With the development of the sensorless approach, a signal processing method is used as a speed or position observer or estimator. The observer or estimator for speed and position is based on the fundamental mathematical models of the machine. The estimation is obtained from the motor back EMF. The estimator shows good performance in the higher speed range and fails at very low or zero speed [5]. The magnitude of back EMF is very small at low speed that has a low signal-to-noise ratio, which is made worse by the non-linear effects of the power converter. The observer or estimator structure used in fundamental mathematical model estimation methods also strongly depends on the machine parameters, which can be changed due to heating and saturation [9]. The fundamental model based sensorless method does not produce good results if the machine has un-modelled nonlinearities and disturbances [11]. Therefore, other approaches to sensorless control methods have been introduced using motor saliency tracking to estimate rotor position. The saliency tracking method can be classified into two groups: one uses a high frequency injection signal to extract saliency position [6, 7, 8], and the other uses the response of the motor to switching pulses to track the rotor position through the measurement of current derivatives [4, 5]. The high frequency injection methods are currently the main trend of research on the sensorless control at low or zero speed [6].

In this chapter, the research for sensorless control of AC machines is reviewed. The fundamental model based methods are presented with a review of observer based methods, model reference adaptive systems (MRAS), and the extended Kalman filter. The magnetic saliency tracking methods are also presented. Both approaches, the high frequency injection method and the switching pulse excitation method, will be introduced. Finally, the tracking mechanisms, including a mechanical observer and a phase locked loop, will be presented. The comparison of the two tracking mechanisms is carried out with experimental results.

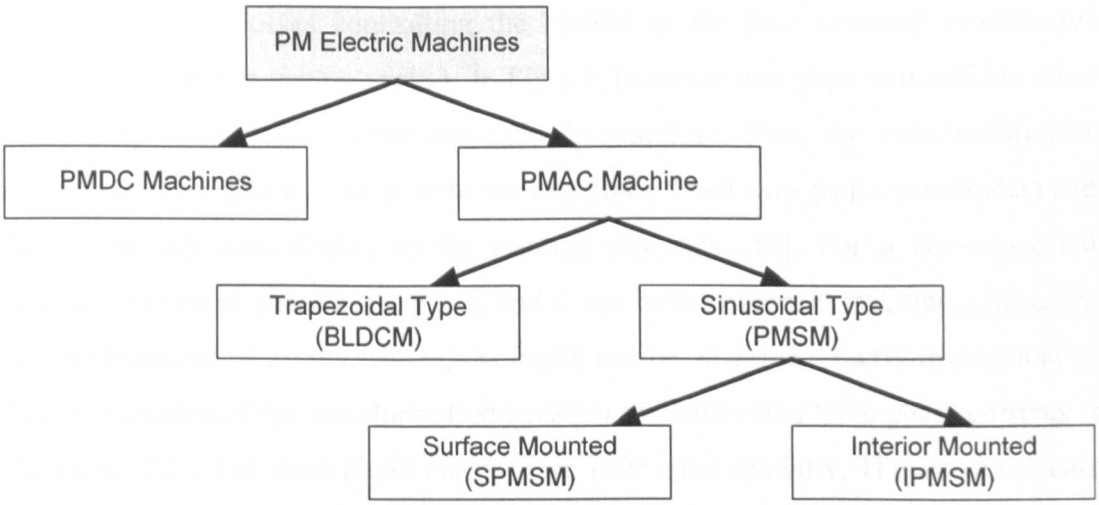

Fig 2.1 permanent magnet machines classification [3]

2.1 Vector Control of a PMSM using an Encoder

The principle of vector control originated in Germany in the work of Hasse and Blaschke in 1960 [1]. A variety of implementation methods has now been developed but these techniques can be broadly classified into two groups: direct vector control and indirect vector control. Indirect control requires a high resolution position sensor, such as an encoder or resolver, to determine the rotor flux position. Direct vector control determines the magnitude and position of rotor flux vector by direct flux measurement or by a computation based on terminal conditions [1]. Vector control requires implementation using a microprocessor for the signal processing and coordinate transformation. All the signal processing required in a high-performance AC servo drive can be executed by a single microprocessor [1]. Vector control is based on the transformation between a three phase time and frequency dependent systems and a two frames (d and q frames) time invariant system [2]. The implementation of vector control requires information about the magnitude and position of the flux vector. Vector control acts in a field-coordinate system using two constants as input references for the stator currents and voltages. They are the torque producing current i_q and the field producing current i_d. Vector control structure deals with instantaneous electrical quantities. This makes the control more accurate in every working operation such as steady state and transient state [2].

Vector control involves controlling the PMSM in the field oriented co-ordinates aligned to an instantaneous angle λ. In Fig 2.2, there are two steps to transform three phase stator quantities into the two axes *dq* quantities. First, the transformation is made from three phase fixed axes to the two phase fixed axes (α-β co-ordinates) and then from α-β co-ordinates to the rotating *d-q* axis [10]. For a star-connected machine, the three phase current i_a i_b and i_c can be transformed to i_a and i_β directly. For the balanced condition $i_a+i_b+i_c= 0$, and i_c can be obtained directly from i_a and i_b. The presentation of the transformation between two phase and three phase currents is shown in (2.2). The three phase currents are 120° apart spatially. The stator currents can be represented by (2.1) as two phase and three phase currents.

$$i_s = i_\alpha + ji_\beta = i_a e^{j0} + i_b e^{j\frac{2\pi}{3}} + i_c e^{j\frac{4\pi}{3}} \tag{2.1}$$

From (2.1), the currents in stationary frame *α-β* are given by [10]

$$\begin{cases} i_{s\alpha}(t) = \frac{3}{2} i_{sa}(t) \\ i_{s\beta}(t) = \frac{\sqrt{3}}{2} i_{sb}(t) - \frac{\sqrt{3}}{2} i_{sc}(t) \end{cases} \tag{2.2}$$

The currents in the *dq* rotating frame can be obtained from the currents in the stationary frame by rotating by the instantaneous angle λ, which is shown as: [10]

$$\begin{cases} i_{sd}(t) = i_{s\alpha}(t)\cos\lambda + i_{s\beta}(t)\sin\lambda \\ i_{sq}(t) = -i_{s\alpha}(t)\sin\lambda + i_{s\beta}(t)\cos\lambda \end{cases} \tag{2.3}$$

In Fig 2.2, the stator frequency is ω_e and orientation angle is θ_r.

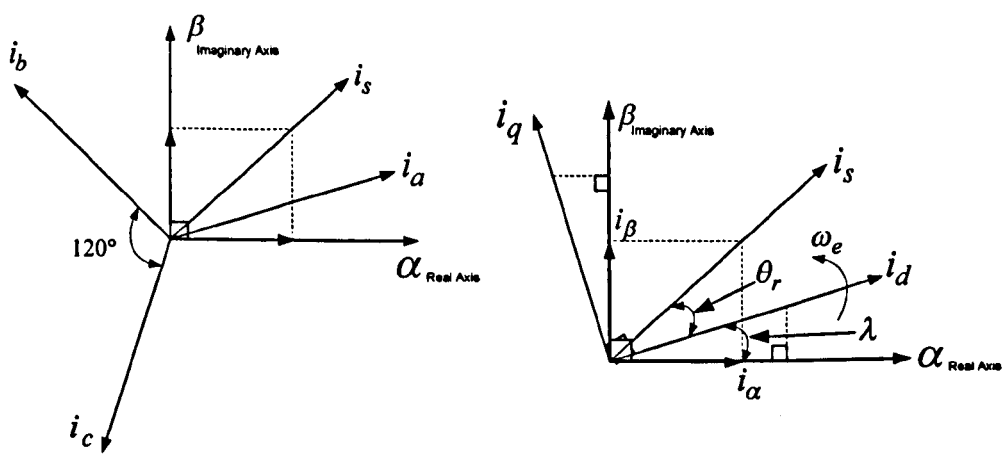

Fig 2.2 transformation to *α-β* co-ordinates and transformation to *d-q* axis

The vector control of a PMSM is based on controlling the rotor flux and torque independently. For a PMSM this is achieved by aligning λ to the rotor magnet position such that the d-axis is aligned with the axes of the magnet. This can be derived from a shaft mounted position encoder, or through sensorless means. The two resulting current, i_d and i_q control the flux and torque respectively. In Fig 2.3, the currents references i_d and i_q in the dq rotating frame are compared with their feedback generated from the three-to-two current transformation to create an error signal. At this point, this control structure shows an interesting advantage: it can be used to control either synchronous or induction machines by simply varying the flux reference and correctly obtaining the rotor flux position [2]. In a PMSM, the rotor flux is determined by the magnets which have the fixed values. Therefore, the flux reference current i_d^* is usually set to zero, when controlling a PMSM below base speed. The current error signals pass through a PI controller to produce the reference voltage v_d and v_q. These two voltage components are transformed into a three phase voltage reference using an inverse transformation for PMSM. The inverse transformation is shown in equation (2.4) and (2.5). The same transforms hold for the current and fluxes.

$$\begin{cases} V_\alpha = V_d \cos\lambda - V_q \sin\lambda \\ V_\beta = V_d \sin\lambda + V_q \cos\lambda \end{cases} \tag{2.4}$$

$$\begin{cases} V_a = \frac{2}{3} V_\alpha \\ V_b = -\frac{1}{3} V_\alpha + \frac{1}{\sqrt{3}} V_\beta \\ V_c = -\frac{1}{3} V_\alpha - \frac{1}{\sqrt{3}} V_\beta \end{cases} \tag{2.5}$$

The PWM modulation is implemented with a voltage source inverter to supply the three phase voltage to the PMSM. In this project, a Space Vector PWM modulation method is used to generate the pulse signals required for the inverter. An encoder or resolver is used to obtain the rotor position information. In this project, an optical incremental encoder is implemented and a pulse signal is generated for each incremental step in its rotation. The rotor speed is calculated from the differentiation of position angle, and is used for controlling the speeds of the PMSM with a closed

loop speed controller. The obtained position angles are used for the current or voltage transformations.

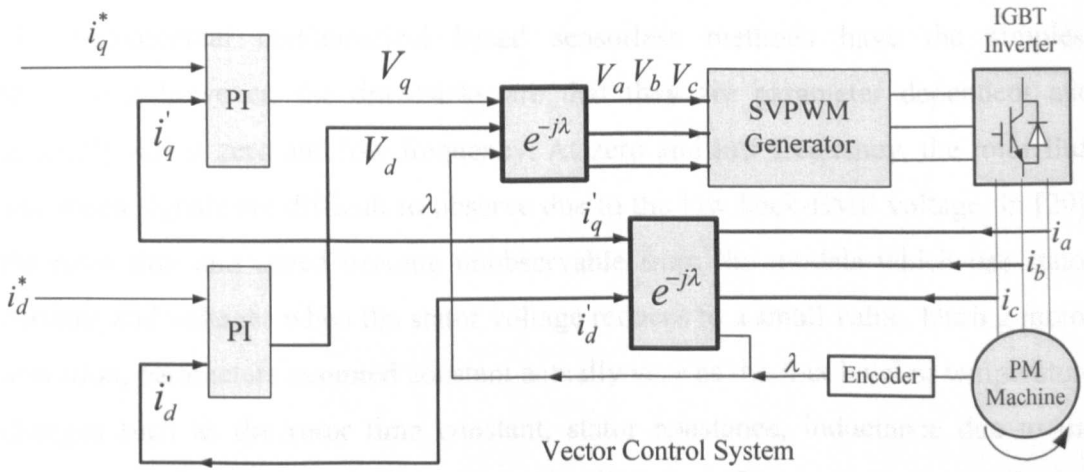

Fig 2.3 basic scheme of vector control for PM Machine

2.2 Sensorless Control Based on the Fundamental Mathematical Model

In this section, mathematical model based sensorless control methods are reviewed. Model based sensorless methods have been developed by many researchers over two decades. The fundamental mathematical model based estimators can be classified as: [12-19]

1. Observer Based Methods
2. Model Reference Adaptive Methods (MRAS)
3. Extended Kalman Filter Methods (EKF)

The objective of this section is to discuss the basic structures of model based estimators, and the advantages, and disadvantages of these methods. Comparisons of three methods have been made by researchers in recent years. In [12], the Luenberger observer provides the best performance but this method is parameter dependent. When information on the system noise is available, the EKF method can give the best behaviour with respect to the dynamic response. The EKF is a noise

dependent method for flux and speed estimation, which can be considered as one case of a full order model with the observer gain producing the error with white Gaussian noise by applying minimum least square estimation [70].

The fundamental mathematical based sensorless methods have the simplest realization; however, the drawbacks are that they are parameter dependent and generally fail at zero and low frequency. At zero and low frequency, the rotor flux and speed signals are difficult to observe due to the low back-EMF voltage. In [20], the rotor flux and speed become unobservable from the models which use stator currents and voltages when the stator voltage reduces to a small value. During motor operation, parameters assumed constant actually vary as the flux level or temperature changes such as the rotor time constant, stator resistance, inductance due to the saturation and magnet flux. The online identification of parameters or an adaptive controller has to be implemented for a good estimation. Alternatively, the saliency tracking methods are introduced as the non-model based methods for position estimation. These methods are applicable for sensorless control at zero and low frequency. The saliency tracking methods will be discussed later.

2.2.1 Observer Based Methods

A state observer models a real system. The state observer estimates the internal variables of the real system from the measurements of the input and output signals. Typically, the state observer is a computer-implemented mathematical model, which can be used for flux estimation in sensorless control of AC drives. The observer based method uses the voltage model (Resistive, Inductive, and Back EMF voltage) to determine the rotor speed and position. In [21], the permanent magnet flux can be estimated by the integration of back-EMF. At low speed, rotor flux is difficult to estimate due to noise and measurement resolution. The mismatch of stator resistance due to heating effects at low speed can also give a poor estimation quality. In some papers, the current model and voltage model are combined to operate because the current model does not use the stator resistance. Alternatively, a full-order adaptive flux observer can be used for position estimation and the stator resistance can be

identified online at the same time [22]. In [23], the state variables of the full order observer are stator current and rotor flux and the state equation of an PMSM motor can be expressed as (2.6) in the stationary frame [23].

$$AX + Bu_s = \frac{d}{dt}\begin{bmatrix} i_s \\ \psi_r \end{bmatrix} = \begin{bmatrix} A_{11} & A_{12} \\ A_{21} & A_{22} \end{bmatrix}\begin{bmatrix} i_s \\ \psi_r \end{bmatrix} + \begin{bmatrix} B \\ 0 \end{bmatrix} u_s \tag{2.6}$$

where $u_s = \begin{bmatrix} u_{s\alpha} \\ u_{s\beta} \end{bmatrix}$ is the stator voltage, $i_s = \begin{bmatrix} i_{s\alpha} \\ i_{s\beta} \end{bmatrix}$ is the stator current, and $\psi_r = \begin{bmatrix} \psi_{r\alpha} \\ \psi_{r\beta} \end{bmatrix}$ is permanent magnet rotor flux vector. In (2.6), the coefficient matrix A is presented by [23]

$$\begin{cases} A_{11} = -\dfrac{R_s}{L_s} I \\ A_{12} = -J\dfrac{\omega_m}{L_s} \end{cases} \quad \text{and} \quad \begin{cases} A_{21} = 0 \\ A_{22} = J\omega_m \end{cases} \tag{2.7}$$

The coefficient matrix B is given by [23]:

$$B = \frac{1}{L_s} \tag{2.8}$$

$$\begin{cases} C = \begin{bmatrix} I \\ 0 \end{bmatrix} \quad I = \begin{bmatrix} 1 & 0 \\ 0 & 1 \end{bmatrix} \quad J = \begin{bmatrix} 0 & -1 \\ 1 & 0 \end{bmatrix} \end{cases} \tag{2.9}$$

R_s is the stator and rotor resistance. The stator inductance is L_s. ω_m is the motor mechanical angular velocity. For the estimated stator current and rotor flux, the full order observer can be written as: [21]

$$\frac{d}{dt}\hat{X} = \hat{A}\hat{X} + Bu_s + G(\hat{i}_s - i_s) \tag{2.10}$$

In order to make the observer stable in any speed range, the pole position of the observer is assigned as k times of that of the motor. G is defined as a feedback gain of the observer that is chosen to ensure the observer can provide a good performance under the stable condition to meet the Lyapunov criterion [5]. The estimated stator current is obtained from (2.10). Therefore, the full order observer is constructed by

comparing the estimated states with the measured values. Fig 2.4 shows the estimation scheme of the rotor speed and stator resistance by equations [21], as expressed in (2.11). The estimated stator current is compared to the measured stator current [21], as shown in (2.12).

$$\begin{aligned} \hat{R}_s &= -K_{RP}\left(\hat{i}_{s\alpha}\varepsilon_1 + \hat{i}_{s\beta}\varepsilon_2\right) - K_{RI}\int\left(\hat{i}_{s\alpha}\varepsilon_1 + \hat{i}_{s\beta}\varepsilon_2\right)dt \\ \hat{\omega}_r &= K_{\omega P}\left(\hat{\psi}_{r\beta}\varepsilon_1 - \hat{\psi}_{r\alpha}\varepsilon_2\right) + K_{\omega P}\int\left(\hat{\psi}_{r\beta}\varepsilon_1 - \hat{\psi}_{r\alpha}\varepsilon_2\right)dt \end{aligned} \tag{2.11}$$

$$\varepsilon_1 = i_{s\alpha} - \hat{i}_{s\alpha} \quad \varepsilon_2 = i_{s\beta} - \hat{i}_{s\beta} \tag{2.12}$$

In the PMSM motor model, the coefficient matrix A contains the unknown speed. Additionally, as mentioned the stator resistance at low speed can be inaccurate due to heating. An adaptive speed estimator and stator resistance estimator is added to overcome the problems. In (2.12), the current error between measured and estimated values is used to estimate the speed and stator resistance by adaptive algorithms. The adaptive algorithms for speed and resistance is realized by PI controllers and the PI parameters in (2.11) are K_{RP}, K_{RI}, $K_{\omega P}$, and $K_{\omega I}$.

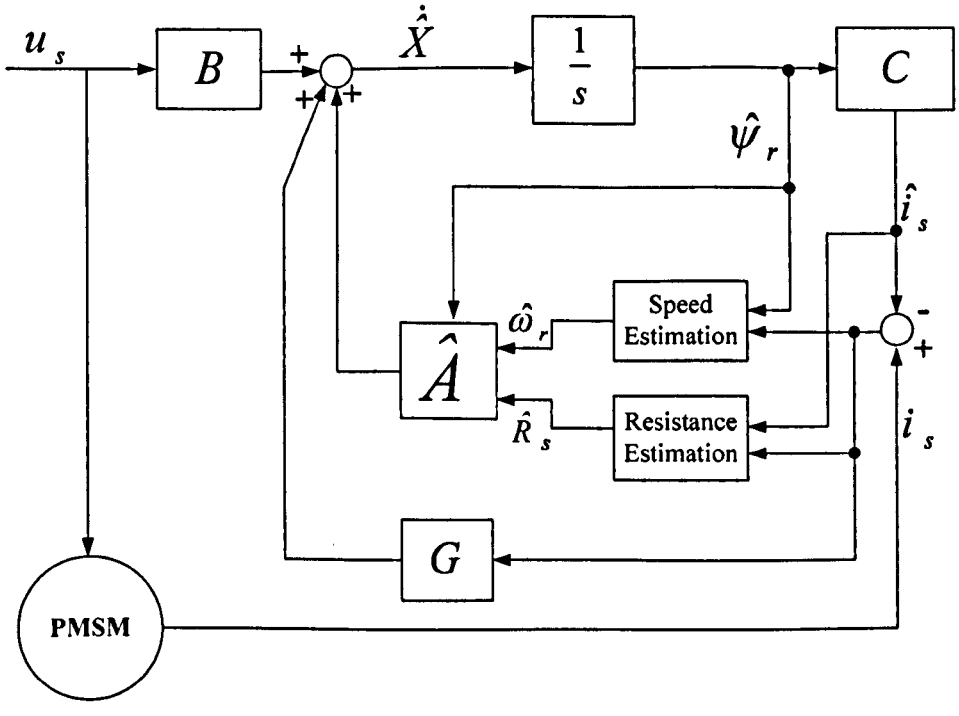

Fig 2.4 full observer with both rotor speed and stator resistance estimation

The full order observer sensorless control in [21] can operate the PMSM motor well at higher operation speed. Another model based estimator, MRAS is discussed next.

2.2.2 Model Reference Adaptive System

One of the major methods for model based closed loop adaptive control is the model reference adaptive system (MRAS). A MRAS consists of a reference model and an adjustable model, which have a parallel configuration [24]. The error vector is produced by comparing two outputs of the reference model and the adjustable model for a PMSM motor. The adjustable model continuously updates and corrects the unknown parameters to perform the adaptive function. The aim of using the adaptive model is to ensure that the system has excellent stability and dynamic performance. The error signal can be guaranteed to approach zero by this adaptive operation.

The voltage model is regarded as the reference model, while the current model is used to estimate the rotor speed and flux adaptively as the adjustable model. In [24], at zero and low speed, "the main drawback of this algorithm is its sensitivity to inaccuracies in the reference model, and difficulties of designing the adaption mechanism block in MRAS." The noise and disturbance occurs under low speed conditions and also the stator resistance in the voltage model is not accurate. The mechanism is constructed by a PI controller with the parameters K_p and K_I. The stator equation (2.13) is presented as the voltage reference model and in (2.14) the rotor equation is expressed as the current adjustable model for a PMSM motor. The current model requires the rotor speed ω_r estimate as an input to the model. To determine the rotor flux vector, pure integration is carried out in (2.13) and (2.14). The integration is difficult to implement in practice for both models because drift can be caused by small analogue offsets. In [15], low pass filters are used for both models and the model outputs can be optimized.

$$\frac{d}{dt}\begin{bmatrix} i_d \\ i_q \end{bmatrix} = \frac{1}{L_s}\begin{bmatrix} -R_s i_d + \omega_r L_s i_q + u_d \\ -R_s i_q + \omega_r L_s i_d + u_q \end{bmatrix} \tag{2.13}$$

$$\frac{d}{dt}\begin{bmatrix}\hat{i}_d\\ \hat{i}_q\end{bmatrix}=\begin{bmatrix}-\frac{R_s}{L_s} & \omega_r\\ -\omega_r & -\frac{R_s}{L_s}\end{bmatrix}\cdot\begin{bmatrix}\hat{i}_d\\ \hat{i}_q\end{bmatrix}+\frac{1}{L_s}\begin{bmatrix}\hat{u}_d\\ \hat{u}_q\end{bmatrix} \tag{2.14}$$

where the PMSM stator voltages u_d, u_q, stator currents i_d, i_q are represented in the rotating frame, as shown in Fig 2.5. R_s represents the stator resistance. The stator inductance is L_s. The reference equation contains stator voltage and current; and the adjustable model gives the estimated equation with stator current and estimated rotor speed. ω_r is representing the motor angular velocity. Reference [15] illustrates the basic configurations of MRAS in Fig 2.5. In Fig 2.5, two equations from both the reference and adjustable model are compared to determine the error signal. The error signal is sent to the adaption mechanism to obtain the estimated speed, and then the estimated speed is used to update the current adjustable model.

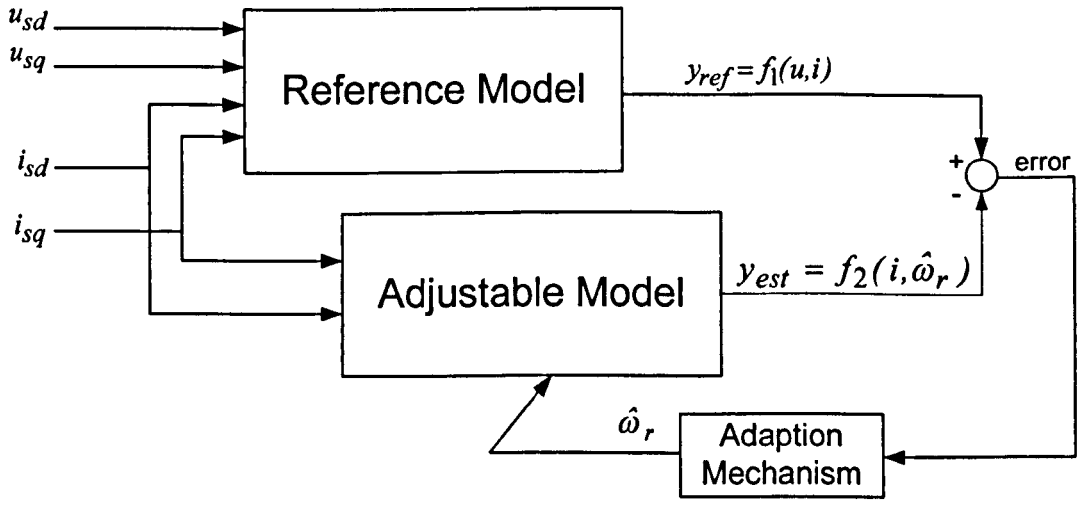

Fig 2.5 configuration of a parallel model reference adaptive system

Another MRAS structure is proposed in [25] that uses the back-EMF vector instead of rotor flux vector and the rotor speed is also identified. The advantage of this scheme is that it avoids the open loop integration. The stator resistance is not involved in this scheme. This scheme consists of stator current vector and back-EMF using maths operation to represent the instantaneous reactive power. This scheme also provides a closed loop flux observer for the low speed operation that can improve the estimation of rotor flux and rotor speed. This scheme is named as MRAS-CLFO because the closed loop flux observer is used. However, the

estimation failed at zero speed because of the unknown and incorrect mechanical parameters.

Two different MRAS structures have been reviewed. MRAS schemes are accurate at high rotor speed but fail at zero or low speed. The implementations of MRAS schemes are very simple and also efficient. In the voltage reference model, the stator voltage needs a pure integration to determine the desired rotor flux and this can cause the drift problems. All MRAS models are parameter dependent; therefore, the online tuning of parameters is necessary and important.

2.2.3 Extended Kalman Filter

In 1960, R.E. Kalman published his famous paper describing a recursive solution to the discrete-data linear filtering problem [26]. The Kalman filter consists of mathematical equations to estimate the state of a process and also attenuates the mean of the squared error recursively. The Kalman filter is basically an observer for the optimization of linear systems. The Kalman filter can be represented either in continuous or discrete form. The implementation of a discrete Kalman filter can be classified as two procedures, prediction and correction and they are circulated in a closed loop shown in Fig 2.6. The discrete Kalman filter involves the linearization of the model around an operation point. In Fig 2.6, the first prediction part is presenting the predicted state and the error covariance. As an update process, the second part is to correct the state using the measurement. The Kalman gain is then calculated and the error covariance is also updated after the estimation. The detailed equations for both parts are derived in [26]. The discrete extended Kalman filter (EKF) is the nonlinear version of the Kalman filter [26]. The state transition and observation models are nonlinear and a Kalman filter is not applicable to estimate for nonlinear motor models. Therefore, the EKF is suitable for estimation in motor applications because the EKF can provide an optimal estimation from a noisy measurement. [27] and [28] has implemented the EKF method for sensorless speed and position control. [16] reported the EKF technique using the discrete time domain to present the EKF equations for the estimation of stator current and rotor speed. The observer gain matrix is calculated in each step according to the noise covariance matrices [16]. The

Kalman filter with the observer gain produces the recursive least square estimation error with white Gaussian noise. Comparisons have been made in [16] through experimental results for different estimators. The conclusion is that the EKF algorithm may cause the problem when it implemented in a DSP system since the EKF is very complex and a 5th order matrix manipulation is needed [27]. The accuracy in using the EKF tends to be poor at zero and low speed; however, the EKF is suitable for estimation in a noisy system.

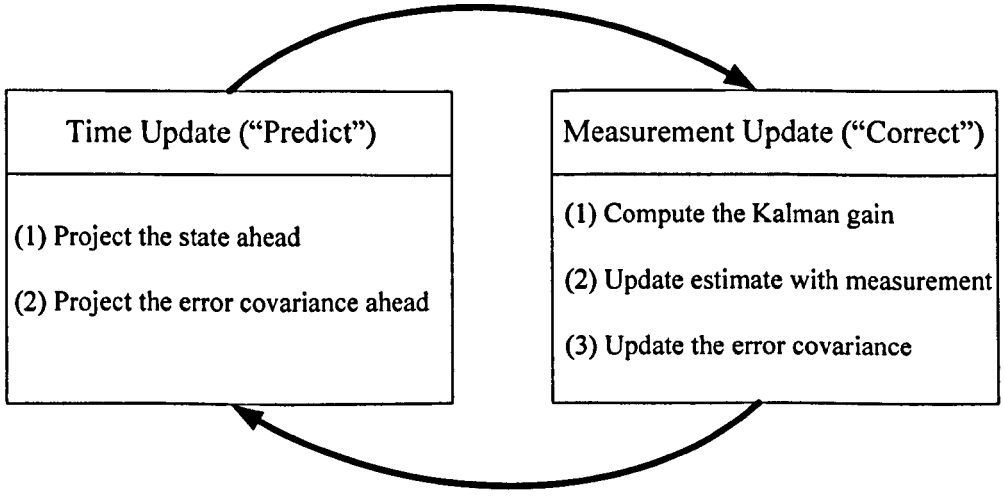

Fig 2.6 the operation of Kalman filter [26]

2.3 Saliency Tracking in Sensorless Control of PMSM

An alternative approach is introduced to track the inherent anisotropic properties of the machine. This approach uses the variations of stator inductance for the rotor position tracking. This approach is usually called "saliency tracking" by researchers. The saliency tracking methods can be divided into two groups: one uses the additional high frequency current or voltage injection signal to excite the motor saliency for position tracking, and the other uses the transient current response for the position estimation. In this section, the saliency of the PMSM is firstly discussed - its physical structures and properties. Secondly, some high frequency injection methods are described. Thirdly, the voltage vector excitation methods are discussed. Finally, two tracking mechanisms for position estimation are compared from the obtained experimental results so that one of them will be selected for this project.

2.3.1 Saliency in PMSM

The saliencies of a PMSM are asymmetric properties of the PMSM. The saliencies are related to the machine geometric structures, but also saturation. The *d* axis is defined to be the axis of the rotor magnets, and the q axis is at 90° to this. The physical structure of the rotor results in a longer "net" air gap in the *d* axis than the *q* axis, and therefore electrically, the *q* axis inductance L_q is higher than the d axis inductance L_d. Local saturation around the magnet poles can cause saturation and additional influences on the variation of L_d and L_q. The variations of inductance L_d and L_q represent the saliency and if it can be identified, it can be used to track rotor position. The tracking methods use the saliency/anisotropy effects to estimate the rotor position. Various saliencies have been investigated for PMSM: rotor inherent saliency [29], saturation based saliency [5], rotor and stator teeth harmonics [29], lamination direction based saliency [30], eddy current based saliency [31], and rotor eccentricity based saliency [31]. Because the saliency tracking methods using high frequency injection signal are investigated in this research project, the saliencies appearing in PMSM are described. PMSMs are starting to replace other types of machines in various applications as they have a higher efficiency, better power factor, better specific output power, and a better dynamic performance than induction motors without sacrificing reliability [17]. PMSMs can also operate over an extended speed range at approximate constant power by controlling the angle, between the stator and the rotor field [30].

In comparison with induction machines, PMSMs perform poorly with open-loop scalar control (Voltage/Frequency control), since the PMSMs do not have any electric coils in the rotor to provide mechanical damping in transient conditions. The rotor configurations of PMSMs become an important topic for sensorless control of AC drives. The different rotor configurations produce different effective saliencies. Additionally, different shapes of rotor can provide different inherent saliency and saturation induced saliency. The air gap and L_d and L_q variation is different. Obviously, the injection based sensorless control methods estimate speed and position from the differences in the inductance. According to the different rotor configurations, PMSM can be defined as the three different types that are shown in

Fig 2.7. Figure 2.7(a) shows that the magnets are mounted to the rotor's surface, which is defined as surface mount PMSM or SMPMSM. For example, in Fig 2.7(a), there are four pieces of magnet mounted on the rotor's surface and they are symmetrically facing each other. This geometrical structure provides a constant effective air gap length because the unique permeability of rare earth magnets is near unity. The second type shown in Fig 2.7(b) is inset-magnet rotor. The magnets are placed in shallow slots crating an inset-magnet rotor. This structural saliency can be defined as its inherent saliency due to the shape of the rotor. The rectangular magnets are placed in slots inside the rotor as shown in Fig 2.7(c) and this type of construction of rotor is called interior-magnet machine or IPM. IPM has been investigated for model based sensorless control by many researchers. IPM can avoid the centrifugal forces and demagnetization due to its inherent structure design. In [5], IPM "is highly salient and shows a significant amount of reluctance torque".

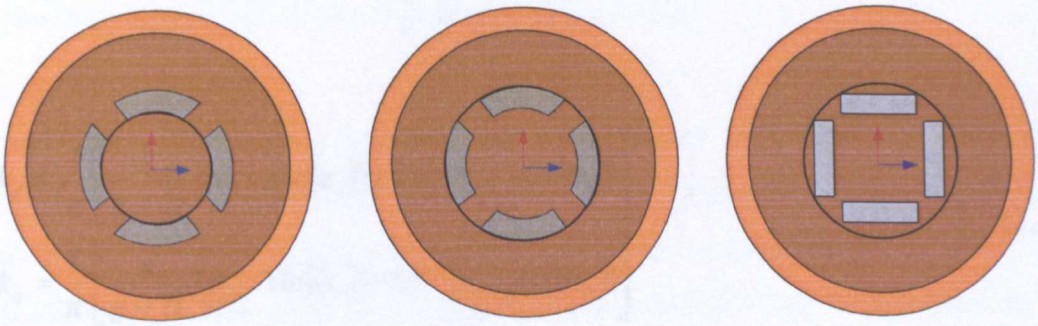

(a) (b) (c)

Fig 2.7 rotor structure of PMSM (a) Surface mounted (b) Inset (c) Interior

In theory, the saliency in surface mounted machines is defined as variations of stator inductances. In [32], the synchronous *d-q* axis inductances are presented by:

$$\begin{cases} L_d = L_{ld} + L_{md} \\ L_q = L_{lq} + L_{mq} \end{cases} \tag{2.15}$$

where L_{ld}, L_{lq} are the leakage inductance and L_{md}, L_{mq} are the magnetising inductance, which represent the fundamental flux crossing the air-gap. The leakage inductances are representing the tooth-top leakage flux, the slot, and end-connection of machine. The corresponding magnetizing inductances are also representing the fundamental

flux crossing the air gap [32]. For the high frequency injection scheme in PMSMs, an analysis of the effect of the rotor geometry saliency, and saturation saliency on leakage and magnetizing inductance is presented as follows.

1. Geometrical Saliency

The rotor geometry in IPM affects the values of magnetizing inductances L_{md} and L_{mq} in (2.15), when the air gap is sufficiently larger than the stator slot opening. The rotor geometry is represented as:

$$\begin{cases} L_{md} = k_d L_m \\ L_{mq} = k_q L_m \end{cases} \quad (k_d < k_q) \tag{2.16}$$

where L_m is the average magnetizing inductance, k_d and k_q are the form factors. The values of both form factors in [32] can be analytically calculated as a function of the rotor geometrical parameters. The equation for both form factors are expressed as: [6]

$$\begin{cases} k_d = \dfrac{1}{\pi}\left[\dfrac{g}{g+H}(\alpha_i + sin(\alpha_i)) + (\pi - \alpha_i - sin(\alpha_i))\right] \\ k_q = \dfrac{1}{\pi}\left[\dfrac{g}{g+H}(\alpha_i - sin(\alpha_i)) + (\pi - \alpha_i + sin(\alpha_i))\right] \end{cases} \tag{2.17}$$

where α_i is the angle spanned by magnets, g is the air gap length, and h is the width of rotor core. According the analysis of rotor geometry, the saliency is oriented with the rotor and $L_{md} < L_{mq}$. The ratios of L_q to L_d in IPM are 3:1 or higher [32].

2. Saturation Saliency

Sensorless speed and position control is achieved by injecting sinusoidal or additional transient excitation voltage pulses onto the PMSM [34]. It is based on spatial differences in the leakage inductance and utilizes these differences by evaluating the response of the PMSM due to the transient excitations. This excitation is generated with the voltage source inverter by applying the short voltage pulses. The saliency in the PMSM can provide the most important tracking information for position estimation purposes. In surface mounted PMSMs, without considering

significant structural saliency, there are some parts of the iron core that are saturated because the rotor magnets can generate a high air gap flux density. During the magnetic saturation of the machine, a spatial difference in the synchronous stator inductance appears in the machine. The magnetic saturation of the machine's iron may influence the leakage or main flux paths, modulating the leakage, and magnetizing inductances [5]. Therefore, the important discussion on saturation saliency is carried out for both effective inductances as follows.

- Saturation Saliency in the Magnetizing Inductance

Under no load, the rotor magnets generate a maximum flux density close to sinusoidal distribution around the air gap and it is aligned in the *d-axis* direction. Once the stator teeth and tooth tips are saturated by the flux, the air gap length is effectively increased for the main flux in *d-axis* and L_{md} is decreased. The saliency in the magnetizing inductance is presented as $L_{md} < L_{mq}$

Under load conditions, the magnetizing inductances are influenced as a function of load. The additional term $L_m i_q$ is produced by the torque producing current i_q. The air gap flux distribution is shifted by the additional term towards the *q-axis*. Therefore, the saliency position angle in the magnetizing inductance has been shifted in the synchronous *d-q axis*. The new coordinate is alternatively defined as the δ-γ frame, which is shifted from the *d-q axis*. Hence, the saliency in the magnetizing inductance is presented by $L_{m\delta} < L_{m\gamma}$.

- Saturation Saliency in the Leakage Inductance

The saturation effect results in the stator leakage flux path (mainly from machines' slot and tooth-tip leakage) producing a spatial modulation on the leakage inductances. This saturation is produced by the machine's main flux. The leakage inductance saliency can be obtained under no load or load conditions.

With no load, the main flux saturation is produced by the rotor magnets in the *d-axis*. The stator teeth and tooth tips around *q-axis* are influenced by this saturation from *d-axis*. The permeance of the leakage flux path in *q-axis* is reduced by this effect. The

leakage inductance L_{lq} is decreased and the saliency in the leakage inductance is given $L_{ld} > L_{lq}$.

Under load, the saliency position angle in the leakage inductance is shifted with respect to the *d-axis*. The new coordinate frame is defined as δ-γ; therefore, the saliency in the leakage inductance is represented as $L_{m\delta} > L_{m\gamma}$.

The analysis of the saliencies in the magnetizing and leakage inductance shows the flux produced by the rotor magnets can cause saturation in both inductances in *d-q* axis are in opposite direction; therefore, the saturation saliency in the leakage and magnetizing inductance tend to cancel each other. The stator inductance is established by both magnetizing and leakage inductance. The high frequency injection scheme uses the test signal to detect the variation of total stator inductance. This test signal can produce flux in the rotor; however, this flux cannot flow through the main flux path. The leakage inductance saliency is the only required information for saliency tracking. The saturation induced saliency in the synchronous rotor reference frame during the transient can be modelled as [35]

$$L_{\sigma s}^{r} = \begin{bmatrix} L_{\sigma qs}^{r} & 0 \\ 0 & L_{\sigma ds}^{r} \end{bmatrix} = \begin{bmatrix} \Sigma L_{\sigma s} + \Delta L_{\sigma s} & 0 \\ 0 & \Sigma L_{\sigma s} - \Delta L_{\sigma s} \end{bmatrix} \tag{2.18}$$

where the transient leakage inductances on the *d-q* axis are $L_{\sigma ds}^{r}$ and $L_{\sigma qs}^{r}$, the differential stator transient inductance is $\Delta L_{\sigma s} = \frac{1}{2}\left(L_{\sigma ds}^{r} - L_{\sigma qs}^{r}\right)$, and the average stator transient inductance is $\Sigma L_{\sigma s} = \frac{1}{2}\left(L_{\sigma ds}^{r} + L_{\sigma qs}^{r}\right)$. The equation (2.18) can be transformed into the stationary reference frame; this can be further represented in equation (2.19) as follows [32].

$$L_{\sigma s}^{s} = \begin{bmatrix} L_{\sigma \alpha s}^{s} \\ L_{\sigma \beta s}^{r} \end{bmatrix} = \begin{bmatrix} \Sigma L_{\sigma s} + \Delta L_{\sigma s} \cos(2\theta_r) & -\Delta L_{\sigma s} \sin(2\theta_r) \\ -\Delta L_{\sigma s} \sin(2\theta_r) & \Sigma L_{\sigma s} - \Delta L_{\sigma s} \cos(2\theta_r) \end{bmatrix} \tag{2.19}$$

where θ_r is the position of saliency in electrical degrees. In (2.19), the electrical frequency of rotor is doubled to give the inductance modulation, according to the obtained the position angle. The fact is the saturation existing around two rotor poles in one electrical period. As mentioned, the position of saliency is changed by an angle offset due to the total air gap flux distribution towards the *q-axis*. The

saturation angle can be obtained by this deviation as: $\varphi = \theta_\delta - \theta_r$. That means the saturation saliency is displaced from the rotor reference frame by angle offset φ. The angle offset needs to be compensated when the load condition is applied on the PMSM. Therefore, the saliency for estimation is proportional to the torque produced current i_q. For more details of angle offset calibration, it can be found in chapter 4.

2.3.2 Position Estimation Using High Frequency Signal Injection

The high frequency (HF) signal injection method uses an additional HF signal added to the fundamental excitation component. The induced HF signal is modulated by saliency. The rotor position or flux position can be tracked through the measurement and demodulation of the HF response. The injection signal is sinusoidal or square wave and the frequency range is between several hundred Hz to several KHz. The saliency position information is tracked continuously by the HF sinusoidal or square wave excitation. The excitations can be a voltage vector injected to the output of the current PI controller [36] or a current vector injected to the input of the current PI controller [37]. The comparison of both types injection signal is made in [6]. The HF current injection is generally noisier than the HF voltage injection and the limitation of carrier frequency is caused by the bandwidth of current controller. Therefore, the HF voltage injection signal is most commonly used to measure the resulting HF currents for position estimation. Several proposed voltage injection methods are presented as follows.

2.3.2.1 The Rotating Signal Injection in the Stationary Frame

This voltage injection method is often called "α-β injection" because the rotating voltage signal is applied in a stationary frame. The voltage signal with constant voltage amplitude rotating at the injected high frequency can be represented as:

$$\tilde{V}_{\alpha\beta} = \hat{V}_i e^{j\omega_i t} = \hat{V}_i \begin{bmatrix} \cos\omega_i t \\ \sin\omega_i t \end{bmatrix} \tag{2.20}$$

where $\hat{V}_i$ is the amplitude and ω_i is the frequency of the HF voltage vector $\tilde{V}_{\alpha\beta}$, so three phase voltage vector is persistently rotating as an injection signal in the stationary frame. In [5], the resultant HF current vector was derived from the applied voltage vector as:

$$\begin{bmatrix} \tilde{i}_\alpha \\ \tilde{i}_\beta \end{bmatrix} = \frac{\hat{V}_i}{\omega_i L_{\sigma d} L_{\sigma q}} \begin{bmatrix} \Sigma L_{\sigma s} \cos(\omega_i t) + \Delta L_{\sigma s} \cos(2\theta_r - \omega_i t) \\ \Sigma L_{\sigma s} \sin(\omega_i t) + \Delta L_{\sigma s} \sin(2\theta_r - \omega_i t) \end{bmatrix} \tag{2.21}$$

where $L_{\sigma d}$, $L_{\sigma q}$, $\Delta L_{\sigma s}$, and $\Sigma L_{\sigma s}$ are already defined in (2.18). In (2.21), the HF current contains two useful components: One is a positive sequence HF current vector; the other is a negative sequence HF current vector. The positive and negative sequence can be represented by [5]

$$\tilde{i}_{\alpha\beta} = \tilde{i}_{ps} + \tilde{i}_{ns} = \frac{\hat{V}_i}{\omega_i L_{\sigma d} L_{\sigma q}} \left(\Sigma L_{\sigma s} e^{j\omega_i t} + \Delta L_{\sigma s} e^{j(2\theta_r - \omega_i t)} \right) \tag{2.22}$$

In order to separate the HF current components from the fundamental stator current components, a heterodyne demodulation method is proposed in [6]. The filter operation is implemented in an estimated frame synchronous with the negative sequence rotating current vector, which is given by:

$$\tilde{i}_{\alpha\beta} \cdot e^{-j(2\hat{\theta}_r - \omega_i t)} = \frac{\hat{V}_i}{\omega_i L_{\sigma d} L_{\sigma q}} \left(\Sigma L_{\sigma s} e^{-j(2\hat{\theta}_r - 2\omega_i t)} + \Delta L_{\sigma s} e^{j(2\theta_r - 2\hat{\theta}_r)} \right) \tag{2.23}$$

The transformation is shown in (2.23) that can separate the HF carrier and the sideband. The negative sequence with the saliency position information can be extracted by a low pass filter, which is given by [6]:

$$\tilde{i}_{ns} \cdot e^{-j(2\theta_r - \omega_i t)} \approx \frac{\hat{V}_i}{\omega_i L_{\sigma d} L_{\sigma q}} e^{j(2\theta_r - 2\hat{\theta}_r)} \tag{2.24}$$

The heterodyne demodulation process consists of band pass filters, low pass filters, and tracking mechanisms, as shown in Fig 2.8 [6]. In (2.24), the imaginary part can give the result of rotor position estimation error and this drives the tracking observer to estimate the position angle and speed response.

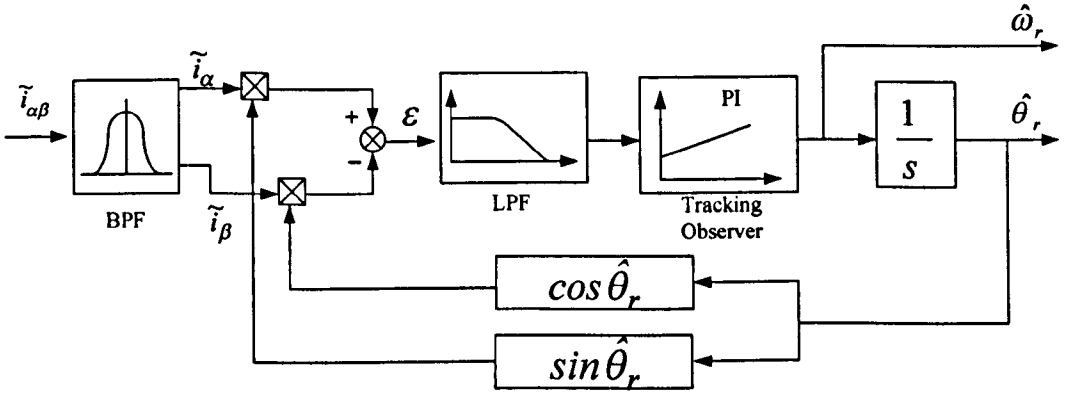

Fig 2.8 heterodyne demodulation method and tracking observer

2.3.2.2 The Pulsating Signal Injection in the Estimated Rotor Frame

An alternative approach uses a pulsating signal injected along a synchronous and specific direction, normally along the estimated rotor frame *d-axis*. There are also some HF injection-methods applied in *q-axis* [38], although they cause large torque oscillations. In this research, four methods using the pulsating voltage vector injection along *d-axis* are investigated under different conditions. The aim of using HF signal injection along the *d-axis* is to minimize the torque ripple. The motor operation is normally considered for zero and low frequency operation. The measurement axis method as one of four examined methods is discussed next.

In [39], the HF impedance during the saturation caused by the machine's main flux is assumed symmetrical along the d or q axis. The measurement axis method uses a synchronous measurement frame (d^m-q^m), which is established at 45° to the estimated rotor frame d-q axis. The amplitude of measured impedance in the d^m and q^m are same when the estimated d-q frame superimposes on the real d-q frame. This method uses the measurement of the HF impedances in both axes (d^m and q^m) and compares their amplitude. The amplitude differences of the impedance in the measurement frame can be defined as the orientation error. Thus this error can be used to estimate the position angle. The HF voltage in the estimated rotor frame d-q can be defined as:

$$\begin{bmatrix} \tilde{v}_d \\ \tilde{v}_q \end{bmatrix} = \hat{V}_i \begin{bmatrix} sin(\omega_i t) \\ 0 \end{bmatrix} \tag{2.25}$$

The HF current response is modulated by the saliency, and can be processed to obtain the error signal using a demodulation process. The error signal drives a tracking observer to estimate the position angle and also provides a speed estimate. A detailed explanation about the demodulation is given in chapter 4 and the selection of the tracking observer is described in the later part of this chapter.

2.3.2.3 Eddy Current Reflected Resistance and Inductance Based Method

This section presents an overview of a proposed sensorless method of the PMSM using HF signal injection. Eddy currents are produced in conductors, when a conductor is exposed to the moving magnetic field; or when a moving conductor is perpendicular to the magnetic field. This can cause a current circulating flow inside conductors and thus induce a magnetic field. The eddy current in conductors can also cause overheating and power losses. In [45] and [46], the eddy current losses have been investigated for predicting the rotor eddy current and compensation of the eddy current caused power losses. In [44], the investigation is based on an IPM machine to determine the source of the eddy current. The rotor eddy current losses are mainly produced in the permanent magnet and induced by the forward and backward non-synchronized armature reaction fluxes in the stator [72]. However, the eddy current

can be utilized to estimate the rotor position. The reason is because the HF injection signal can induce the saliency by reflecting the stator asymmetrical resistances and inductances. Therefore, the additional eddy current losses are also considered due to the non-synchronized HF armature fluxes induced by the superimposed voltage [73]. In the PMSM, eddy currents flow in the rotor magnets and the sensorless technique requires the presence of a machine spatial saliency and an injected HF excitation signal. When the rotor rotates, the spatial saliency can be viewed as either a change in stator inductance or resistance. For the PMSM, the main flux saturation and stator leakage flux saturation can induce the inductance based saliency. The inductance based saliency is used to implement the sensorless closed loop control. The sensorless estimation methods rely on the interaction between a HF excitation signal and the eddy current reflected resistance and inductance based saliencies presented in the PMSM.

Eddy currents are produced by a variation in the magnetic flux according to Faraday's Law. An equivalent circuit is introduced for considering the eddy current loss in [72]. Finite element analysis (FEA) was performed to predict the property of eddy current loss in the machines. The rotor resistance in the *q-axis* is perpendicular to the rotor flux and the eddy current is induced only in the laminated steel. Therefore, the resistance in the *q-axis* only depends on the resistivity of the rotor laminated steel. In [44], for a particular example in a surface mounted PM machine, the resistances in the *d-q* axes mostly depend on the eddy currents induced in the permanent magnets of the rotor surface. For a surface mounted PM machine, the spatial saliency can be seen as a variation in the inductance L_d and L_q as the rotor rotates. The inductance-based saliency is difficult to detect due to the rotor structure being almost symmetric. The inductance-based saliency is mainly caused by the magnetic flux saturation and has a load-dependent property. Tracking the inductance based saliency is difficult in surface mounted machines, in respective of the method (α-β injection, d-axis injection, etc). Therefore, the inductance-based saliency is more sensitive to fundamental torque loads. The quality of estimation is poorer when compared to other motor types. Overall, to use the saliency induced by eddy current for sensorless control, the stator geometry can be designed to create the measurable flux saturations either in the resistance or in the inductance of stator. The persistent

HF voltage vector excitation is superimposed on the fundamental voltage to provide high bandwidth position estimation. The induced current response can be demodulated to produce the error signal, which can drive the tracking observer to obtain the field angle and estimated speed. In chapter 4, the detailed tracking process is presented and its performance is analyzed through comparison with other *d-axis* injection methods in chapter 6.

2.3.2.4 PWM Switching Frequency Injection Method

A method has been proposed in [49, 74], which injects a rectangular waveform rather than a sinusoidal waveform, and can actually create this at a higher frequency as it only requires a few successive PWM switching periods. With the increased "injection frequency", there are fewer requirement for filtering, as the speed or position observer are now sufficient and this can reduce delays incurred by filtering. As a result, the bandwidth of current and speed controllers can be increased to a higher value than when using the sinusoidal injection signal. The injection frequency can be increased up to half the PWM switching frequency used for the voltage modulation. In sinusoidal type injection methods, the demodulation process contains low pass filters, band pass/high pass filters, and maths operations. However, these signal processing operations are all eliminated when using the PWM switching frequency injection method. The only computation is to calculate the error signal for position estimation, obtained from HF current response of the *d-q* frame. The current error signal drives the tracking observer to estimate the position angle for sensorless control. In [49, 74], several possible square wave type voltages are considered using different PWM switching periods. In this project, only two types of desired voltage signals are used: a 1 KHz and a 2.5 KHz square wave signals. The injected voltage signal has positive and negative amplitude during one PWM switching period. The ideal injection signal is shown in Fig 2.9. This can be achieved in the control programming. Reference [49, 74] summarized the advantage of this type injection method as follows:

1. No time delay in tracking the rotor position because there are no low pass filters;

2. Fundamental and injection frequencies are well separated due to a higher injection frequency used;

3. The bandwidth of speed and current controllers can increase for improved system performance.

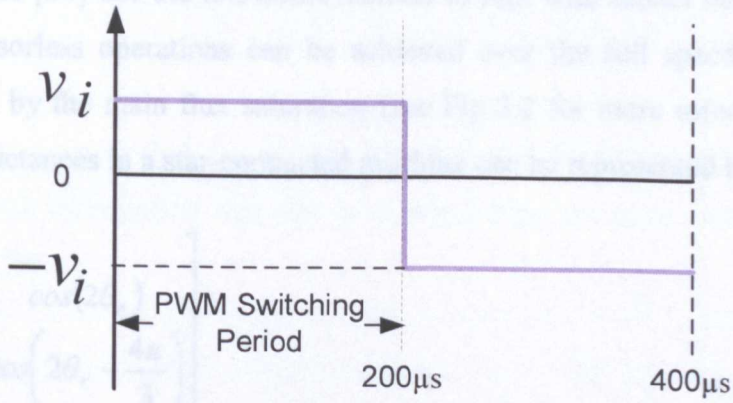

Fig 2.9 the injection signal with half the PWM switching frequency

2.3.3 Position Estimation using Transient Current Response

In this section, another saliency tracking scheme is introduced and this scheme makes uses of the transient motor current response to a change in PWM state [50]. The position dependent saliency can be obtained due to rotor slotting effect for PMSM machines or main magnetic flux saturation for PM machines. The first method for voltage vector excitation is the INFORM (Indirect Flux detection by On-line Reactance Measurement) method [34]. The INFORM method is based on real-time inductance measurements using specific test pulses. The second method uses the PWM switching vector changes to integrate the transient excitations into the fundamental PWM waveform. The estimation can be achieved by measuring the current derivatives associated with each switching vector. For both methods, the position estimation can be achieved, because the PWM voltage vector causes a change in stator current which is limited by the leakage inductance, which varies as a function of position. The position estimation can also be achieved by tracking the leakage inductance variations induced by the saturation saliency.

2.3.3.1 The INFORM Method

The INFORM method is the first method to achieve the saliency tracking by using active voltage test vectors [34]. This method has been investigated by many researchers [5, 50, 51] due to its much improved low speed or standstill operation. Some researchers [54] use the INFORM method to link with model based methods so that the sensorless operations can be achieved over the full speed range. The saliency caused by the main flux saturation (see Fig 3.2 for more information) and the leakage inductances in a star-connected machine can be represented by: [50]

$$\begin{bmatrix} l_a \\ l_b \\ l_c \end{bmatrix} = l_0 + \Delta l \begin{bmatrix} cos(2\theta_r) \\ cos\left(2\theta_r - \frac{4\pi}{3}\right) \\ cos\left(2\theta_r - \frac{8\pi}{3}\right) \end{bmatrix} \tag{2.26}$$

where l_0 is the average inductance, Δl is amplitude of inductance variation caused by saliency, and θ_r is rotor flux angle. The applied voltage vectors during the PWM switching period are defined as six active vectors ($u_1 \sim u_6$) and two null vectors (u_0 and u_7). The voltage vectors produce a transient current response depending on the inverter's switching state, DC link voltage, stator resistance R_s, the phase leakage inductance l_k, and the back EMF voltages E_k. (2.27) shows their relationships as: [5]

$$u_k = R_s i_k + l_k \frac{di_k}{dt} + E_k \tag{2.27}$$

The input voltage u_k depends on the voltage vector used. The value of u_k can be $\pm U_{dc}$ (DC Link Voltage) for active vectors or 0 V for null vectors. The back EMF voltage E_k in (2.27) can be neglected when operating at low speed. In [34], test vectors u_1, u_3, and u_5 are chosen when they align with the spatial direction of the three phases a, b, and c. The rotating position vector $\underline{p}$ for the star-connected machine can be defined and the flux position can be obtained by measuring the current derivatives [34]. Hence, the position vector $\underline{p}$ is given as: [34]:

$$\underline{p} = \frac{di_a^{(u_1)}}{dt} + a^2 \frac{di_a^{(u_3)}}{dt} + a \frac{di_a^{(u_5)}}{dt} \quad (a = e^{j2\pi/3}) \tag{2.28}$$

$$\underline{p} = p_\alpha + jp_\beta \tag{2.29}$$

$$\theta_r = \frac{1}{2} a\tan\left(\frac{p_\beta}{p_\alpha}\right) \tag{2.30}$$

Equation (2.29) is simplified by (2.26) and (2.28) in [50]. (2.29) contains the rotor/field position information that can be obtained thus the rotor flux angle θ_r is calculated in (2.30).

For the current derivative measurement, two ways are considered. The first uses external di/dt sensors or Rogowski coils, and the second uses the motor current samples within a time period to calculate the current derivatives. Successful operation has been reported [5, 34, 50, 55]; however, problems appear on the measurement. High frequency oscillations appear and impede the sampling of current or current derivatives. These high frequency oscillations are due to the response of the parasitic capacitances within the motor and cable reacting to the high dv/dt when the IGBT in the inverter switches state. In [34], a Kalman filter is implemented for the acquisition of current derivatives to reduce the influence of the noise. The rotor flux position varies as load changes and a simple correction method is described in [34]. A novel technique is introduced in chapter 3 of this thesis for the acquisition of current derivatives with reduced noise.

For higher speed operation, the back EMF voltage E_k in (2.27) cannot be neglected. To avoid calculating the back EMF explicitly, two opposite test vectors are applied to cancel these effects. In [50] for the fundamental PWM excitation based method, a position scalar table for three phase position vectors can be established to estimate the rotor flux angle accordingly. In [51], the INFORM method is implemented for a delta-connected machine and the zero sequence currents are measured for the

position estimation. The symmetrical structure of a PMSM can also use the INFORM method in [52] and an improvement of estimation quality is also described in [52] by using the direct axis current. In theory, the INFORM method is only applicable for sensorless operation at the low speed. The reason is that the test vectors are carried by the null vector, and which will be shorter when the rotor speed increased [5]. As mentioned in [54], the combination of a model based method and the INFORM method can be used to operate sensorless control in any speed range.

2.3.3.2 Fundamental PWM Excitation

The fundamental PWM excitation method is a scheme proposed by Gao [50]. This scheme is based on the voltage vector excitation, which employs vectors from the normal PWM to achieve the excitation for di/dt measurement. This scheme can be used with sine wave PWM modulation (SPWM) or space vector PWM (SVPWM) with various sampling methods. The current transients are measured to establish the position vectors. The fundamental PWM excitation has the advantage over the INFORM method in terms of the current ripples and acoustic noise; however, the difficulty of this method is obviously with the di/dt measurement and sampling operation in the acquisition system. The inverter caused high frequency switching oscillations in the stator currents always appear within every PWM period. In chapter 3, a method is proposed to reduce the influence of these oscillations, and is demonstrated by the simulation work.

The aim of using the fundamental PWM excitation scheme is to estimate the position information without additional test vectors as in [34]. The excitation for position estimation is achieved using two active vectors in one standard PWM period. In comparison with the INFORM method, this method does not require any opposite test vectors to cancel the effects induced by back EMF and resistive voltage drop when the rotor rotates at higher speed. Instead of adding the test vectors, the measurements during the null vectors are considered as an advantage of this method. When one of the applied voltage vectors is less than the minimum pulse duration [5, 50], this vector is termed the "Narrow Vector" [5, 50]. The extended modulation

methods is used to extend the active vectors in the first half of the PWM period and are compensated by shifting the switching instants of one or two phases is made in second half of the PWM period [5]. For the measurement of di/dt, three hand made inductive coils are used as di/dt sensors, which work on the same principle as the Rogowski coil [5]. The obtained di/dt samples can be utilized for position estimation for both star-connected and delta-connected machines [50]. For convenience, a simplified position scalar table is proposed in chapter 3, which reduces the number of current derivative samples.

2.3.4 Tracking Mechanism

In this section, an overview of tracking observers is described and a comparison is made. The experimental results are illustrated to confirm the best tracking observer to be used in this thesis.

2.3.4.1 Mechanical Observer

A mechanical observer is shown in Fig 2.10. The input ζ is proportional to the position error. The position error is used to obtain the estimated position information. A phase locked loop could be used instead of a mechanical observer. However the mechanical observer can be tuned to the mechanical parameters of the drive system to act as a filter which tunes itself to the operating speed. In addition, the mechanical observer can incorporate the torque demand (T) as a feed-forward terms to improve dynamic response. Both PLL and mechanical observer use the error signal to estimate rotor position angle and speed. The PLL is constructed by a closed loop PI **(proportional-integral)** controller and a mechanical observer is a closed loop PID **(proportional–integral–derivative)** controller combined with the mechanical parameters of the system. The PID controller is derived from the machine parameters such as inertia (J) and friction (B), thus it is referred to as "mechanical observer". The dynamic properties of the mechanical observer are defined by its mechanical coefficients K_P K_I and K_D in (2.31).

$$H(s) = K_P + \frac{K_I}{S} + K_D S = \frac{K_D S^2 + K_P S + K_I}{S} \tag{2.31}$$

The transfer function of the mechanical observer is expressed in (2.31), which is a closed loop PID controller. The controller is constructed as a second-order transfer function. The advantage using a PID controller is that the estimation noise is reduced because its transfer function acts as a low pass filter and the quality of estimation is improved. The torque is added as a feed forward input to the mechanical observer and this provides zero lag [6] and the error can be effectively minimized to zero. For the four different sensorless methods examined in this thesis, the PID controllers have the same bandwidth of 35Hz and this bandwidth should be faster than the actual dynamics of the control systems. The bandwidth of speed controller is designed to be 7Hz so that the mechanical observer converges 5 times faster than the speed controller.

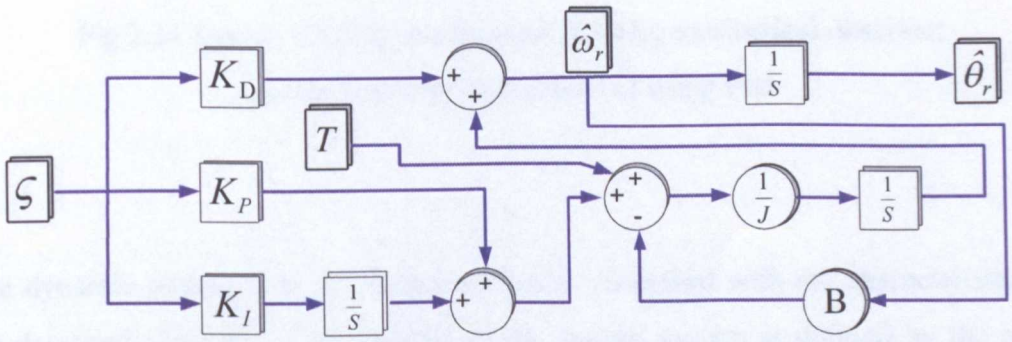

Fig 2.10 mechanical observer block diagram for position/speed estimation

2.3.4.2 A Comparison of the mechanical observer with a Phase Locked Loop

In this section, the mechanical observer and PLL are compared through their design procedures and experimental results. The block diagrams for both are shown in Fig 2.11. The demand torque can be added onto the mechanical observer to improve performance and provide the best response under various conditions; e.g. during the load or speed transient. A conventional PLL with double integration is shown in the lower plot of Fig 2.11. During the changes to the operation on the drive, the PLL response may be tuned easily by adjusting the proportional gain [71]. Both of the tracking mechanisms are obviously different; however, a similar dynamic performance can be obtained from these two different tracking algorithms.

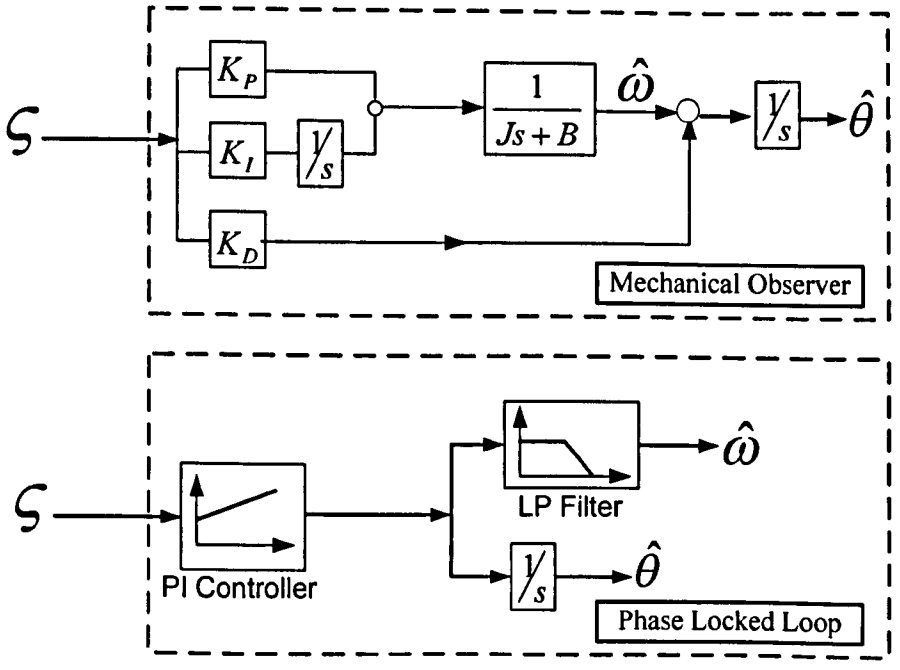

Fig 2.11 Upper: tracking mechanism of using mechanical observer;
Lower: tracking mechanism of using PLL

The dynamic response of the control system is described with the characteristics of the designed controller. The stability of the control system is defined by the poles and zeros. The root-locus method is used to define the gain parameters of mechanical observer (*Left*) or PLL (*Right*) as shown in Fig 2.12. Obviously, the mechanical observer (PID controller) has an additional zero components compared with the PLL (PI controller). The estimation results are different because the structure of a PLL is a first order system and the PID controller is a second order system. On the other hand they have the different attenuations. In the root-locus design, the natural frequency of the PID controller is 35Hz and the damping factor is 0.707. The controller with designed PID parameters with K_p, K_i can be calculated in (2.32).

$$G_c(s) = K_P + \frac{K_I}{s} = 1.1259 + \frac{75.5029}{s} \tag{2.32}$$

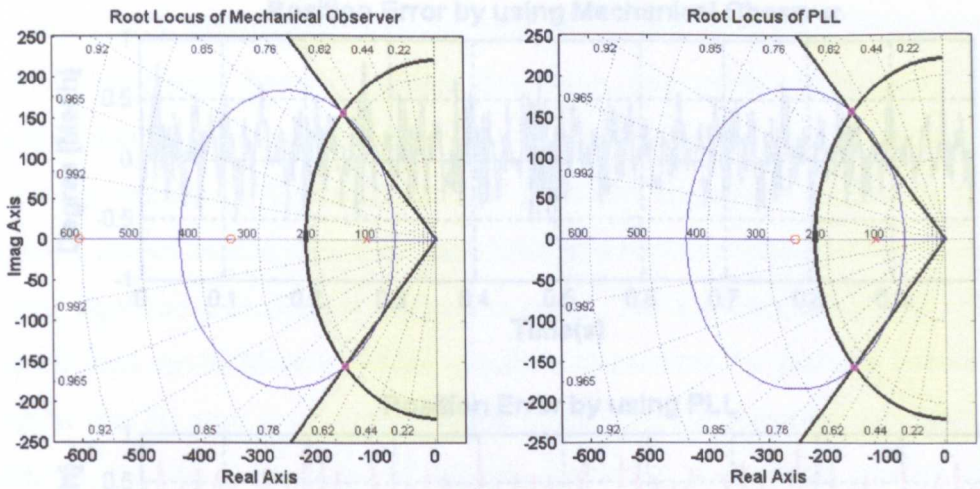

Fig 2.12 Left: root-locus method of mechanical observer (PID Controller)

Right: root-locus method of phase locked loop (PI Controller)

In Fig 2.13, the position estimations from both mechanical observer and PLL are shown at 100 rpm with load. Both methods provide a good quality of estimation in the steady state. The lower plot of Fig 2.13 presents the position error (peak value) by using the PLL method. The maximum amplitude of the error signal is over 1° mechanical. In comparison, the amplitude of the position error from the mechanical observer is lower than from the PLL. Therefore, the mechanical observer can definitely provide excellent performance. The mechanical observer using three terms of gain is applicable to estimate the position and speed instead of the encoder. The flexibility of tuning the parameters can always generate a superior estimation of rotor position and speed than the PLL. Therefore, the mechanical observer is probably the most-used feedback controller in the sensorless control of a PMSM. In this project, the mechanical observer is implemented for the four different *d-axis* injection methods compared.

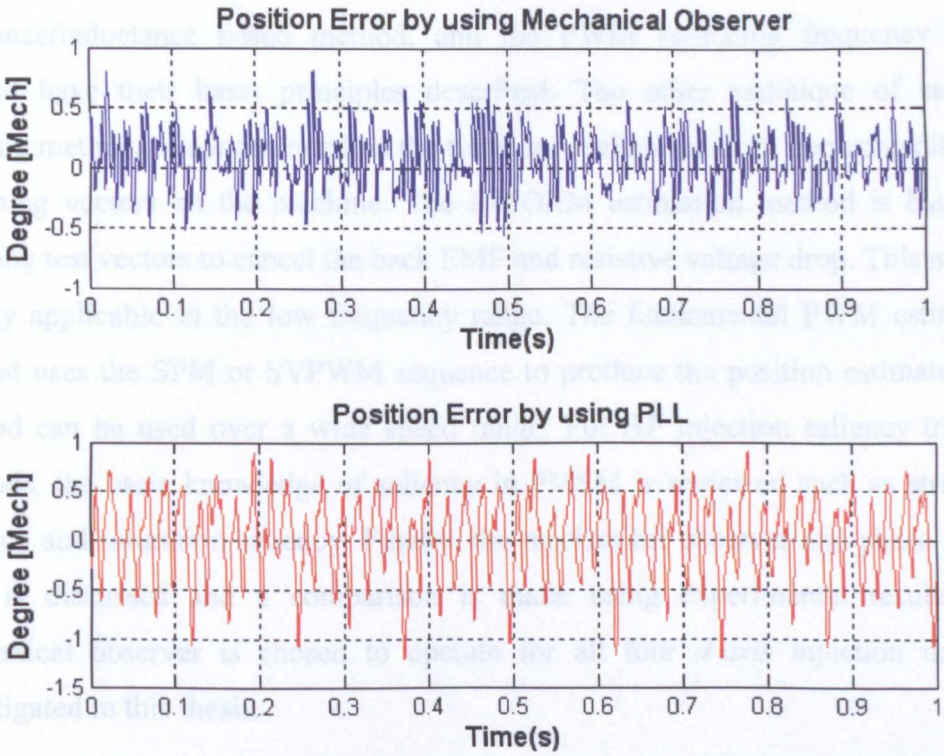

Fig 2.13 Upper: position error in sensorless control (Mechanical observer);
Lower: position error in sensorless control (PLL)

2.4 Conclusions

The literature for sensorless control of AC machines has been reviewed in this chapter. The mathematical model based methods and the saliency tracking methods have been identified. The MRAS method, the full order observer method, and the extended Kalman filter method have been briefly described: they are based on the mathematical model of AC machines. The model based methods can provide a good sensorless control performance at higher speed. However, all the model based methods fail at low frequency. Therefore saliency tracking methods are introduced for position estimation at very low and zero speed. There are two different techniques based on saliency tracking methods. One is to track the saliency effects by injecting a HF signal into the machine. The injection signal is defined to use voltage injection signal rather than current injection signal due to the noise and limitation of the current controller. Both pulsating and rotating injection methods are reviewed. The voltage signal for HF injection methods uses either sinusoidal type or

square wave type injection. The measurement axis method, eddy current resistance/inductance based method, and the PWM switching frequency based method have their basic principles described. The other technique of saliency tracking methods is concentrated on the transient excitations from imposing different switching vectors on the machine. The INFORM estimation method is based on applying test vectors to cancel the back EMF and resistive voltage drop. This method is only applicable in the low frequency range. The fundamental PWM estimation method uses the SPM or SVPWM sequence to produce the position estimate. This method can be used over a wide speed range. For HF injection saliency tracking methods, the basic knowledge of saliency in PMSM is reviewed such as structural saliency and saturation saliency. Finally, the mechanical observer and phase locked loop is discussed and a comparison is made using experimental results. The mechanical observer is chosen to operate for all four *d-axis* injection methods investigated in this thesis.

This thesis will concentrate on the sensorless vector control based on the *d-axis* HF injection methods. There are four different types of *d-axis* injection based sensorless control methods developed and applied to a surface mounted PMSM. The comparisons from four sensorless methods are achieved under the various speed and load conditions. The four methods investigated are: the pulsating sinusoidal type voltage injection signal is applied in the measurement axis method and eddy current reflected resistance/inductance based method, and the pulsating square wave type voltage injection signal applied in the PWM switching frequency injection method. The four sensorless methods all take the main advantage of *d-axis* injection to minimize the HF current in the torque producing axis, hence minimizing the acoustic noise and pulsating torque. To compare the estimation quality and dynamic performance for four sensorless methods, the steady state operation and load impacts are investigated. The phase shift in position error is identified as a function of a load, when adding the load conditions. To ensure the estimated position and speed signals have good quality for the four different sensorless control methods, the angle offset calibration is needed to compensate the angle phase shift by using a look-up table. A mechanical tracking observer is designed to minimize the error signal and filter the noise appearing in the estimated position signals. After the proposed improvements, the four types of sensorless speed and position control are achieved for a surface

mounted PMSM. Their estimation quality and dynamic performance is validated by experimental results. In chapter 3, the other type of sensorless method is also briefly described and overviewed, which uses the tracking method based on the PWM excitation induced saliency for a sensorless control in the PMSM. The sensorless technique using the current derivative measurement is discussed and a new improved position scalar table is also presented. Finally, an optimal method using signal processing is introduced in order to measure the current samples during the oscillation period to obtain the current derivative and estimate the saliency position.

Chapter 3

Enhanced Current Derivative Measurement

3.1 Introduction

Saliency tracking methods for sensorless control of PMSM machines can be classified as high frequency injection or voltage vector excitation. In this section, the saliency tracking by voltage vector excitations method for sensorless control is described and reviewed. The current derivative measurement required for these methods can be achieved in two ways. One uses three low cost current derivative (*di/dt*) sensors to measure the current derivative directly; the other uses the motor line current samples to determine the current derivatives without additional *di/dt* sensors. The position scalars can be established by using the current derivatives alone, in response to specific voltage vectors, as described in [5, 50]. However, these di/dt measurements can be seriously disturbed by parasitic effects within the drive system. The high di/dt associated with inverter switching can excite the parasitic capacitance to ground in the cable, machine, and inverter heatsink, and this causes high frequency oscillations which must die down before di/dt can be measured, and this imposes a minimum vector width t_{min} onto the PWM scheme. This chapter introduces an optimization using a signal processing method in order to measure the current derivative during the oscillation period. Experimental results illustrate the performance of the estimation under various operating conditions.

3.2 Sensorless Control using Current Derivative Measurement

In this section, two methods for sensorless control are introduced which use the motor response to PWM voltage vector excitations. The first method uses the three low cost *di/dt* sensors to obtain the current derivatives directly and the second method uses the current samples within a voltage vector to determine the current derivatives. By using either method for *di/dt* measurement, the estimated position vectors can be established. The measurement of current derivatives with and without *di/dt* sensors is described in this section. The measurement of the current derivatives without three-phase di/dt sensors is demonstrated using simulation results obtained using an *S-function* embedded in a Simulink model. The *S-function* is one of advanced software applications of Matlab/Simulink and has been implemented using the *C language.*

3.2.1 Measurement of *di/dt* Signal using Sensors

Current derivative measurement using three low cost di/dt sensors can be used to track the saliency position. First of all, it is necessary to understand the reason for using the current derivative measurement and how the position estimation can be achieved using the current derivatives. Secondly, the new modified position scalar table for a star-connected PMSM is introduced, which has been modified compared to the previous research in [50]. Finally, the experimental results for the measurement of current derivatives are discussed.

The overall structure of sensorless control using *di/dt* sensors is shown in Fig 3.1. The current derivatives can be obtained by these three sensors and the results of measured *di/dt* signals are sent to the data acquisition system through three ADC channels. The *di/dt* sensors are made from air core mutual inductors [4, 5]. The current derivative measurement in response to two active vectors and one null vector are considered in order to estimate rotor position within one PWM period. Signal processing operations are also required to track the saliency such as software filters (Low pass, SMP, etc) and a tracking observer (PLL or mechanical observer) and

these are described later. The estimated position signal P_α and P_β is derived from the position scalar table. For convenience, a modified scalar table has been derived to improve processing speed. The estimated speed and position as feedback information is sent to the speed and current controller.

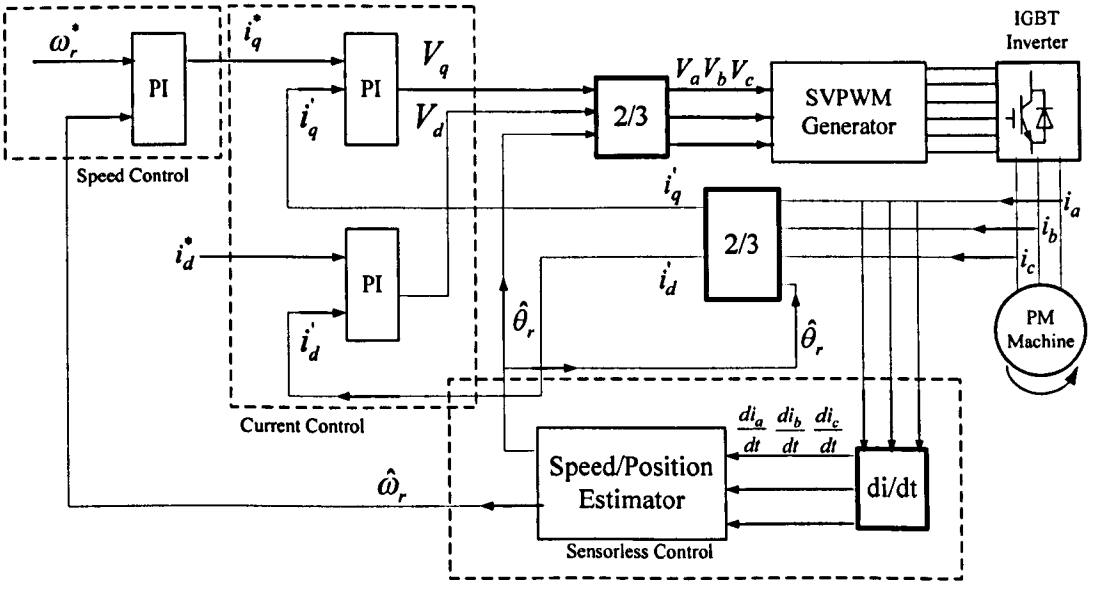

Fig 3.1 overall structure of sensorless control using *di/dt* sensors

The "INFORM" method [34] was the first proposed method to estimate rotor position using the current transient responses to PWM voltage vectors excitations. Table 3.1 defines the voltage vectors during the switching events. 0 and 1 represents switching of the lower and upper of the IGBTs respectively. When the active switching vector $\underline{u_1}$ as shown in Fig 3.2 is applied to a star-connected machine as in this work, the connections of the stator windings with the DC link voltage are those shown in Fig 3.3.

	Switching State		
Active Vector	**Phase A**	**Phase B**	**Phase C**
$\underline{u_1}$	1	0	0
$\underline{u_2}$	1	1	0
$\underline{u_3}$	0	1	0
$\underline{u_4}$	0	1	1
$\underline{u_5}$	0	0	1
$\underline{u_6}$	1	0	1
Null Vector			
$\underline{u_0}$	0	0	0
$\underline{u_7}$	1	1	1

Table 3.1 definition of voltage space vectors

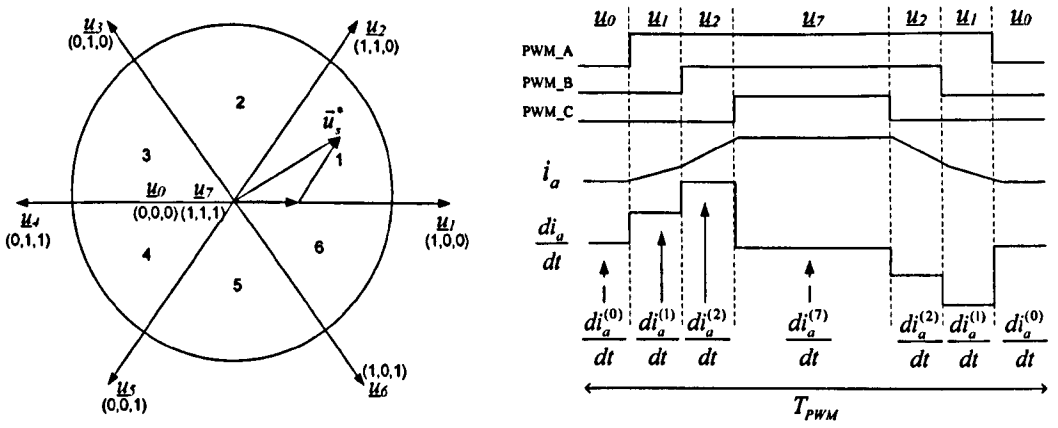

Fig 3.2 (left) space vectors in six sectors; (right) voltage vector, current and di/dt.

In a star-connected PM machine, the transient equivalent circuit of a three phase subjected to an active test voltage vector u_k ($k = 1, 2...6$) is given in Fig.3.3.

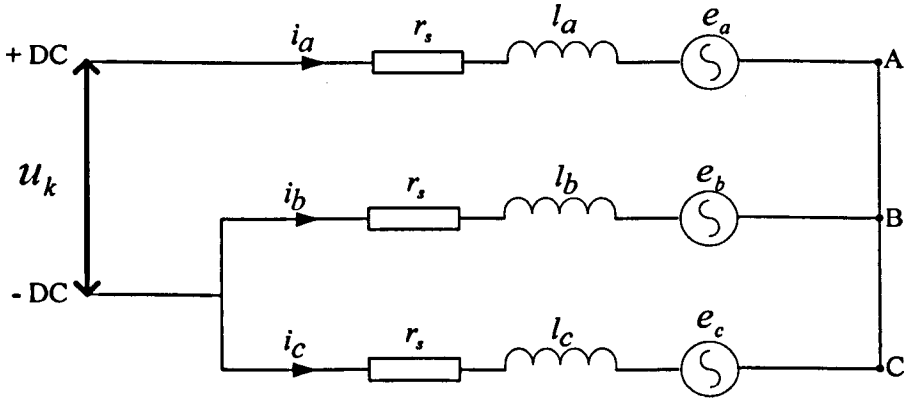

Fig. 3.3 equivalent circuit with $\underline{u}_k$ being applied in the star connection

It is assumed that the stator leakage inductances in PMSM are modulated by the anisotropy arising from either the rotor slotting or the main flux saturation. The stator leakage inductances (l_a, l_b, l_c) during one cycle are represented as: [50]

$$
\begin{aligned}
l_a &= l_0 + \Delta l \cos(n_{an}\theta_{an}) \\
l_b &= l_0 + \Delta l \cos(n_{an}\theta_{an} - \frac{2\pi}{3}) \\
l_c &= l_0 + \Delta l \cos(n_{an}\theta_{an} - \frac{4\pi}{3})
\end{aligned}
\tag{3.1}
$$

where $l_0 = \frac{l_d + l_q}{2}$ is the average inductance, and $\Delta l = \frac{l_d - l_q}{2}$ is the inductance variation caused by the saturation saliency. Also n_{an} represents the number of poles of the saturation saliency, and θ_{an} is the position angle of the saliency. According to Fig 3.3, the voltage vector $\underline{u_1}$ is applied and the equivalent circuit is presented by:

$$
\begin{aligned}
U_{dc} &= (i_a^{(u_1)} r_s + l_a \frac{di_a^{(u_1)}}{dt} + e_a^{(u_1)}) - (i_b^{(u_1)} r_s + l_b \frac{di_b^{(u_1)}}{dt} + e_b^{(u_1)}) \\
0 &= (i_b^{(u_1)} r_s + l_b \frac{di_b^{(u_1)}}{dt} + e_b^{(u_1)}) - (i_c^{(u_1)} r_s + l_c \frac{di_c^{(u_1)}}{dt} + e_c^{(u_1)}) \\
-U_{dc} &= (i_c^{(u_1)} r_s + l_c \frac{di_c^{(u_1)}}{dt} + e_c^{(u_1)}) - (i_a^{(u_1)} r_s + l_a \frac{di_a^{(u_1)}}{dt} + e_a^{(u_1)})
\end{aligned}
\tag{3.2}
$$

where U_{dc} is the DC link voltage, r_s is the stator per phase resistance, e_a, e_b, and e_c is the back EMF in phase A, B and C; i_a, i_b, and i_c are the phase current, and the superscript $\underline{u_0}$ means the measurement is made during the null vector and $\underline{u_1}$ means the measurement is made during the active vector. Three phase back EMF voltages are required during the null vector $\underline{u_0}$ and the active vector $\underline{u_1}$ and are made within one switching period. Thus, they are assumed as:

$$
\begin{cases}
e_a^{(u1)} \approx e_a^{(u0)} \\
e_b^{(u1)} \approx e_b^{(u0)} \\
e_c^{(u1)} \approx e_c^{(u0)}
\end{cases}
\tag{3.3}
$$

If the null voltage vectors u_0 or u_7 is applied, the equivalent circuit changes to: [5, 50]

$$
\begin{aligned}
0 &= \left(r_s i_a^{(u_0)} + l_0 \frac{di_a^{(u_0)}}{dt} + e_a^{(u_0)} \right) - \left(r_s i_b^{(u_0)} + l_0 \frac{di_b^{(u_0)}}{dt} + e_b^{(u_0)} \right) \\
0 &= \left(r_s i_b^{(u_0)} + l_0 \frac{di_b^{(u_0)}}{dt} + e_b^{(u_0)} \right) - \left(r_s i_c^{(u_0)} + l_0 \frac{di_c^{(u_0)}}{dt} + e_c^{(u_0)} \right) \\
0 &= \left(r_s i_c^{(u_0)} + l_0 \frac{di_c^{(u_0)}}{dt} + e_c^{(u_0)} \right) - \left(r_s i_a^{(u_0)} + l_0 \frac{di_a^{(u_0)}}{dt} + e_a^{(u_0)} \right)
\end{aligned}
\tag{3.4}
$$

In addition, the stator resistive voltage drop can be neglected as it is small compared with DC-Link voltage U_{dc}. Therefore, combining (3.2) - (3.4) gives

$$\frac{di_a^{(u_1)}}{dt}-\frac{di_a^{(u_0)}}{dt}=U_{dc}\cdot\frac{l_b+l_c}{l_al_b+l_bl_c+l_cl_a}$$

$$\frac{di_b^{(u_1)}}{dt}-\frac{di_b^{(u_0)}}{dt}=U_{dc}\cdot\frac{l_b}{l_al_b+l_bl_c+l_cl_a} \tag{3.5}$$

$$\frac{di_c^{(u_1)}}{dt}-\frac{di_c^{(u_0)}}{dt}=U_{dc}\cdot\frac{l_c}{l_al_b+l_bl_c+l_cl_a}$$

Substituting (3.1) into (3.5) yields:

$$\frac{di_a^{(u_1)}}{dt}-\frac{di_a^{(u_0)}}{dt}=\frac{1}{c_2}\left(2-\frac{\Delta l}{l_0}\cos n_{an}\theta_{an}\right)$$

$$\frac{di_b^{(u_1)}}{dt}-\frac{di_b^{(u_0)}}{dt}=-\frac{1}{c_2}\left(1+\frac{\Delta l}{l_0}\cos n_{an}\left(\theta_{an}-\frac{4\pi}{3}\right)\right) \tag{3.6}$$

$$\frac{di_c^{(u_1)}}{dt}-\frac{di_c^{(u_0)}}{dt}=-\frac{1}{c_2}\left(1+\frac{\Delta l}{l_0}\cos n_{an}\left(\theta_{an}-\frac{2\pi}{3}\right)\right)$$

where $c_2=\dfrac{3l_0(1-(\frac{\Delta l}{2l_0})^2)}{U_{DC}}$

A similar set of equations can be derived for $\underline{u_2}$, and these can then be combined [4, 5] to create a set of position scalars.

$$p_a=-1+c_2\left(\frac{di_b^{(u2)}}{dt}-\frac{di_b^{(u0)}}{dt}\right)$$
$$p_b=-1-c_2\left(\frac{di_a^{(u2)}}{dt}-\frac{di_a^{(u0)}}{dt}\right) \tag{3.7}$$
$$p_c=-1-c_2\left(\frac{di_b^{(u1)}}{dt}-\frac{di_b^{(u0)}}{dt}\right)$$

and this can be transformed to a position vector $\underline{P}$ where the angle of $\underline{P}$ is the saliency angle in (3.11)

$$\underline{p} = p_\alpha + jp_\beta = p_a + ap_b + a^2 p_c$$

$$= (\frac{di_b^{(u2)}}{dt} - \frac{di_b^{(u0)}}{dt}) - a(\frac{di_c^{(u1)}}{dt} - \frac{di_c^{(u0)}}{dt}) - a^2(\frac{di_b^{(u1)}}{dt} - \frac{di_b^{(u0)}}{dt}) \tag{3.8}$$

where $a = e^{j2\pi/3}$, the orthogonal components p_α and p_β are represented as: [4, 5]

$$p_\alpha = p_a - \frac{1}{2}(p_b + p_c) = c_2((\frac{di_b^{(u2)}}{dt} - \frac{di_b^{(u0)}}{dt}) + \frac{1}{2}(\frac{di_c^{(u1)}}{dt} - \frac{di_c^{(u0)}}{dt}) - \frac{1}{2}(\frac{di_b^{(u1)}}{dt} - \frac{di_b^{(u0)}}{dt})) \tag{3.9}$$

$$P_\beta = \frac{\sqrt{3}}{2}(p_b - p_c) = \frac{\sqrt{3}}{2}c_2((\frac{di_b^{(u1)}}{dt} - \frac{di_b^{(u0)}}{dt}) - (\frac{di_c^{(u1)}}{dt} - \frac{di_c^{(u0)}}{dt})) \tag{3.10}$$

$$\theta_{an} = \frac{1}{n_{an}}\tan^{-1}\left(\frac{P_\alpha}{P_\beta}\right) \tag{3.11}$$

	p_a	p_b	p_c
Sector 1	$-1+c_2(\frac{di_b^{(u2)}}{dt} - \frac{di_b^{(u0)}}{dt})$	$-1+c_2(\frac{di_a^{(u2)}}{dt} - \frac{di_a^{(u0)}}{dt})$	$-1-c_2(\frac{di_b^{(u1)}}{dt} - \frac{di_b^{(u0)}}{dt})$
Sector 2	$-1+c_2(\frac{di_b^{(u2)}}{dt} - \frac{di_b^{(u0)}}{dt})$	$-1+c_2(\frac{di_a^{(u2)}}{dt} - \frac{di_a^{(u0)}}{dt})$	$-1-c_2(\frac{di_a^{(u3)}}{dt} - \frac{di_a^{(u0)}}{dt})$
Sector 3	$-1-c_2(\frac{di_c^{(u3)}}{dt} - \frac{di_c^{(u0)}}{dt})$	$-1+c_2(\frac{di_c^{(u4)}}{dt} - \frac{di_c^{(u0)}}{dt})$	$-1-c_2(\frac{di_a^{(u3)}}{dt} - \frac{di_a^{(u0)}}{dt})$
Sector 4	$-1-c_2(\frac{di_b^{(u5)}}{dt} - \frac{di_b^{(u0)}}{dt})$	$-1+c_2(\frac{di_c^{(u4)}}{dt} - \frac{di_c^{(u0)}}{dt})$	$-1+c_2(\frac{di_b^{(u4)}}{dt} - \frac{di_b^{(u0)}}{dt})$
Sector 5	$-1-c_2(\frac{di_b^{(u5)}}{dt} - \frac{di_b^{(u0)}}{dt})$	$-1-c_2(\frac{di_a^{(u5)}}{dt} - \frac{di_a^{(u0)}}{dt})$	$-1+c_2(\frac{di_a^{(u6)}}{dt} - \frac{di_a^{(u0)}}{dt})$
Sector 6	$-1+c_2(\frac{di_c^{(u6)}}{dt} - \frac{di_c^{(u0)}}{dt})$	$-1-c_2(\frac{di_c^{(u1)}}{dt} - \frac{di_c^{(u0)}}{dt})$	$-1+c_2(\frac{di_a^{(u6)}}{dt} - \frac{di_a^{(u0)}}{dt})$

Table 3.2 position scalars for estimation in different sectors

It can be seen that by correct selection of the current derivatives used in each sector, the position can be estimated without needing to calculate c_2 explicitly, and can be achieved purely from the di/dt measurements. Table 3.2 presents the required di/dt measurements for each sector of operation [4, 5]. Although three balanced position scalars can be obtained from each active switching state combined with the null vector $\underline{u}_0$ or $\underline{u}_7$, the coefficient c_2 is unknown and may vary with the saturation level. However, the position determination is using different combinations of the active voltage vectors without knowing the value of the c_2. During the calculation of the saliency angle, c_2 can be also easily cancelled by the division of P_α and P_β. The saliency angle is established by (3.11) from which the rotor position angle can be constructed. For an SVPWM algorithm waveform, if both the active voltage vectors and the null voltage vectors reside in one sector from Sector 1 to Sector 6, the vector sequences within a PWM period are normally assigned as follows [55].

- Sector 1: O1 (ccc) →1 (acc) → 2 (aac) →O7 (aaa) →2 (aab) →1(abb) →O1 (bbb).
- Sector 2: O1 (ccc) →3 (acc) → 2 (aac) →O7 (aaa) →2 (aab) →3(abb) →O1 (bbb).
- Sector 3: O1 (ccc) →3 (acc) → 4 (aac) →O7 (aaa) →4 (aab) →3(abb) →O1 (bbb).
- Sector 4: O1 (ccc) →5 (acc) → 4 (aac) →O7 (aaa) →4 (aab) →5(abb) →O1 (bbb).
- Sector 5: O1 (ccc) →5 (acc) → 6 (aac) →O7 (aaa) →6 (aab) →5(abb) →O1 (bbb).
- Sector 6: O1 (ccc) →1 (acc) → 6 (aac) →O7 (aaa) →6 (aab) →1(abb) →O1 (bbb).

In Fig 3.4, two active vectors e.g. $\underline{u}_1$ and $\underline{u}_2$, $\underline{u}_3$ and $\underline{u}_4$, etc are used in the formation of position scalars. The vector sequence and Fig 3.4 show the details of all the active vectors and null vectors. Additionally, from (3.7), ±1 and c_2 can be cancelled during the substitution in order to form the position vector $\underline{P}$. The position estimation methods therefore use two active and one null voltage vector. A new position scalar table is shown in Table 3.3.

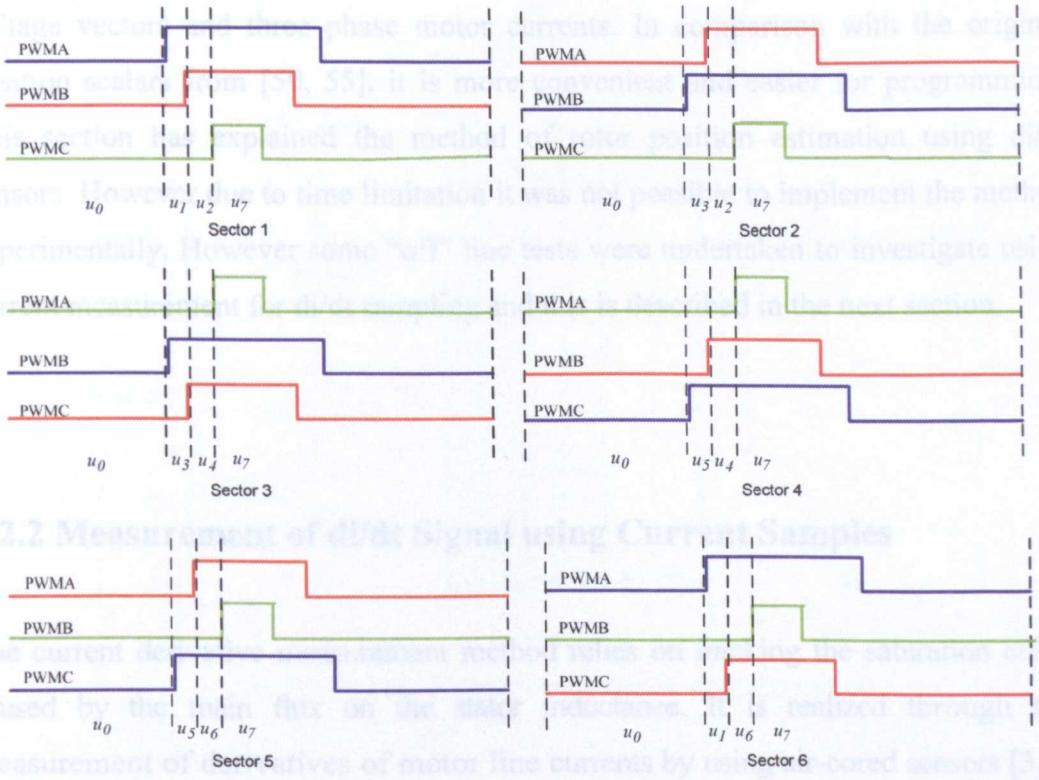

Fig 3.4 two active and two null vectors are presented in each sector

	p_a	p_b	p_c
Sector 1	$\frac{di_b^{(u2)}}{dt}-\frac{di_b^{(u0)}}{dt}$	$\frac{di_a^{(u2)}}{dt}-\frac{di_a^{(u0)}}{dt}$	$-(\frac{di_b^{(u1)}}{dt}-\frac{di_b^{(u0)}}{dt})$
Sector 2	$\frac{di_b^{(u2)}}{dt}-\frac{di_b^{(u0)}}{dt}$	$\frac{di_a^{(u2)}}{dt}-\frac{di_a^{(u0)}}{dt}$	$-(\frac{di_a^{(u1)}}{dt}-\frac{di_a^{(u0)}}{dt})$
Sector 3	$-(\frac{di_c^{(u1)}}{dt}-\frac{di_c^{(u0)}}{dt})$	$\frac{di_c^{(u2)}}{dt}-\frac{di_c^{(u0)}}{dt}$	$-(\frac{di_a^{(u1)}}{dt}-\frac{di_a^{(u0)}}{dt})$
Sector 4	$-(\frac{di_b^{(u1)}}{dt}-\frac{di_b^{(u0)}}{dt})$	$\frac{di_c^{(u2)}}{dt}-\frac{di_c^{(u0)}}{dt}$	$\frac{di_b^{(u2)}}{dt}-\frac{di_b^{(u0)}}{dt}$
Sector 5	$-(\frac{di_b^{(u1)}}{dt}-\frac{di_b^{(u0)}}{dt})$	$-(\frac{di_a^{(u1)}}{dt}-\frac{di_a^{(u0)}}{dt})$	$\frac{di_a^{(u2)}}{dt}-\frac{di_a^{(u0)}}{dt}$
Sector 6	$\frac{di_c^{(u2)}}{dt}-\frac{di_c^{(u0)}}{dt}$	$-(\frac{di_c^{(u1)}}{dt}-\frac{di_c^{(u0)}}{dt})$	$\frac{di_a^{(u2)}}{dt}-\frac{di_a^{(u0)}}{dt}$

Table 3.3 reforming the new position scalars in the star connected machine

The new derived table of the position scalars provides the relationships between two voltage vectors and three phase motor currents. In comparison with the original position scalars from [50, 55], it is more convenient and easier for programming. This section has explained the method of rotor position estimation using di/dt sensors. However due to time limitation it was not possible to implement the method experimentally. However some "off" line tests were undertaken to investigate using current measurement for di/dt sampling and this is described in the next section.

3.2.2 Measurement of di/dt Signal using Current Samples

The current derivative measurement method relies on tracking the saturation effect caused by the main flux on the stator inductance. It is realized through the measurement of derivatives of motor line currents by using air-cored sensors [3, 4, 5, 50]. In total three low cost external current derivative sensors are required, however, they increase the component count and require other resources such as ADC channels, etc. In this section, these *di/dt* sensors are removed and a new current measurement approach is introduced which calculates the current derivative values from current measurements. This section describes through simulation how this may be ideally achieved, whereas the next section looks at practical implementation problems. Two active vectors and one null vector are needed for estimation. The proposed sampling instants are indicated by the arrows in Fig 3.5 when operating in sector 1. In total, four current samples, I_1, I_2, I_3, and I_4 need to be considered for the determination of three current derivatives. The HF oscillations during the switching can result on the poor current sampling; therefore, sampling the middle point of PWM voltage vector period would be less disturbed by the oscillations. The colour arrows in Fig 3.5 show the current sampling in the middle of each PWM voltage vector period. The rotor position of the PMSM machine can be effectively estimated by this proposed method. The detailed sampling scheme is presented in Fig 3.5.

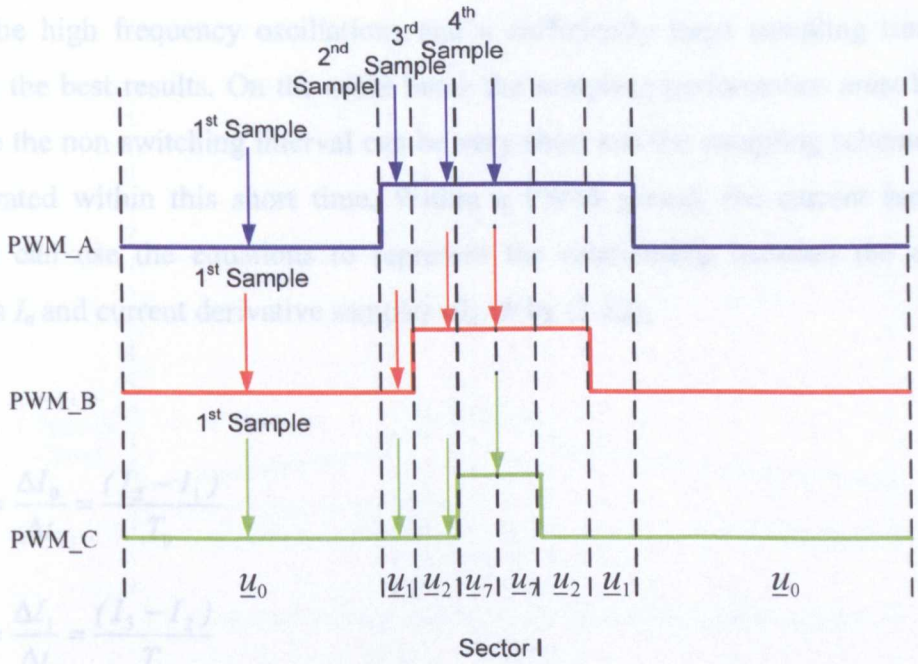

Fig 3.5 proposed current sampling instants in sector 1

In the practical experiment, the current samples cannot be made until the high frequency caused oscillations due to parasitic capacitances have died down. It is necessary to sample each phase line current within a voltage vector before or after the switching event starts. In the experiment, a minimum vector time (approximate within 6μs) is needed because the current oscillation takes time to die down and then a more accurate measurement can be obtained. The operation of sampling takes place at the start and end of the switching vector that is implemented. The current measurement scheme is based on the differentiation process of the current measurements during a short period. One current derivative value takes the difference of two current samples with a time interval Δt, which is calculated as $di/dt = \Delta i/\Delta t$. This scheme is direct and there are no di/dt sensors required; however, the three important points need to be noticed that will be directly related to the calculation of the current derivatives.

a. Amplified the noise appearing in the line current signal;
b. The system must have sufficient sampling ability;
c. The current measurement must be performed within a short time interval;

The explanations of these three points indicate that the sampling operation must avoid the high frequency oscillations and a sufficiently large sampling time can provide the best results. On the other hand, the sampling performance must be fast because the non switching interval can be very short and the sampling scheme must be operated within this short time. Within a PWM period, the current sampling scheme can use the equations to represent the relationship between the current samples I_n and current derivative samples di_n/dt by (3.12);

$$\frac{di_{u_0}}{dt} = \frac{\Delta I_0}{\Delta t} = \frac{(I_2 - I_1)}{T_0}$$

$$\frac{di_{u_1}}{dt} = \frac{\Delta I_1}{\Delta t} = \frac{(I_3 - I_2)}{T_1} \tag{3.12}$$

$$\frac{di_{u_2}}{dt} = \frac{\Delta I_2}{\Delta t} = \frac{(I_4 - I_3)}{T_2} = \frac{(I_3 - I_1)}{T_0 + T_1}$$

where I_1, I_2, I_3, and I_4 are the motor current samples in one phase, T_0, T_1, T_2 is the time for the voltage vector $\underline{u}_0$, $\underline{u}_1$, $\underline{u}_2$ in half a switching period, they are shown in Fig 3.6 and di_{u0}/dt, di_{u1}/dt, and di_{u2}/dt is the samples of current derivatives. When it comes to implementation according to (3.12), the measured line currents require a number of samples. In Fig 3.6, there are four current samples taken for the determination of the current derivatives. In (3.12), the second and the third sample are used twice for three current derivatives; therefore, it does not need to consider the forth current sample. Three current derivatives are calculated and stored within a PWM period, the estimated position signals can be established by these current derivatives according to the position scalar table in Table 3.2. In each sector of SVPWM, the position signal P_a, P_b, and P_c can be estimated by choosing the appropriate samples of current derivatives. These estimation processes are exactly same as the PWM voltage vector excitation method and the challenges are on the different sampling objects. The simulation results for sampling the line currents are discussed later in this section.

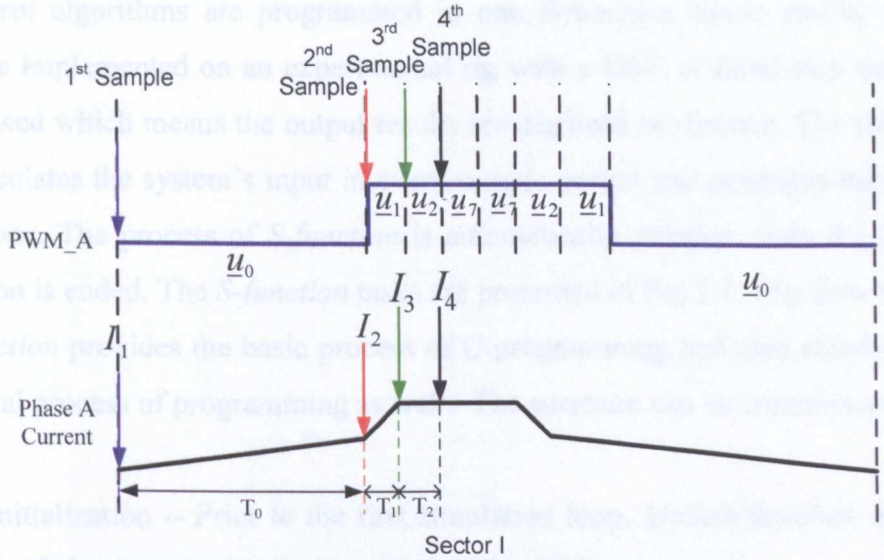

Fig 3.6 proposed current sampling for di/dt calculation in phase A

3.2.3 Simulation Results of Sensorless Control using S-function

In this section, the proposed method using current measurement is implemented in simulation and the simulation results are obtained. In this simulation work, an advanced functional block, *S-function* is implemented for sensorless operation. A brief introduction to the *S-function* is now given.

Matlab/Simulink is used for the simulation work using standard models for the machine and power components. The PMSM machine control is emulated by implementing the control law as a *C Mex S-function*. The *S-function* is a computer language description of a Simulink block. There are several computer languages which can be used such as *MATLAB-M-file, C, C++, ADA, or FORTRAN* [56]. A real-time microprocessor normally is programmed in *C* to achieve its control; therefore, a C *Mex S-function* is implemented in the simulation of sensorless control of PMSM. The form of the *S-function* can accommodate continuous, discrete, and hybrid systems. The *S-function* is created as a *MEX-file* in a block which can connect to other *Simulink* models. The *S-function* block is designed to execute its algorithm in every simulation step. Each *S-function* block has inputs and outputs. The number of inputs and outputs can be defined in *C programme.* The PMSM sensorless vector control is a mathematical algorithm which can be operated at specific time instants.

The speed and current PI controllers are digitized and programmed in the *S-function*. All control algorithms are programmed in one *S-function* block, similar to what would be implemented on an experimental rig with a DSP. A fixed step simulation time is used which means the output results are digitized or discrete. The simulation loop calculates the system's input in every sample period and generates each output one by one. The process of *S-function* is automatically stopped when the system's simulation is ended. The *S-function* tasks are presented in Fig 3.7. The flow structure of *S-function* provides the basic process of C programming and also clearly defines the logical process of programming as well. The structure can be summarised as:

- Initialization -- Prior to the first simulation loop, *Matlab/Simulink* initializes the *S-function*. In this Period, *Matlab/Simulink*:
  - Initializes the *S-function's* conditions.
  - Defines which library should be used.
  - Defines the number and size of input and output ports.
  - Sets sample times of the *S-function* block.
  - Allocates storage areas and the sizes array.

- Computation of the outputs in the major time step -- All the controlled output ports of the simulation blocks is valid for the current time step, after calls are completed.
- Update of the discrete states in the major time step -- In this call, all simulation blocks will perform activities once at every simulation step such as updating discrete states for next time around the simulation loop, and storing the previous outputs for the next calculations.

In Fig 3.7, the overview of the flow chart shows how the *S-function* internally executes in the *Matlab/Simulink* software application. The *S-function* has many useful but complicated commands that should be discussed since the Fig 3.7 only provides the limited information. The general format of a *C MEX S-function* is shown in appendix C and the useful commands are also explained in details.

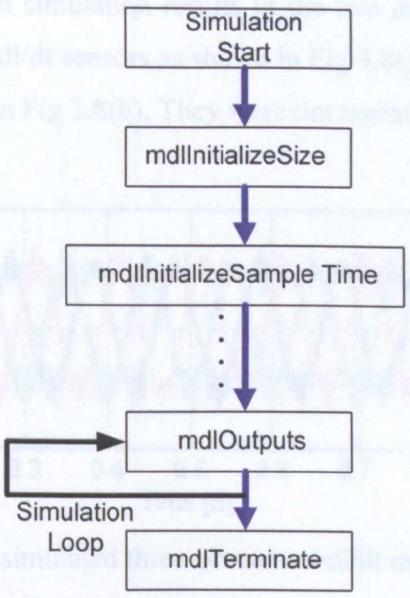

Fig 3.7 the flow chart of *S-Function*

For the simulation studies undertaken here, the parameters are given in Table 3.4. To avoid the oscillation caused by switching, the current sampling can be carried out at the end of switching. According to equation (3.12), in each phase current, there are four current samples used for calculation of di/dt within one PWM period. The time interval ΔT is defined as the sampling time between two required samples, which are not next to each other so ΔT is longer than the sample time of 0.2μs in Table 3.4.

Simulation Configuration Parameters	*Required Time / Frequency*
Simulation Max Time Step	0.2μs
Speed Sampling Time	10 μs
Current Sampling Time	0.2μs
Speed Controller Bandwidth	10Hz
Current Controller Bandwidth	250Hz
Time of Adding Load	0.7s
Rotor Demand Speed	100rpm
Rotor Starts Running at	0.1s

Table 3.4 related time or frequency in simulation

Fig 3.8 shows the obtained simulation results in the two different experiment; one uses three-phase air-cored di/dt sensors as shown in Fig 3.8(a), and the other uses the current samples as shown in Fig 3.8(b). They were not measured at the same time.

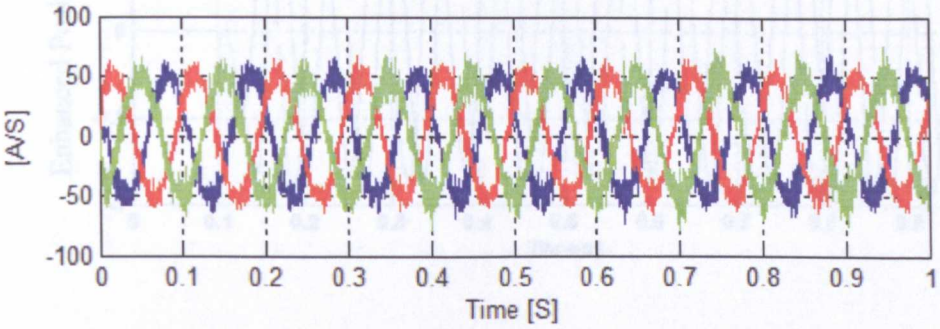

Fig 3.8 (a) the simulated three-phase real di/dt using sensors;

Obviously, the calculated di/dt waveforms have less noise than the captured di/dt waveforms because the sampling scheme is applied. The current sampling technique can provide good di/dt samples for the position estimation.

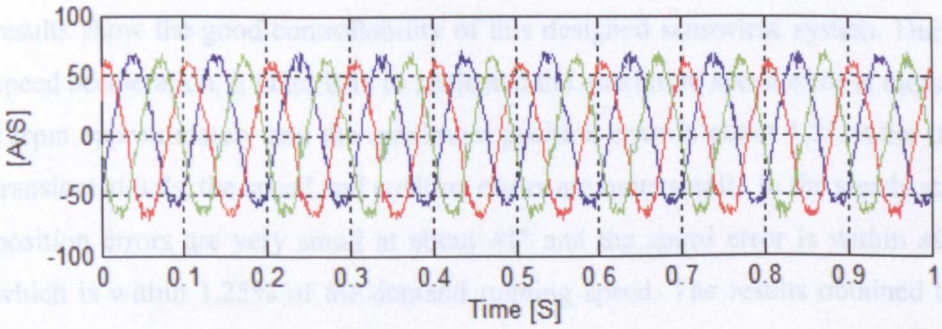

Fig 3.8 (b) the calculated three-phase di/dt using current samples;

This simulation work was carried out using the selected current samples to achieve position estimation. The sampling time for current control loop is set to 40ns and the speed control loop has a slower sampling time of 100ns. The bandwidth of the current loop is 25 times larger than the speed loop so that the design of the two loops can be decoupled. A reference speed at 100rpm is applied. The 70% load was added at 0.7s. The dynamic and steady state responses are observed and the sensorless operation is fully implemented in this simulation work. The estimated position signals obtained from the simulation are shown in Fig 3.9. As expected these look noise free – the simulation conditions are ideal. The amplitude increases at 0.7s due to the load change, but the phase – which is the quantity of concern – is not affected.

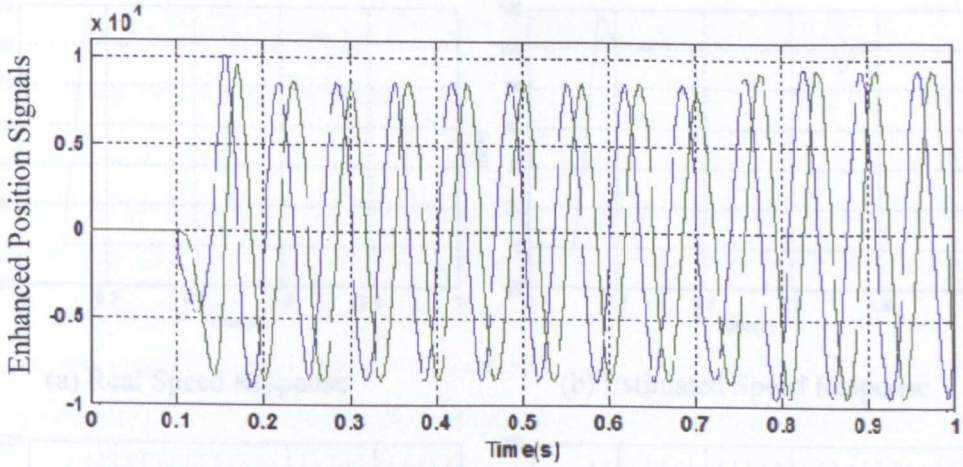

Fig 3.9 the estimated position signal $P\alpha$ and $P\beta$

The measured and estimated speed, position angle, speed and position errors for the sensorless operated simulation system are shown in Fig 3.10. These simulation results show the good controllability of this designed sensorless system. During the speed acceleration, it takes 0.1s to settle and the maximum speed error is measured at 12rpm approximately and the maximum position error is about 1.2°. After the load transient at 0.7s, the speed and position errors are quite small. In the steady state, the position errors are very small at about ±1° and the speed error is within ±0.5rpm, which is within 1.25% of the demand running speed. The results obtained through simulation show the feasibility of this approach to sensorless control, and demonstrate that di/dt measurements can be used for position estimation. It was not possible to implement this control on the experimental system due to time constraints. However the difficulties of obtaining an accurate di/dt measurement are discussed in the next section.

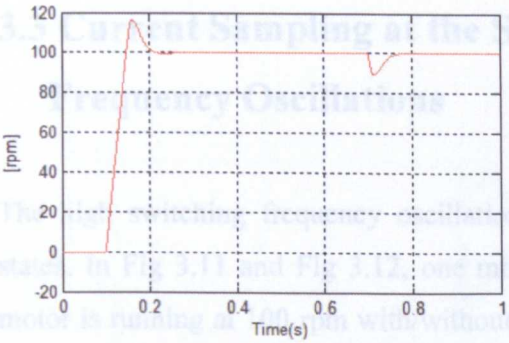

(a) Real Speed Response

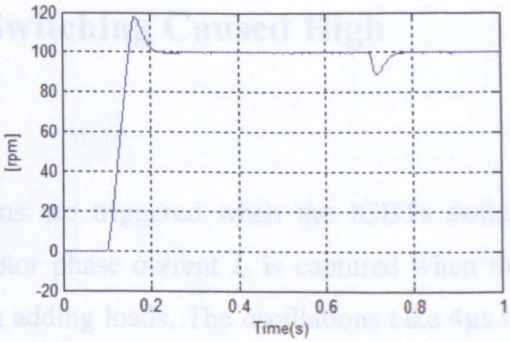

(b) Estimated Speed Response

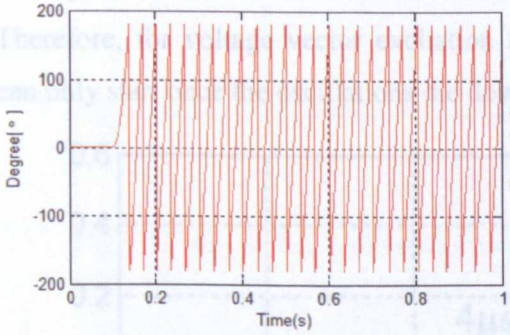

(c) Real Position Angle

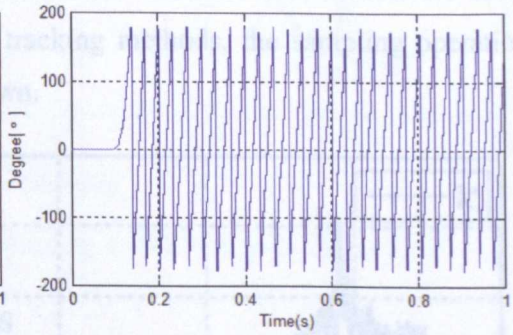

(d) Estimated Position Angle

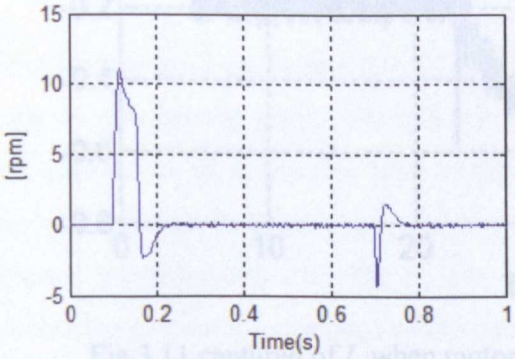

(e) Speed error

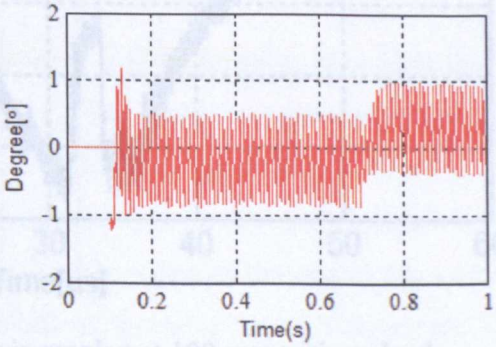

(f) Position error

Fig 3.10 (a), (b), (c), (d) real and estimated simulation results;

(e) speed error; (f) position error

3.3 Current Sampling at the Switching Caused High Frequency Oscillations

The high switching frequency oscillations are triggered when the IGBTs switch states. In Fig 3.11 and Fig 3.12, one motor phase current I_c is captured when the motor is running at 100 rpm with/without adding loads. The oscillations take 4μs to settle down and the sampling can be made after this. These switching oscillations also appear on the current derivatives measurement when the *di/dt* sensors are used. Therefore, for voltage vector excitation tracking methods, the sampling operation can only start once the oscillations die down.

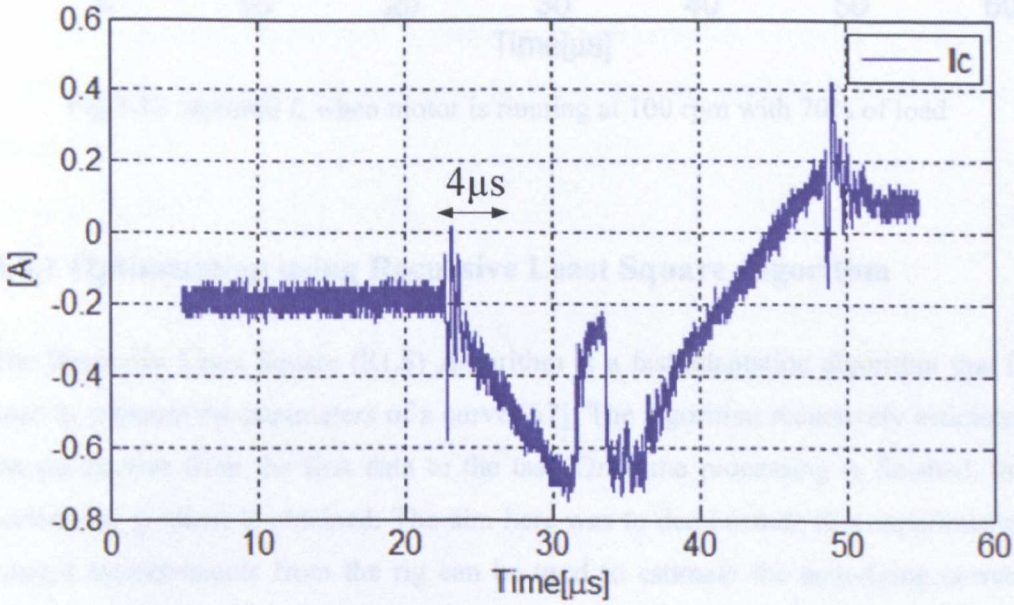

Fig 3.11 captured of I_c when motor is running at 100 rpm with no load

To reduce the oscillations impact, there are some modifications made to improve the system's stability via hardware modification or software compensation [5]. However, the minimum vector time is still needed even after the modifications applied. Therefore, a new method is proposed and introduced in this section, which can reduce the minimum vector time and operate sampling during the oscillation period. The aim is to sample the current at a high sample frequency, and then use a curve fitting algorithm on this data to try to extract the underlying gradient before the oscillations die down.

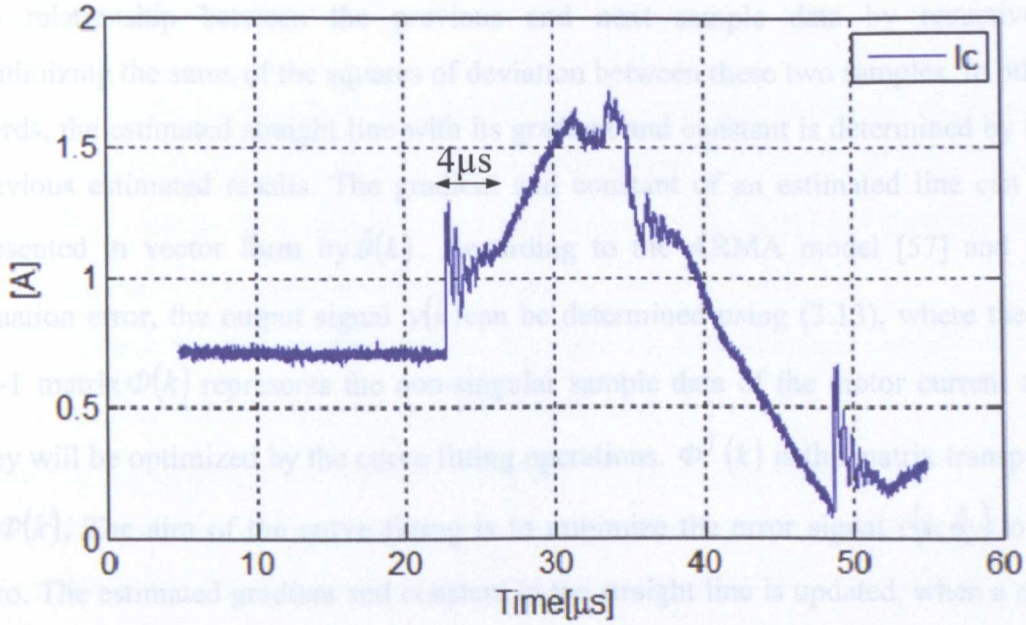

Fig 3.12 captured I_c when motor is running at 100 rpm with 70% of load

3.3.1 Optimization using Recursive Least Square Algorithm

The Recursive Least Square (RLS) Algorithm is a fast adaptation algorithm that is used to estimate the parameters of a curve [57]. The algorithm recursively estimates the parameters from the first data to the last. Once the processing is finished, the underlying gradient is obtained. The aim here was to demonstrate that experimental current measurements from the rig can be used to estimate the underlying current derivative even in the presence of the oscillations, by using the RLS algorithm. The RLS algorithm is the simplest and most commonly applied form of linear equation which recursively provides the best solution to find out the best fitted straight line through a set of samples [57]. The advantage of this technique is that it continuously improves the estimation quality, and an accurate estimation can be achieved by processing a higher number of samples. In this section, offline curve fitting to experiment data is demonstrated and the experimental results are presented under various speed and load conditions. The explanations of RLS algorithms are discussed next.

As mentioned, the RLS algorithm is a method of the curve fitting that best describes the relationship between the previous and next sample data by recursively minimizing the sums of the squares of deviation between these two samples. In other words, the estimated straight line with its gradient and constant is determined by the previous estimated results. The gradient and constant of an estimated line can be presented in vector form by $\hat{\theta}(k)$. According to the ARMA model [57] and the equation error, the output signal $y(k)$ can be determined using (3.13), where the n-by-1 matrix $\Phi(k)$ represents the non-singular sample data of the motor current and they will be optimized by the curve fitting operations. $\Phi^T(k)$ is the matrix transpose of $\Phi(k)$. The aim of the curve fitting is to minimize the error signal $e(k;\hat{\theta}_e)$ to be zero. The estimated gradient and constant in the straight line is updated, when a new sample data is obtained. The equation of the estimated straight line with errors is presented by [57]

$$y(k) = \Phi^T(k)\hat{\theta}(k) + e(k;\hat{\theta}_e) \tag{3.13}$$

$$L(k+1) = P(k)\Phi(k+1)\left(1 + \Phi^T(k+1)P(k)\Phi(k+1)\right)^{-1} \tag{3.14}$$

$$\hat{\theta}(k+1) = \hat{\theta}(k) + L(k+1)\left(y(k+1) - \Phi^T(k+1)\hat{\theta}(k)\right) \tag{3.15}$$

$$P(k+1) = P(k)\left(I - L(k+1)\Phi^T(k+1)\right) \tag{3.16}$$

Where $P(k) = \alpha I$, $L(k+1)$ is correction gain, $\alpha = \frac{10}{N+1}\sum_{i=0}^{N} y^2(i)$ and $I = \begin{bmatrix} 1 & 0 \\ 0 & 1 \end{bmatrix}$ is the identity matrix. (3.14) - (3.16) are derived in [57], and constitute an algorithm for determining $\hat{\theta}_e$ recursively. $\hat{\theta}(k)$ and $\hat{\theta}(k+1)$ represent the estimated straight line in matrix form and they are the previous and next sample. The sample of an estimated straight line in matrix form $\hat{\theta}_e$ is represented as $\hat{\theta}_{e1}$ (estimated gradient) and $\hat{\theta}_{e2}$ (estimated constant); therefore, the estimated and updated straight line is presented by

$$\hat{\theta}_e = \begin{bmatrix} \hat{\theta}_{e1} \\ \hat{\theta}_{e2} \end{bmatrix} = \begin{bmatrix} gradient \\ constant \end{bmatrix} \tag{3.17}$$

The design procedures for using the RLS algorithm with Matlab software is described as followed: [57]

1. Select the initial values of the first current sample and derive the large scalar α. Enter amount of data with time to be analyzed.
2. Form $\Phi(k)$, by collecting output and input sample data, and then calculate the correction gain $L(k+1)$ using (3.14):
3. Collect the next output sample data y(k+1) from the next sample of line current with their time t to get the estimated $\hat{\theta}_e$ in (3.15)
4. A new derived $P(k)$, which is expressed as $P(K+1)$ by using (3.16);
5. Recursively, in (3.17), the new sets of estimated gradients and constants of the curve are obtained and the straight line through the last estimated set of points can be plotted.

3.3.2 Experimental Results

The aim of this section is to show the potential of using the RLS algorithm to estimate di/dt using real data obtained from the experimental system described later in the thesis. This offline signal processing uses the motor line currents captured using an oscilloscope [91] to estimate the gradient of the current. The test data from operation of the drive is at 100, 200, and 300 rpm with/without adding load. The current of phase C, I_c is measured and processed by the RLS algorithms offline. The real gradient of current waveform I_c is defined and obtained using the RLS for all of the samples. The estimated gradient of I_c is also defined and obtained using the RLS for smaller numbers of current samples. The estimation error is defined as the difference between the real and estimated gradient for the current. The following figures illustrate the estimation results and the data table is also presented to summarise the position errors. The number of samples for estimation is decreased from 60 to 30 but the sample rate is kept same.

Fig 3.13 – Fig 3.24 respectively shows captured current measurements using a high resolution oscilloscope, and the current samples used for estimation are presented using the diamond mark in the figures. These current samples are captured at different machine speeds, with or without adding load. The sample time is 0.04 μs and the oscillation period of I_c due to parasitic effects approximately 3 - 6μs. Fig 3.13 shows the current measured for phase C after switching the lower IGBT in phase C when running at 100rpm without load. The current has been sampled over a 5μs period, and a significant oscillation occurs for at least 3μs. The gradient (di/dt) calculated using all the samples shown is -2.7603e-004 A/S. If only the first 30 samples are used (sampled at 0.04μs, giving a sample length of 1.2μs) then the estimated gradient is -2.1103e-004 A/S. For this first test, the error in estimation is 23% which is high, but the minimum vector time can be potentially reduced to 1.2 μs.

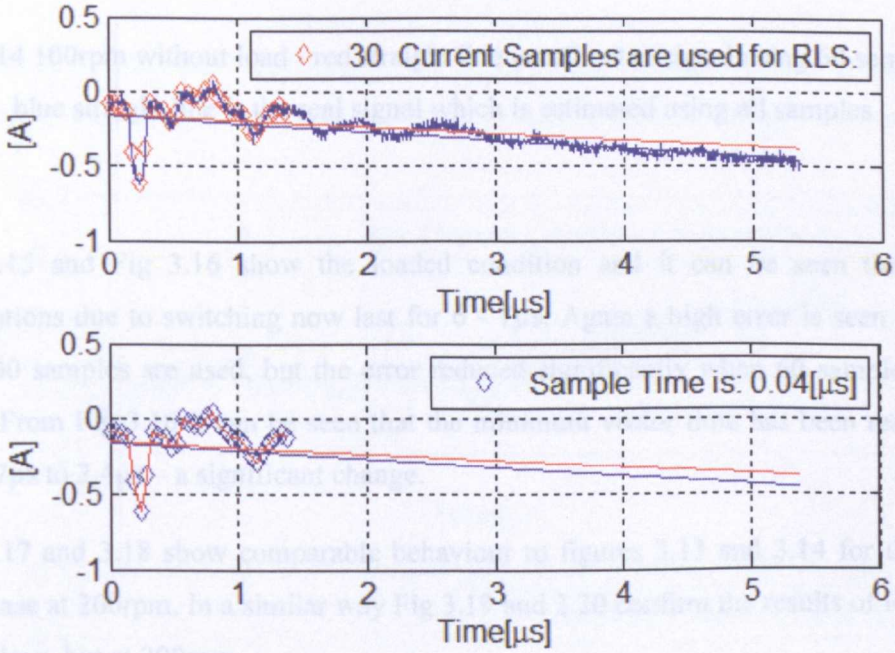

Fig 3.13 100rpm without load - red straight line is estimated signal using 30 samples; blue straight line is the real signal which is estimated using all samples

Fig 3.14 shows the improvement that can be achieved for the same operating conditions, but using 60 samples (2.4μs) rather than 30. The error is now 5%, but a longer minimum vector time is required.

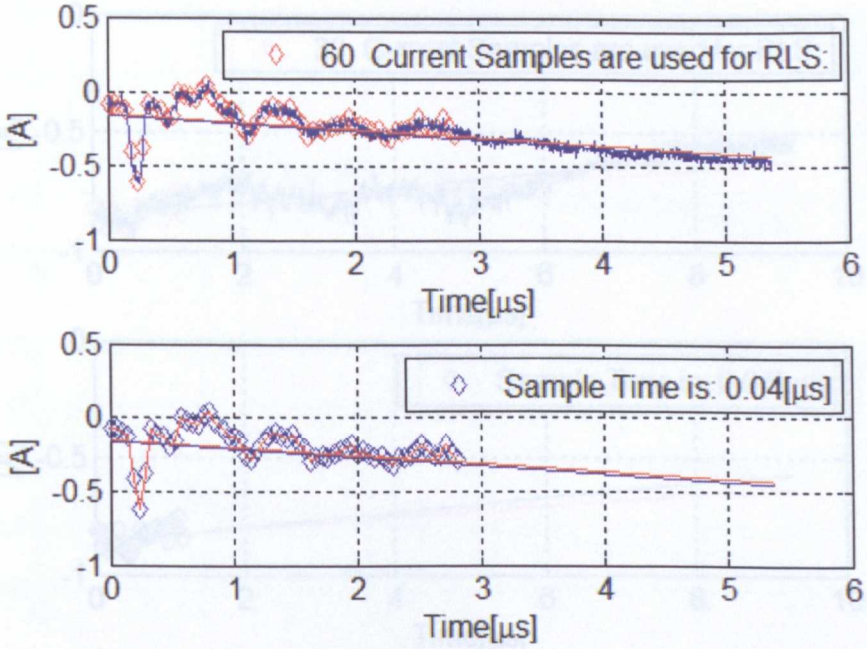

Fig 3.14 100rpm without load - red straight line is estimated signal using 60 samples; blue straight line is the real signal which is estimated using all samples

Fig 3.15 and Fig 3.16 show the loaded condition and it can be seen that the oscillations due to switching now last for 6 - 7μs. Again a high error is seen when only 30 samples are used, but the error reduced significantly when 60 samples are used. From Fig 3.16 it can be seen that the minimum vector time has been reduced from 7μs to 2.4μs – a significant change.

Fig 3.17 and 3.18 show comparable behaviour to figures 3.13 and 3.14 for the no load case at 200rpm. In a similar way Fig 3.19 and 3.20 confirm the results of loaded behaviour, but at 200rpm.

Fig 3.21 – 3.24 show comparable performance at 300rpm. Table 3.5 summarises the errors in the gradient measured for these various test conditions. It can be clearly seen that better accuracy is seen when 60 samples are used for the RLS algorithm. This means that the minimum pulse width required is 2.4μs. This is a significant reduction compared to the 6μs previously used.

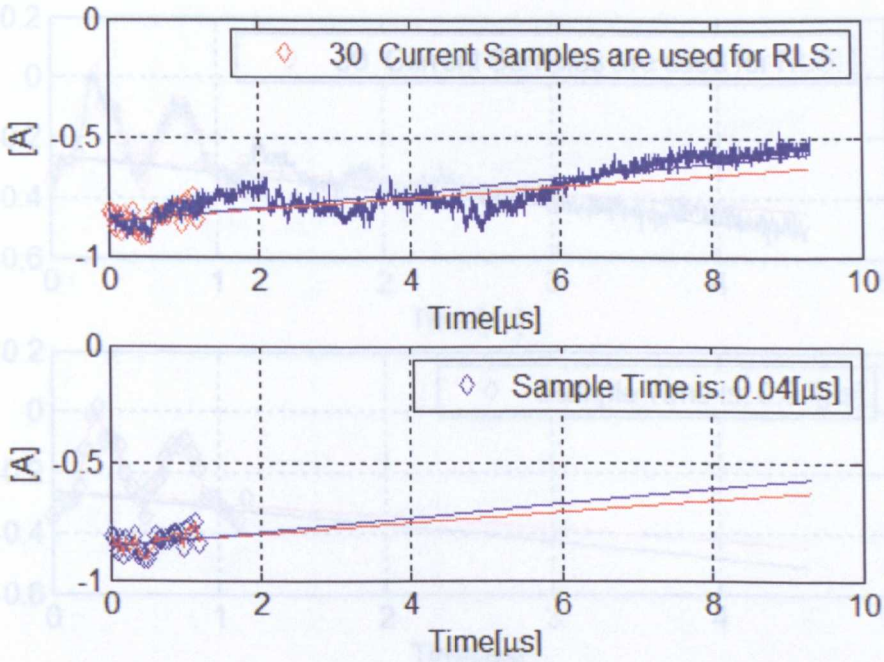

Fig 3.15 100rpm with 70% of load - red straight line is estimated signal using 30 samples; blue straight line is the real signal which is estimated using all samples

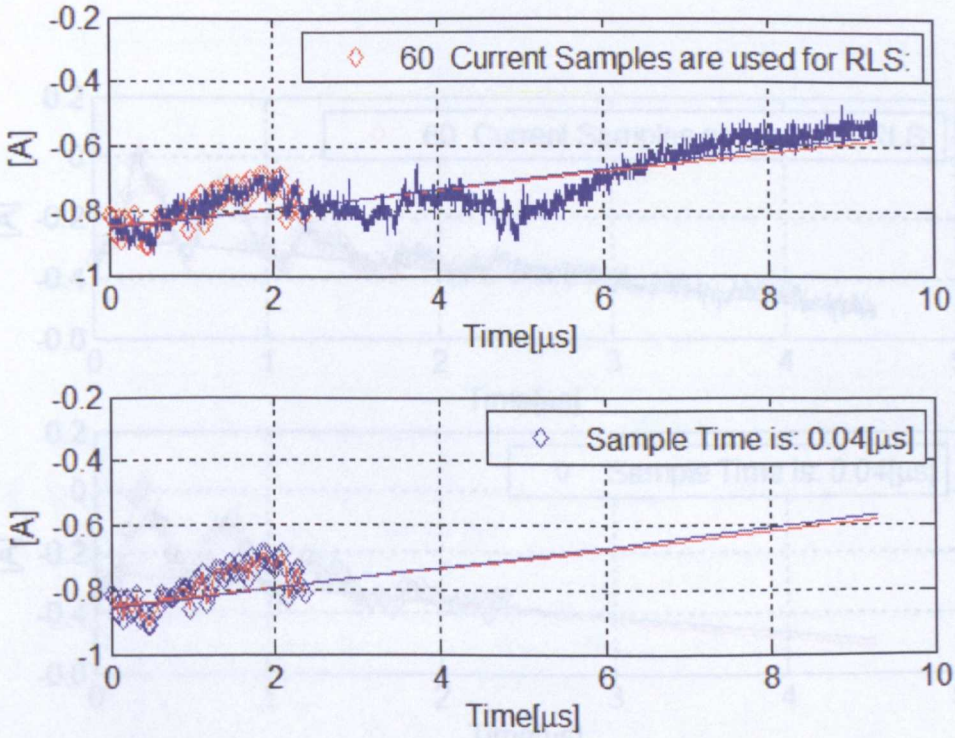

Fig 3.16 100rpm with 70% of load - red straight line is estimated signal using 60 samples; blue straight line is the real signal which is estimated using all samples

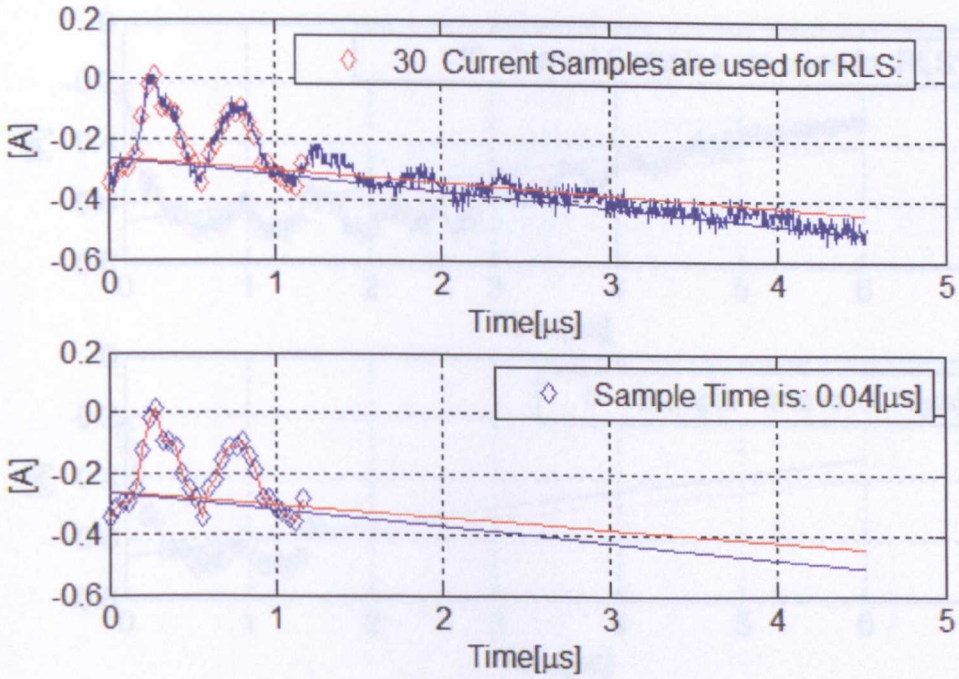

Fig

Fig 3.17 200rpm without load - red straight line is estimated signal using 30 samples; blue straight line is the real signal which is estimated using all samples

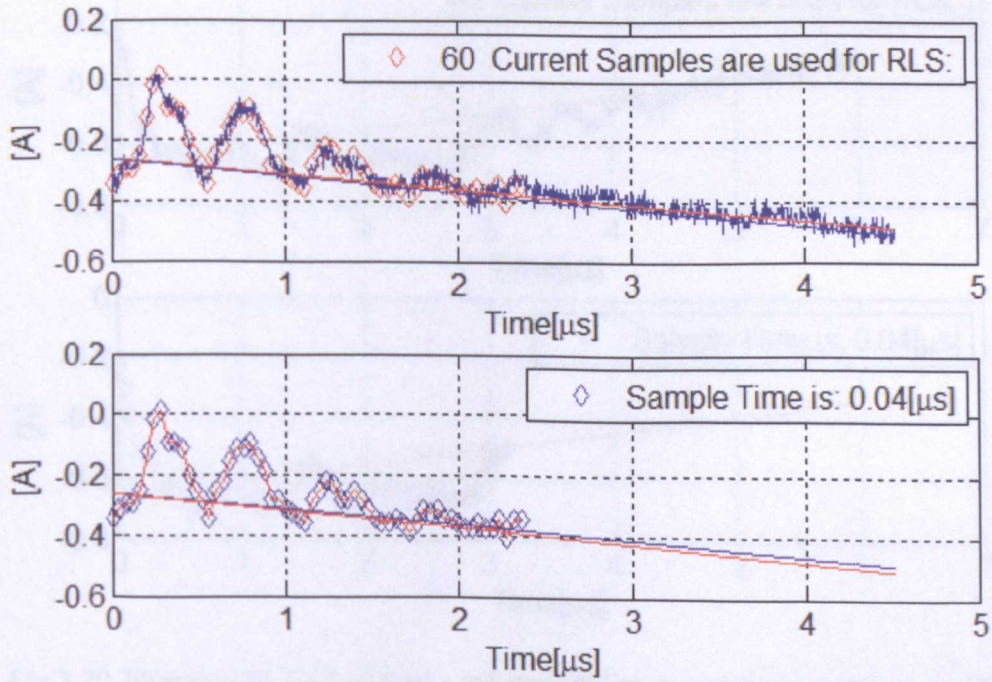

Fig 3.18 200rpm without load - red straight line is estimated signal using 60 samples; blue straight line is the real signal which is estimated using all samples

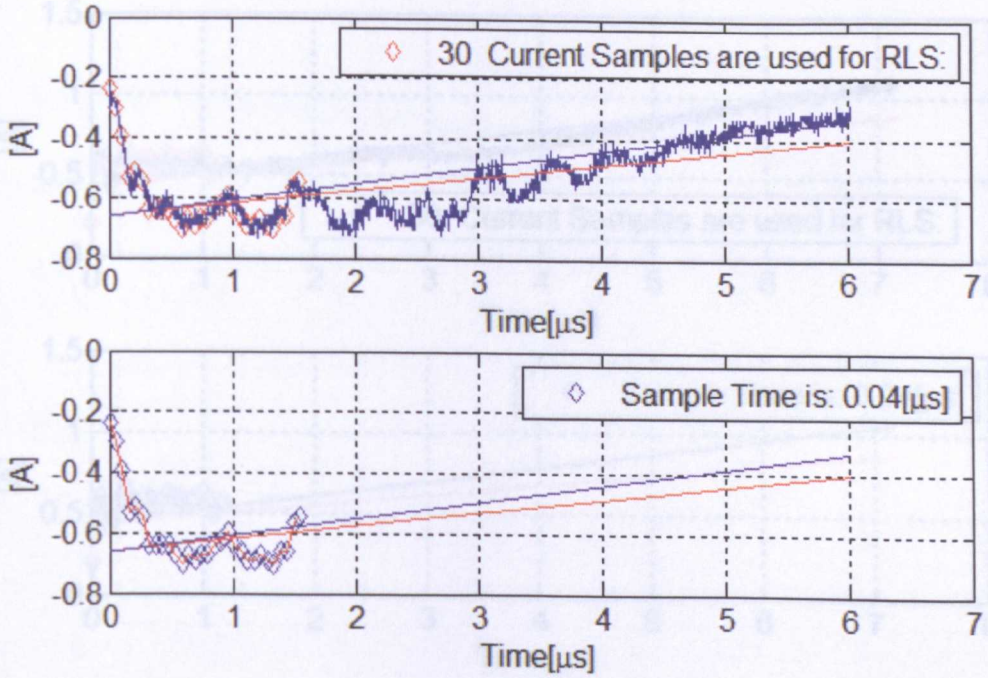

Fig 3.19 200rpm with 70% of load - red straight line is estimated signal using 30 samples; blue straight line is the real signal which is estimated using all samples

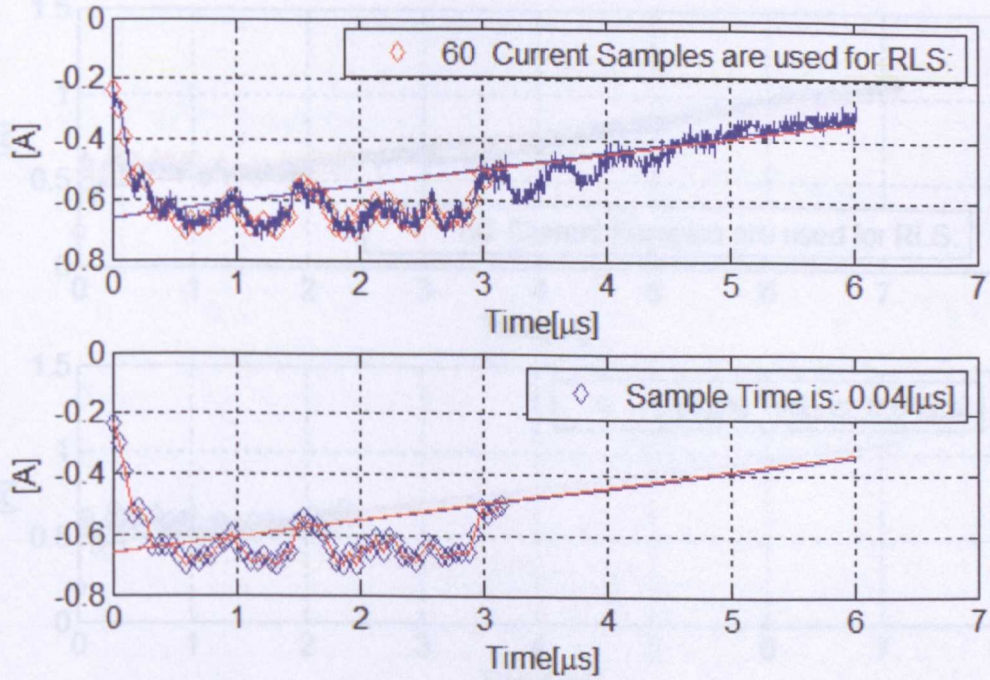

Fig 3.20 200rpm with 70% of load - red straight line is estimated signal using 60 samples; blue straight line is the real signal which is estimated using all samples

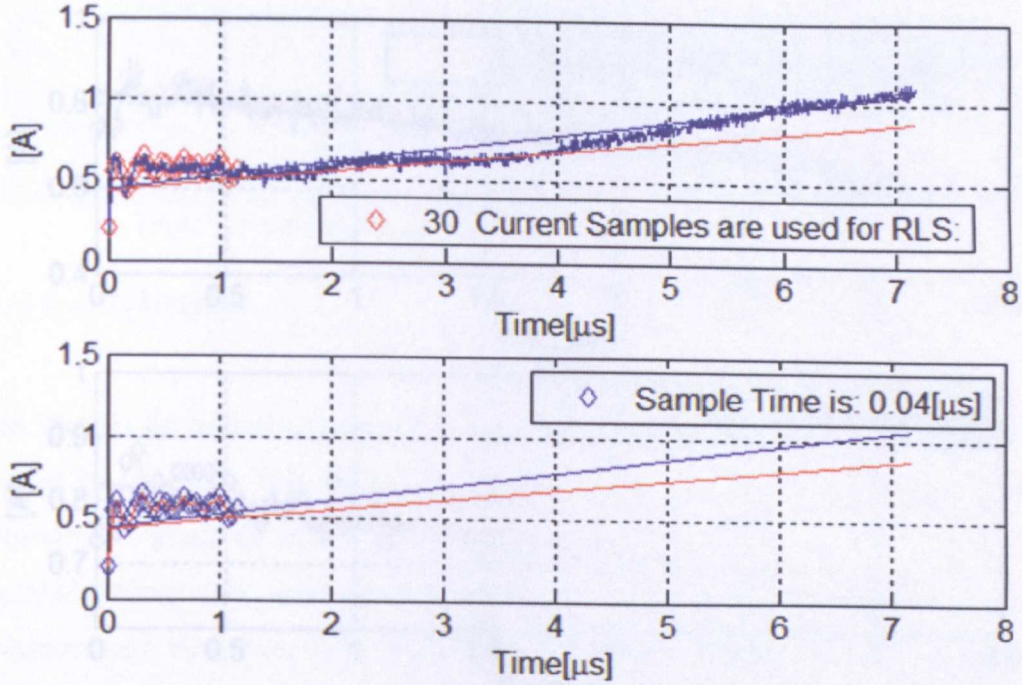

Fig 3.21 300rpm without load - red straight line is estimated signal using 30 samples; blue straight line is the real signal which is estimated using all samples

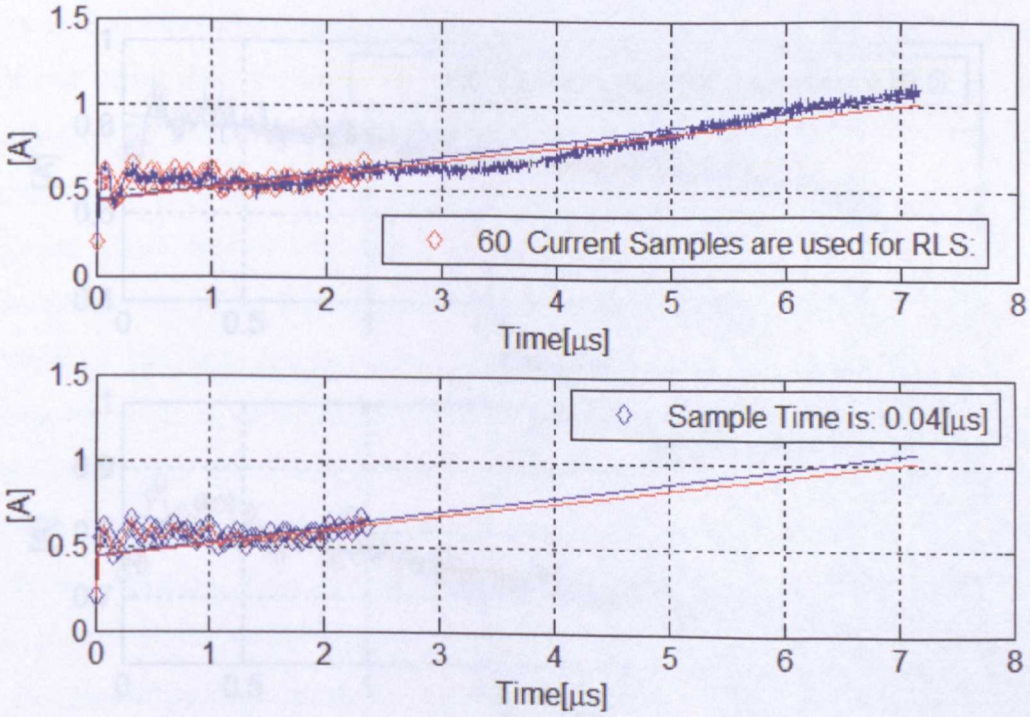

Fig 3.22 300rpm without load - red straight line is estimated signal using 60 samples; blue straight line is the real signal which is estimated using all samples

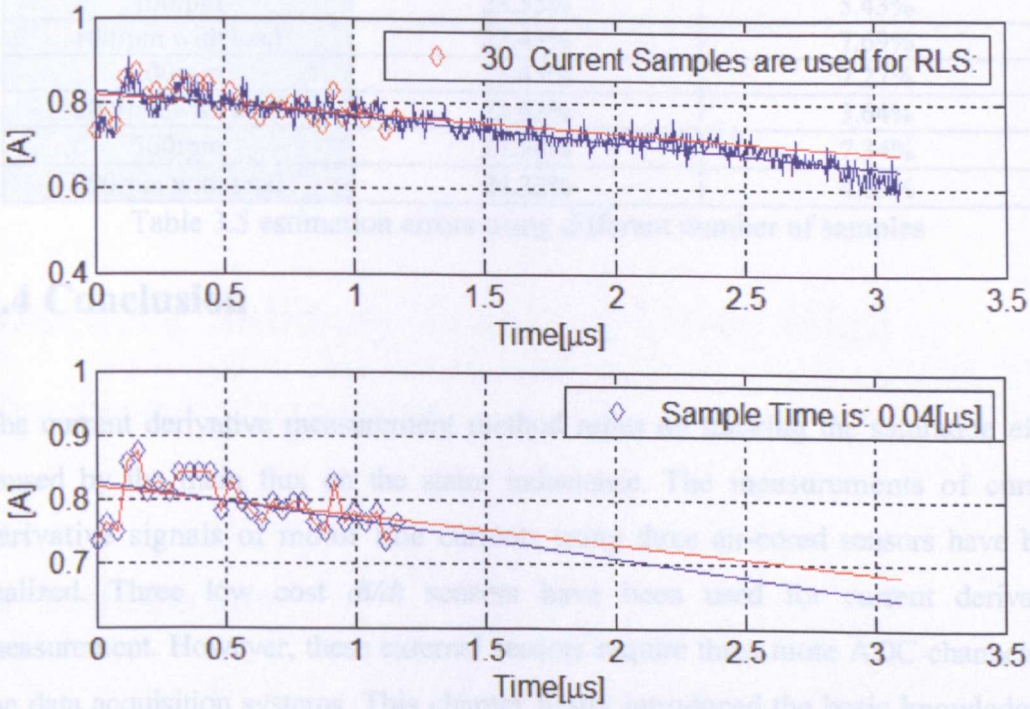

Fig 3.23 300rpm with 70% of load - red straight line is estimated signal using 30 samples; blue straight line is the real signal which is estimated using all samples

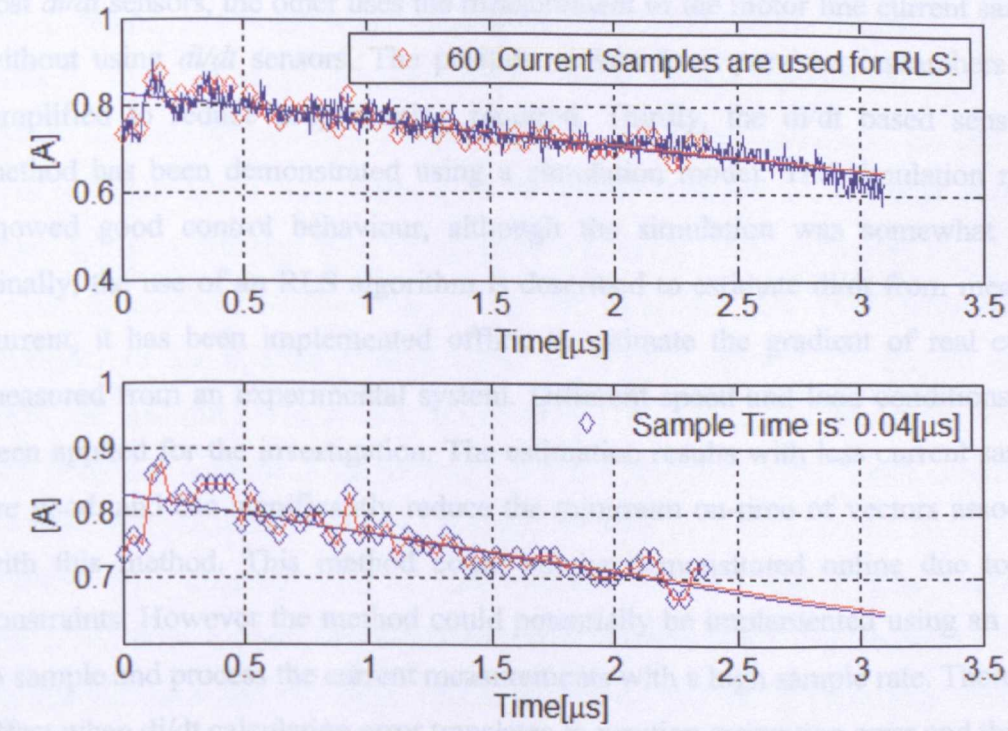

Fig 3.24 300rpm with 70% of load - red straight line is estimated signal using 60 samples; blue straight line is the real signal which is estimated using all samples

	Number of Samples 30	Number of Samples 60
100rpm	23.55%	5.43%
100rpm with load	22.43%	7.69%
200rpm	25.45%	7.27%
200rpm with load	21.82%	3.64%
300rpm	27.98%	7.34%
300rpm with load	24.32%	4.05%

Table 3.5 estimation errors using different number of samples

3.4 Conclusion

The current derivative measurement method relies on tracking the saturation effect caused by the main flux on the stator inductance. The measurements of current derivative signals of motor line currents using three air-cored sensors have been realized. Three low cost *di/dt* sensors have been used for current derivative measurement. However, these external sensors require three more ADC channels on the data acquisition systems. This chapter firstly introduced the basic knowledge of saliency tracking using voltage vector excitation method. Secondly, two types of current derivative measurement methods are briefly described; one uses three low cost *di/dt* sensors, the other uses the measurement of the motor line current samples without using *di/dt* sensors. The position scalars from previous researchers were simplified to reduce programming required. Thirdly, the di/dt based sensorless method has been demonstrated using a simulation model. The simulation results showed good control behaviour, although the simulation was somewhat ideal. Finally, the use of an RLS algorithm is described to estimate di/dt from measured current, it has been implemented offline to estimate the gradient of real current measured from an experimental system. Different speed and load conditions have been applied for the investigation. The estimation results with less current samples are good, and can significantly reduce the minimum on-time of vectors associated with this method. This method could not be demonstrated online due to time constraints. However the method could potentially be implemented using an ASIC to sample and process the current measurements with a high sample rate. There is an effect when di/dt calculation error translates to position estimation error and this will result on the accuracy of position estimation, however, the results from the simulation were good and this effect can be investigated when this method is applied online with a robust and capable data acquisition system.

Chapter 4

Magnetic Saliency Tracking Using High Frequency Injection

4.1 Introduction

In this chapter, four different sensorless methods based on saliency tracking are discussed in more detail namely the measurement axis frame estimation method, eddy current reflected resistance-based method, eddy current reflected inductance-based method, and Pulse Width Modulation (PWM) switching frequency injection method. Three of these methods extract the saturation-induced saliency of the PMSM machine by injecting a high frequency sinusoidal voltage in the estimated rotor reference frame. The fourth uses the current response to the PWM switching edges and is a different type of injection waveform. These methods identify the spacial inductance variation caused by the magnetic path [8]. Generally, the frequency of the injected voltage signal is selected between the current control bandwidth and the PWM switching frequency [74]. The processing of the resulting high frequency currents in the rotating frame can produce a signal which is related to the error in the estimated and true saliency position in order to obtain the estimated position. The injection axis is superimposed to the saliency axis, when the orientation error is zero. The orientation error represents the displacement between the injection axis and flux axis. The demodulation process in these four sensorless methods are completely different, however, the parameters of mechanical observer are kept same to aid compensation.

For the measurement axis method, the theory of saliency tracking is introduced. The analysis of this injection method is presented using relevant machine model equations. The demodulation process using the mathematical model is presented and tracking mechanisms are also illustrated using a block diagram. In this method, the phase shift occurring as a function of load is analyzed. The offset compensation is achieved by using a look-up table.

For the eddy current reflected resistance and inductance based method, the estimated rotor speed/position is obtained from the eddy current reflected resistance and inductance based saliency induced by the high frequency voltage injection [72]. The analysis of the asymmetric resistance effect in the machine model is carried out. The current error signals from resistance and inductance based saliency is presented using mathematical equations. The demodulation process for both methods has a similar structure but the structure of the tracking method is different. The eddy current losses are also analyzed in their relationship to the position estimation.

For PWM switching frequency injection method, a novel signal processing method is proposed using two current samples within one PWM period. The demodulation process is also presented in the derived equations. There are no low pass filters used since the position estimation is achieved at every current sampling step. The advantage using this novel method in a SMPMSM is described and system stability, bandwidth of speed controller, and higher injection frequency are all improved.

4.2 Measurement Axis Method

The measurement axis frame estimation method is used to track the saliency of PM Machines by injecting a high frequency voltage signal in the synchronous d-axis. The resulting high frequency currents (*d-q*) are mathematically processed to obtain the orientation error which represents the displacement between the injection axis and saliency axis [6]. The estimated speed and position angle are obtained from the tracking mechanisms, which use Phase Locked Loop control algorithms or mechanical observers.

Fig 4.1 shows the basic structure of a sensorless drive using a pulsating signal injection method. In this section, the theory behind the saliency tracking algorithm and the demodulation process are presented. One aspect for investigation is the frequency of the injection signal. Low and high injection frequencies are used in this work for the measurement axis frame method and implemented in the practical experiment, to investigate the trade-offs associated with injection frequency. In Fig 4.1, one speed controller and two current controllers are implemented for a vector controlled PMSM machine. The pulsating voltage signal is injected in the *d-axis* to track the saliency, and then the estimated speed is obtained.

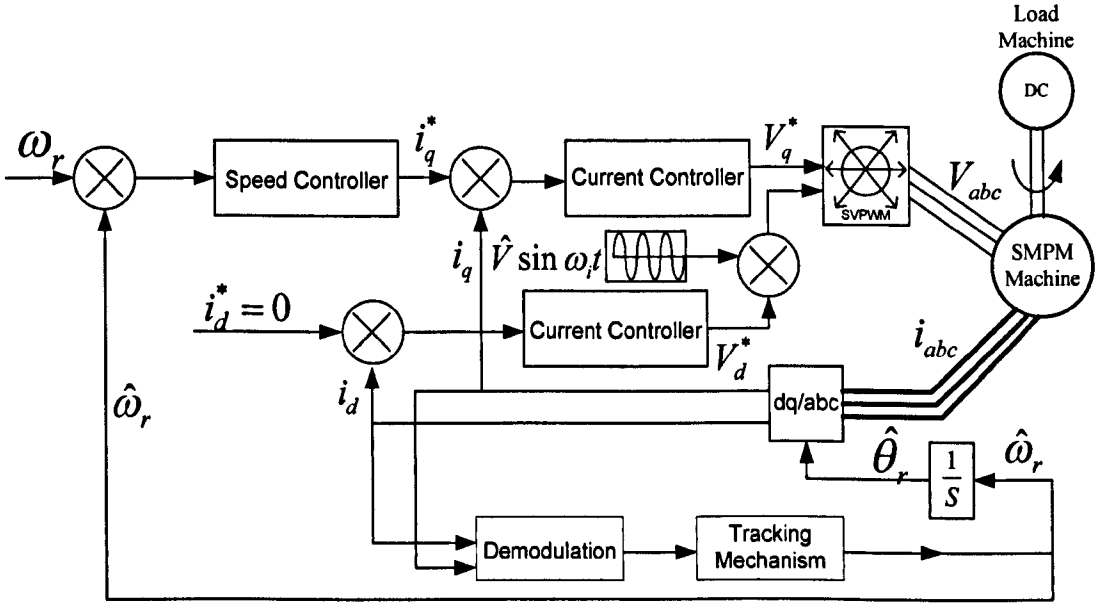

Fig 4.1 block diagram of pulsating signal injection sensorless method

4.2.1 Theory of Saliency Tracking

The pulsating injection method in the synchronous *d-axis* has been introduced in the literature review of chapter 2. The main advantage of using the *d-axis* injection method is to minimize the high frequency current in the *q-axis* as this will reduce the pulsating torque and acoustic noise. The rotor position estimation is achieved to track the saturation-induced saliency directly. The stator phase inductances have been introduced in chapter 2. Here, the HF salient model equation [6] can be established using the estimated saliency current, the stator inductance as shown in (4.1). The position error is presented as $\Delta\theta_\delta = \hat{\theta}_\delta - \theta_\delta$ [6], [8].

$$\begin{bmatrix} \tilde{v}_\delta^e \\ \tilde{v}_\gamma^e \end{bmatrix} = \frac{d}{dt}\begin{bmatrix} L_s - \Delta L_s \cos(2\Delta\theta_\delta) & -\Delta L_s \sin(2\Delta\theta_\delta) \\ -\Delta L_s \sin(2\Delta\theta_\delta) & L_s + \Delta L_s \cos(2\Delta\theta_\delta) \end{bmatrix} \cdot \begin{bmatrix} \tilde{i}_\delta^e \\ \tilde{i}_\gamma^e \end{bmatrix} \tag{4.1}$$

where $\Delta L_s = (L_d + L_q)/2$; $L_s = (L_d - L_q)/2$. $\tilde{v}_\delta^e$ and $\tilde{v}_\gamma^e$ represents the voltage signal in the estimated saliency orientated *d-q* frame. $\tilde{i}_\delta^e$ and $\tilde{i}_\gamma^e$ represents the current vectors when the high frequency voltage injection are applied into the HF saliency model [6] The voltage is represented by its amplitude and frequency in (4.2) [6][73]

$$\begin{bmatrix} \tilde{v}_\delta^e \\ \tilde{v}_\gamma^e \end{bmatrix} = \hat{V}\begin{bmatrix} \sin(\omega_i t) \\ 0 \end{bmatrix} \tag{4.2}$$

The high frequency current response given in (4.3) is derived from (4.1) and (4.2). The pulsating current is shown in (4.3) [76] and needs to be processed in order to obtain the error signal. Four methods are proposed to generate the error signal and are discussed in this chapter.

$$\begin{bmatrix} \tilde{i}_\delta^e \\ \tilde{i}_\gamma^e \end{bmatrix} = \frac{-\hat{V}\cos(\omega_i t)}{L_\delta L_\gamma \omega_i}\begin{bmatrix} L_s - \Delta L_s \cos(2\Delta\theta_\delta) \\ -\Delta L_s \sin(2\Delta\theta_\delta) \end{bmatrix} \tag{4.3}$$

The measurement axis method is based on injecting a pulsating signal onto the estimated *d-axis* of the rotating frame. This method is developed in Fig 4.2. The pulsating currents can be derived from the currents in the estimated saliency frame. The pulsating currents $\tilde{i}_\delta^m$ and $\tilde{i}_\gamma^m$ have the same amplitude if the estimated saliency frame d^e and q^e is correctly oriented with the actual saliency frame *d-q*. In other words, the pulsating currents have the same amplitude in the estimated saliency frame. Therefore, the two frames have a 45° displacement [76] [77]. The measurement frame is defined by δ^m and γ^m, which is 45° away from the estimated saliency frame by (d^e and q^e) and the injected signal is aligned to this estimated saliency frame.

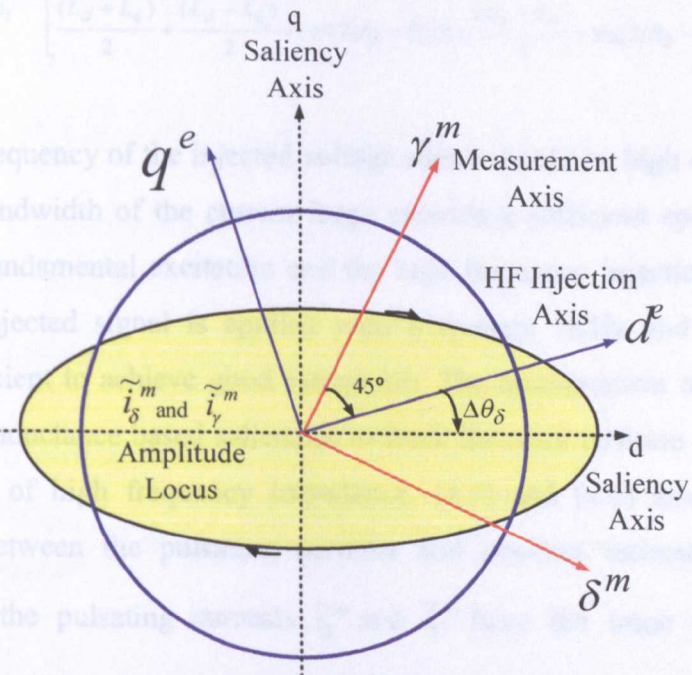

Fig 4.2 the measurement axis method by using HF injection

The measurements of the HF currents in this measurement axis are extracted from the measurements made using the estimated saliency. The coordinate rotation between the measurement axis and estimated saliency frame is presented by [7], [77]

$$\begin{bmatrix} \tilde{i}_\delta^m \\ \tilde{i}_\gamma^m \end{bmatrix} = (\cos 45°) \cdot \begin{bmatrix} 1 & -1 \\ 1 & 1 \end{bmatrix} \cdot \begin{bmatrix} \tilde{i}_\delta^e \\ \tilde{i}_\gamma^e \end{bmatrix} \tag{4.4}$$

In (4.3), the high frequency current is related to the stator's inductance in the *d-q* frame as given by: [6, 77]

$$\begin{bmatrix} \tilde{i}_\delta^e \\ \tilde{i}_\gamma^e \end{bmatrix} = \frac{-\hat{V}\cos(\omega_i t)}{L_d L_q \omega_i} \begin{bmatrix} \frac{(L_d + L_q)}{2} + \frac{(L_d - L_q)}{2} \times \cos[2(\theta_\delta - \hat{\theta}_\delta)] \\ -\frac{(L_d - L_q)}{2} \times \sin[2(\theta_\delta - \hat{\theta}_\delta)] \end{bmatrix} \tag{4.5}$$

Therefore, the measurement frame values can be calculated from the rotating HF current response using (4.6): [6, 7, 76, 77]

$$\begin{bmatrix} \tilde{i}_\delta^m \\ \tilde{i}_\gamma^m \end{bmatrix} = \frac{-\sqrt{2}\hat{V}\cos(\omega_i t)}{2L_d L_q \omega_i} \begin{bmatrix} \frac{(L_d+L_q)}{2} + \frac{(L_d-L_q)}{2} \times \cos[2(\theta_\delta - \hat{\theta}_\delta)] - \frac{(L_d-L_q)}{2} \times \sin[2(\theta_\delta - \hat{\theta}_\delta)] \\ \frac{(L_d+L_q)}{2} + \frac{(L_d-L_q)}{2} \times \cos[2(\theta_\delta - \hat{\theta}_\delta)] + \frac{(L_d-L_q)}{2} \times \sin[2(\theta_\delta - \hat{\theta}_\delta)] \end{bmatrix} \tag{4.6}$$

In (4.6), the frequency of the injected voltage signal should be high enough as to fall beyond the bandwidth of the current loops providing sufficient spectral separation between the fundamental excitation and the high frequency injection signal. In this project, the injected signal is applied with frequency 1KHz and amplitude 25V which is sufficient to achieve good estimation. The measurement axis method uses resistance or inductance based saliencies to track the rotor position according to the characteristics of high frequency impedance. (4.5) and (4.6) also represents the relationship between the pulsating currents and position estimation errors. The amplitude of the pulsating currents $\tilde{i}_\delta^m$ and $\tilde{i}_\gamma^m$ have the same value when the estimated frame δ^e and γ^e is correctly superimposed with the actual saliency frame δ and γ. If this is not true, the error signal can be constructed as the difference between the amplitude of $\tilde{i}_\delta^m$ and $\tilde{i}_\gamma^m$. In other words, the position estimation errors can be represented as $\theta_\delta - \hat{\theta}_\delta$ and the two current amplitudes $\tilde{i}_\delta^m$ and $\tilde{i}_\gamma^m$ are the same if the position estimation error is equal to zero. The control processing drives the error to zero, by making the amplitude of the current $|\tilde{i}_\delta^m|$ and $|\tilde{i}_\gamma^m|$ equal.

4.2.2 Demodulation Process

The demodulation process required to obtain the error signals from the HF current response is shown in Fig 4.3. Two measured current signals pass through the band pass filters so that the HF current carrier signal remains with the information of the saliency. The HF carrier current signal is multiplied by the HF injection pulsating signal. The multiplication and the low pass filtering are used to demodulate the signal in the measurement reference frame. In [6, 77], orthogonal carriers are used to avoid the influence of any phase shift due to the stator resistance, or signal processing delay. The resulting carrier signals are multiplied by themselves to

produce the amplitude square of the carrier signal in the measurement frame. This demodulation process can be represented in the equation (4.7) and (4.8).

$$i_1 = i_2 = \frac{-\sqrt{2}\hat{V}}{4L_\delta L_\gamma \omega_i}\cdot\left(L_s + \Delta L_s \cos(2\Delta\theta_\delta) - \Delta L_s \sin(2\Delta\theta_\delta)\right)$$
$$i_3 = i_4 = \frac{-\sqrt{2}\hat{V}}{4L_\delta L_\gamma \omega_i}\cdot\left(L_s + \Delta L_s \cos(2\Delta\theta_\delta) + \Delta L_s \sin(2\Delta\theta_\delta)\right) \tag{4.7}$$

$$i_1^2 + i_2^2 = \frac{1}{4}\cdot[I_0 + I_1\cos(2\Delta\theta_\delta) - I_1\sin(2\Delta\theta_\delta)]^2 = \frac{\left|\tilde{i}_\delta^m\right|^2}{4}$$
$$i_3^2 + i_4^2 = \frac{1}{4}\cdot[I_0 + I_1\cos(2\Delta\theta_\delta) + I_1\sin(2\Delta\theta_\delta)]^2 = \frac{\left|\tilde{i}_\gamma^m\right|^2}{4} \tag{4.8}$$

where $I_0 = \dfrac{-\sqrt{2}\cdot(L_d + L_q)}{4L_d L_q \omega_i}$ and $I_1 = \dfrac{-\sqrt{2}\cdot(L_d - L_q)}{4L_d L_q \omega_i}$. The error signal is represented by

$$\zeta = \frac{\left|\tilde{i}_\delta^m\right|^2}{4} - \frac{\left|\tilde{i}_\gamma^m\right|^2}{4} = I_0 I_1 \sin(2\Delta\theta_\delta) + \frac{I_1^2}{2}\sin(4\Delta\theta_\delta) \tag{4.9}$$

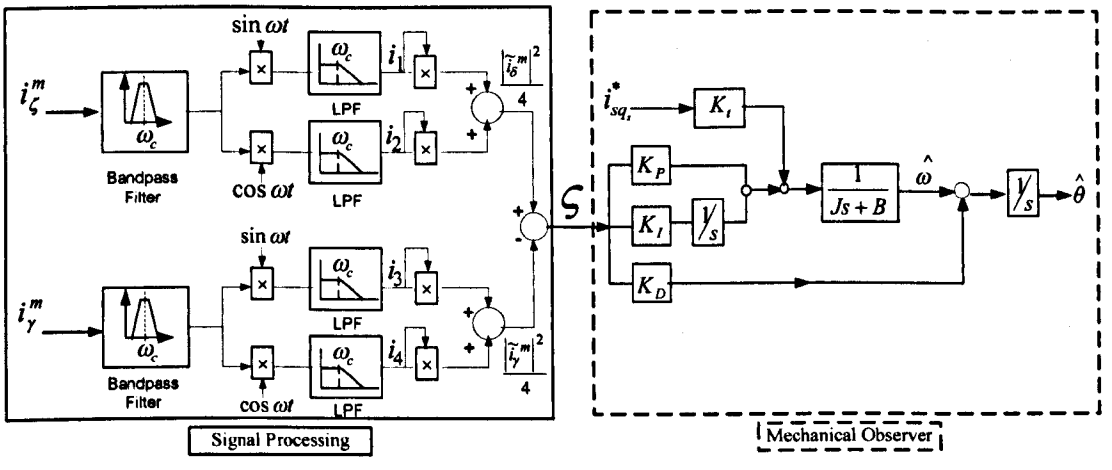

Fig 4.3 structure of signal processing procedures and mechanical observer

Two software band pass filters are used to extract the HF components in the tracking loop. For 1KHz injection, the band pass filter is selected with cut-off frequencies of 800 and 1200 Hz. i_1, i_2, i_3 and i_4 are obtained after four low pass filters (cut-off frequency of 60Hz). The saliency tracking is achieved using this high frequency component. The high frequency carrier signal is separated from the fundamental excitation current in the estimated synchronous frame. The use of the low pass filter is to minimize the noise inside the current error signal during the demodulation process. The band pass and low pass filters must be used in software rather than in

the hardware, because the frequency of the injection current is changing with the rotor speed due to the synchronous rotation on the injection axis. Hence, the phase shift introduced by any hardware filter will vary with rotor speed. In addition, the power loss and noise amplification can impair the system response when any additional hardware is used.

In Fig 4.3, the demodulation process and the tracking mechanism are linked altogether by the error signal. Demodulation generates orientation error and the tracking mechanism can produce the estimated position using this error signal. The disadvantage of this demodulation method is that it relies on a sinusoidal saliency induced by saturation. Due to the appearance of high order saliency or spatial harmonics, the amplitude of the current vector is not unique and it can generate errors in the saliency position estimation that are difficult to compensate because the tracking observer may lock onto any of the points that satisfy this condition. The direct demodulation method is preferred for the development of the measurement axis method. The current in *q-axis* is obtained from the measurement of α-β currents and then is separated from the fundamental using one band pass filter. The processed signal is multiplied by the high frequency current and the error signal is generated after passing through a low pass filter. The tracking mechanism is implemented exactly same as the one used in Fig 4.3. A first order of low pass filter is used to obtain a smooth estimated speed signal. A double integration is used in the tracking mechanism (either PLL or observer) to give the error signal contained $2\Delta\theta_\delta$ in (4.10) [6]

$$\zeta = \frac{-\hat{V}\cos(\omega_i t)}{L_\delta L_\gamma \omega_i}\sin(2\Delta\theta_\delta) \tag{4.10}$$

4.2.3 Calibration of the Position Angle Offset

The saturation saliency changes in phase and magnitude as the load on the PMSM machine is varied. The rotor magnets produce a maximum flux density in the *d-axis* direction under the no load condition. This flux is distributed in the air-gap and the stator iron saturates directly around the *d-axis*. However, the saturation saliency is

oriented with the air-gap flux position, instead of the rotor position. The current in the *q-axis* stator windings establishes a flux, which moves the air-gap flux distribution towards the *q-axis* when loaded. The saturation saliency is displaced from the rotor direction indicated by the *d-axis*. This displacement angle between the measured rotor position and the estimated saliency position is cancelled as the phase shift or angle offset. The position angle offset is measured as a function of load for the measurement axis sensorless method. The phase shift calibration is made to obtain the offset angle by applying different load conditions.

A look-up table for phase shift compensation is implemented to correct the estimated angle with load. The offset angles can be measured approximately under the different load conditions at steady state. The look-up tables are created from the offset angle and torque current i_{sq}. In the experiment, the torque current i_{sq} is represented between 0 and 8A in the look-up table. During the load transient, the corresponding offset angle is automatically chosen from the look-up table. The look-up table is measured for the machine used in this work shown in the table 4.1.

Load	**20%**	**40%**	**50%**	**60%**	**70%**	**80%**	**100%**
i_{sq} *(A)*	1.49	3.09	3.59	4.43	4.87	5.93	7.63
θ_{offset} **(radians)**	**-0.029**	**-0.064**	**-0.075**	**-0.092**	**-0.096**	**-0.116**	**-0.151**

Table 4.1 a look-up table for phase shift compensation

An experimental result illustrating the position estimation error before and after phase shift compensation is shown in Fig 4.4. The measured position estimation error in the figure is under the full load condition. The estimated results are improved when the phase shift is compensated. This process can provide the best position feedback for either current transformation or speed control. The result in Fig 4.13 is a good example to show the importance of the phase shift compensation and

this method is also suitable for other motor applications. Without compensation, the orientation of vector control is incorrect and the system may go out of control.

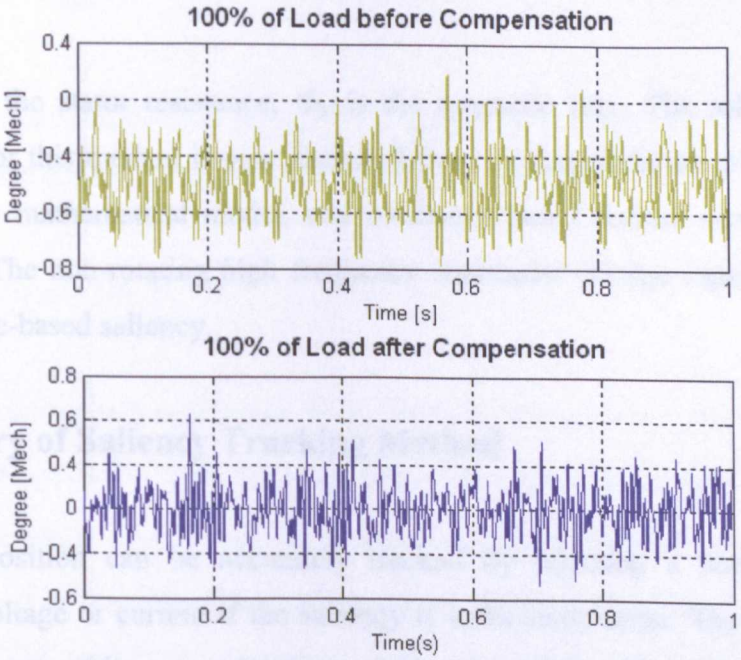

Fig 4.4 position errors before and after the phase shift compensation (rotor speed at 160rpm)

4.3 Eddy Current Reflected Resistance Based Saliency Tracking Method

The second saliency tracking methods using non-rotating high frequency voltage is based on the eddy current reflected resistance-based saliency [72]. Eddy current effects are complicated to model mathematically. Eddy currents can be modelled as the currents circulating through a pair of short-circuited coils along the *d-q* rotating frame. The high frequency magnetic excitation generates a power loss due to eddy currents. The power loss can be used to detect the rotating frame *d-axis*. Eddy currents are produced from the induced electromotive force (EMF). The EMF is generated by a change in the magnetic flux according to Faraday's Law. The eddy current is presented in terms of resistance and magnetic flux shown in (4.11).

Equation (4.11) is negative to indicate that the eddy current can produce an opposite magnetic field compared to the EMF [30, 46].

$$I_{Eddy_Current} = -\frac{1}{R_s}\frac{d\Phi_B}{dt} \tag{4.11}$$

where R_s is the stator resistance, Φ_B is the magnetic flux. The saliency tracking algorithms for this method is now reviewed from its demodulation process, analysis of resistance mathematical model, and resistance based current error for position estimation. The non-rotating high frequency sinusoidal voltage signal is used with the resistance-based saliency.

4.3.1 Theory of Saliency Tracking Method

The rotor position can be accurately tracked by injecting a non-rotating high frequency voltage or current if the saliency is sufficiently large. The first person to observe current eddies was François Arago in 1824. These discoveries were explained by Michael Faraday. The eddy current is generated as a feedback loop inside the stator coil of a PMSM. The eddy current creates induced magnetic fields that oppose the change of the original magnetic field. For the PMSM machine, the eddy current reflected resistance-based saliency can be utilized for position estimation. The stator coil resistance and eddy current reflected resistance are used for this saliency tracking method. The eddy current reflected resistance is an additional element when the eddy current caused power loss is considered. The equivalent resistance is presented in equation (4.12).

$$R_{eq} = R_s + R_{eddy} \tag{4.12}$$

where the stator resistance is R_s, and the eddy current reflected resistance is R_{eddy}. The three phase eddy current reflected resistance can be defined in a similar way to the stator inductances in the high frequency saliency model for PMSM machine. Therefore, the eddy currents can be modelled as the current circulating through the

resistance along the *d-axis* and *q-axis*. The expression of three phase eddy current reflected resistances is presented in equation (4.13) [72].

$$\begin{cases} R_{eq_d} = R_s + R_{Eddy_d} \\ R_{eq_q} = R_s + R_{Eddy_q} \end{cases} \tag{4.13}$$

and, as well be discussed later $R_{Eddy_d} <> R_{Eddy_q}$. It is assumed that if the inductance variation is negligible, the equivalent impedance is given by

$$Z_{eq}^{r'} = R_{eq_dq}^{r'} + (p + j\omega_e)L_s \tag{4.14}$$

In (4.14), Ls is the self inductance of the PMSM machine and p is the differential operator. The injection frequency imaginary element $j\omega_c$ can be used instead of the differential operator p in (4.14). The cross coupling term $j\omega_e L_s$ has a very small value compared to the large injection frequency, which can be considered negligible in (4.14). The stator coil resistance and eddy current reflected resistance is modulated by the saturation induced saliency in the rotor estimated synchronous reference frame r'. From (4.13) the asymmetric resistance can be presented in matrix form as [72]:

$$R_{eq_dq}^{r} = \begin{bmatrix} R_{dd} & R_{dq} \\ R_{qd} & R_{qq} \end{bmatrix}^{r} = \Sigma R \begin{bmatrix} 1 & 0 \\ 0 & 1 \end{bmatrix} + \Delta R \begin{bmatrix} cos(2\theta_{error}) & -sin(2\theta_{error}) \\ -sin(2\theta_{error}) & -cos(2\theta_{error}) \end{bmatrix} \tag{4.15}$$

Transforming (4.15) to the rotating reference frame, the asymmetric resistance is expressed by [72]:

$$R_{eq_dq}^{r} = \begin{bmatrix} \Sigma R + \Delta R\, cos\, 2\theta_{error} & -\Delta R\, sin\, 2\theta_{error} \\ -\Delta R\, sin\, 2\theta_{error} & \Sigma R - \Delta R\, cos\, 2\theta_{error} \end{bmatrix}^{r'} \tag{4.16}$$

where the average and differential value of asymmetric resistance are $\Sigma R = R_s + \frac{R_{Eddy_d} + R_{Eddy_q}}{2}$ and $\Delta R = R_s + \frac{R_{Eddy_d} - R_{Eddy_q}}{2}$, the position error θ_{error} is defined as the angle difference between the real and estimated synchronous frame.

In the rotating synchronous frame, the pulsating injection voltage equation is expressed in term of asymmetric resistance and pulsating current by [72]

$$\begin{bmatrix} \tilde{v}_d^e \\ \tilde{v}_q^e \end{bmatrix} = \begin{bmatrix} \Sigma R + \Delta R \cos 2\theta_{error} & -\Delta R \sin 2\theta_{error} \\ -\Delta R \sin 2\theta_{error} & \Sigma R - \Delta R \cos 2\theta_{error} \end{bmatrix} \cdot \begin{bmatrix} \tilde{i}_\delta^e \\ \tilde{i}_\gamma^e \end{bmatrix} \tag{4.17}$$

The non-rotating high frequency signal is injected in the estimated *d-axis* and is represented by

$$\begin{aligned} \begin{bmatrix} \tilde{v}_d^e \\ \tilde{v}_q^e \end{bmatrix} &= \hat{V}\begin{bmatrix} \cos(\omega_i t) \\ 0 \end{bmatrix} = -\frac{1}{2}\hat{V}e^{j\omega_i t} + \frac{1}{2}\hat{V}e^{-j\omega_i t} \\ \begin{bmatrix} \tilde{v}_d^e \\ \tilde{v}_q^e \end{bmatrix} &= \begin{bmatrix} R_{dd}\tilde{i}_d^e + L_s(p + j\omega_i t)\tilde{i}_d^e + R_{dq}\tilde{i}_q^e \\ = R_{qq}\tilde{i}_q^e + L_s(p + j\omega_i t)\tilde{i}_q^e + R_{qd}\tilde{i}_d^e \end{bmatrix} \end{aligned} \tag{4.18}$$

In (4.18), L_s is assumed as a constant and machine will have inductance-based saliency if consider the stator tooth saturation. The injection method could be applied in the rotating *q-axis* synchronous frame and in this case the estimation can also provide excellent results. However, in this project, *d-axis* injection technique is used, and is considered to compare with the other three *d-axis* sensorless injection methods. As a result, the pulsating current in the *d* frame can be derived from (4.16) – (4.18). The current equation (4.19) in d-axis is therefore presented as

$$\begin{aligned} \tilde{i}_d^e &= \frac{\tilde{v}_d^e - R_{dq}\tilde{i}_q^e}{R_{dd} + L_s(p + j\omega_i)} = \frac{\tilde{v}_d^e\left[R_{qq} + L_s(p + j\omega_i)\right] - R_{dq}\tilde{v}_q^e + R_{dq}R_{qd}\tilde{i}_d^e}{\left[R_{dd} + L_s(p + j\omega_i)\right]\left[R_{qq} + L_s(p + j\omega_i)\right]} \\ &= \frac{-R_{dq}}{-L_s\omega_i^2 + (R_{dd} + R_{qq})L_s j\omega_i + (R_{dd} + R_{qq})L_s j\omega_i + R_{dd}R_{qq} - R_{dq}R_{qd}}\hat{V}\cos(w_i t) \end{aligned} \tag{4.19}$$

The magnitude of $\tilde{i}_d^e$ can be defined by the differential asymmetric resistance ΔR. The position estimation error θ_{error} is used to drive a tracking mechanism to obtain the estimated position from the resistance-based saliency. The pulsating current signal also tracks the saturated saliency rather than the rotor position. The pulsating

currents are obviously obtained from (4.19) and the demodulation process can be achieved by using signal processing methods such as high pass and low pass filters. The desired resistance-based saliency error $\tilde{i}_d^e$ and $\tilde{i}_q^e$ can be isolated by the demodulation process. As discussed previously for comparison purpose, from (4.19), $\tilde{i}_d^e$ is the only term required for saliency position estimation. The eddy current is created by a "feedback loop" inside the stator coil and this stator coil can be considered to be the shorted circuit. In the stationary frame α-β, Fig 4.5 shows the stator short-circuit resistance is represented as R_α and R_β. The short-circuit stator resistance R_d and R_q is represented in the rotating frame *dq-axis*. For the d-axis pulsating injection saliency tracking method, the pulsating vector voltage can be superimposed along the estimated d-axis to obtain the spatial saliency signals from orthogonal axes [72]. The eddy current loss occurs in the stator, the stator resistance is therefore asymmetric. In stator teeth, additional load-dependent saturation must occur as the fundamental current increases. This leads to a change in the stator eddy current loss distribution [72]. The eddy current reflected resistances are different in the *d-q* axis. In [72], CW SPM is analyzed and the asymmetric resistance reflected by the eddy current loss variation can be achieved. The resistance-based saliency is $R_q > R_d$. In [72], DW SPM machine with a ring magnet is analyzed and the variation of stator eddy current loss can be higher. The overall resistance-based saliency is $R_q > R_d$. If the rotor is made from a fractional magnet, the air gap is between two magnet poles and the power loss at $\theta_e = 90°$ is reduced in the permanent magnet. The different resistance-based saliency is $R_d > R_q$ .In a PMSM machine, the eddy currents can be modelled as the currents circulating through these shorted stator coils along the synchronously rotating axes *d-q*. The *d-axis* is aligned with the N-pole of the rotor and *q-axis* is 90° apart from the *d-axis*. For simplicity, the basic structure of a PMSM machine with shorted stator coils is shown in Fig 4.5. For the stator winding, the voltage and flux linkage equations in rotating frame are [5]

$$\hat{V}_d = R_s i_d + \frac{d\lambda_d}{dt} - \omega_e L_q i_q \tag{4.20}$$

$$\hat{V}_q = R_s i_q + \frac{d\lambda_q}{dt} + \omega_e (L_d i_d + \Psi_m) \tag{4.21}$$

where $\hat{V}_{d,q}$ is the stator voltage, $i_{d,q}$ is the stator current, R_s is the stator resistance, $L_{d,q}$ is the stator inductance, and Ψ_m is the magnet flux. In (4.20) and (4.21), the rotating term is negligible because the rotor speed ω_e is small in comparison with the higher injection frequency. Obviously, from these two simplified equations, the flux increases in direct proportion to the currents in the *d-q axis*. Furthermore, the *d-q axis* current increases more than the increase of the flux due to magnetic saturation.

As shown in Fig 4.10, all the HF injection methods contain three main parts:

1. Signal injection or modulating signal;
2. Demodulation process;
3. Speed and position estimation;

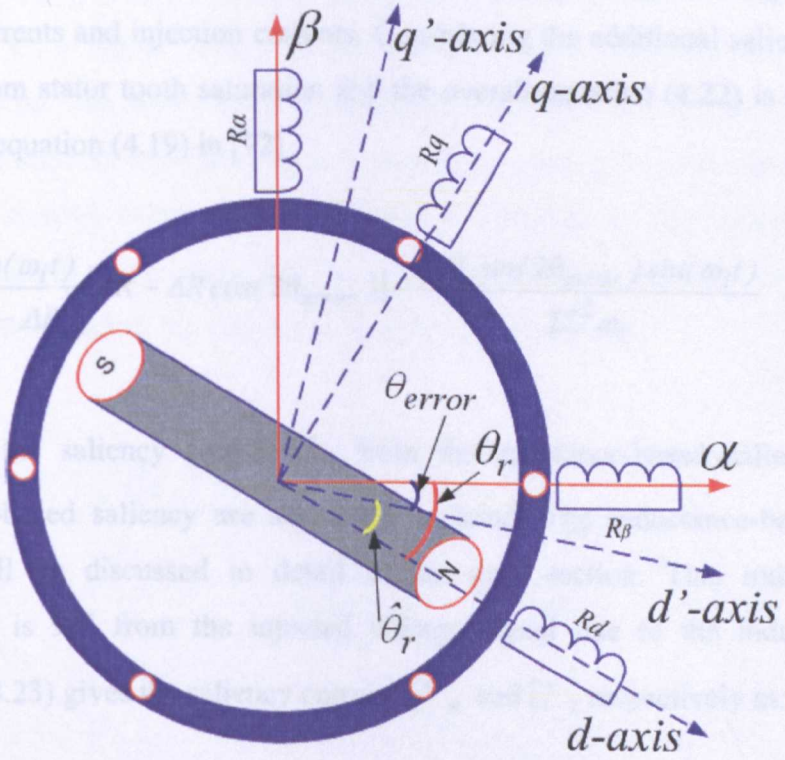

Fig 4.5 PMSM with stator resistance accounting for eddy current

As the high frequency injection sensorless methods change, it is obvious that either the injection signal is different, or the demodulation process is different. The demodulation process can indicate the quality of sensorless estimation scheme. A

good signal processor can give a good estimated response. On the other hand, the signal processing can cause a delay that result in the estimation quality deteriorating. The demodulation using the eddy current resistance-based method is different to the measurement axis method. The eddy current is induced when the high frequency voltage signal is injected in the rotating frame *d-axis*. The high frequency injection signal can be defined as a voltage vector that is not synchronized with the spinning of the rotor. This voltage vector is always applied and can reflect the eddy current into the stator coils. The saliency information is detectable when the eddy currents are induced on the stator and rotor cores. The injected high frequency voltage signals are superimposed on the fundamental excitation.

4.3.2 Demodulation Process

The demodulation process is used to obtain the error signal using the rotating frame's currents and injection currents. Considering the additional saliency which is induced from stator tooth saturation and the overall equation (4.22) is derived from the matrix equation (4.19) in [72]

$$\tilde{i}_d^e = \frac{\hat{V}\sin(\omega_i t)}{\Sigma R^2 - \Delta R^2}\left[\Sigma R - \Delta R\cos(2\theta_{error})\right] - \frac{\hat{V}\Delta L\sin(2\theta_{error})\sin(\omega_i t)}{\Sigma L^2\omega_i} \tag{4.22}$$

In (4.22), the saliency current $\tilde{i}_d^e$, from the resistance-based saliency and the inductance-based saliency are separately isolated. The inductance-based saliency current will be discussed in detail in the next section. This induced current component is 90° from the injected voltage signal due to the inductive effect. Equation (4.23) gives the saliency current $\tilde{i}_{d_R}^e$ and $\tilde{i}_{d_L}^e$ respectively as:

$$\begin{aligned} \tilde{i}_{d_R}^e &= \frac{\hat{V}\sin(\omega_i t)}{\Sigma R^2 - \Delta R^2}\left[\Sigma R - \Delta R\cos(2\theta_{error})\right] \\ \tilde{i}_{d_L}^e &= -\frac{\hat{V}\Delta L\sin(2\theta_{error})\sin(\omega_i t)}{\Sigma L^2\omega_i} \end{aligned} \tag{4.23}$$

For the position estimation tracking, the resistance based saliency component in (4.23) is isolated. According to the Fourier theory, $\tilde{i}_{d_R}^{e}$ multiplying by $cos(\omega_i t)$ and following a low pass filter [6][74], becomes the error signal for resistance-based saliency method

$$\zeta = LPF\left(\tilde{i}_d^{\,e} \times cos\left(\omega_i t\right)\right) = \frac{\hat{V}\Delta R\, sin(2\theta_{R_error})}{\Sigma L^2 \omega_i^{\,2}} - \frac{\hat{V}\Delta L_s\, sin(2\theta_{L_error})}{\Sigma L^2 \omega_i} \tag{4.24}$$

where ΣL is the average asymmetric values of inductance and ΔL is the differential asymmetric values of inductance., θ_{R_error} is the resistance-based position error, and θ_{L_error} is the inductance-based position error. Due to the inductive variation, both of position errors are the position dependent signal. For the eddy current reflected resistance-based saliency tracking, the sinusoidal saliency components in (4.24) are isolated by multiplying the high frequency carrier followed by the low pass filter to obtain the error signal shown in Fig 4.6. The high frequency components are separated from the noise by this advanced demodulation process. The tracking mechanism algorithm is then used. Compared to the other non-injection tracking sensorless control methods, the mechanical observer in the four HF injection tracking methods of this thesis has been designed with a lower bandwidth due to the noisy characteristics of the estimated signals from this process.

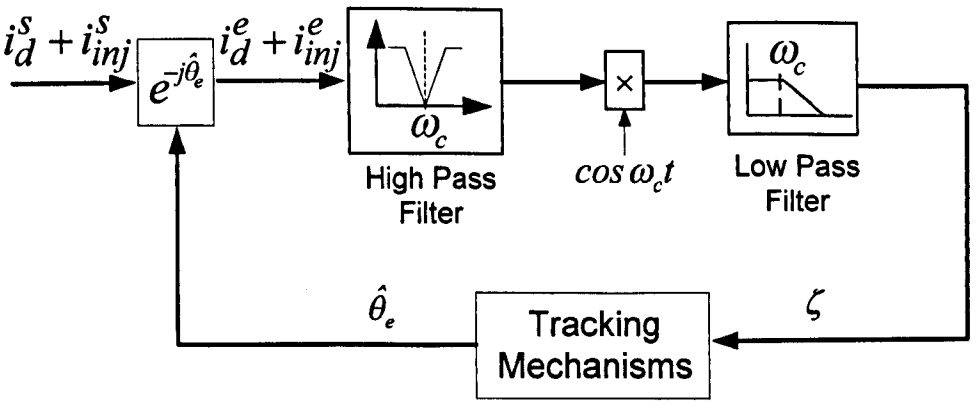

Fig 4.6 demodulation process for position estimation based on resistance-based saliency

4.3.3 Eddy Current Effects on Position Estimation

The eddy current is produced due to the changes of magnetic flux. Heat and losses are generated when the eddy current flows in conductors. The eddy current caused losses are obvious especially with high frequency signal injection. In other words, the eddy current effects can produce a poor estimation in some cases of motor applications based on the sensorless control. Eddy currents always exist when an AC source is applied to the coils [47]. The eddy current effects are analyzed in this section. As discussed at the beginning of this section, the eddy current effect can be modelled by a shorted coil occurring in the rotating frame *d, q-axis*.

$$\begin{cases} \hat{V}_{\alpha\beta} = R_s i_{\alpha\beta} + \dfrac{d\hat{\lambda}_{\alpha\beta}}{dt} \\ \hat{\lambda}_{\alpha\beta} = L_s(2\theta) i_{\alpha\beta} + \lambda_m \begin{bmatrix} \sin\theta \\ \cos\theta \end{bmatrix} \end{cases} \tag{4.25}$$

In this project, we focus on the lower speed range; therefore, equations (4.25) are derived by (4.20) and (4.21) without the rotational term. The rotating frame voltage mathematical form is constructed by the stator currents and magnetic flux arrived in *d, q-axis*. Therefore, after the high frequency injection, the magnetic flux can be represented by [46]

$$\begin{cases} \hat{\lambda}_\alpha = L_s(2\hat{\theta}_r)\cdot i_\alpha + L_{sr}(\hat{\theta}_r)\cdot i_d + \lambda_m(\hat{\theta}_r) \\ \hat{\lambda}_\beta = L_s(2\hat{\theta}_r)\cdot i_\beta + L_{sr}(\hat{\theta}_r)\cdot i_q + \lambda_m(\hat{\theta}_r) \end{cases} \tag{4.26}$$

where $\hat{\lambda}_{\alpha\beta}$ is the stator flux linkage in α-β coordinates and $\hat{\lambda}_{dq}$ is the rotor flux linkage in *d-q* coordinates; λ_m is the flux linkage of permanent magnet; $L_s(2\hat{\theta}_r)$ is the stator inductance matrix for salient pole synchronous machine and $L_{sr}(\hat{\theta}_r)$ is the rotor inductance matrix for salient pole synchronous machine. The related voltage and flux linkage equations in the stationary reference α-β frame shows the eddy current term can produce the additional voltage or power losses when the eddy current losses are considered in equation (4.26). In (4.26), the estimated angle $\hat{\theta}_r$ is derived from these two equations for the high frequency injection method. The

resistance term of both stator and rotor in (4.25) is neglected because the high frequency injection induced voltage is much larger than the voltage across the resistance.

In (4.26), $L_s(2\hat{\theta}_r)$ and $L_{sr}(\hat{\theta}_r)$ are represented by [46]

$$L_s(2\hat{\theta}_r) = \begin{bmatrix} L_{ls} + \frac{3}{2}L_m + \frac{3}{2}L_{\Delta m}\cos(2\hat{\theta}_r) & \frac{3}{2}L_{\Delta m}\sin(2\hat{\theta}_r) \\ \frac{3}{2}L_{\Delta m}\sin(2\hat{\theta}_r) & L_{ls} + \frac{3}{2}L_m - \frac{3}{2}L_{\Delta m}\cos(2\hat{\theta}_r) \end{bmatrix} \tag{4.27}$$

$$L_{sr}(\hat{\theta}_r) = \begin{bmatrix} L_{md}\sin\hat{\theta}_r & L_{mq}\sin\hat{\theta}_r \\ -L_{md}\cos\hat{\theta}_r & -L_{mq}\cos\hat{\theta}_r \end{bmatrix} \tag{4.28}$$

The stator inductance L_s can be presented in terms of the self inductance L_m, rotor position dependent inductance $L_{\Delta m}$ and leakage inductance L_{ls} as: [45] [46]

$$L_s = L_m - L_{\Delta m}\cos(2\hat{\theta}_r) + L_{ls} \tag{4.29}$$

where $L_m = \frac{L_{md} + L_{mq}}{2}$ and $L_{\Delta m} = \frac{L_{md} + L_{mq}}{2}$. The magnetizing inductance in *d, q-axis* is L_{md} and L_{mq} which is involved in the mapping of inductance equation (4.27). Between L_{md}, L_{mq} and $L_{\Delta m}$, L_m their relationships are given by

$$\begin{cases} L_{mq} = \frac{3}{2}(L_m - L_{\Delta m}) \\ L_{md} = \frac{3}{2}(L_m + L_{\Delta m}) \end{cases} \tag{4.30}$$

The d-axis high frequency injection component is given as:

$$\tilde{v}^e_{d_i} = \hat{V}\begin{bmatrix} \cos(\omega_i t) \\ 0 \end{bmatrix} \tag{4.31}$$

The flux linkages can be obtained in (4.32) due to $\omega_i L >> R_s$

$$\hat{\lambda}_{d_i} = L_s(2\hat{\theta}_r)\cdot i_{d_i} \approx \int \tilde{v}^e_{d_i}dt \tag{4.32}$$

Hence, the eddy current can be derived from (4.26) to (4.32), given by:

$$i'_{d_i} = \left[L_s\left(2\hat{\theta}_r\right)\right]^{-1} \int \tilde{v}_d^e \tag{4.33}$$

The eddy current effects are dependent on the estimated rotor position and the eddy current effects are given in equation (4.33).

4.4 Eddy Current Reflected Inductance-based Saliency Tracking Method

Usually an inductance-based saliency is used to track the rotor position information. For a PMSM machine, the inductance-based saliency is very low because the rotor structure is almost symmetrical. The inductance-based saliency is produced when the magnetic flux is saturated. On the other hand, the inductance-based saliency has a load dependent property. The magnetic saturated saliency, multiple saliencies, and nonlinear inverter harmonics can also limit the performance of sensorless control. In the previous section, the mathematical model of the inductance has been analyzed and demodulation for saliency current error is also presented using equations and block diagram.

4.4.1 Inductance-based Saliency Tracking Method

In comparison with resistance-based saliency tracking method, the inductance-based saliency tracking is more sensitive to fundamental torque load. The inductance-based saliency can be caused by the stator leakage flux saturation or main flux saturation. According to the derived inductance-based saliency in the negative term of (4.22), the position tracking can be achieved by isolating and tracking the inductance-based position signals. The basic tracking method is similar to the resistance-based saliency tracking method. The demodulation process is the only different part between two tracking methods.

4.4.2Demodulation Process

For inductive effect, the inductance components contain the position information. The tracking mechanisms have the same functions which have been described in the previous methods. In comparison with other sensorless injection methods, the same parameters of mechanical observer are applied in order to investigate the sensorless performance at the same condition.

The block diagram in Fig 4.7 shows the basic structure for demodulation. The current components in the *d-axis* are transformed to its rotating frame as mentioned previously. The transformation using estimated position angle is achieved and both high pass and low pass filters can isolate the saliency current error signal effectively. These operations can be analyzed through the mathematical equation so that each operation in the demodulator can be explained in a theoretical way. Transforming the stator currents to the rotating reference frame is given by: [72]

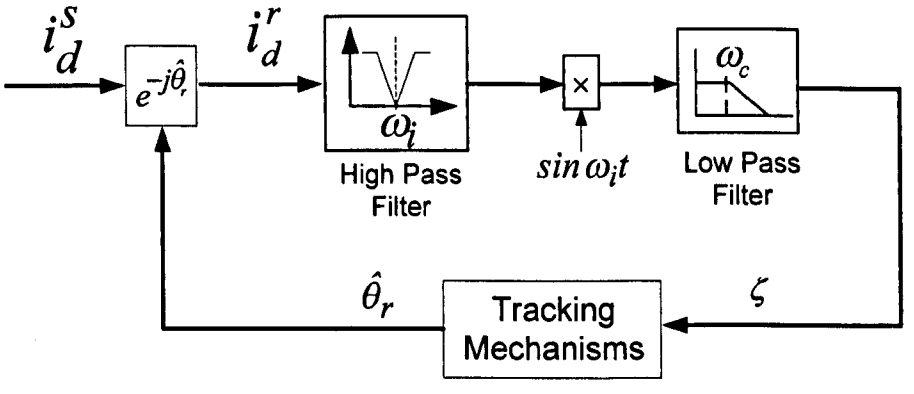

Fig 4.7 demodulation process for inductance-based saliency

$$\begin{bmatrix} i_q^r \\ i_d^r \end{bmatrix} = \begin{bmatrix} i_q^s \\ i_d^s \end{bmatrix} \left(e^{-j\hat{\theta}_r}\right) \tag{4.34}$$

According to the transformation functions, the current in the rotating frame *d-axis* can be derived by:

$$i_d^r = i_d^s \cos\left(\hat{\theta}_r\right) - i_q^s \sin\left(\hat{\theta}_r\right) \tag{4.35}$$

The estimated position angle from mechanical observer is directly involved for current transformation. The injected high frequency signal and fundamental current signal are summed and the transformation of both currents is processed respectively. In the further development of the equation, the position error can be represented as the difference between the real and estimated angle. From (4.23), the inductive current in the rotating reference frame *d-axis* is given by [46, 72]

$$\tilde{i}_{d_L}^{e} = -\frac{\hat{V}\Delta L\, sin(2\theta_{error})\, sin(\omega_i t)}{\Sigma L^2 \omega_i} \tag{4.36}$$

The high pass filter is used to isolate the high frequency components especially for inductance-based saliency components. The multiplication of $sin(\omega_i t)$ using Fourier theory in (4.37) is implemented to separate the signal and noise and this operation can also increase the speed of signal processing. [8, 46, 72]

$$\tilde{i}_{d_L}^{e} \times sin(\omega_i t) = -\frac{\hat{V}\Delta L\, sin(2\theta_{error})\, sin(\omega_i t)^2}{\Sigma L^2 \omega_i} \tag{4.37}$$

After passing through the low pass filter, the error signal is isolated as: [6]

$$\zeta = LPF\left(\tilde{i}_d^{e} \times cos(\omega_i t)\right) \approx -\frac{\hat{V}\Delta L_s\, sin(2\theta_{L_error})}{\Sigma L^2 \omega_i} \tag{4.38}$$

The low pass filter has a cut-off frequency between 100-200 Hz and is first order. The low pass filter is used to isolate the current saliency error signal. In comparison with equation (4.37), the carrier frequency sinusoidal term in (4.38) is removed by low pass filtering. This error signal is provided by demodulation and the tracking mechanisms drive the error to approach zero. This is the characteristics of using a closed loop tracking observer. For a good dynamic response of tracking observer, the observer controller is definitely to be tuned so that the noise in the estimated signal can be suppressed effectively.

4.5 PWM Switching Frequency Injection Method

Typically, the high frequency injection signal is sinusoidal. Signal processing such as the filtering and mathematical operations always introduces a time delay. To avoid this delay, a square wave type of injection signal can be implemented as a high frequency injection sensorless method [74]. The bandwidth of speed and current controllers using a square wave type injection can be broadly increased when compared to the conventional sinusoidal type injection. In this method it is implemented as a pulsating signal injection. As mentioned before, the injection voltage signal is added together with the fundamental voltage reference in the *d-axis* only. The control platform uses a Space Vector PWM algorithm to calculate the switching events for the IGBTs. The PWM switching frequency is 5KHz and current sampling frequency is 5KHz. It is therefore possible to implement an injection voltage signal of 1KHz or 2.5KHz. There are two reasons for using up to 2.5KHz injection frequency; (1) to compare with the other three methods; (2) to achieve the better estimation performance. Similar tracking mechanisms are also used, i.e. the mechanical observer. The low pass filters, high pass filters, and math operations are not needed in this method. The same parameters of mechanical observer are used as the other methods. This error signal is produced by the variations of sampled current between successive samples. The error signal is defined as the position error which is the difference between the real and estimated position angle. The estimated position angle can be tracked using this error signal. This is because the sampled current error is proportional to the rotor position error.

4.5.1 Theory of Saliency Tracking Method

As discussed in the measurement axis method, the measurement reference frame is related to the rotating frame *d-q axis* and flux axis. The measurement axis is placed 45° from the *d-q axis* as shown in Fig 4.8. The high frequency voltage signal is injected aligned with the estimated *d-q axis*. The position estimation error is indicated between the *d-axis* and the flux axis. The estimated position angle can be obtained when the injection axis is aligned with the flux. The error signal can be

calculated without using low pass filters, and that means no time delay in the signal processing. The square wave signal injection method is proposed based on the induced high frequency stator current variations [8, 39, 74].

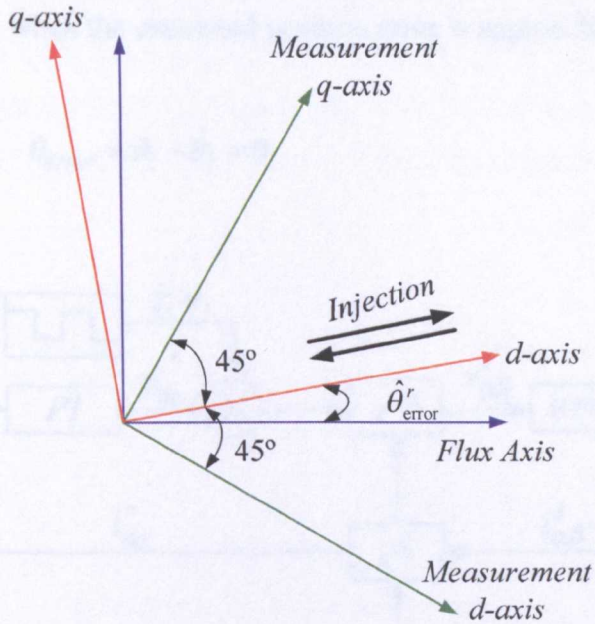

Fig. 4.8 real axis, estimated axis, and measurement axis in rotor reference frame

Fig 4.9 shows the basic structure of PWM switching frequency injection method and the square wave type signal is injected into *d-axis* in the estimated rotor frame. The transformation between rotating frame and stationary frame uses the estimated rotor position angle. To transform the stator current to the measurement frame, a displacement of 45° is used in the calculation of the position angle. The estimated position angle is extracted by using the variances of sampling current. [28, 43, 74] Before the demodulation process, the error signal is required. The calculated position estimation error is defined as the error signal, and is obtained at every sampling time without any low pass filters. The demodulation process is discussed in the next sub-section. The mechanical observer is used as one of the tracking mechanisms, which process the error signal for position tracking. The parameters of the mechanical observer have the same values as other three HF saliency tracking methods in this thesis. The current transformation uses the estimated angle, which is estimated from

the mechanical observer. The induced high frequency current in the stationary reference frame is the only measurable quantity [31, 74]. Therefore, the induced high frequency current should be analyzed. Fig 4.9 shows the square wave signal uses a pulsating voltage injection. This pulsating voltage is injected in the d-axis of the estimated rotor reference frame and this high frequency injected voltage can be described as (4.39), when the estimated position error is approaching to zero.

$$\begin{bmatrix} v_{di}^{r} \\ v_{qi}^{r} \end{bmatrix} = \begin{bmatrix} \cos \omega_i t \\ 0 \end{bmatrix} \qquad \theta_{error} = \theta_r - \hat{\theta}_r \approx 0 \tag{4.39}$$

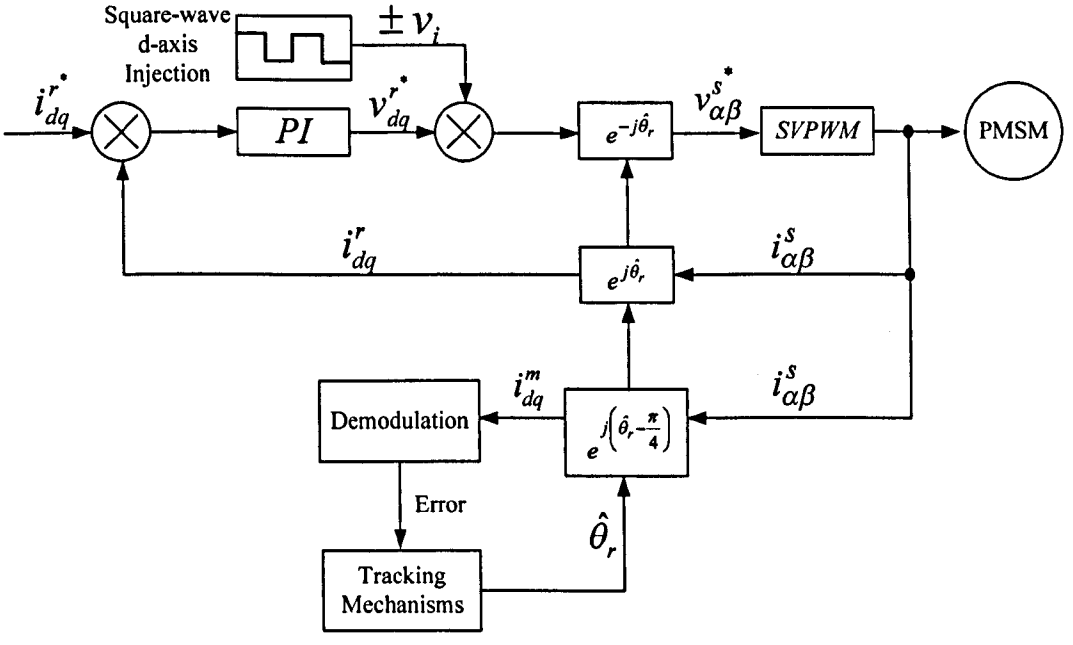

Fig 4.9 block diagram of the PWM switching frequency injection method

To create a square wave injection signal, the injected voltage signal can be defined as: [39, 74]

$$v_{di}^{s'} = \begin{cases} v_i, \\ -v_i, \end{cases} \quad (v_i > 0), (v_{qi}^{s'} = 0) \tag{4.40}$$

where v_i is magnitude of injection voltage. To consider the PWM period and sampling time, there are four possible types of injection voltage presented in Fig 4.10. The PWM period and sampling time can define which type of injection voltage signal is suitable for the sensorless injection control method. The frequency of the

injected voltage signal is related to the sampling frequency because the injected high frequency is established by using one or more sampling frequency. For example in Fig 4.10 (d), five times the sampling time period, (200μs) is used so that 1KHz injection voltage signal can be created. The magnitude of injection voltage signal can be determined from the desired SNR. In this experiment, an injection signal with 1KHz and 2.5KHz has been implemented. Therefore, Fig 4.10 (a) and (d) is suitable for both high frequency injection signals. Fig 4.10 (b) and (c) gives the injection frequencies of 1667 Hz and 1250 Hz, when the sampling time is 200μs.

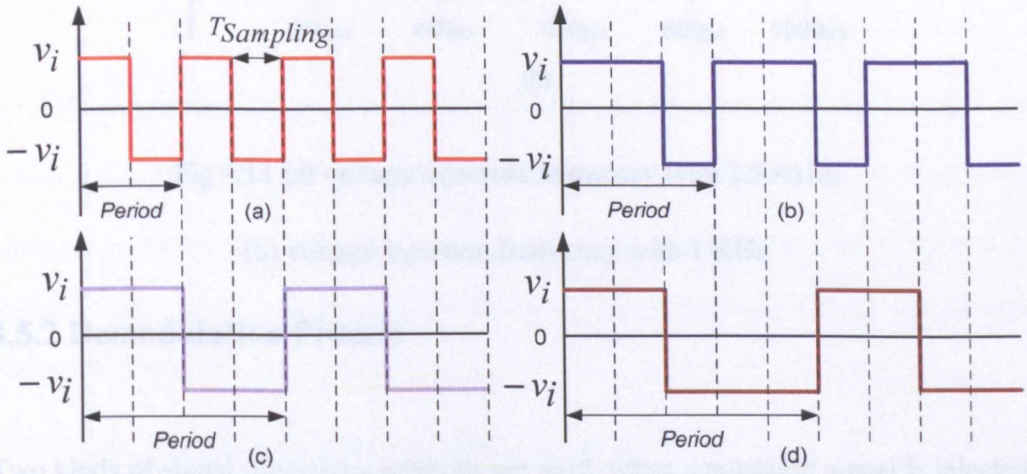

Fig 4.10 four possible square-wave injection voltage types

The sampling time is utilized to create the desired square wave type injection signal [43]. In Fig 4.11 (a), the frequency of injection voltage is 2.5 times larger than injection voltage with 1KHz in Fig 4.11 (b) to keep the SNR ratio at the same level for both injection signals. The PWM period and sampling time are kept at 5KHz in this project.

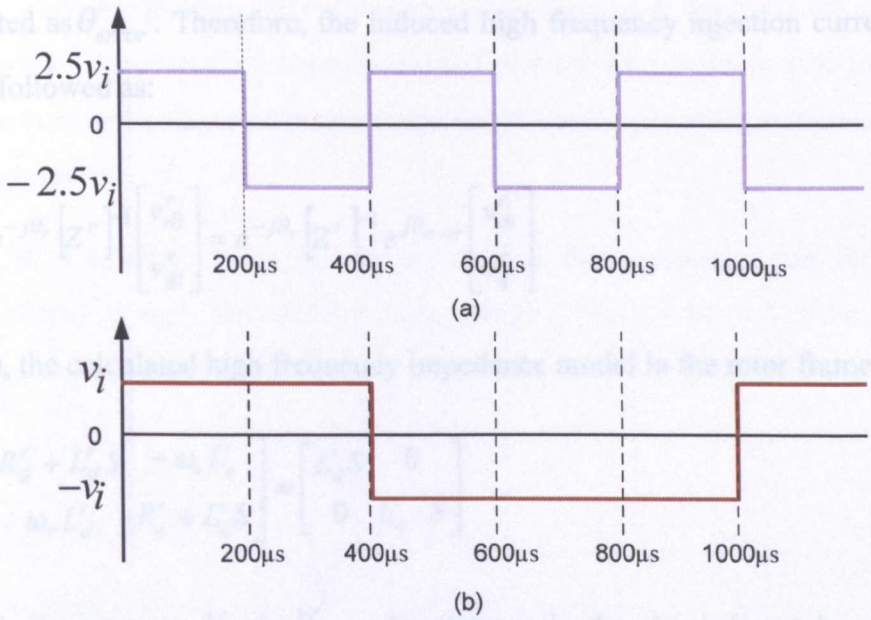

Fig 4.11 (a) voltage injection frequency with 2.5 KHz;

(b) voltage injection frequency with 1 KHz

4.5.2 Demodulation Process

Two kinds of signal processing methods are used, when a pulsating signal is injected in *d-axis* on the estimated rotor frame. These methods are all concentrated on the current measurement reference frame. One method uses the stator reference frame current 45° apart from the estimated rotor reference frame. The other method uses *q-axis* current in the estimated reference frame. Fig 4.9 shows the method, which uses the first approach as the signal processing method for position estimation. This signal processing method can be represented by a mathematical model and hence the induced high frequency current and voltage can be described with the rotor frame impedance model as follows. [8, 39]

In Fig 4.9, the relationship between the induced high frequency current and voltage can be presented by [74]

$$\begin{bmatrix} v_{di}^{r} \\ v_{qi}^{r} \end{bmatrix} = \left[Z^{r}\right] \begin{bmatrix} i_{di}^{r} \\ i_{qi}^{r} \end{bmatrix} = \left[Z^{r}\right] e^{j\theta} \begin{bmatrix} i_{\alpha i}^{s} \\ i_{\beta i}^{s} \end{bmatrix} \tag{4.41}$$

Z^r is the impedance in the rotor reference frame. The position estimation error is represented as θ_{error}. Therefore, the induced high frequency injection current in the stator is followed as:

$$\begin{bmatrix} i_{\alpha i}^s \\ i_{\beta i}^s \end{bmatrix} = e^{-j\theta_r}\left[Z^r\right]^{-1}\begin{bmatrix} v_{di}^r \\ v_{qi}^r \end{bmatrix} = e^{-j\theta_r}\left[Z^r\right]^{-1} e^{j\theta_{error}}\begin{bmatrix} v_{di}^{\hat{r}} \\ v_q^{\hat{r}} \end{bmatrix} \tag{4.42}$$

In (4.43), the calculated high frequency impedance model in the rotor frame is [74]

$$\left[Z^r\right] = \begin{bmatrix} R_d^r + L_d^r S & -\omega_r L_q^r \\ \omega_r L_d^r & R_q^r + L_q^r S \end{bmatrix} \approx \begin{bmatrix} L_d^r S & 0 \\ 0 & L_q^r \cdot S \end{bmatrix} \tag{4.43}$$

In (4.43), the terms $\omega_r L_d^r, \omega_r L_q^r$, and resistance in the *d-q axis* can be eliminated because the induced high frequency has a larger value compared to the fundamental frequency components. When $\theta_{error} = \theta_r - \hat{\theta}_r \approx 0$, the inverse of the induced high frequency impedance can be derived from (4.43) in order to obtain the estimated position information.

The inverse of impedance in matrix form is given by

$$\left[Z^r\right]^{-1} \approx \begin{bmatrix} 1/L_d^r \cdot s & 0 \\ 0 & 1/L_q^r \cdot s \end{bmatrix} \tag{4.44}$$

Using (4.39), (4.42) and (4.44), the induced high frequency current in the stationary frame is given by: [74]

$$\begin{bmatrix} i_{\alpha i}^s \\ i_{\beta i}^s \end{bmatrix} \approx \frac{\sin\omega_i t}{\omega_i}\begin{bmatrix} \cos(\theta_r)\cos(\theta_{error})/L_d^r + \sin(\theta_r)\sin(\theta_{error})/L_q^r \\ \sin(\theta_r)\cos(\theta_{error})/L_d^r - \cos(\theta_r)\sin(\theta_{error})/L_q^r \end{bmatrix} \tag{4.45}$$

Under the assumption that the position estimation error is zero, equation (4.45) can be simplified as:

$$\begin{bmatrix} i_{\alpha i}^s \\ i_{\beta i}^s \end{bmatrix} \approx \frac{\sin\omega_i t}{\omega_i L_d^r}\begin{bmatrix} \cos(\theta_r) \\ \sin(\theta_r) \end{bmatrix} \tag{4.46}$$

The simplified induced high frequency current in (4.46) has a relationship with the angle θ_r. When a high frequency voltage signal is injected in the *d-axis* of estimation rotor reference frame under the assumption of zero error between the true rotor angle and estimated angle, the rotor position can be detected by tracking the induced high frequency current.

The true θ_r is equal to the estimated angle under the assumption that the position estimation error is zero. Therefore, using arctangent function in (4.47), the estimated angle can be calculated as:

$$\begin{cases} \begin{bmatrix} cos(\theta_r) \\ sin(\theta_r) \end{bmatrix} \approx \begin{bmatrix} i^s_{\alpha i} \\ i^s_{\beta i} \end{bmatrix} \dfrac{\omega_i L^r_d}{sin\,\omega_i t} \\ \theta_r = \hat{\theta}_r = a\,tan\left(\dfrac{i^s_{\beta i}}{sin\,\omega_i t} / \dfrac{i^s_{\alpha i}}{sin\,\omega_i t} \right) \end{cases} \tag{4.47}$$

In Fig 4.12, the stator reference frame current is displaced by 45° from estimated rotor reference frame. The current sampling is achieved by the difference in a current sample within a sampling interval. This difference between the current samples also has a displacement from the estimated rotor reference frame. To be aligned with measurement reference axis, the transformation between the two frames is needed. According to the induced high frequency current in equation (4.42), the difference between the high frequency induced stator current samples in the stationary frame is determined as:

$$\begin{bmatrix} \Delta i^s_{\alpha i} \\ \Delta i^s_{\beta i} \end{bmatrix} = e^{-j\theta_r} \left[Z^r \right]^{-1} e^{j\theta_{error}} \begin{bmatrix} v^{\hat{r}}_{di} \\ v^{\hat{r}}_q \end{bmatrix} \tag{4.48}$$

When the square wave type voltage in 4.11(a) and (d) injected, the induced high frequency current sample difference in the stationary frame is given as:

$$\begin{bmatrix} \Delta i^s_{\alpha i} \\ \Delta i^s_{\beta i} \end{bmatrix} \approx sign(v_i)\Delta T \begin{bmatrix} cos(\theta_r)cos(\theta_{error})/L^r_d + sin(\theta_r)sin(\theta_{error})/L^r_q \\ sin(\theta_r)cos(\theta_{error})/L^r_d - cos(\theta_r)sin(\theta_{error})/L^r_q \end{bmatrix} \tag{4.49}$$

For the consideration of polarity of injection voltage, "*sign* (v_i)" is used. The stator reference frame current is along the injection axis shown in previous Fig 4.9. There is no filtering in the current feedback loop. The position angle can be directly estimated using the current samples. The detection of position estimation angle is shown in Fig 4.12.

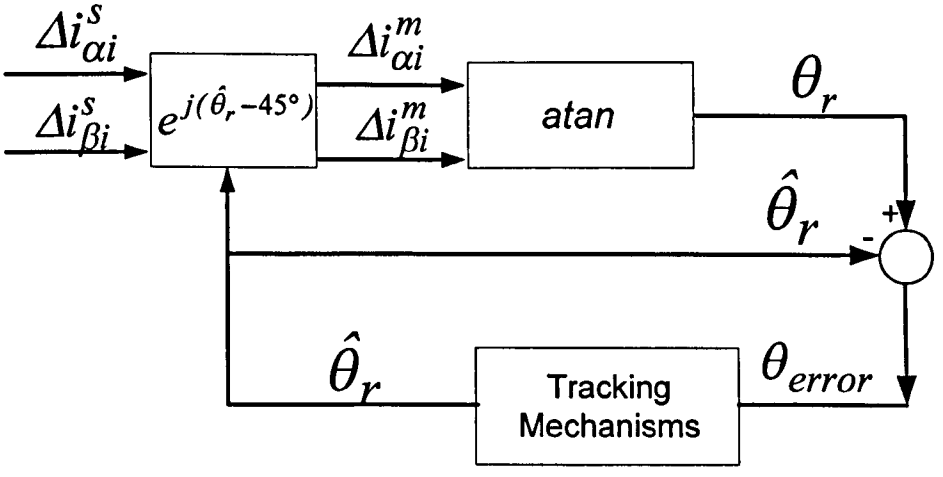

Fig 4.12 block diagram of the proposed signal processing and observer

Fig 4.13 shows how the sampling for the high frequency induced stator current is made over two PMW periods. In the first sampling period, the first current sample subtracted from the second current sample gives the difference of current represented as $\Delta i^s_{\alpha 1}$. $\Delta i^s_{\alpha 2}$ is calculated over the second sampling interval. The fundamental voltage reference with the injection voltage is shown on the right of Fig 4.13. In the first PWM period, the pulsating injection voltage signal is positive and the injection voltage is negative in the second PWM period. Therefore, the polarity of injection voltage is varied as time changed. The currents in the stationary frame are also influenced by this change but they always have a same sign.

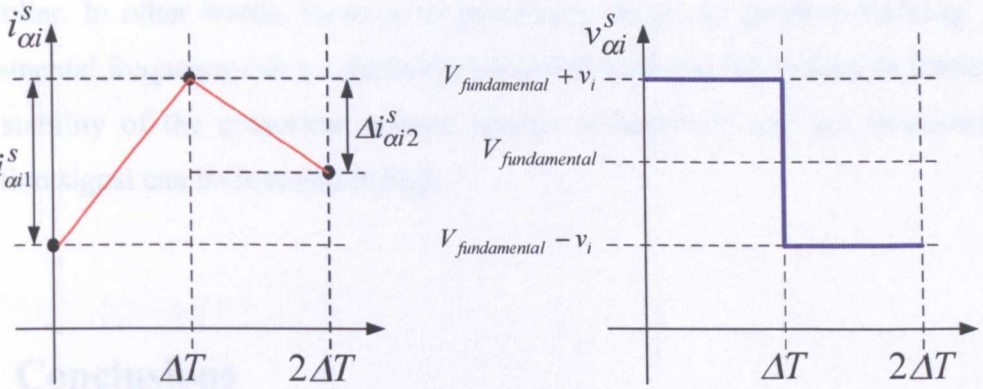

Fig 4.13 the *d-axis* voltage injection signal in two PWM periods and the corresponding current samples

The voltage polarity is inverted in successive PWM periods. Use (4.49), the sampling current can be approximated by [74]

$$\begin{bmatrix} \Delta i^s_{\alpha i} \\ \Delta i^s_{\beta i} \end{bmatrix} \approx \frac{sign(v_i)\Delta T}{L^r_d} \begin{bmatrix} cos(\theta_r) \\ sin(\theta_r) \end{bmatrix} \quad (\text{Assuming } \theta_{error} \approx 0) \tag{4.50}$$

$$\begin{bmatrix} cos(\theta_r) \\ sin(\theta_r) \end{bmatrix} \approx \frac{L^r_d}{sign(v_i)\Delta T} \begin{bmatrix} \Delta i^s_{\alpha i} \\ \Delta i^s_{\beta i} \end{bmatrix} \tag{4.51}$$

$$\begin{cases} \theta_r = a\,tan\left(\Delta i^s_\beta / \Delta i^s_\alpha\right) \\ \theta_{error} = \theta_r - \hat{\theta}_r \end{cases} \tag{4.52}$$

where $\hat{\theta}_r$ is the estimated position angle. Using equation (4.50), the position angle can be calculated in (4.51) and position estimation error signal can be obtained without a low pass filter in (4.52). In Fig 4.12, the mechanical observer is used to process the error signal, of (4.52) and the rotor position estimation is achieved by using this proposed method. The current sampling scheme is applied to calculate the difference between the current samples and therefore the estimated position angle is calculated at every sampling step. The bandwidth of the speed controller can be

increased because the use of a low pass filter can restrict the bandwidth of the speed controller. In other words, there is no processing delay for position tracking. The fundamental frequency can be obviously separated from the high injection frequency. The stability of the sensorless control system is improved and the frequency of injection signal can be reasonably high.

4.6 Conclusions

In this chapter, four different saliency tracking methods for position estimation were reviewed. For the four methods, all using considered they use pulsating signal injection. There are also two types of pulsating injection signal reviewed in this chapter. One is a sinusoidal type used for the measurement axis method, the eddy current reflected resistance and the inductance methods. The other is a square wave type injection signal used for the PWM switching frequency injection method. The saturation saliency is tracked when these types of signal are injected into the machine. The position tracking technique is always based on either inductance based saliency, or resistance based saliency. The mathematical model for each method was presented and also the block diagrams of signal processing with a tracking observer showed the position estimation methods. These methods will be compared for steady state, speed variation, and load variation impact.

The advantage of the mechanical observer has been also discussed. To achieve the comparisons for these four methods, the injection signal, bandwidth of speed/current controller and mechanical observer have the same design parameters. The chapter 6 will present the obtained experimental results by using the discussed methods in this chapter. In chapter 6, the comparison of the results using the four methods are finalized to confirm which HF injection method can provide a good estimation.

Chapter 5

Experimental Rig

In this chapter, the experimental system is described. An IGBT inverter has been constructed in order to implement the sensorless control strategies discussed in chapters 2, 3, and 4. This description of the AC system is divided into two parts. Firstly, the important devices in the inverter are described. Secondly, the data acquisition and motor control systems are presented. Software listings are given in the appendices.

5.1 Overall Structure of Rig

Fig 5.1 shows the experimental rig comprising 3-phase rectifier, the DC link, the inverter, and the PMSM constructed as part of this project. Separate heat sinks with cooling fans are placed underneath the rectifier and IGBTs. The main circuit board was designed by Dr. Dang in 2004 (PEMC Group, EEE, Nottingham University) [81]. Three IGBT modules are used, which are mounted under the gate drive boards. There are six individual optical receivers placed on the gate drive boards and connected to six optical transmitters by six individual optical cables. The pulse signals for voltage modulation are generated in an FPGA (Field Programmable Field Array) and sent to the optical transmitters. The FPGA subsystem also provides the control interfaces associated with the DSP such as analogue to digital conversion, and the encoder interface. The communication between the DSP and the PC is established by a Matlab/Simulink interface (HPI Daughter card) [80].

Four 400V and 2000μF dual series capacitors are placed in parallel for the DC link. These DC link capacitors are used to store energy and filter the switching frequency components from the supply. The rectifier, the DC link circuit, the PWM inverter circuit, pulse signal circuit, gate drive circuit, and measurement transducer circuit are all assembled together on one Print Circuit Board (PCB), and connected to an AC source (a VARIAC-**VARI**able **AC** transformer), and the PMSM. The whole system has a power rating of 15 KW [5]. The detailed parameters of the PMSM are given in the appendices. Three di/dt sensors are directly connected to the output of the three-phase inverter, for investigating the PWM excitation saliency tracking method in [5], [50], [55], and [78]. Although sensorless control is the main research task, the incremental encoder is still used to obtain the benchmark results to compare with the estimated results.

One voltage Hall Effect transducer LEM (LV25-P [65]) and three Hall Effect current transducers LEM (LAH 100-P [64]) are placed on the PCB. The DC link voltage and three-phase motor currents are measured by these sensors. The measured signals are transmitted through 9 way D-connecters and sent to the FPGA system by a screened signal cable. The PCB is connected to two DC power supplies. The first supplies the 5V for the gate drive circuit. The second supplies the 15V for voltage and current transducers. The photo of the PCB for this research is shown in Appendix B (Fig.B1). The three-phase current derivative sensors are connected to the output of the inverter for the current derivative measurement. The captured current, voltage and current derivative signals are transmitted to the data acquisition system, which is established by a DSP, HPI daughter card, position encoder interface, and an FPGA. The data acquisition system is directly connected to the user's PC in order to obtain the information of control and measurement. Appendix A. gives some brief introductions about these devices. In Fig 5.1, the DC load machine is connected to a commercial drive controller, "Eurotherm DC Drive". The armature current of the DC motor is controlled to provide a load for PMSM. The PMSM is controlled using vector control, which enables independent flux and torque control. A space vector PWM (SVPWM) scheme is used for voltage modulation for the inverter.

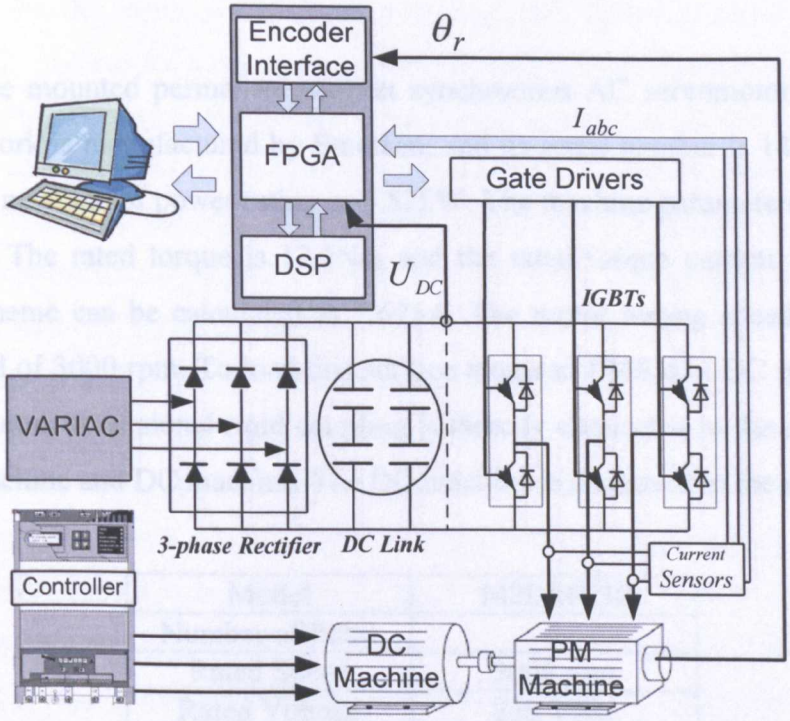

Fig 5.1: overall structure of AC PMSM drive system

5.2 Overview of the Drive System

Fig 5.1 has demonstrates the overall structures of an AC drive system and it is important to understand the important components on PCB board. In addition, the protection circuit has been introduced in detail and several possible short-circuit faults in the three-phase inverter have been identified and discussed.

5.2.1 Machine and Control

In this section, the PM machine and DC machine are briefly introduced. The maximum operating conditions for the machines are considered to avoid over-current, over-speed, and over-temperature. The protection circuits were described in [5].

5.2.1.1 PMSM Machine and Control

The surface mounted permanent magnet synchronous AC servomotor used in this research work is manufactured by Emerson, and its serial number is 142UMC30. It is a 6 pole machine of power rating as 3.82kW. The machine parameters are listed in Table 5.1. The rated torque is 12.2Nm and the rated torque current in the vector control scheme can be calculated as 7.625A. The motor testing speed is below its rated speed of 3000 rpm. To load this surface mounted PMSM, a DC machine drive system is used. A torsional rigid coupling is directly connected to the shafts of both PMSM machine and DC machine. The DC machine is discussed in the next section.

Model	142UMC30
Number of Poles	6
Rated Speed	3000 rpm
Rated Voltage	230 VAC
Torque Constant	1.6 Nm/A
Inertia of Moment	20.5 $kgcm^2$
Friction	0.0036 $kg{\cdot}m^2/s$
R(Ph-Ph)	0.94Ω
L(Ph-Ph)	8.3mH
Continuous Stall	15.3Nm
Peak	45.8Nm
Connection	Y

Table 5.1 parameters of surface mounted PMSM

5.2.1.2 DC Machine and Control

In order to put the load on the PM machine, a second drive is used and shown in Fig 5.1. The required machine used in the load drive is a 5.6kW *Dursley Mawdsley* DC motor to allow operation up to 2000 rpm. The excitation voltage is 370V and the excitation current is 0.676A.

To drive the DC motor, a Eurotherm 590 series DC digital converter is directly connected. Two control loops can be chosen to operate either by current (torque) or speed control. However, the current control loop is only used in this research for adding load to the PM motor. The converter usually provides a current feedback signal in order to monitor the DC motor more effectively. The built-in current sensor provides current or current feedback in current percentage directly from the armature sensing circuit. Fig 5.2 shows the photo of digital converter and its external control unit. Any information from the controller will be shown on the LED screen and the functions of controller can be chosen by key inputs and outputs. The external control unit as shown on the right of Fig 5.2, and it is connected to control terminals of digital controller. The optical switch is connected to FPGA system, which is implemented as an optical emergency stop, if over current or over voltage occurs. The operating control in this project is used to increase or decrease the load torque level The emergency stop button does not show in the figure, and which is also an external device connected to the converter controller for the safety purposes. This commercial drive system is flexible to use for controlling the DC motor in this research.

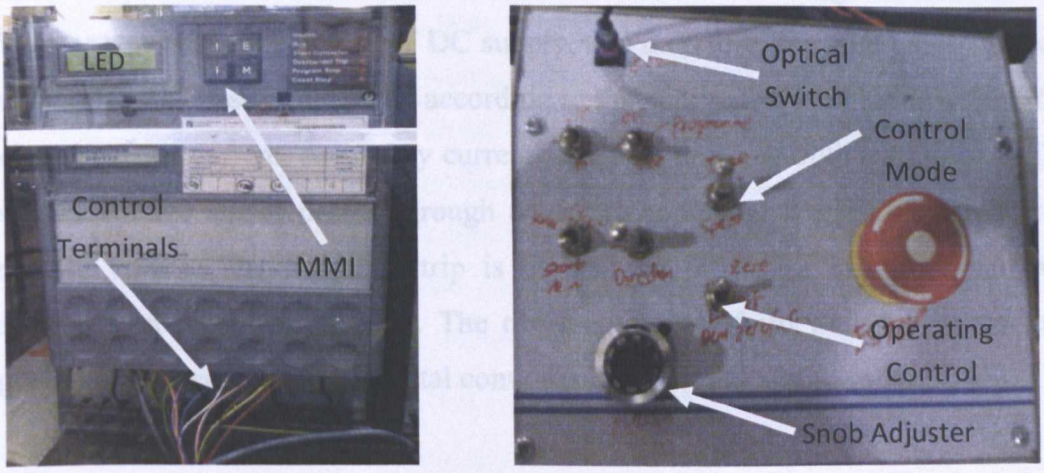

Fig 5.2 the digital converter and external control unit

5.3 Measurement Circuit

5.3.1 Current and Voltage Measurement

In this research, one voltage transducer and three current transducers are installed to measure the three phase currents and the DC link voltage. The voltage transducer LEM (LV25-P [65]) and the current transducers (LAH 100-P [64]) are used in this thesis. They are all Hall-effect devices to provide the precise measurement and electric isolation. Fig 5.3(a) and (b) present the input and output of measured signals, series resistor in voltage measurement, and measurement resistors for both transducers. The supply voltage for both transducers is ±15V and the output is a current signal in proportional to the measured current or voltage. This is then transformed to a voltage signal by passing through a selected high precision resistor for both transducers. In Fig 5.3(b), two resistors of 66K are connected in series to the voltage transducer (R_s) to create a potential divider circuit to lower the input voltage. The measurement resistors (R_m) are placed on the FPGA platform. The measurement resistance is 200Ω for current transducers, and is 220Ω for voltage transducer. The FPGA system is supplied by a 5V DC supply, and therefore, the ADC measurement resistance can be easily calculated according to the parameters mentioned in [64, 65] such as primary current, secondary current, and turn ratios of both transducers. The obtained voltage signal passes through analogue comparators preset with the trip threshold values. The hardware trip is defined by providing instantaneous over current trip in these comparators. The obtained signals from transducers are then digitalized by the analogue-to-digital converters.

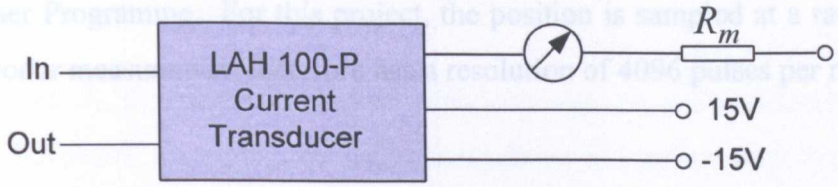

(a) Hall Effect Current Transducer

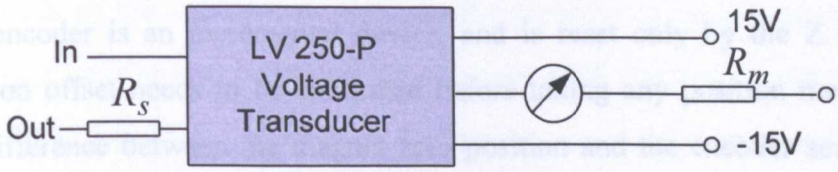

(b) Hall Effect Voltage Transducer

Fig 5.3 measurement transducers

5.3.2 Position Measurement Circuit

An incremental encoder is commonly used in motor applications especially for PMSMs. The device has three outputs – two pulse-trains offset by 90°, and a zero marker. Channels A and B can indicate the position and direction of rotation. For example, if A leads B, the disk is rotating in a clockwise direction. If B leads A, then the disk is rotating in a counter-clockwise direction. Therefore, the position and direction of rotor can be tracked by monitoring both the number of pulses and the relative phase of signals A and B. Additionally, the encoder used in this research has the third output channel, which generates a single pulse per resolution to reset the counter. This single pulse channel can be used to determine the absolute position.

The encoder interface board is a platform between encoder and FPGA system, which is built to convert the incremental quadrature pulse signals of 1024 pulses per resolution into an absolute position signal. In this research, the captured position signal is used for position measurement, which is also seen as a reference to compare the estimated results in sensorless control. The encoder board consists of 16-bit (IC HCTL-2016) binary counter which counts on the positive and negative clock edges, which quadruples the resolution to 4096 per resolution. The speed information is

directly calculated by the rate of change of the position signal in DSK Code Composer Programme. For this project, the position is sampled at a rate of 250Hz. The encoder measurement therefore has a resolution of 4096 pulses per revolution.

5.3.3 Initial Position from the Encoder

The encoder is an incremental device, and is reset only by the Z pulse. Its zero position offset needs to be calibrated before taking any position measurement, i.e. the difference between the magnet zero position and the encoder zero. Initial rotor position detection is achieved in [85] by detecting the spatial orientation of the PMSM anisotropy when the machine has zero speed. In [82], the initial rotor position is estimated by using the phase difference between the applied current and voltage references. A simple and low cost approach is introduced in [83] and the initial rotor position without requiring a position encoder can be achieved by applying a DC current to the stator phases. This DC current is involved to physically align the rotor to an initial position. This detection method is implemented in this research and the initial rotor position is detected successfully. Moreover, a novel detection method can be found in [84], and which uses the low frequency harmonic current injection to obtain the initial position. However, the application of the harmonic injection is mostly limited to initialize the control system with the correct initial position for the PMSM. Several test results are obtained and demonstrate that the method is capable to detect the initial rotor position in PMSM.

If an incremental encoder is used, the position obtained will not be correct until the first zero pulse is detected. To reset the encoder, the rotor of a PM machine must be rotated over 360°. This can be achieved by using the DC machine to spin the PM machine for a few seconds or using the scalar (V/F) control of PM machine to rotate the motor. The first can be implemented when there is another DC drive or other load machine connected with the PM machine. In this thesis, the DC machine and PM machine is separately controlled due to their own controllers. Therefore, the resetting of encoder by V/F control and vector control are achieved in the same control programme.

5.3.4 Current Derivative Measurement Circuit

In this research, three air-core current derivative sensors are used to implement the current derivative measurement. The construction of current derivative sensors is based on the Faraday's induction law. A magnetic field is formed around the electric wire as a conductor when the output current passed through this conductor. The magnitude of the magnetic field is directly proportional to the current, and can be expressed as $|B(t)| \propto i(t)$. The varied magnetic field induces an electromotive force (EMF) as a voltage signal within a electric wire which is loacted perpendicular to the field. The output voltage of the wire is therefore proportional to the time-differentiation of the current, which is represented as $E(t) \propto \frac{di}{dt}$. For the purpose of the measurement, three current derivative sensors are directly connected to the output of three-phase voltage source inverter, which is shown in Appendix B (Fig B1). In addition, three-phase low pass filters are implemented to reduce the noise. The filtered current derivative signals go through the ADC channels, and are stored in the FPGA acquisition system.

The method is used for calibrating these sensors uses an external calibrator [92]. The calibrator can act as an AC current source to the test devices. The offset and gain of a non-adjusted signal can be captured. The average gain and offset can be calculated from these. For the calibration of the three current derivative sensors, three sensors are placed in series connection and connect to the calibrator as shown in Fig 5.4. This advantage of calibration can effectively obtain the correct information from three sensors at the same time. The correct results can indicate that three captured current derivative signals are superimposed together with minimum or zero displacement. Fig 5.4 also provides the basic measurement structure for current derivative sensors. Additionally, a comparison is made between the calculated and measured three-phase current derivative signals. In Fig 5.4, three-phase current derivative sensors are placed in series and connected to the current transducer only in one phase. Three phase current derivative signals are obtained through these sensors. The current derivative signals are also calculated by taking the rate of change of the current samples. These current samples are obtained from the current transducers

simultaneously. In theory, the calculated current derivative samples should be very similar to the measurement from the transducers.

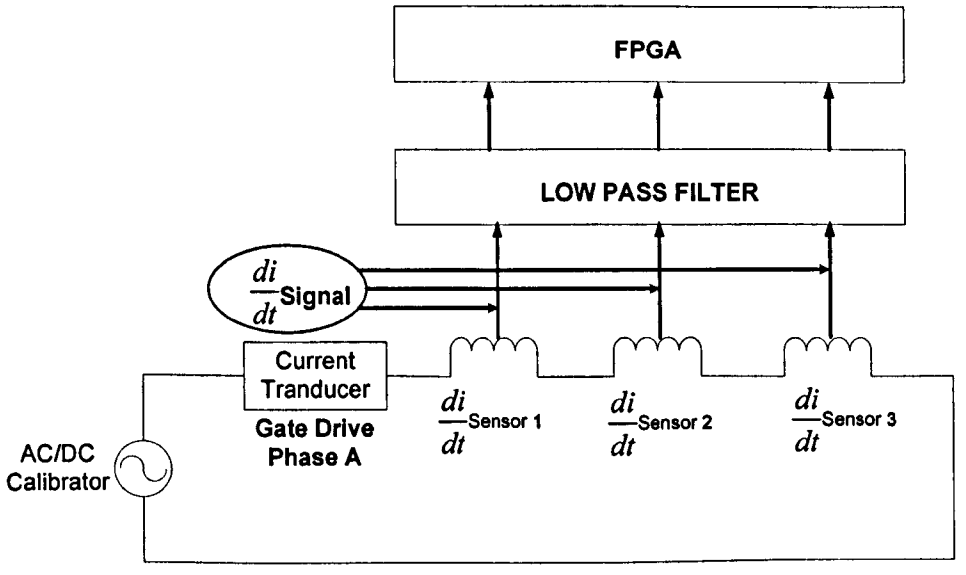

Fig 5.4 calibration and testing of current derivative sensors

In practice, a sampling time of 200μs is used for the measurement of the transient current. The calculated current derivative samples have a delay of 100μs when compared to the obtained three-phase current derivative samples, as shown in Fig 5.5. The reason is related to the effect of sample and hold of the data measurement. The fundamental frequency component is shifted for half of sampling time, which is exactly 100μs. In this proposed testing method, the current and current derivative samples must be captured at the same time. The advantage of this test method can provide the accurate measurement and also the transducer fault of each sensor can be easily indentified.

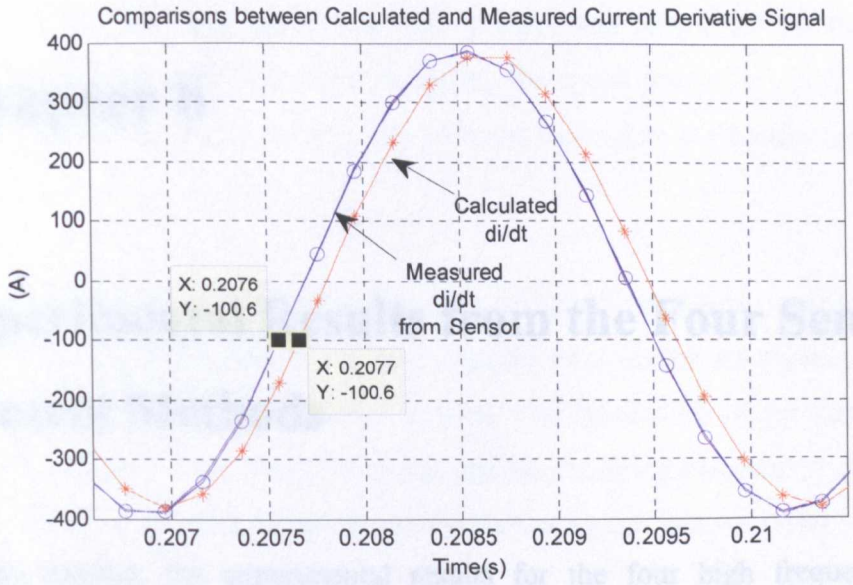

Fig 5.5 comparison between calculated and measured current derivatives signals

5.4 Conclusion

The experimental system has been described. A versatile variable speed PM motor drive has been constructed, fed from a bespoke voltage source inverter and loaded using a DC machine fed from a commercial DC drive. The system is controlled by a DSP/FPGA control platform which also provides data acquisition. The system is capable of running all of the sensorless control schemes described.

Chapter 6

Experimental Results from the Four Sensorless Control Methods

In this chapter, the experimental results for the four high frequency injection sensorless techniques are presented and compared. The first section introduces experimental results for the sensored control experiments to provide a benchmark for the sensorless control system. The second section provides comparative results for position and speed estimation in the steady state. The maximum errors of position and speed are represented (peak and RMS values) under different load conditions and at different rotor speeds. The third section looks at the motor current harmonic distortion in steady state under various load and speed conditions. Finally, two different injection amplitudes and frequencies, 1KHz and 2.5KHz have been applied to the eddy current resistance-based method for comparison.

6.1 Benchmark Results for Sensored Control

The bandwidths of speed sensorless controllers are limited to up to a few hertz because the demodulation and tracking observer can cause a time delay for the speed/position feedback signal. In order to evaluate the performance of a sensorless control system, they should be compared with the performance of a well tuned sensored system. To design the speed control loop, the root locus technique is applied to determine the gains of the speed controller by specifying the damping ratio, and controller bandwidth (*Natural Frequency*), and using the system inertia and friction. The transfer function of the speed controller is established by the PI gains. As a closed loop speed controller, the PI controller is used to minimize the

steady state speed error and provide a good transient response. The bandwidth of the current controller was 400Hz for this project and therefore the current control dynamics can be neglected when designing the speed controller. This bandwidth of the current loop is approximately 20 -30 times faster than the bandwidth of the speed loop.

In this section, the transfer function of this speed controller is derived from the mechanical model equations. The best experimental results are presented with a fast speed controller when the encoder is used. The bandwidth of the sensorless speed control must be 5 times slower than the position tracking observer [5, 6]. The design using root-locus and the performance for both sensored and sensorless are compared and illustrated.

6.1.1 Experimental Results from Sensored Control

The speed, position and torque producing current for the sensored control system are shown in Fig 6.1. The rotor speed is increased to 160rpm (mechanical) for 4 seconds, reversed for 4 seconds, and then stopped after 10 seconds. There are no obvious distortions appearing in the obtained results. The relatively fast bandwidth of the speed controller provides a good performance when the rotor starts acceleration or deceleration. During the changes of speed, motor supply currents need to be increased or decreased sufficiently to satisfy the desired torque. Therefore, the design of the speed controller uses a damping factor of 0.707, and a bandwidth of 20Hz for this sensored motor control experiment. The torque produced current i_{sq} has been limited to ±10A and the actual level is measured at 0.67A in steady state without adding the external load. The obtained position signals from the encoder are also presented in Fig 6.1 and there is a very short time transient during the change of the direction. This short transient actually indicates that the sensored control system has a good and fast speed response during the speed reversal operation. This speed controller is therefore ensuring that the PMSM machine can accurately work under sensored control.

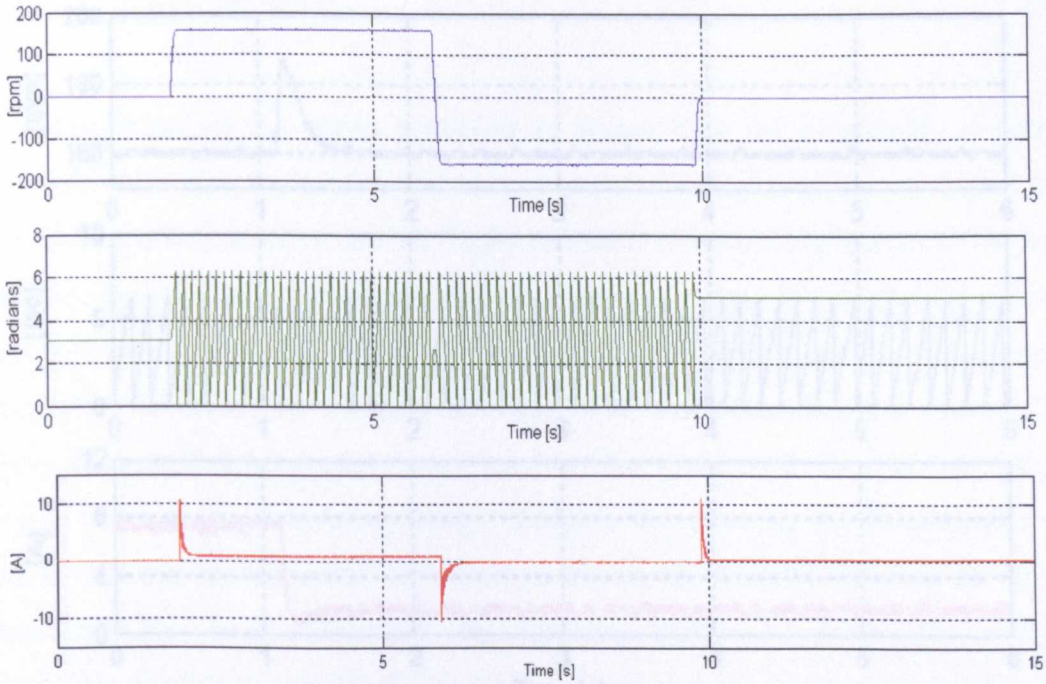

Fig 6.1 sensored control for speed reversal operation

The speed, position response, and torque produced current when external load is applied are shown in Fig 6.2 and Fig 6.3, for the sensored control with different load impacts respectively. The machine is running at 160rpm in steady state.

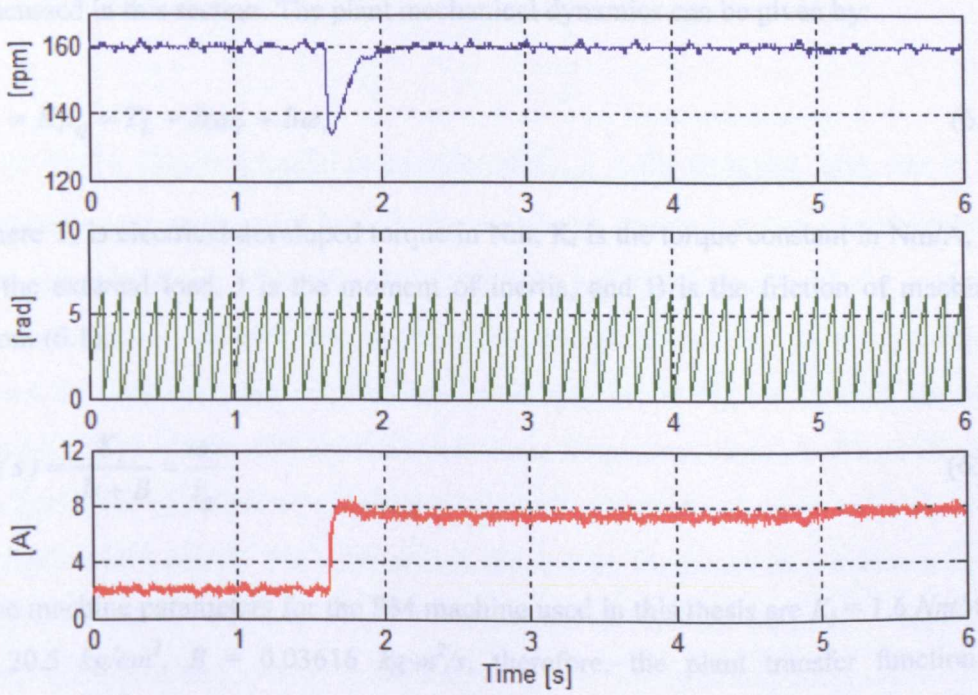

Fig 6.2 load impact – increasing load from 0 to 100%

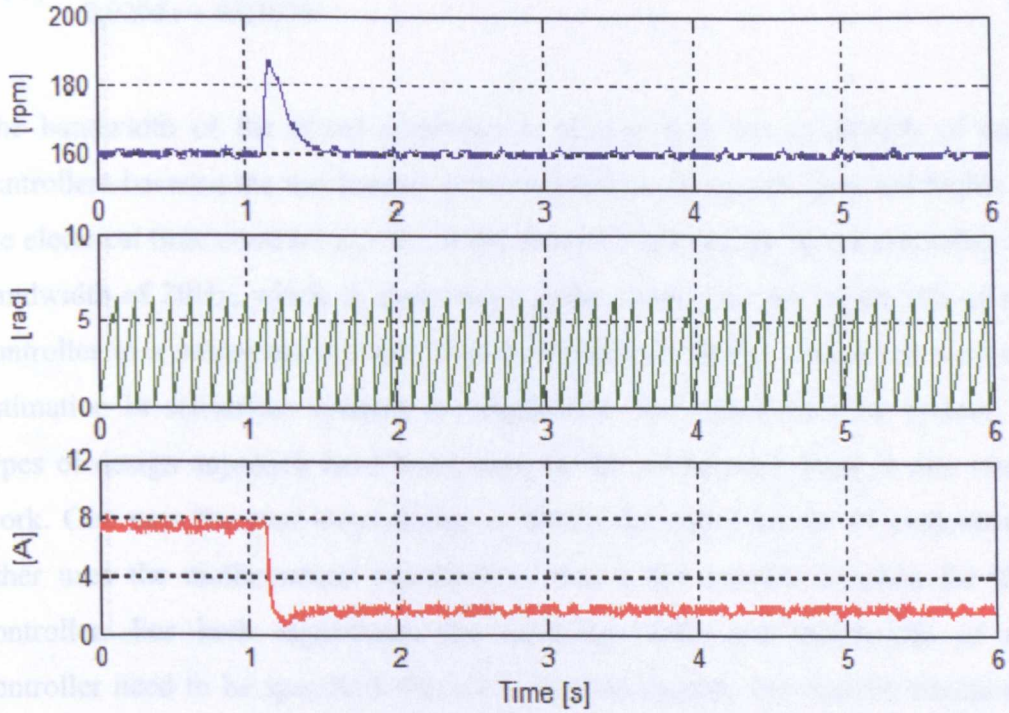

Fig 6.3 load impact – decreasing load from 100% to 0

6.1.2 Speed Control Bandwidth when using Sensorless Control

The design of the speed controller and determination of the transfer function are discussed in this section. The plant mechanical dynamics can be given by:

$$T_e = K_t i_q = T_L + Js\omega_r + B\omega_r \tag{6.1}$$

where T_e is electrical developed torque in Nm, K_t is the torque constant in Nm/A, T_L is the external load, J is the moment of inertia, and B is the friction of machine. From (6.1),

$$G(s) = \frac{K_t}{Js + B} = \frac{\omega_r}{i_q} \tag{6.2}$$

The machine parameters for the PM machine used in this thesis are $K_t = 1.6\ Nm/A$, $J = 20.5\ kg/cm^2$, $B = 0.03616\ kg{\cdot}m^2/s$, therefore, the plant transfer function is expressed by

$$G(s) = \frac{1.6}{0.0205s + 0.03616} \tag{6.3}$$

The bandwidth of the speed controller is slower than the bandwidth of current controllers because the mechanical time constant of the system is much higher than the electrical time constant L_σ / R_s. In the sensored system, the speed controller has a bandwidth of 20Hz, which is about three times faster than the bandwidth of speed controller in a sensorless system. This is because the delays associated with speed estimation in sensorless systems are significant, and destabilize the system. Two types of design approach have been used for the speed controllers in this research work. One uses the root-locus design to obtain the gains for the PI controller; the other uses the mathematical equations to derive the transfer function for the PI controller. For both algorithms, the damping factor and bandwidth of speed controller need to be specified. For a closed loop system, the transfer function and characteristic equation are described as:

$$\begin{cases} \dfrac{G(s)}{1+G(s)H(s)} = 0 \\ s^2 + 2\zeta\omega_n s + \omega_n^2 = 0 \\ 1+G(s)H(s) = 0 \end{cases} \tag{6.4}$$

where *G(s)* is the plant model in equation (6.4), ζ is the damping ratio, and ω_n is the bandwidth of speed control loop. In the root-locus design uses the specified damping ratio and bandwidth to derive the numerator and denominator of the closed loop transfer function and uses this to determine the poles and zeros of the controllers as shown for both the sensored and sensorless systems in Fig 6.4 and 6.5. Bode plots are commonly used to display the steady state frequency response of a stable system. The bode plot provides an alternative view of system response in order to optimize the controller's design. For comparison, the system frequency response in a sensored control system as shown in Fig 6.4 is much faster than the frequency response in a sensorless controlled system as shown in Fig 6.5. The zero and poles can be selected for the transfer function of a controller by setting the bandwidth and damping factor of the controller in the root-locus design tool [56].

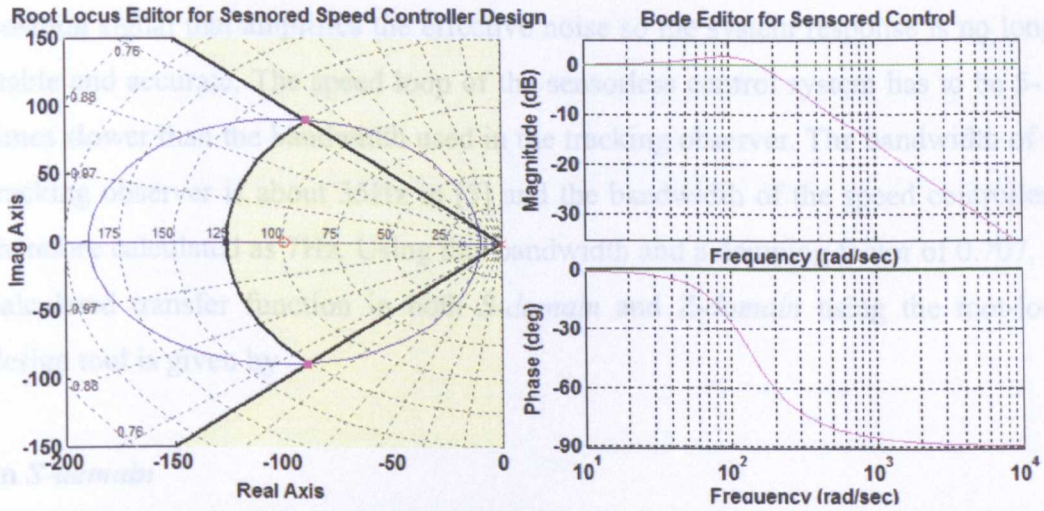

Fig 6.4 root-locus design of sensored speed controller

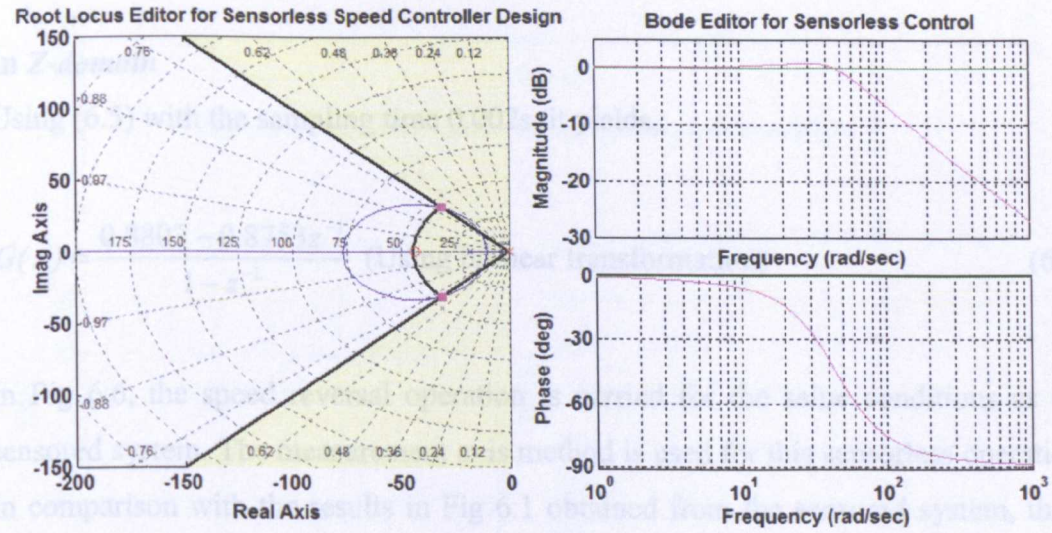

Fig 6.5 root-locus design of sensorless speed controller

For the sensorless control system, the bandwidth of speed controller is limited. The design of speed controller is related to the design of the position tracking observer that has been mentioned in chapter 4. Due to the noise and delay effects on the estimated results, the dynamic response of the tracking observer is poorer when a higher bandwidth of speed controller is used in the sensorless control system [5]. The sensorless system requires the time to execute the demodulation process, mathematical operations, and tracking mechanisms to obtain the estimated position and speed information. These processes obviously also caused a delay and impair the dynamic response. This delay is represented as the distortion on the estimated signals.

A high bandwidth speed controller can provide an estimated feedback speed or position signal that amplifies the effective noise so the system response is no longer stable and accurate. The speed loop of the sensorless control system has to be 5- 10 times slower than the bandwidth used in the tracking observer. The bandwidth of the tracking observer is about 35Hz in [5] and the bandwidth of the speed controller is therefore calculated as 7Hz. Using this bandwidth and a damping factor of 0.707, the calculated transfer function in both *S-domain* and *Z-domain* using the root-locus design tool is given by

In *S-domain*

$$G(s) = K_p + \frac{K_i}{s} = 0.878 + \frac{27.443}{s} \tag{6.5}$$

In *Z-domain*

Using (6.5) with the sampling time 0.002s, it yields,

$$G(z) = \frac{0.8807 - 0.8753z^{-1}}{1 - z^{-1}} \text{ (Using bilinear transformation)} \tag{6.6}$$

In Fig 6.6, the speed reversal operation is carried for the same conditions as the sensored system. The measurement axis method is used for this sensorless operation. In comparison with the results in Fig 6.1 obtained from the sensored system, there are delays in the estimated speed signal and also the settling time is longer than that in the sensored system. In Fig 6.4 and Fig 6.5, the bode-plot shows the difference of system response between the designed sensorless and sensored control system. The sensored control system provides a faster settling response. For most of the settling curve, the sensorless speed control has little difference at 0.15s from the sensored speed control as shown in Fig 6.7 which shows the enlarged speed settiling responses obtained from both sensored and sensorless control systems. The speed response from sensorless control has more oscillations than the response from sensored control system due to the time delay caused by position estimation process.

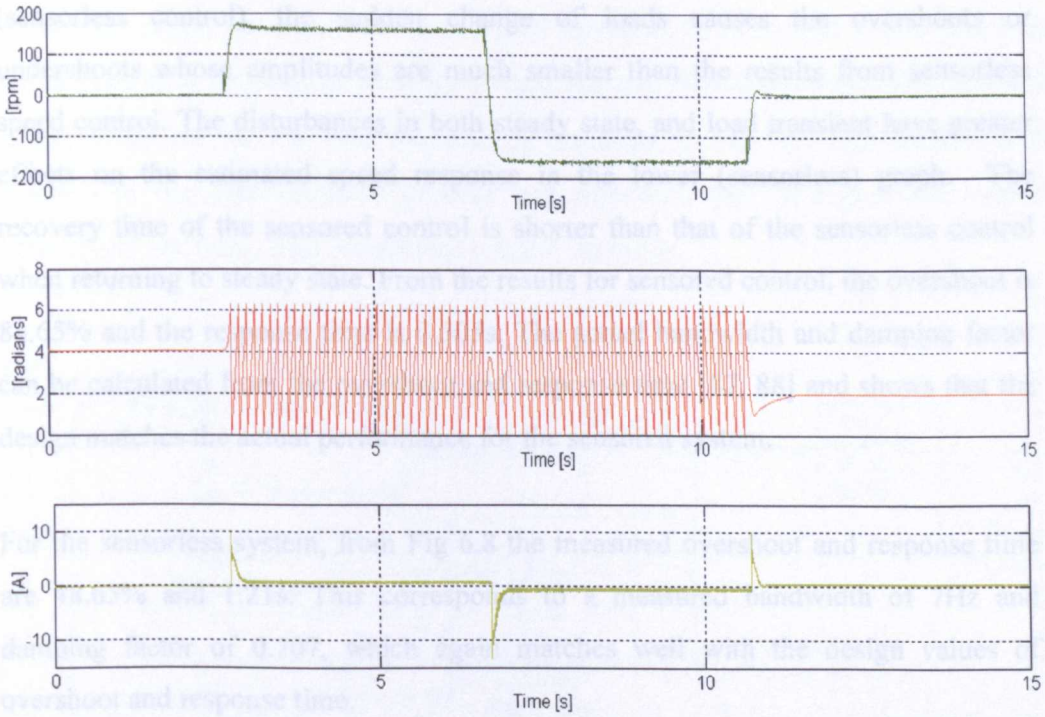

Fig 6.6 sensorless control for speed reversal operation

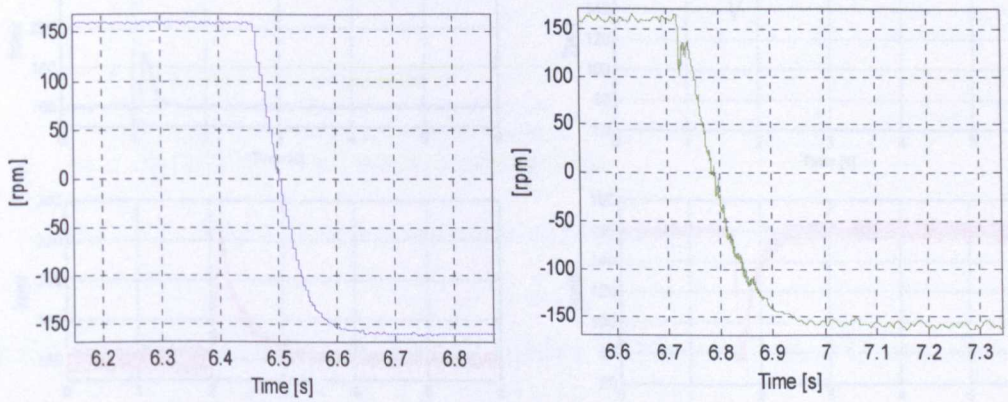

(1) (2)

Fig 6.7 enlarged speed response from Fig 6.1 and Fig 6.6.

The variations of speed response during load transients for both control systems are shown in Fig 6.8. 50% of nominal load is applied to and removed from the PMSM machine. These sudden changes of loads can test the performance of sensored and sensorless control systems. This test can also examine whether a controller matches its design value. In the upper graph of Fig 6.8, the results are obtained from the sensored speed control. In comparison with the results in lower graph of Fig 6.8

(sensorless control), the sudden change of loads causes the overshoots or undershoots whose amplitudes are much smaller than the results from sensorless speed control. The disturbances in both steady state, and load transient have greater effects on the estimated speed response in the lower (sensorless) graph. The recovery time of the sensored control is shorter than that of the sensorless control when returning to steady state. From the results for sensored control, the overshoot is 84.65% and the response time is 0.505s. The actual bandwidth and damping factor can be calculated from the overshoot and response time [87, 88] and shows that the design matches the actual performance for the sensored system.

For the sensorless system, from Fig 6.8 the measured overshoot and response time are 48.65% and 1.21s. This corresponds to a measured bandwidth of 7Hz and damping factor of 0.707, which again matches well with the design values of overshoot and response time.

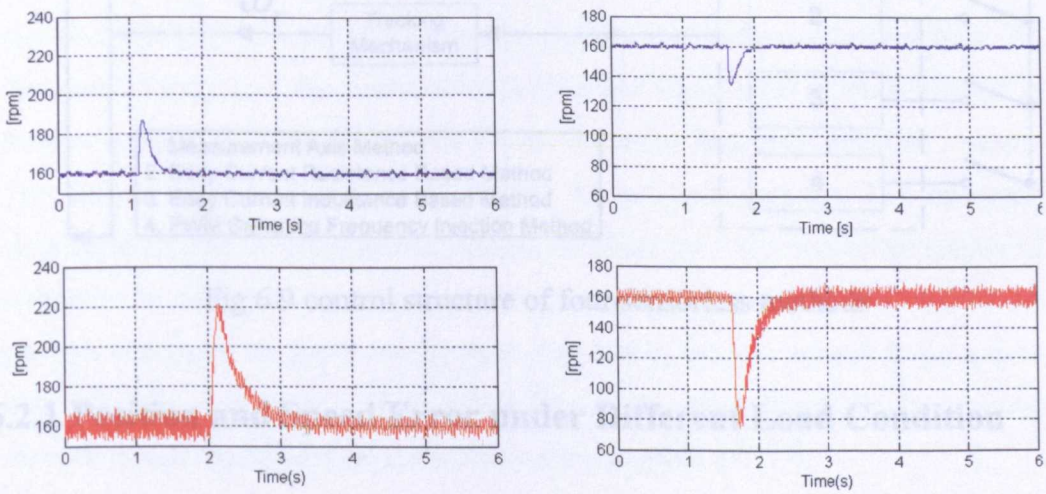

Fig 6.8 Upper: speed response from sensored control during load transient; Lower: estimated speed response from sensorless control during load transient.

6.2 Comparison of Position and Speed Estimation in the Steady State

In this section, the position estimation performance for the four sensorless methods is evaluated at different rotor speeds and various loads. Three fixed values of rotor

speed: 0rpm, 60rpm, and 160rpm are used. In addition, three fixed added load percentage values are applied to the PMSM machine: 0, 50%, and 100%. The load is represented as a percentage of rated torque current. The basic simplified sensorless control structure for the four methods is depicted in Fig 6.9. The multi-selection switches in the demodulation process and injection type of signal are presented respectively for these four sensorless control methods.

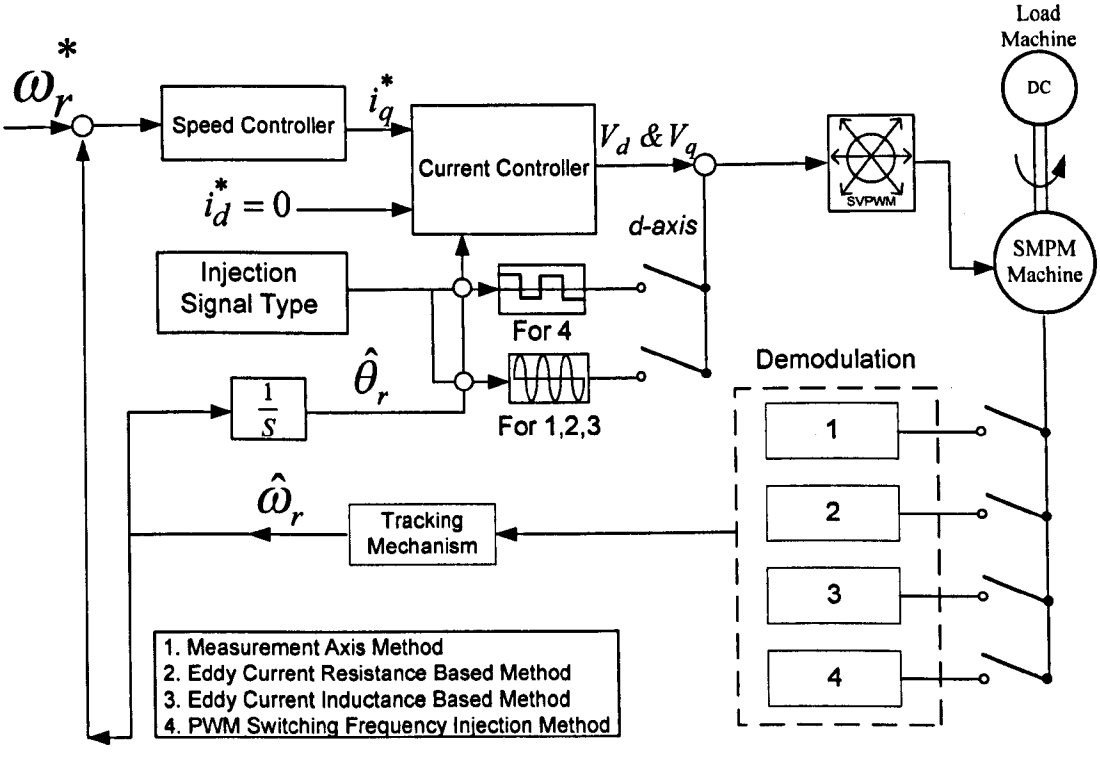

Fig 6.9 control structure of four sensorless methods

6.2.1 Position and Speed Error under Different Load Condition

In this experiment, the viability of the sensorless control is assessed by the effect of load on the quality of the rotor position and speed estimation. Additionally, this test is not only to evaluate the estimation results, but also to inspect the performance of the speed controller.

The load is changed by changing the armature current reference in the DC drive using a step change. The rated torque current is 7.625A, which is determined from the rated power of the PMSM machine. The load transient can be represented as the variation of torque current i_q as shown in Fig 6.10.

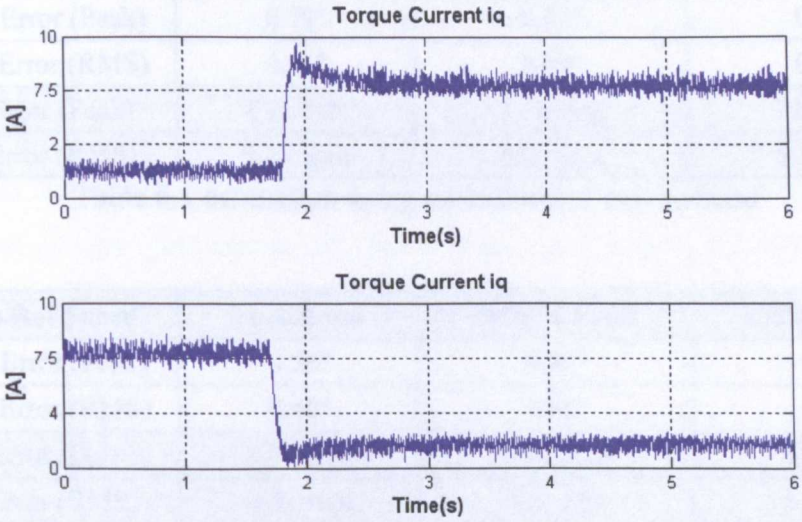

Fig 6.10 Upper: step change in load from 0 to 100% load;

Lower: reducing the load from 100% to 0

The experimental tests are repeated for load values of 0, 50%, and 100% to show the quality of sensorless estimation at various load conditions. The amplitude of the injection voltage is 25V for both sinusoidal and square wave sensorless methods. As discussed in chapter 4, the sinusoidal type injection signal with 1KHz is applied in three sensorless methods but not the PWM switching frequency injection method. The demand reference speed is at 160rpm for all four methods. The estimated position and speed are presented in Table 6.1 – Table 6.4. To compare the quality of estimation in each method, the errors in both mechanical peak and RMS values for position and speed are given for the three load levels, when compared to the values obtained from the encoder. For comparison, the resolution of the incremental encoder measurement used for sensorless control is given in (6.7):

$$R_{encoder} = \frac{1}{N_p} \times \frac{1}{Ts} \times 60 = 4096 \tag{6.7}$$

Where $R_{encoder}$ is the resolution of the encoder, N_p is the number of encoder pulses and T_s is the sampling time of speed. In this research work, the current sampling time is 0.002s and the speed sampling time is 0.02s because in [5] the current loop is always faster than the speed loop.

160rpm Ref Speed	Zero Load	50% of Load	100% of Load
Position Error (Peak)	0.79°	0.92°	0.88°
Position Error (RMS)	0.56°	0.65°	0.63°
Speed Error (Peak)	7.26 rpm	8.53 rpm	7.88 rpm
Speed Error (RMS)	5.13 rpm	6.03 rpm	5.57 rpm

Table 6.1 estimation using measurement axis method

160rpm Ref Speed	Zero Load	50% of Load	100% of Load
Position Error (Peak)	0.56°	0.96°	0.92°
Position Error (RMS)	0.40°	0.68°	0.65°
Speed Error (Peak)	5.70 rpm	9.62 rpm	8.75 rpm
Speed Error (RMS)	4.03 rpm	6.81 rpm	6.19 rpm

Table 6.2 estimation using eddy current resistance-based method

160rpm Ref Speed	Zero Load	50% of Load	100% of Load
Position Error (Peak)	0.93°	1.50°	1.40°
Position Error (RMS)	0.66°	1.06°	0.99°
Speed Error (Peak)	9.18 rpm	12.22 rpm	12.90 rpm
Speed Error (RMS)	6.49 rpm	8.64 rpm	9.12 rpm

Table 6.3 estimation using eddy current inductance-based method

160rpm Ref Speed	Zero Load	50% of Load	100% of Load
Position Error (Peak)	0.36°	0.40°	0.44°
Position Error (RMS)	0.25°	0.29°	0.31°
Speed Error (Peak)	3.01 rpm	3.90 rpm	3.96 rpm
Speed Error (RMS)	2.13 rpm	2.76 rpm	2.80 rpm

Table 6.4 estimation using PWM switching frequency injection method

Under zero load conditions, the estimated position error using the eddy current inductance-based method has the largest amplitude of ripple, which is 0.66° (RMS) for position error. For the speed error, the estimation using this method is poorer and the amplitude of ripple is 6.49rpm (RMS). The result for the PWM switching frequency injection method is shown in Table 6.4. The amplitude of position and speed estimation error is smallest compared to the other three methods and this error is measured (RMS) as 0.25° and 2.13rpm. Under this load condition, both measurement axis method and eddy current resistance-based method can provide acceptable results.

Under the 50% load condition, the best results are obtained using the PWM switching frequency injection method. The maximum amplitude of position and speed error (RMS) is at 0.29° and 2.76rpm. The position and speed errors using the eddy current inductance based method are three times larger than the PWM method. In [72], the saturation ratio for eddy current tracking methods is introduced and represented as the proportion of the average and differential values of the asymmetric resistance. The saliency ratio decreases as fundamental load increases. In comparison with the measurement axis method, the maximum amplitude of the position and speed error, (0.65° and 6.03rpm RMS) is smaller than the results obtained from the eddy current resistance-based method. The measurement axis method uses both resistance and inductance-based saliencies to track the position and speed information. A look-up table is also used as well as phase shift compensation. These operations can influence the system response; therefore, the PWM frequency injection method can obtain lower position and speed errors.

At full load, 12Nm torque is applied to the PMSM. The amplitude of position and speed error is the largest for the eddy current inductance-based method that means the poorest estimation is obtained in comparison with the other three sensorless methods. The inductance-based saliency is again decreased as the load increases to the full load condition. The amplitude of position error is 0.31° and the amplitude of speed error is 2.80rpm for the PWM frequency injection method. These obtained results are two times smaller than the results of both the measurement axis method and the eddy current resistance-based method. For both methods the results are very similar and they have only 0.02° and 0.6rpm difference for the errors of position and speed. Both methods also present poorer estimated results than the PWM frequency injection method. The signal processing caused disturbances therefore influence the position and speed estimation.

As discussed in chapter 4, the four sensorless methods must use the same speed and current controllers, same injection amplitude and frequency, and same mechanical parameters for the tracking observer to provide a true comparison. The signal processing in each method is different. The eddy current reflected resistance and inductance-based method has a similar demodulation process; however, the tracked

saliency is completely different. Due to the lower saliency of the rotor structure, the resistance-based saliency can provide a better estimation quality than the inductance-based saliency. To consider the eddy current losses, the estimation results under load conditions are influenced by both the eddy current reflected resistance and the inductance-based methods. This is because the supply currents are broadly increased as the load increases. The eddy currents are also increased so the eddy current caused losses are definitely increased. The eddy current reflected either inductance or resistance-based saliency is therefore disturbed. To compare the measurement axis method under the load conditions of 50% or 100% of nominal load, the estimation quality is poorer to both the eddy current related methods. A phase shift is introduced as a function of the load when using measurement axis method. In other words, there is no offset error on the position error when no load conditions are applied. As mentioned in chapter 4, each load value indicates each corresponding offset angular value. The phase shift compensation technique uses these obtained offset angles to enhance the estimated results for the measurement axis method during the load transients.

When comparing the results, some conclusions can be reached. Firstly, the estimation quality of the PWM switching frequency injection method under 100% nominal load is the best. In the steady state, the position error is measured to within 0.31° (mechanical RMS value). Secondly, in comparison with the measurement axis method, the eddy current reflected resistance-based method gives a better estimation without load. However, a poorer estimation occurs in both eddy current methods when load is applied to the motor. Finally, in comparison with the PWM switching frequency injection method, the results for the measurement axis shows the larger amplitude of error because a low pass filter is used in measurement axis method. This may be due to the complicated signal processing and maths operation which can also degrade the quality of estimation. There are no demodulation processes in the PWM frequency injection method, therefore, the best quality of estimation is provided. However, without any low pass filters, the induced larger noise in the motor currents must be considered and this discussion will be carried out in next section. The bandwidth of the speed controller for PWM frequency injection methods can be broadly increased and a comparison will be made as a further work.

6.2.2 Position and Speed Error at Different Rotor Speeds

In this section, the steady state, sensorless control tests for different rotor speeds with and without adding external load is carried out and the position and speed error results are compared for the four high frequency injection methods. The same injection signals are applied as in last section. In Tables 6.5 – 6.8, the amplitude of the maximum ripple on the position and speed errors are presented under zero load condition and the measurements were taken at 0, 60rpm, and 160rpm.

No Load	0rpm	60rpm	160rpm
Position Error (Peak)	0.11°	1.28°	0.79°
Position Error (RMS)	0.08°	0.91°	0.56°
Speed Error (Peak)	1.53 rpm	10.41 rpm	7.26 rpm
Speed Error (RMS)	1.08 rpm	7.36 rpm	5.13 rpm

Table 6.5 estimation with no load using measurement axis method

No Load	0rpm	60rpm	160rpm
Position Error (Peak)	0.26°	0.92°	0.56°
Position Error (RMS)	0.18°	0.65°	0.40°
Speed Error (Peak)	2.68 rpm	6.82 rpm	5.70 rpm
Speed Error (RMS)	1.90 rpm	4.82 rpm	4.03 rpm

Table 6.6 estimation with no load using eddy current resistance based method

No Load	0rpm	60rpm	160rpm
Position Error (Peak)	0.45°	1.50°	0.93°
Position Error (RMS)	0.32°	1.06°	0.66°
Speed Error (Peak)	4.08 rpm	11.59 rpm	9.18 rpm
Speed Error (RMS)	2.88 rpm	8.20 rpm	8.32 rpm

Table 6.7 estimation with no load using eddy current inductance based method

No Load	0rpm	60rpm	160rpm
Position Error (Peak)	0.14°	1.27°	0.36°
Position Error (RMS)	0.10°	0.90°	0.25°
Speed Error (Peak)	1.64 rpm	9.91 rpm	3.01 rpm
Speed Error (RMS)	1.16 rpm	7.01 rpm	2.13 rpm

Table 6.8 estimation with no load using PWM frequency injection method

Obviously, the inductance-based saliency is very low due to the rotor structure and this saliency is dependent on the saturation. There is no load on the PMSM and magnetic flux saturation cannot provide a good saliency for position tracking. The obtained results were not bad when using the inductance-based saliency methods. For the PWM switching frequency injection method, the position information can be tracked when the rotor is moving. The estimation gives poor quality when the rotor is at zero frequency or at low rotating speed. However, the PWM method can provide accurate estimated results with medium speed e.g. 160rpm, - the RMS position error is 0.25° and RMS speed error is 2.13rpm mechanical. The best estimation results at the zero and low speed are obtained by using the PWM tracking method. Therefore, the zero and low speed comparison are made next between the measurement axis method and eddy current reflected resistance-based method.

At different rotor speeds, the load affects the position estimation and comparisons are made for the four methods. The signal processing is completely different for each method; therefore, the torque current caused effects for position tracking process are considered. The disturbances on the position estimation have an effect when the full load is applied to the PMSM machine. The position and speed errors for each method are presented in Table 6.9 – 6.12.

100% Load	**0rpm**	**60rpm**	**160rpm**
Position Error (Peak)	0.09°	1.60°	0.89°
Position Error (RMS)	0.07°	1.13°	0.63°
Speed Error (Peak)	0.58 rpm	12.66 rpm	7.88 rpm
Speed Error (RMS)	0.41 rpm	8.95 rpm	5.58 rpm

Table 6.9 estimation with 100% load using measurement axis method

100% Load	**0rpm**	**60rpm**	**160rpm**
Position Error (Peak)	0.21°	0.96°	0.92°
Position Error (RMS)	0.15°	0.68°	0.65°
Speed Error (Peak)	2.70 rpm	8.51 rpm	8.75 rpm
Speed Error (RMS)	1.91 rpm	6.02 rpm	6.19 rpm

Table 6.10 estimation with 100% load using eddy current resistance based method

100% Load	0rpm	60rpm	160rpm
Position Error (Peak)	1.88°	2.77°	1.40°
Position Error (RMS)	1.33°	1.96°	0.99°
Speed Error (Peak)	12.41 rpm	22.50 rpm	12.90 rpm
Speed Error (RMS)	8.78 rpm	15.91 rpm	9.12 rpm

Table 6.11 estimation with 100% load using eddy current inductance based method

100% Load	0rpm	60rpm	160rpm
Position Error (Peak)	0.12°	1.24°	0.44°
Position Error (RMS)	0.09°	0.88°	0.31°
Speed Error (Peak)	1.43 rpm	10.41 rpm	3.96 rpm
Speed Error (RMS)	1.01 rpm	7.36 rpm	2.80 rpm

Table 6.12 estimation with 100% load using PWM frequency injection method

The same comparative analysis is used again under the full load condition. In the rotor reference frame, *d-axis* flux is generated as the sum of flux produced by the magnets and flux produced by the d-axis current. As the full load is applied, the flux produced by the *q-axis* current can reach the maximum level, however, there are no effects on the d-axis current. At zero speed, the measurement axis method provides the smallest position error (0.07°) and speed error (0.41rpm). At 60 rpm, the eddy current resistance-based method provides the best results on both position error (0.68°) and speed error (6.02rpm). At 160rpm with full load condition, the best position error (0.31°) and speed error (2.80rpm) are obtained by the PWM method. To accomplish the comparison of the four methods, the accurate estimated position and speed errors can be obtained by taking the measurement on the absolute average values. In Table 6.13 – 6.17, the absolute average position and speed error are listed when rotor runs at the different speed with/without applying load. The results show the least speed and position errors were obtained by the eddy current resistance based method.

Absolute Average Position Error			
	Zero Load	50% of Load	100% of Load
0rpm Ref Speed	0.04°	0.06°	0.03°
60rpm Ref Speed	0.53°	0.28°	0.89°
160rpm Ref Speed	0.23°	0.25°	0.25°
Absolute Average Speed Error			
0rpm Ref Speed	0.35 rpm	0.61 rpm	0.16 rpm
60rpm Ref Speed	3.84 rpm	2.51 rpm	5.66 rpm
160rpm Ref Speed	2.49 rpm	2.49 rpm	2.49 rpm

Table 6.13 estimation using measurement axis method

Absolute Average Position Error			
	Zero Load	**50% of Load**	**100% of Load**
0rpm Ref Speed	0.07°	0.09°	0.06°
60rpm Ref Speed	0.33°	0.39°	0.41°
160rpm Ref Speed	0.20°	0.34°	0.33°
Absolute Speed Error			
0rpm Ref Speed	0.66 rpm	0.84 rpm	0.52 rpm
60rpm Ref Speed	2.72 rpm	3.64 rpm	3.79 rpm
160rpm Ref Speed	1.91 rpm	3.43 rpm	3.32 rpm

Table 6.14 estimation using eddy current resistance-based method

Absolute Average Position Error			
	Zero Load	**50% of Load**	**100% of Load**
0rpm Ref Speed	0.04°	0.03°	0.02°
60rpm Ref Speed	0.46°	0.59°	0.67°
160rpm Ref Speed	0.12°	0.14°	0.16°
Absolute Average Speed Error			
0rpm Ref Speed	0.38 rpm	0.22 rpm	0.14 rpm
60rpm Ref Speed	3.46 rpm	3.88 rpm	4.20 rpm
160rpm Ref Speed	1.08 rpm	1.20 rpm	1.17 rpm

Table 6.15 estimation using eddy current inductance-based method

Absolute Average Position Error			
	Zero Load	**50% of Load**	**100% of Load**
0rpm Ref Speed	0.07°	0.09°	0.06°
60rpm Ref Speed	0.33°	0.39°	0.41°
160rpm Ref Speed	0.20°	0.34°	0.33°
Absolute Average Speed Error			
0rpm Ref Speed	0.66 rpm	0.84 rpm	0.52 rpm
60rpm Ref Speed	2.72 rpm	3.64 rpm	3.79 rpm
160rpm Ref Speed	1.91 rpm	3.43 rpm	3.32 rpm

Table 6.16 estimation using PWM switching frequency injection method

Considering all the applied conditions, the best method is the eddy current resistance based method. The spatial variation of the HF voltage induced eddy current loss is the key to use this saliency tracking estimation method. The stator resistance is not affected by the spacial variation when the external conditions are applied. The other three sensorless methods all use the inductance based saliency that will be affected when the saliency is varied. Therefore, in steady state with/without adding the load conditions, the best saliency tracking estimation can be achieved by using the eddy current resistance based method.

6.3 Comparison of Total Harmonic Distortion in the Current

In this section, a comparison of total harmonic distortion of the motor current is carried out for the four sensorless methods. The total harmonic distortions or THD of the motor three-phase current are calculated using the Fast Fourier Transform (FFT). The THD is indicated as a measurement of the harmonic distortion present and is defined as the ratio of the sum of the powers of all harmonic components to the power of the fundamental frequency, which is expressed in (6.8). In order to compare quantitatively the current harmonic distortion in the four position estimation schemes, the PMSM machine is controlled with speed at 160 rpm to output 0, 50% and 100% load torque with the four sensorless schemes being applied.

$$THD\% = \frac{\sqrt{V_2^2 + V_3^2 + V_4^2 + \cdots + V_n^2}}{V_1} \times 100\% \tag{6.8}$$

where V_n is the RMS voltage of the nth harmonic and n=1 is the fundamental frequency. The total harmonic distortion in percentage can be obtained from above equation. The same conditions are applied for the comparison of these sensorless schemes such as the bandwidth of the speed controller, bandwidth of current controller, the injection signal with 25V amplitude and 1KHz frequency, and the parameters of mechanical observer. The injection signal type in the PWM switching frequency injection method is square wave and is different to the other three sensorless methods. It has a higher harmonic content and therefore there are likely to be more harmonic distortion on the measured motor line currents when the square wave type injection signal is used. The motor line currents are influenced by the various loads. These effects also influenced the calculated THD in the line three–phase currents. The eddy current reflected resistance-based method has a load independent property. The secondary harmonic is reduced as load increases; therefore, less harmonic distortion is found in this resistance-based sensorless method. Under no load condition, although there are more disturbances appearing on the estimated results at the zero speed, the measurement axis method can provide a good estimation at any speed compared to the other three methods. The THD of three-phase currents is calculated for each method, as listed in Table 6.17 – 6.20 respectively.

160rpm	Zero Load	50% of Load	100% of Load
THD% of I_a	2.37%	0.89%	0.53%
THD% of I_b	2.20%	0.85%	0.51%
THD% of I_c	2.33%	0.90%	0.53%

Table 6.17 measurement axis method under load condition

160rpm	Zero Load	50% of Load	100% of Load
THD% of I_a	2.50%	0.87%	0.52%
THD% of I_b	2.39%	0.84%	0.51%
THD% of I_c	2.44%	0.87%	0.52%

Table 6.18 eddy current resistance based method under load condition

160rpm	Zero Load	50% of Load	100% of Load
THD% of I_a	2.78%	0.90%	0.55%
THD% of I_b	2.40%	0.83%	0.51%
THD% of I_c	2.55%	0.85%	0.53%

Table 6.19 eddy current inductance based method under load condition

160rpm	Zero Load	50% of Load	100% of Load
THD% of I_a	4.02%	1.15%	0.60%
THD% of I_b	4.04%	1.15%	0.60%
THD% of I_c	3.94%	1.14%	0.60%

Table 6.20 PWM frequency injection method under load condition

6.3.1 THD Measurement under Different Load Conditions

The biggest distortion of line current (as shown in Table 6.17) occurs at zero load. As the load is increased up to 100%, the best results are obtained when using the eddy current resistance-based method. However, compared with the measurement axis method, there is only approximately 0.1% difference in current distortion in the eddy current resistance-based method. The fundamental current obviously increases as the load increases because more torque current is required to control the motor at the reference or demand speed and this is the main reason why the THD changes significantly with load. THD of the PWM switching frequency injection is higher, because the injection is square wave rather than sine wave.

6.3.2 THD Measurement at Different Rotor Speed

In this section, 0 and 100% of the nominal load are applied to the machine whilst operating at different speeds. The measured THDs for the current are shown in Table 6.21 – 6.28. The THD measured at 0% load is a reflection of the high cogging torque in the machine rather than the quality of the sensorless control. For the measurement axis method, an unacceptable angle offset exists which is a function of load which is compensated by the use of a look-up table. The position estimation is directly influenced by the load impact and the current harmonics will also be affected. However, the eddy current reflected resistance-based method is insensitive with the load. The inductance-based method has a poorer saliency when the load is applied to the PMSM machine. The square wave type injection signal introduces harmonics of the PWM switching frequency.

Zero Load	0rpm	60rpm	160rpm
THD% of I_a	0.22%	3.01%	2.37%
THD% of I_b	9.71%	2.90%	2.20%
THD% of I_c	3.28%	3.07%	2.33%

Table 6.21 estimation with no load using measurement axis method

Zero Load	0rpm	60rpm	160rpm
THD% of I_a	0.65%	3.56%	2.50%
THD% of I_b	5.06%	3.54%	2.39%
THD% of I_c	9.13%	4.83%	2.44%

Table 6.22 estimation with no load using eddy current resistance based method

Zero Load	0rpm	60rpm	160rpm
THD% of I_a	0.44%	3.17%	2.78%
THD% of I_b	7.30%	2.95%	2.40%
THD% of I_c	8.15%	3.14%	2.55%

Table 6.23 estimation with no load using eddy current inductance based method

Zero Load	0rpm	60rpm	160rpm
THD% of I_a	1.42%	3.34%	4.02%
THD% of I_b	10.68%	3.10%	4.04%
THD% of I_c	4.86%	4.02%	3.94%

Table 6.24 estimation with no load using PWM frequency injection method

For all the methods at zero and low speed, THD is poor, but improving with motor speed. There is a decrease in THD for 160rpm over 60rpm for all the methods as shown in Table 6.25 – 6.28. This is mostly due to the decrease in cogging torque and mechanical disturbances, but also the signal processing functions better at higher speeds. This is because the harmonics to be eliminated are more spread out and more easily separated by the software filters. When loaded, the THD reduces dramatically compared to zero load. This is because the increases of load can increase the machine fundamental current as well as the THD decreases as shown in equation (6.8). For all loading and speed conditions, the HF injection eddy current resistance based saliency tracking method provided the lowest current distortions compared to the other three methods.

100% Load	**0rpm**	**60rpm**	**160rpm**
THD% of I_a	0.84%	0.66%	0.53%
THD% of I_b	5.37%	0.70%	0.51%
THD% of I_c	0.43%	0.82%	0.53%

Table 6.25 estimation with 100% load using measurement axis method

100% Load	**0rpm**	**60rpm**	**160rpm**
THD% of I_a	2.27%	0.56%	0.52%
THD% of I_b	2.48%	0.54%	0.51%
THD% of I_c	0.04%	0.54%	0.52%

Table 6.26 estimation with 100% load using eddy current resistance based method

100% Load	**0rpm**	**60rpm**	**160rpm**
THD% of I_a	0.28%	0.75%	0.55%
THD% of I_b	4.45%	0.69%	0.51%
THD% of I_c	1.11%	0.81%	0.53%

Table 6.27 estimation with 100% load using eddy current inductance based method

100% Load	**0rpm**	**60rpm**	**160rpm**
THD% of I_a	1.52%	0.66%	0.60%
THD% of I_b	4.59%	0.68%	0.60%
THD% of I_c	0.33%	0.77%	0.60%

Table 6.28 estimation with 100% load using PWM frequency injection method

6.4 Position Error for Different Load Transients

In this section, the transient response of sensorless control techniques are tested at two rotor speeds (0 and 160rpm) by applying a step change of load (0-100% and 100% - 0). For this experiment, the speed from the encoder, the estimation, the position errors, and the variation of torque current are observed during the load transient. The tests are carried out to investigate the dynamic performance of sensorless control system when the rotor speed is at both 0 and 160 rpm. For the four sensorless methods, the same parameters are applied such as the injected frequency is 1 KHz and the amplitude of pulsating voltage signal (25V). The speed controller's bandwidth is at 7Hz which can provide a good response during the load transient. The bandwidth of the observer is 35Hz, which is five times of speed controller's bandwidth [5].

The quality of performance of the control can be indicated by the maximum or minimum position errors and the recovery time can indicate the settling time of the signal processing algorithm. Here, the recovery time is defined in terms of the time duration which is between the rising and falling of speed/position error signals, when the load conditions added or reduced to the machine suddenly. The comparison of the estimation results from the four sensorless methods is shown in Tables 6.29 – 6.32. The results are presented using the speed from the encoder, the estimation, the position errors, and the variation of torque current.

0rpm	**0-100% of Load**	**100% - 0 of Load**
Peak Position Error [Electrical]	5.02°	2.71°
Recovery Time (s)	1.36 s	1.62 s
160rpm	**0-100% of Load**	**100% - 0 of Load**
Peak Position Error [Electrical]	5.32°	2.97°
Recovery Time (s)	1.44 s	1.05 s

Table 6.29 position error using measurement axis method

0rpm	**0-100% of Load**	**100% - 0 of Load**
Peak Position Error [Electrical]	3.58°	2.19°
Recovery Time (s)	0.87 s	1.70 s
160rpm	**0-100% of Load**	**100% - 0 of Load**
Peak Position Error [Electrical]	5.1°	2.16°
Recovery Time (s)	0.74 s	1.00 s

Table 6.30 position error using eddy current resistance based method

0rpm	0-100% of Load	100% - 0 of Load
Peak Position Error [Electrical]	7.58°	2.86°
Recovery Time (s)	0.99 s	1.37 s
160rpm	**0-100% of Load**	**100% - 0 of Load**
Peak Position Error [Electrical]	8.6928°	5.59°
Recovery Time (s)	0.998 s	1.31 s

Table 6.31 position error using eddy current inductance based method

0rpm	0-100% of Load	100% - 0 of Load
Peak Position Error [Electrical]	7.45°	3.19°
Recovery Time (s)	0.987 s	1.572 s
160rpm	**0-100% of Load**	**100% - 0 of Load**
Peak Position Error [Electrical]	6.679°	5.05°
Recovery Time (s)	2.06 s	1.19 s

Table 6.32 position error using PWM frequency injection method

For the rising load transient, the smallest position and recovery time is obtained (when rotor speed is at standstill) using the eddy current resistance-based method. When rotor mechanical speed is at 160 rpm, the best performance is also achieved by the eddy current resistance-based method.

For the falling load transient, the best performance is again achieved using the eddy current resistance based saliency tracking method. However, the recovery time is worse when load is removed at standstill. The position error is defined as difference between the position angle from encoder and the position angle from estimation. Therefore, for all the methods, the estimated position angles are decreased as well as the position error increased, when load removal is applied from 100% to 0. The position error at load removal is bigger than the position error at increasing load condition. With the same argument, the recovery time is longer at load removal compared to the results where the load increases from 0 to 100%. At high load conditions, position estimation performances for all the sensorless methods are good. The good result of the position estimation using all methods can also be obtained at zero and low load conditions. The best results of eddy current resistance-based saliency can be obtained when a HF voltage carrier signal is superimposed. Compared to the other three saliency tracking methods, the eddy current resistance-based saliencies are mainly caused by the superimposed HF voltage and therefore, are less sensitive to fundamental torque loads. In addition, the secondary harmonic effects are also reduced as load increases.

The best performance has been obtained during the load transient by the eddy current reflected resistance-based method. Therefore, the eddy current resistance-based method must be looked at in more detail.

(1) 0 – 100% of Load

In Fig 6.11, the machine is at standstill (0 rpm) and both the real and estimated speed with *d-axis* voltage injection is presented when the load transient is increased from 0 to 100%. The estimated and real speed response reached maximum speed of 59.6rpm.

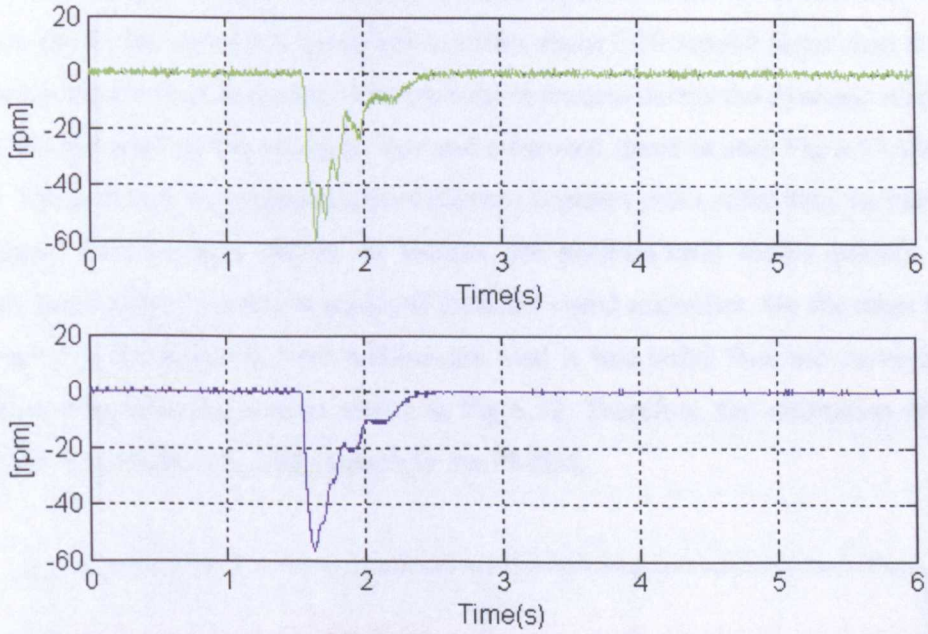

Fig.6.11 Upper: rotor speed from encoder; (rotor at 0rpm)
Lower: the estimated rotor speed using eddy current resistance-based method

The position error is calculated in mechanical degrees as the difference between the measured and the estimated rotor angle as shown in Fig 6.12. A minimum position error of -3.94° and a maximum position error of 1.98° can be seen.

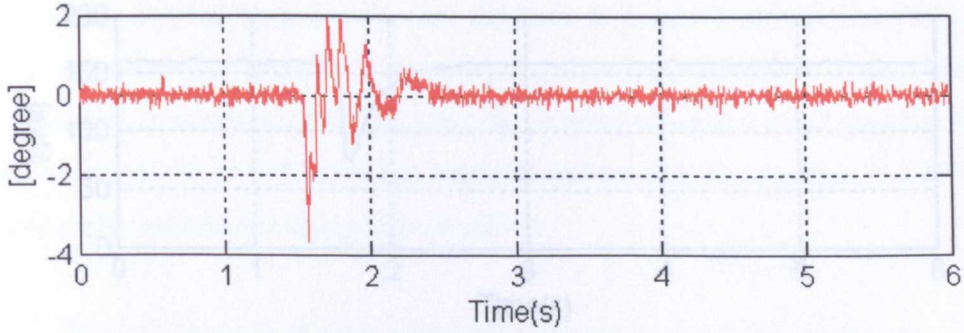

Fig.6.12 position error during the load increased from 0 to 100%

In Fig 6.13, both real and estimated mechanical speed at 160rpm decrease when the load torque is added up to full load level. In comparison with the estimation results at zero speed, the estimated speed curve settles about 0.56 second faster than at zero speed during the load increased. The estimation process delays the dynamic response which is distorted on the position error and estimated speed in both Fig 6.13 and Fig 6.14. The curve of the estimated speed (Green) contains more noise than the curve of the speed from encoder (Blue). At 160rpm, the position error settles quickly. This shows that a good response is achieved from the speed controller. On the other hand, the curve of the position error without the load is less noisy than the curve of the position error with the load as shown in Fig 6.13. Therefore, the estimation error is changed if there are any load impacts to the PMSM.

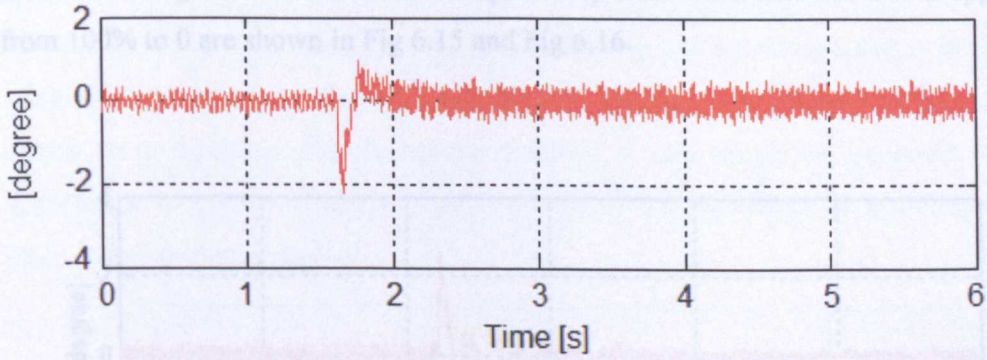

Fig 6.13 position error during the load increased from 0 to 100% (160rpm)

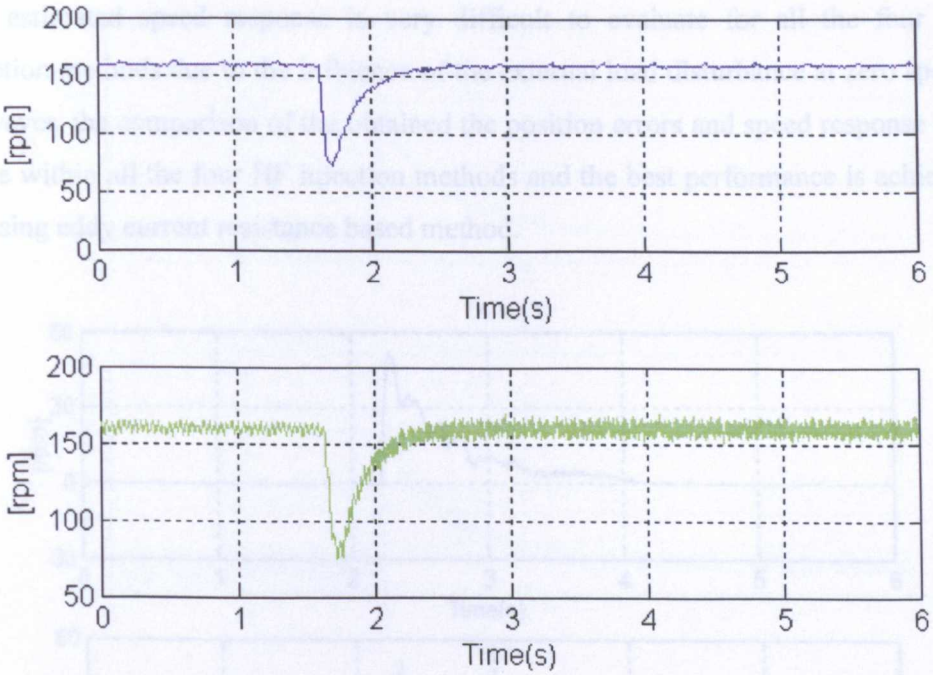

Fig 6.14 Upper: rotor speed from encoder; (rotor at 160rpm in electrical)

Lower: the estimated rotor speed using resistance-based method

(2) 100% - 0 of Load

The response of the sensorless control using the eddy current resistance based method to step changes in load have been tested. At zero speed, the position error in mechanical degrees and real/estimated speed responses when external load is applied from 100% to 0 are shown in Fig 6.15 and Fig 6.16.

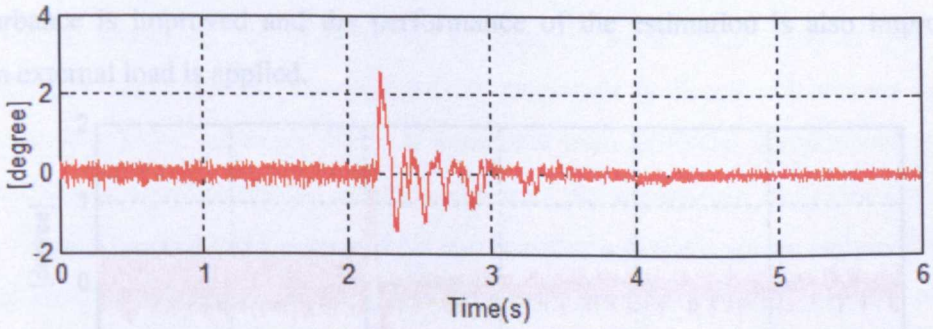

Fig 6.15 position error during the load increased from 100% to 0 (at 0rpm)

The estimated speed response is very difficult to evaluate for all the four HF injection methods due to the influence of the external load disturbance at zero speed. However, the comparison of the obtained the position errors and speed response was made within all the four HF injection methods and the best performance is achieved by using eddy current resistance based method.

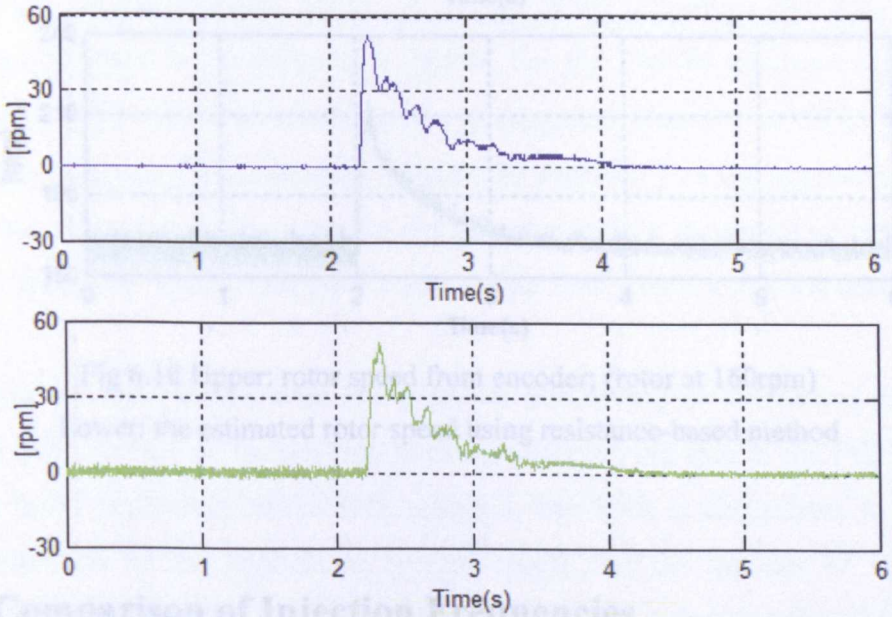

Fig 6.16 Upper: rotor speed from encoder; (Rotor at 0rpm)

Lower: the estimated rotor speed using resistance-based method

At 160rpm, the position error in mechanical degrees and speed response is obtained as shown in Fig 6.17 and Fig 6.18 and the load impact can be obviously seen on the results. In comparison with the results obtained at zero speed, the influence of the disturbance is improved and the performance of the estimation is also improved when external load is applied.

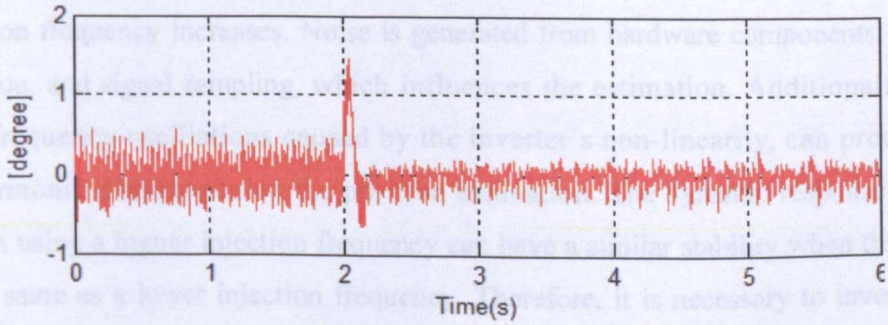

Fig 6.17 position error during the load increased from 100% to 0 (160rpm)

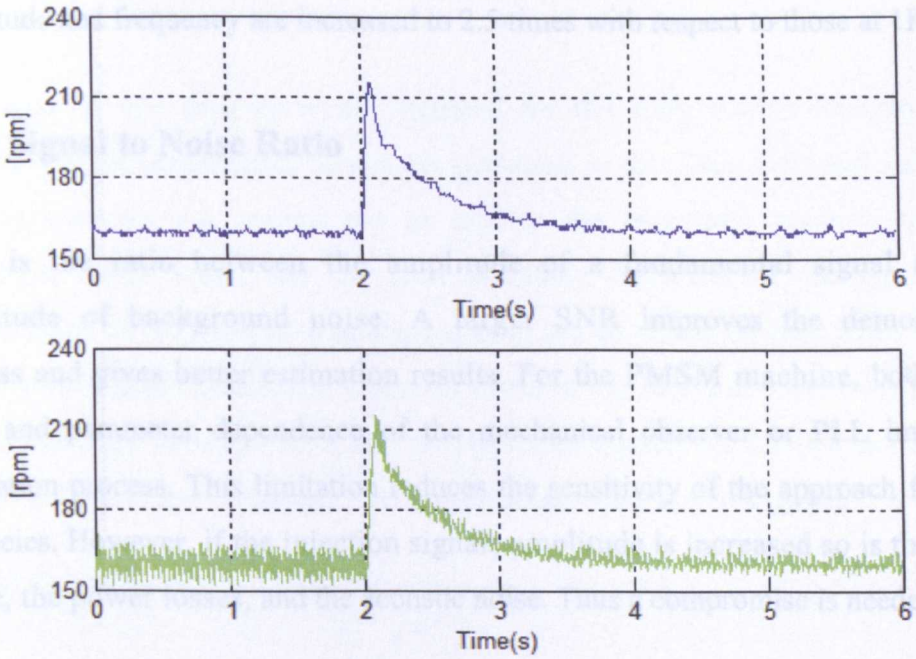

Fig 6.18 Upper: rotor speed from encoder; (rotor at 160rpm)
Lower: the estimated rotor speed using resistance-based method

6.5 Comparison of Injection Frequencies

The position estimation is dependent on the level of noise and the injection signal; therefore, the signal-to-noise ratio (SNR) is used to define the accuracy of the estimation. In the previous tests, an injected signal with a 25V amplitude and a 1 KHz frequency was used. A higher SNR can give a better quality of the system response. However, if the signal is too large, then it causes excessive audible noise and losses. Therefore, the SNR should be kept the same when a higher injection frequency is implemented. The induced HF amplitude is therefore increased as the injection frequency increases. Noise is generated from hardware components, signal injection, and signal sampling, which influences the estimation. Additionally, the high frequency oscillations caused by the inverter's non-linearity, can produce a 6th harmonic disturbance on the position estimation. The dynamic response of the system using a higher injection frequency can have a similar stability when the SNR is the same as a lower injection frequency. Therefore, it is necessary to investigate the differences when using two different kinds of injection signals. Therefore an

injected signal with 62.5V amplitude and 2.5KHz frequency is considered. Both amplitude and frequency are increased to 2.5 times with respect to those at 1KHz.

6.5.1 Signal to Noise Ratio

SNR is the ratio between the amplitude of a fundamental signal and the amplitude of background noise. A larger SNR improves the demodulation process and gives better estimation results. For the PMSM machine, both a poor SNR and parameter dependence of the mechanical observer or PLL impair the estimation process. This limitation reduces the sensitivity of the approach for small saliencies. However, if the injection signals amplitude is increased so is the torque ripple, the power losses, and the acoustic noise. Thus a compromise is needed.

The best solution is achieved using signal processing or a filtering method to reduce interference. In the position tracking observer, the gain of the PID controller can be tuned depending on the SNR required. The SNR is also related to the phase and amplitude of the modulated current signal and the amount of saliency or anisotropy in the PMSM. The SNR can be increased by increasing the amplitude and frequency of the injected signal. However, the mechanical observer can lose track if the saliency or anisotropy is too small. This is because that the SNR in the resultant current signal can be changed depending on the saliencies, saturation and operating point of the PMSM. A suitable SNR can result in a good quality of position/speed estimation. This investigation is made to compare experimental results from the eddy current resistance-based method at two different frequencies of injection. As the main motor component of the injection frequencies is inclusive, the amplitude of the injection should be proportional to the frequency to maintain the same SNR. The noise can be represented as all the harmonics in the motor current. As an example using resistance-based method, the SNR of output current is 47dB for the two injection frequencies, at 1KHz and 2.5KHz, when the rotor is running at 160rpm without any load. The SNR is 56dB when the load is increased to its maximum.

6.5.2 Comparative Results for the Two Injected Frequencies

The previous test procedures are repeated for the eddy current resistance-based method and the comparative results are presented in the Table 6.33 and Table 6.34. The experiments are carried out to capture the maximum position error, the maximum speed error, and the total harmonic distortion of the current. The amplitude of the position error and speed error are measured for both RMS and peak value in mechanical quantities. The rotor speed in this test is at 0 and 160rpm which is presented and followed in A and B. The loads applied are 0, 50% and 100%. In addition, the speed reversal and load transient operation is investigated.

A. At Zero Speed

To compare the results for current distortion, the injection frequency with 1KHz has more distortion in the line currents than using 2.5KHz injected signal. Additionally, the results for both the speed and position error are similar for both injection frequencies. In Table 6.33, the amplitude of the speed and position error with a 1KHz injection frequency is slightly larger than the one with 2.5 KHz injection signal at all load conditions.

0rpm	**Zero Load**	**50% of Load**	**100% of Load**
25V – 1 KHz HF Injection	(Speed Mechanical rpm; Position Mechanical Degree °)		
Position Error (Peak)	0.26°	0.36°	0.21°
Position Error (RMS)	0.18°	0.26°	0.15°
Speed Error (Peak)	2.68 rpm	3.77 rpm	2.70 rpm
Speed Error (RMS)	1.90 rpm	2.67 rpm	1.91 rpm
THD% of I_a	0.63%	1.43%	1.33%
THD% of I_b	5.81%	2.34%	2.14%
THD% of I_c	7.64%	0.37%	0.17%
62.5V - 2500Hz HF Injection	(Speed Mechanical rpm; Position Mechanical Degree °)		
Position Error (Peak)	0.26°	0.27°	0.30°
Position Error (RMS)	0.18°	0.19°	0.21°
Speed Error (Peak)	2.70 rpm	2.28 rpm	2.98 rpm
Speed Error (RMS)	1.91 rpm	1.62 rpm	2.11 rpm
THD% of I_a	1.80%	2.38%	2.10%
THD% of I_b	7.68%	3.41%	4.13%
THD% of I_c	8.65%	6.45%	5.48%

Table 6.33 comparative results under the different load condition at standstill

B. Speed At 160rpm

In Table 6.34, the estimation results in terms of position error and speed error are presented and THD of the line currents are also presented for a speed of 160rpm. The better quality of speed and position estimate is obtained under load conditions. The estimated results with 1KHz injection frequency have slightly bigger errors than the injection frequency at 2.5KHz. The total harmonic distortion using 1KHz injected signal is 0.1% less at zero load, 0.2% less at 50% of load, and 0.07% less at full load compared to 2.5KHz injected signal. The current distortion is reduced when the injected frequency and amplitude of the voltage is decreased.

160rpm	Zero Load	50% of Load	100% of Load
25V - 1000Hz HF Injection	(Speed Mechanical rpm; Position Mechanical Degree °)		
Position Error (Peak)	0.03°	0.05°	0.05°
Position Error (RMS)	0.02°	0.04°	0.03°
Speed Error (Peak)	0.67 rpm	0.91 rpm	0.84 rpm
Speed Error (RMS)	0.47 rpm	0.64 rpm	0.60 rpm
THD% of I_a	2.50%	0.87%	0.52%
THD% of I_b	2.39%	0.84%	0.51%
THD% of I_c	2.44%	0.87%	0.52%
62.5V - 2500Hz HF Injection	(Speed Mechanical rpm; Position Mechanical Degree °)		
Position Error (Peak)	0.06°	0.04°	0.02°
Position Error (RMS)	0.04°	0.03°	0.02°
Speed Error (Peak)	0.82 rpm	0.60 rpm	0.41 rpm
Speed Error (RMS)	0.58 rpm	0.43 rpm	0.29 rpm
THD% of I_a	2.48%	1.01%	0.59%
THD% of I_b	2.28%	0.96%	0.57%
THD% of I_c	2.37%	1.01%	0.59%

Table 6.34 comparative results of position error, speed error, and THD of I_{abc}

6.5.3 Comparative Results at Speed Reversal

In this section, the speed reversal operations with and without external load are carried out for both frequencies of injection signals. The speed reversal is applied from 160rpm to -160rpm (i.e. the fundamental frequency at 8Hz) as shown in column (a) and (b) of Fig 6.19. The same bandwidth of speed controller has been used; however, two different results are obtained for the two different injection

frequencies. During the speed reversal operation, the signal processing such as filtering and the observer can reduce the noise interference in the resultant signal, but at the cost of reduced bandwidth. The speed transient of using 1KHz is 0.3 seconds faster than the performance with 2.5KHz as load increased from 0 to 100%. On the other hand, the speed transient of using 1KHz is 0.1 seconds faster than the performance with 2.5KHz as load removed from 100% to 0. The amplitude of the undershoot on the position errors in mechanical degrees are -5.99° using 1KHz injection frequency and -5.69° using 2.5KHz injection frequency. They look very similar.

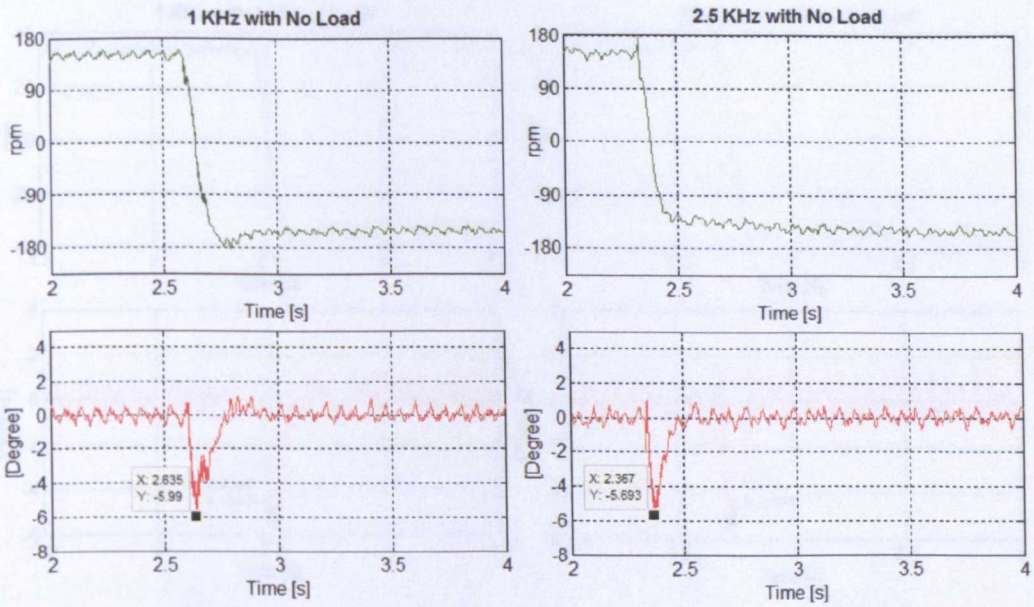

(a) HF Injection 1 KHz; (b) HF Injection 2.5 KHz

Fig 6.19 (a), estimated speed and (b), position error with no load

The speed reversal operations with added external load (100%) are shown in Figure 6.20 (a), (b). The estimated speed, and position error between real and estimated, are all shown in Fig 6.20. The amplitude of the undershoot on the position errors in mechanical degrees are -5.43° using 1 KHz injection frequency and -5.24° using 2.5KHz injection frequency. The speed reversal control with lower injection frequency does not present a big difference from the control with the higher injection frequency and the reversal duration difference is approximate 0.07 seconds. In

comparison, with a 2.5KHz injection signal, there are more disturbances on the estimated results such as estimated speed and position. In Table 6.31, the maximum peak amplitude of the position errors are obtained for the method using the 2.5KHz injection signal. This measurement is achieved in the negative direction of rotation. In addition, there is an overshoot occurred on the estimated speed response when the speed reversal operation initiates. This is the limitation of the bandwidth of the speed controller for a higher injection frequency signal. As mentioned in chapter 4, the estimation and dynamic response for this higher frequency can be improved significantly according to the advantage of the resistance-based saliency. However, the method with the lower injection frequency is recommended as a conclusion.

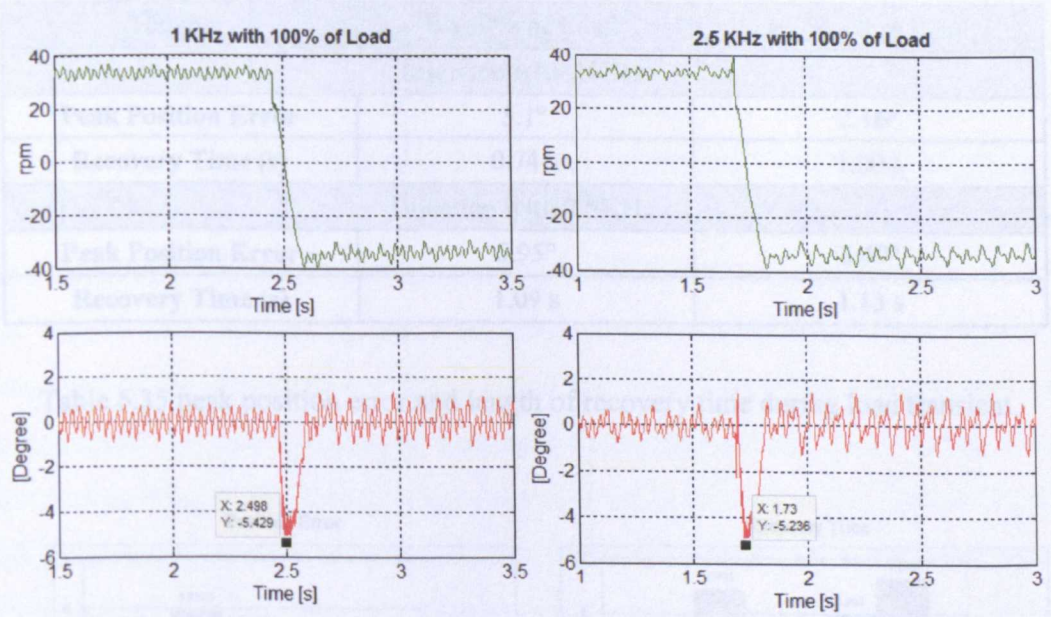

(a) HF Injection 1 KHz; (b) HF Injection 2.5 KHz

Fig 6.20 (a), estimated speed and (b), position error with 100% of load

6.5.4 Comparative Results during Load Transients

Table 6.35 compares the peak position error and the recovery time for the two injection frequencies undergoing a load transient. In Fig 6.21, the histogram shows the comparative results by applying different load impacts. The length of the recovery time is shorter for the method with 1KHz injection frequency for both increased and decreased load transients. The higher injection frequency produced a

higher error signal to the input of the mechanical tracking observer. The function of the mechanical observer does not only provide the estimated result, but also operates as a low pass filter according to the characteristics of PID controller. The lower peak amplitude of position error is obtained for the method at 1KHz injection frequency. In comparison with the method at 2.5KHz as shown in Fig 6.21, there is no big difference from the amplitude at 1KHz which is 0.8° when the transient is an increase in load. As the load is decreased, a better estimation is obtained from the signal at 1KHz and there is 1.1° difference with the injection frequency at 2.5KHz. Therefore, the estimation quality and dynamic response is achieved better when using a lower injection frequency signal.

160rpm	0-100% of Load	100% - 0 of Load
Injection with 1KHz		
Peak Position Error	5.1°	2.16°
Recovery Time (s)	0.74 s	1.00 s
Injection with 2.5KHz		
Peak Position Error	5.95°	3.49°
Recovery Time (s)	1.09 s	1.13 s

Table 6.35 peak position error and length of recovery time during load transient

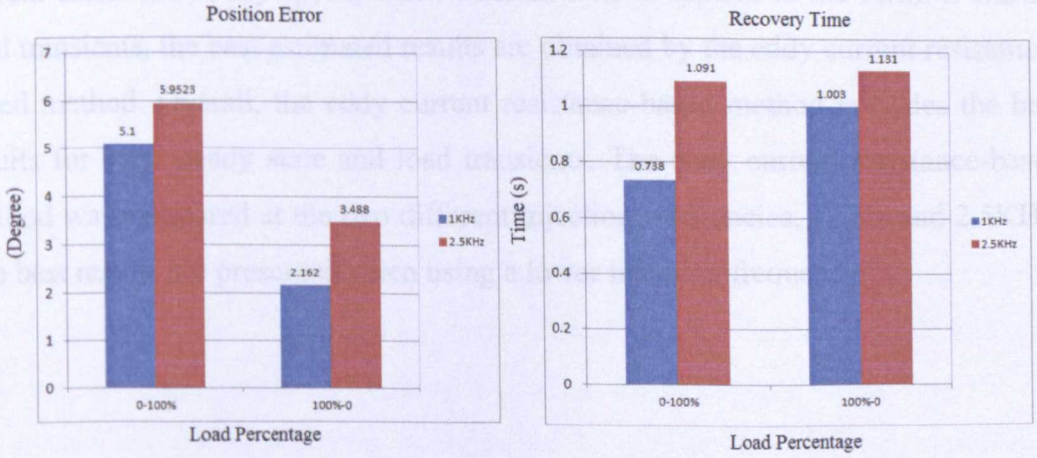

(a) (b)

Fig 6.21 comparison of (a), position error, and (b), recovery time with 1KHz and 2.5KHz HF injection frequencies during load transient

6.6 Conclusions

Sensorless control systems based on the measurement axis method, the eddy current resistance-based method, the eddy current inductance-based method, and the PWM switching frequency injection method have been tested under various conditions such as steady state, steady state under the load, load transient operation, and speed reversal operation. The results obtained from the sensored control are used as a benchmark for the determination of the behaviour of the sensorless speed controller. A comparison of speed bandwidth of both controllers is made which indicate that the sensored speed controller can have a higher bandwidth. Due to the noise characteristics of the tracking observer, the bandwidth of the sensorless speed controller is limited to 7Hz. The more important part in this section is the comparison of the results from four different sensorless control methods under various conditions. The conclusions from these comparative results can be made. In steady state with or without added load, the best estimation results are obtained by PWM switching frequency method when rotor speed is at 160rpm. At zero speed, the best results are obtained by the measurement axis method. The total harmonic distortions of the motor current at any speed are biggest from the measurement axis method under no load. The eddy current resistance-based method provides the lowest current distortion at any speed, when external load is applied to the PMSM. During load transients, the best estimated results are obtained by the eddy current resistance-based method. Overall, the eddy current resistance-based method provides the best results for both steady state and load transients. The eddy current resistance-based method was compared at the two different injection frequencies, 1KHz and 2.5KHz. The best results are presented when using a lower injection frequency.

Chapter 7

Conclusions and Discussions

In this thesis, four d-axis HF injection saliency tracking methods and a RLS signal processing method for the enhanced current derivative measurement have been investigated. This chapter will discuss their functional specifications and experimental results respectively. In the four HF injection sensorless control methods, a brief discussion of the comparison is carried out from their respective experimental results. Finally, the RLS algorithms are discussed for the enhancement and improvement of current derivative measurement during the switching events of IGBTs.

7.1 Sensorless Control using HF Injection Saliency Tracking

The four HF injection methods investigated have the same bandwidth in speed/current controller, tracking observers, and continuous injection signals to allow a fair comparison of their estimation performance. In steady state, the results of the position estimation and total harmonic distortions are obtained under various load conditions, and the estimated speed and the position errors are obtained during load transients. The discussion is concentrated on the comparison of the four saliency tracking methods. It is hard to define which method is the best for any conditions but the comparison is separated to analyze the different conditions. Overall, the eddy current resistance based method represents a promising approach because this method shows that the spatial variation of resistance can be enhanced when a high frequency voltage is superimposed. The PM machine can achieve the position estimation performance with reduced degradation when high load conditions apply.

The results from the eddy current reflected resistance based method were compared with the results from the eddy current reflected inductance based method. In comparison with the inductance-based saliencies, the resistance based saliencies are mainly caused by the superimposed high frequency injection voltage signal and therefore, are less sensitive to fundamental torque loads. Additionally, the second harmonic effects are also reduced as load increases. The estimation from inductance-based method is poor in steady state and also during the load transient. The reason is that the inductance-based saliency is weak as the load increase. The demodulation process for *d-axis* injection sensorless control using resistance has been presented in chapter 4 and is similar between the resistance-based and inductance-based method. The current error signal by using high frequency injection signal can be obtained by tracking the resistance and inductance based saliency. This signal processing can cause a delay in the dynamic system response. With no load, both methods can provide a good quality for position/speed estimation. With load, the resistance based tracking method can provide a better performance than the inductance based saliency tracking method.

The steady state, performance in terms of the speed error, position error, and total harmonic distortion has been presented in chapter 6. Comparing all the methods, the eddy current resistance-based method can provide the best estimation quality at zero speed. In addition, it has the lowest total harmonic distortion when the various loads are applied. The eddy current resistance-based methods have less current distortion at the 0 and 160 rpm speed with 1 KHz injection frequency.

For the load transient, the eddy current resistance based method also provides a good estimation with injection frequency 1 KHz. The peak position error measured at zero speed in mechanical degree is 3.58° as load increased and 2.1859° as load decreased from 100% to 0. The recovery time is 0.872 second and 1.702 second for both transient. At 160 rpm speed, the peak position error is 2.162° as load decreased and the recovery time is 1.003 second. As load rises, the peak position error is 5.1° and the recovery time is 0.738 second. In conclusion, the eddy current resistance-based method can provide the best performance with or without adding the full load and also the best performance was achieved during the speed reversal from 160 rpm to -160 rpm. The last comparison in chapter 6 was made for the eddy current resistance

based method using two HF injection frequencies, 1 KHz and 2.5 KHz. The lower frequency with lower amplitude of injection signal can provide a better performance due to the smaller signal to noise ratio.

Finally, the PWM injection method is mentioned again because the square wave voltage signal injection scheme is always advocated for the high frequency injection method. The reason is that this method does not use any software filters and there is no time delay in the system response. This method also enhanced the dynamic response and estimation performance. However, comparing to the eddy current resistance method, this PWM method doe not provide a good quality with load impact. In conclusion of four sensorless control methods, the precise estimation results have been obtained from the eddy current reflected resistance based method under various conditions. However, the other three methods can also provide some good results. The prospect of using the four methods is expected for position estimation of industrial motor applications.

7.2 Signal Processing for Current Derivative Measurement

For sensorless control using response to IGBT switching, two schemes have been investigated using di/dt sensors and using current samples. The di/dt sensors can directly measure the current derivative signal. Sampling the line current within a voltage vector, the current derivative can be digitally calculated given the known sampling time interval. It is known that the high frequency switching oscillation will occur for both methods. In the practical experimental approach, an interval is needed to allow the current oscillation to decay sufficiently. The line current can not be measured within the period of current oscillation. The use of a recursive least squares estimation in order to estimate the underlying gradient in the presence of HF oscillations has been investigated. The accuracy of the estimation depends on the number of samples, and in this work different numbers of samples were used.

The measurement of sample numbers, gradient error, and minimum sample time was carried out in chapter 3, at different motor speeds and under various load conditions. The comparison between real and estimated results has been made. The "real"

gradient is assumed by using all the motor current samples. Two different number of samples 30, and 60 were used for gradient estimation. It can be clearly seen that better accuracy is seen when more numbers of samples are used for the RLS algorithm. The estimated error is less, but a longer minimum vector time is required. However, the required minimum pulse width with this proposed method is 3.6μs shorter than the minimum pulse width without this method and the estimation accuracy of the gradient is also significantly improved. The estimation results were good, and can reduce the minimum on-time of vectors associated with this advanced sensorless method significantly. Unfortunately due to time constraints within the project, it was not possible to implement the approach in real-time on the data acquisition system. However the method could potentially be implemented and the motor current measurements could be with a high sample rate.

7.3 Further Work

The development of a high sampling frequency data acquisition system is required to expectedly investigate the PWM excitation tracking method, which can sample the motor current measurements at a high rate and obtain the desired position dependent di/dt component from the high frequency oscillation. To achieve this, the implementation of high sampling rate hardware based (FPGA) is worth researching as a way to enhance the current measurement (read more current samples) and hence rotor position estimates.

Appendix A

System Control Platform

The digital control system consists of the DSP (digital signal processor) and the FPGA (field-programmable gate array) acquisition system, produces the user interface and provides the control platform. The FPGA and DSP cooperate together to realize the command implementing, signal interfacing, and data processing. In addition, the encoder interface is cooperated with FPGA and DSP to obtain the rotor position information from the encoder of PM machine.

A1. Digital Signal Processor Kit (DSK)

In this research, a Texas Instrument TMS320C6713 DSP Starter Kit [68] is used to as a signal processor by interfacing the signal and controlling the machine. The DSP is a high speed processor basically, which can operate at the frequency of 225MHz and can also perform eight operations at maximum per cycle. Fig A1 illustrates the details of DSP. Due to the high speed operations and control ability of DSP, the DSP is connected with its external peripherals through a 32-bit external memory interface (EMIF). The EMIF does not only support 16Mbytes of Flash ROM, on board SDRAM memory, I/O port, but also provide a memory interface expansion connector for a plug-in HPI daughter card. All accesses of the EMIF are clocked at up to 100MHz while the CPU is clocked at 225MHz. The DSK processor is programmed by implementing C program to action the standard procedures in a periodic interruption service routine. Many tasks are achieved by using DSP program including data signal processing, position estimation, position pulse decoding, three drive PI control algorithms, software circuit protection, system initialization, space vector PWM algorithms, calibration of unbalanced signals, and signal compensations.

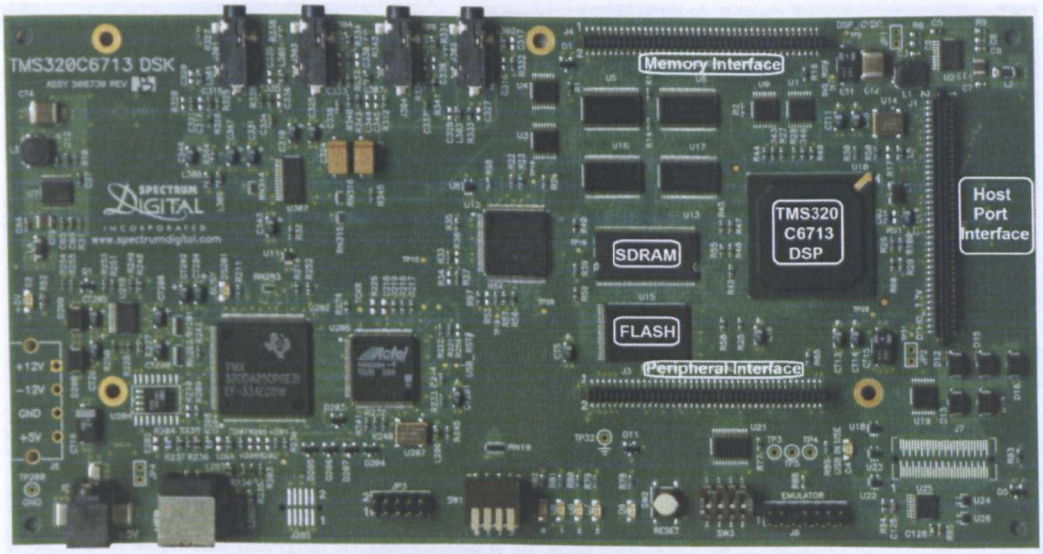

Fig A1 TMSC6713 DSP starter kit

A2. Field Programmable Gate Array (FPGA)

The FPGA essentially is a programmable logic device, which generally allows the users to interface the hardware by a hardware description language (HDL). FPGAs can be used to implement any logical functions that an ASIC (Application-specific integrated circuit) could perform. Libero® Integrated Design Environment (IDE) is the comprehensive software toolset for designing with all Actel FPGAs. A ProASIC3 is the third-generation product of Actel Flash FPGAs. It has high performance, low cost, low power, high density and large capacity. Therefore, the ProASIC A3P400 is selected in this research to support 400 system gates as shown in Fig A2. Additionally, The ProASIC A3P400 has four I/O (Input/Output) banks, 54K bits RAM, and 194 high performance user I/Os. A developed FPGA acquisition system in a board contains the Actel-FPGA unit, ADC channels, LED display, DAC converter, user I/Os, etc. The FPGA is collaborated with DSP and FPGA will implement any functional operations that C program could be executed in DSP. On the other hand, DSP receives all the desired information from the FPGA system for the functional operations. The main function of FPGA system in this research are pulse generation, online measurement, data sampling, data conversion, signal reading and incorporation with external interface boards.

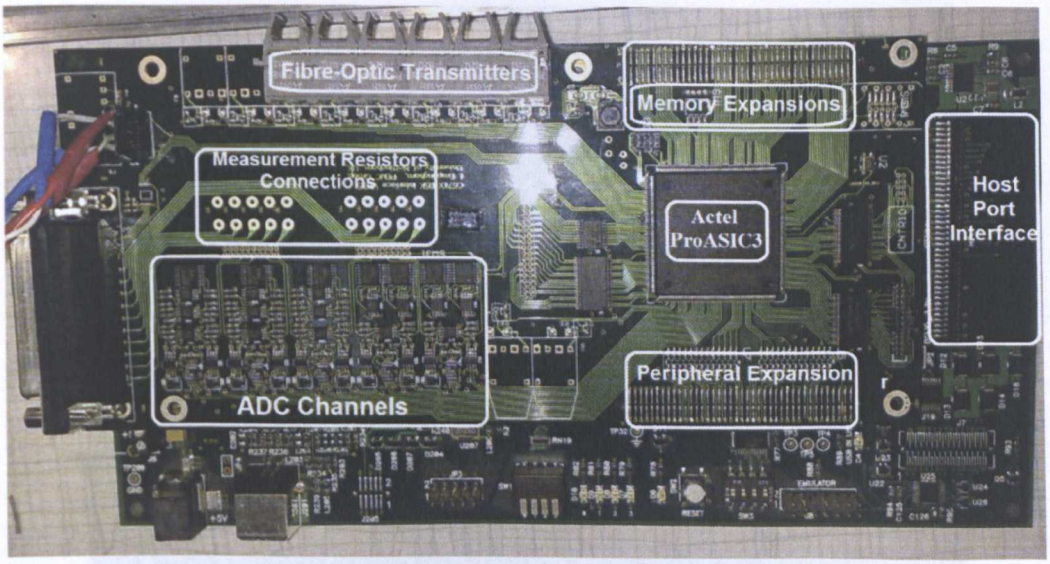

Fig A2 FPGA data acquisition system

A3. Encoder Interface Board

The external encoder board is plugged into the FPGA system by a small 20-way socket as shown in Fig A3. The encoder interface board is seen as the link between encoder from rotor shaft and encoder interface board. An external cable is used to connect both encoder and encoder interface board. There are six-pulse signals in total passing through encoder interface board. The generation of pulse is achieved by the D-flip-flop logical algorithms. The quadrature (incremental) encoder is used in this project, two-phase output signal output are 90° displaced each other, which is all that the quadrature means. The position measurement is achieved in the FPGA by processing the quadrature signals from the encoder board. A clock pulse signal is also used to reset the counting of pulse per resolution. Three-phase signals can be identified as A, B, and Z in clockwise and three counter-clockwise three-phase signals are also defined as $\overline{A}$, $\overline{B}$, and $\overline{Z}$. During the decoding in the FPGA system, A & B outputs are read by the FPGA, via either an interrupt on any edge or polling, in order to decode the rotor rotating direction. The other types of encoders are also capable for the motor control use such as absolute encoder, sine wave encoder, etc. In general, different motor applications have their own suitable types of encoders.

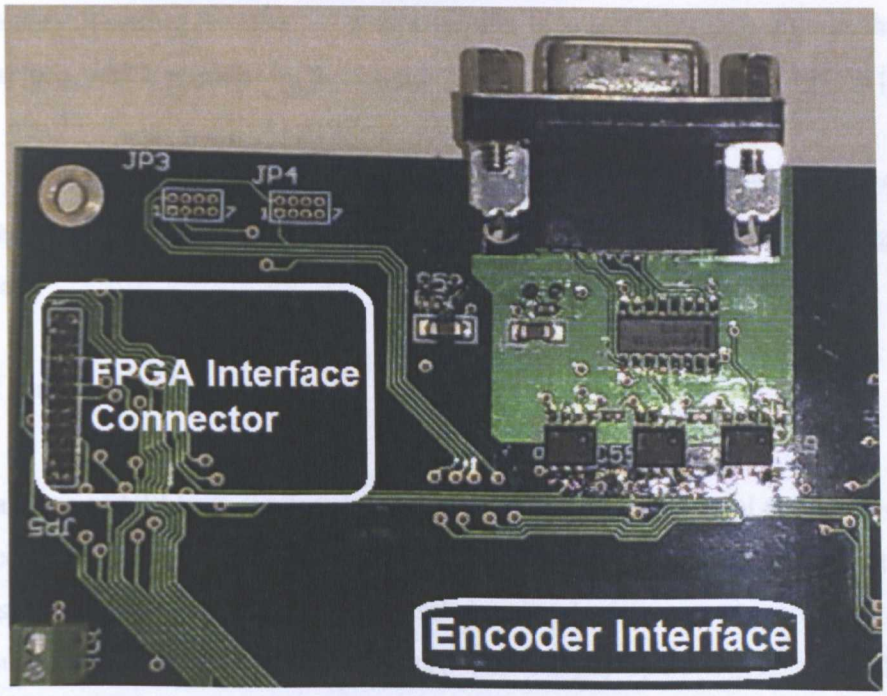

Fig A3 encoder interface board

A4. HPI Daughter Card and Host Programme

1. HPI Daughter Card

In a HPI daughter card as shown in Fig A4, there are sixteen pins available for digital I/Os and eight of them can be used as the analogue inputs. Two types of the resistors used here are pull-up resistors and series resistors. The pull-up resistor has a resistance of 100kΩ and series resistor has a resistance of 180Ω. If there is no potential on the pin, the pull-up resistor can provide a voltage to be presented on the microprocessor input pin. The aim of using the series resistor is to avoid the hazards of electrostatic discharge and provide 5V logic signal to input pin. In general, the input voltage applied to the pin should be in the range between 0V and 3.3V [69]. Below are some important issues to understand when using the daughter card.

A) All data variables for reading or modification through the HPI port must be 32-bits or larger.

B) The default setting for DSK- C code compiler is to load any programmes through the interface, which must be built with the "runtime auto-initialization" option [69].

C) In C67XX architecture, all memory accesses should be aligned with 4-byte boundaries; otherwise non-aligned words will still not be accessible through the interface.

2. HPI Matlab Host Programme

The package of HPI host services is designed to develop the control applications and also execute programme in the DSK C6713 processor. The LED of HPI daughter card starts flashing, when the host service mode is correctly connected and communicated with the DSK processor. The simple operation is controlled by reading and writing the memory of DSK processor. The required maths functions and relevant commands are written in the M-file in order to control applications. The host program is used to capture the data, which is from measurement transducers, position encoder, etc.

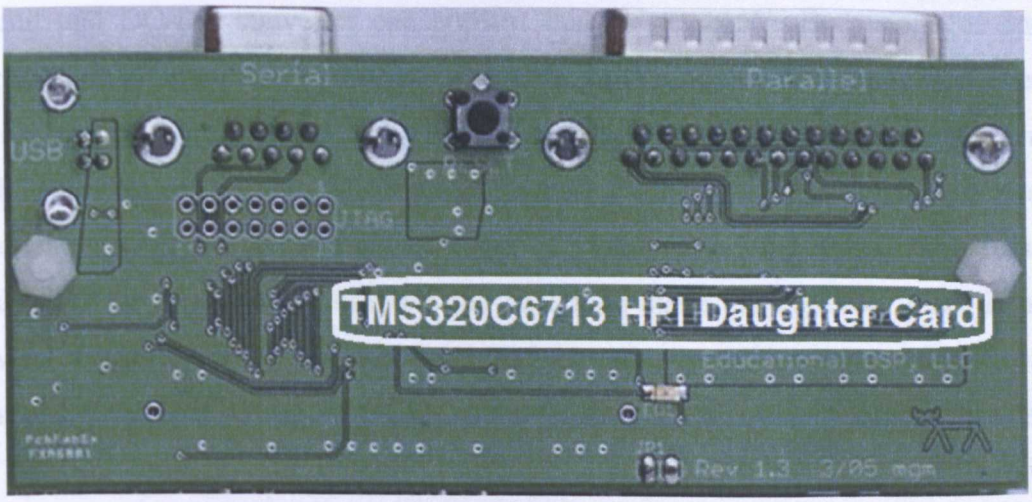

Fig A4 HPI daughter interface card

A5. Gate Drive Circuit

The gate driver circuit is designed to control the voltage of IGBTs and so the required gate current will flow through the collector to the emitter. Therefore, IGBTs are operated through the gate drive circuit. The gate drive circuit is used to supply the voltage of 15V for IGBT modules. Therefore, this type of inverter with its own specific structures is named as voltage source inverter. The modulated voltage is applied across its gate and emitter of IGBTs.

The gate drive circuit can also use the logic level control signals to adjust the switching state of IGBTs. Traditionally, most of gate drive circuit designs take into account the consideration of isolation so that the low voltage logic signals are not connected to the dangerous high voltage in the power circuit. The optocoupler consists of an infrared light-emitting diode and a silicon phototransistor, which separates low and high voltage region as shown in Fig A5. The opotocoupler requires separate power supply. In this research, only one optocoupler is used for dual IGBT switches module in each phase. This arrangement can reduce power dissipation and save space on the gate drive board. In the low voltage region, 5V DC voltage is supplied to the whole gate drive circuit and DC-DC converter can convert this 5V to ±15V. Both voltages and currents are all amplified by DC-DC converter. In Fig A5, ±15V voltage is applied across the push-pull circuit, which consists of PNP and NPN transistors. The IGBTs always produce the uncompleted switching states due to the high switching frequency performance. The combination of push-pull circuit is mainly used to assist IGBTs' switches to complete the switching states. In addition, there is no power dissipation by using this combined circuit. An IGBT is switched on when a positive voltage of 15V from push-pull circuit is applied across its gate and emitter. Although the IGBT can also be switched off when there is no voltage applied between the gate and emitter at steady state, a negative voltage bias is still supplied to switch off the IGBT to avoid the voltage integral caused noise. This operation is especially designed for the IGBT bridge application [60].

The fast switching of IGBTs, high voltage, and high current IGBT power circuit can be the source of the severe electromagnetic noise [59]. However, the produced noise can be filtered out by the appropriately designed gate drive circuit. For a safe operation and a good dynamic characteristic of IGBTs, the components on the PCB designed by [Si Dang 2004] has been carefully selected and laid out to avoid problems such as coupled noise. The PCB uses completely electrical isolated gate drive circuits for IGBTs. In other words, in each gate drive circuit, the logic level control signals of 5V are isolated from the power supply of IGBTs. The advantages and disadvantages of isolated gate drive have been outlined below [5].

Main advantages:

(1) The gate drive is stable and is not affected by the power device switching.
(2) The gate drive can provide current at a high level for large IGBT modules.
(3) In the control circuit, the power circuit switching noise and high voltage potential are isolated.

Main disadvantages:

(1) All of the power supplies are assumed to be isolated. Therefore, the cost, complexity and the size of PCB board has to be considered for the research development.
(2) It is also difficult to filter out the noise and achieve isolated voltage at a high level. The simplified isolated gate drive designs are presented in [59], and the performance of the simplified circuit has been also developed.

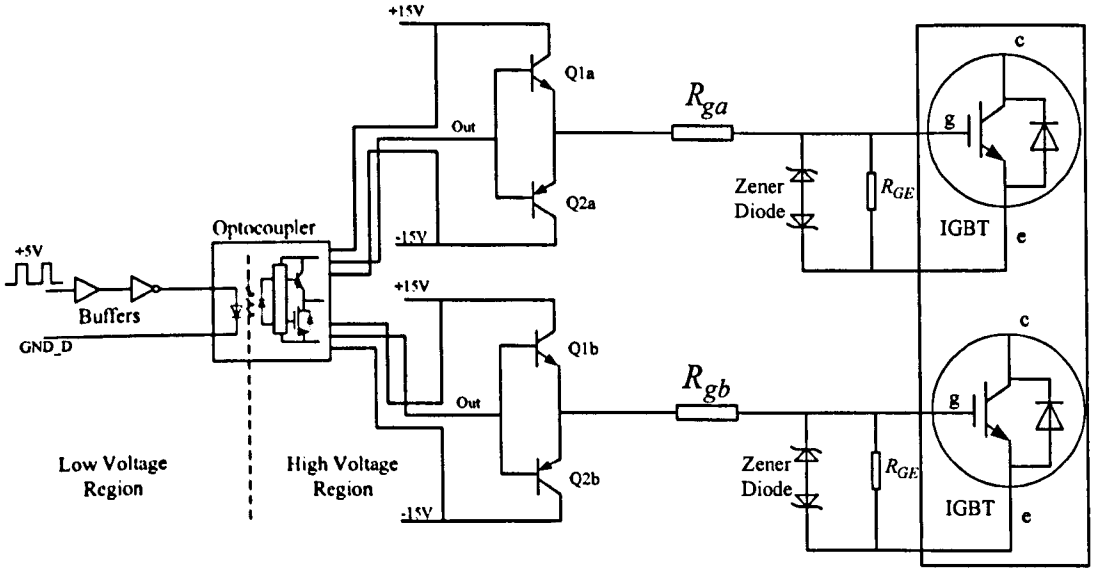

Fig A5 Gate drive circuit for dual igbt switches

In the design process, some components and devices are used to provide the electrical isolation such as digital transistors, pulse transformers, optocouplers, and optical fibre cables. In the design, some of the components do not provide the sufficient noise immunity and safety such as bus buffers, Schmitt trigger buffers, zener diodes, and some discrete transistors. However, some protection circuits are considered to avoid the problems and some components are added to improve the noise immunity and reduce the dangerous level. There are six phases gate drive circuits are printed on the PCB and they are placed separately but they have same applied power source. In this thesis, the three phase gate drive circuits are only used to supply and control the PMSM. This gate drive PCB has two layers on both sides, which is a suitable design for the PMSM or IM of low-medium power rating of 5-50KW. Table A1 gives the details of the electronic components used in the designed gate drive circuits, and also their functions are briefly described. Some capacitors and some resistors like pull-up resistors are not discussed in details. The entire gate drive circuit for each IGBT module will be also presented in Appendix Fig B3.

Components	Type	Functions
Fibre Optics Receiver/transimitter	HFBR-1524 (Transmitter) HFBR-2524(Receiver)	Generate and receive the PWM voltage pulses
Optocoupler	HCPL-315J	Isolate low and high voltage and dive the voltages to IGBTs
DC-DC converter	DCP020515DU	Supply Optocoupler
Schmitt Trigger Buffer	SN74AHC1G14DBVR	Cancel the noise and inverting the signals
Bus Buffer	SN74AHC1G125	Buffering and transmitting the signals
Zener Diode	BZV55C2V4	Protection and Balance the gate voltage
PNP-NPN	FTZ951(PNP) FTZ851(NPN)	Push-pull circuit Amplify the gate voltage

Table A1: the used components of gate drive circuits

A6. DC Link Power Circuit

The DC link power circuit consists of a three-phase diode rectifier module, DC link capacitors, and discharging resistors. The DC link power circuit is used to feed the inverter to supply AC voltage for AC machines. In this thesis, DC link voltage is produced by connecting to three-phase rectifier and DC link capacitors. The DC link capacitors are charged and discharged electrons to establish the DC voltage. The one of common used capacitors is chosen as DC link capacitor in this research, which is called electrolytic capacitor. The reason why choose it because the electrolytic capacitor is capable to provide the high capacitance density. Additionally, compared with other types of capacitors, they have relatively low breakdown voltage, higher leakage current and inductance, poorer tolerances and temperature range, and shorter lifetimes [62]. Fig A6 (a) shows the equivalent circuit of an electrolytic capacitor,

which is established by dual parallel resistance for leakage current (R_{Leak}), the equivalent series resistance (R_{ESL}), the equivalent series inductance (L_{ESL}), and the capacitance (C) [62]. The connections of DC link capacitors are shown in Fig A6 (b), according to the structure of their equivalent circuits. The DC link capacitors can be also connected either in parallel or series, which depends on the requirement of DC link voltage. The parallel resistors for leakage current are designed to balance the DC link voltage and also discharge safety applications in high voltage circuit, as shown in Fig A6 (b).

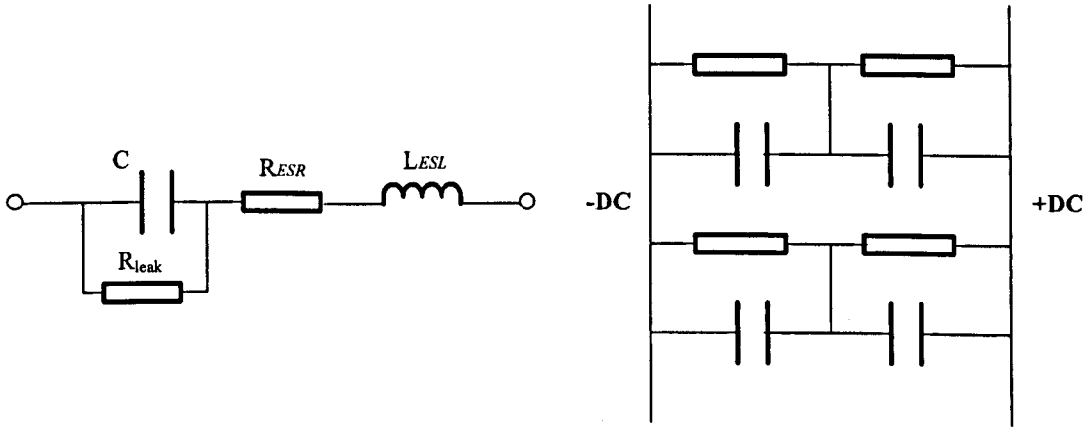

(a) Equivalent circuit of an electrolytic capacitor (b) Connection of DC link capacitors

Fig A6 Structure of DC link capacitors

Fig A7 shows the photo of DC link circuit on the PCB. On the left of the photo, three inputs and three outputs are placed in parallel. Four electrolytic capacitors are not seen in the photo, because the capacitors are placed underneath the PCB and connected to the discharging resistors. The DC link capacitors are used to smooth the voltage produced from the diode rectifier. The capacitance has been calculated in [5], which is approximate $2016\mu F$. The value of the capacitance is derived from [61] by using the load power, maximum and minimum output voltage from the diode rectifier, and the frequency of output voltage ripple. Due to the limitation of electrolytic capacitor, the maximum capacitor voltage is limited between 500 and 600 V [63]. It is important to observe the DC link voltage because the VARIAC only provide the percentage of AC power supply rather than the actual DC voltage values. The multimeter is always placed next to the rig. Once the power switch is turned on, the multimeter can show the DC voltage readings when the knob of VARIAC is

rotated manually. The DC voltage must be increased slowly; otherwise high level current may damage the components on the PCB.

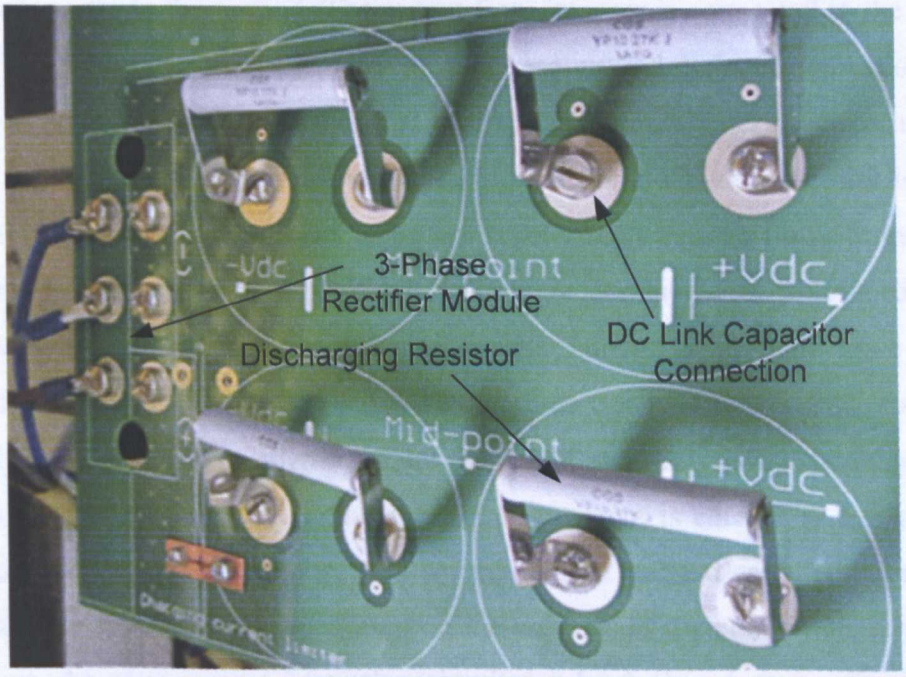

Fig A7 DC link circuit of the test rig

A7. Protection Circuit

For the reason of safety and reliable operation, the consideration of protection circuit becomes really important in motor drive experiments. The protection circuit is designed to avoid the emergencies happened during the control operation. High current and high power can kill lives and damage the expensive equipments. Therefore, the protection circuits in this research are introduced in this section and some common electrical faults are described. In fact, the considerations about the protection can rapidly improve the design of power electronics in the field. Additionally, the temperature protection is also considered on the top of the electrical protections.

The short circuit can always cause over current in the entire control systems. In [66], three possible fault conditions are introduced and analyzed. And the approach of over current protection is identified. All fault considerations fall in the DC to AC inverter circuit. The first fault condition is described as the current flow, which is from the inverter to the ground. The output from inverter is connected to the ground in error due to the incorrect wiring or motor phase-ground dielectric breakdown [5]. Therefore, three-phase output cables must be tested by multimeter to make sure they are not grounded before the operation starts. The second fault condition is called "shoot through fault". It happens when the short circuit current flows through one IGBT module. In other words, IGBT module is conducted or shortened like a connected electric wire. This may cause serious damage to the gate drive circuit. Any incorrect control caused by software or noises can lead to this fault condition. To avoid this, several considerations are discussed in [5]. The last consideration is the line to line fault condition. The short circuit current is caused by miswiring or connection of two-phase outputs. And so, the double isolated cable is essential for three-phase motor drive system. Based on the analysis of the above mentioned fault conditions, the over current protection circuit can be designed more effectively on the ADC channels. The current transducer is an analogue device, which provides the actual data readings for each phase current to FPGA acquisition system. The over current protection can be setup by comparing the actual current level to a certain current value either in the control C-programme or in the potentialmeter.

The setting for current trip level can be distinguished as software trip level setting and hardware trip level setting. In FPGA system that used in this research, there are 10 ADC channels and every two channels share one ADC chip. Each channel has its own potential meter and comparator for the trip level. The hardware trip level setting can be calibrated by using DSK software Code Composer. Once the calibration is done, the current trip level will be stored in the memory of DSP permanently. The software trip always acts more slowly than the hardware trip; and therefore, the hardware trip level setting in the protection circuit is crucial to avoid the short circuit fault conditions.

Over voltage protection circuit is used in the measurement of DC link voltage. To avoid the overcharge of four DC link capacitors, the voltage across DC link is always observed and early measured through a multi-meter. The predetermined threshold value is between 500 and 600 V. Another concern is the IGBT bridge-circuits because high frequency switching events always cause the high voltage at IGBT terminals due to the stray inductance in the circuit. The switching states of IGBTs especially a sharp rise of frequency is generated and cause the interruption in voltage and current during the turned off period. The spike is likely to be observed during the current or voltage transients and this spike can cause electromagnetic interference in other near circuits [67]. This spike can also damage and lead to failure of the controlling devices. The snubbers are frequently used in electrical system to prevent the spike during voltage or current transients. In [66], several snubber circuits are described and proposed to reduce the interruption in the transients of voltage and current. In this research, three snubber capacitors of 0.47μF are placed in parallel and across each IGBT module, as shown in Fig A8. In terms of temperature protection, some cooling equipments are considered to reduce the heat produced by the high switching devices such as IGBTs and three-phase diode rectifier. Both devices are placed on the top of two pieces of heat sink and the thermal grease is filled in between two devices to increase the thermal conductive. Silicone paste is used to aid IGBTs and rectifier to dissipate the heat through the heat sinks. The cooling fans are also used as shown in Fig B1 of Appendix B.

Fig A8 snubber capacitors for circuit protection

Appendix B

Schematics and Rig Photos

In chapter 5 and Appendix A, the details regarding to the constructions of the whole AC drive control system have been discussed. In this section, the main power schematic circuit diagrams are shown FigB.2 and the gate drive circuit diagrams of IGBTs are presented in Fig B5. The photo of both DC machine and the PMSM is presented in Fig B4 and they are connected together by the rigid coupling shaft. The main power circuit is built on a two layers PCB and the photo shoot of the circuit is shown in Fig B1. Both negative and positive DC link currents respectively go through the upper and lower layers of this PCB. This whole PCB contains all the integrated devices for the constructions of the inverter such as the rectifier, DC-link capacitors, IGBT modules, 3-phase current and DC link voltage measurement transducers, cooling heat sink with cooling fans, and protection circuits.

B1. Power Circuit

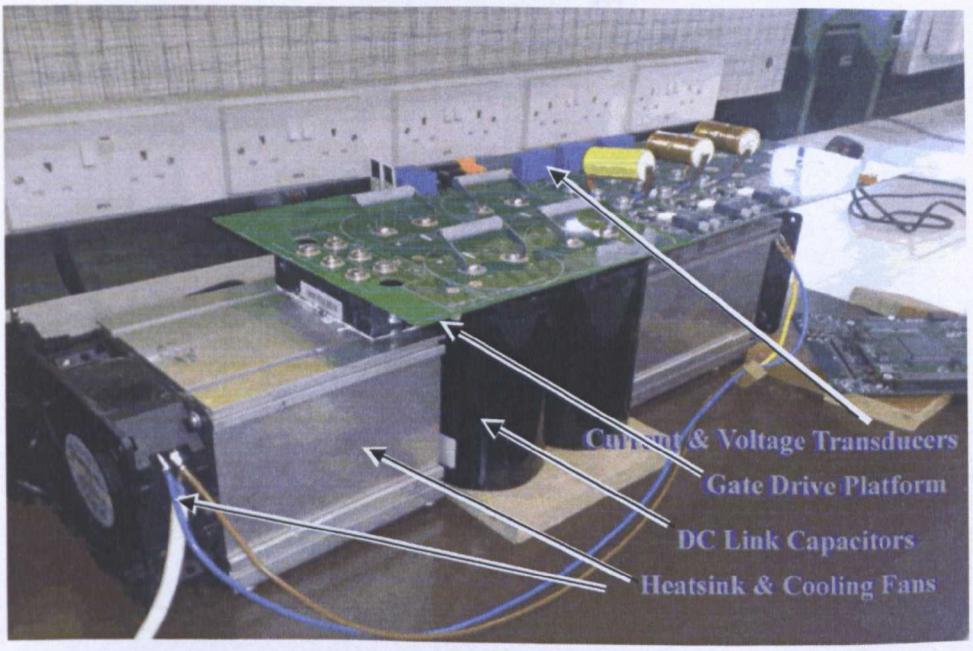

Fig B1 the inverter test bed

B2. Main Power Circuit Schematics

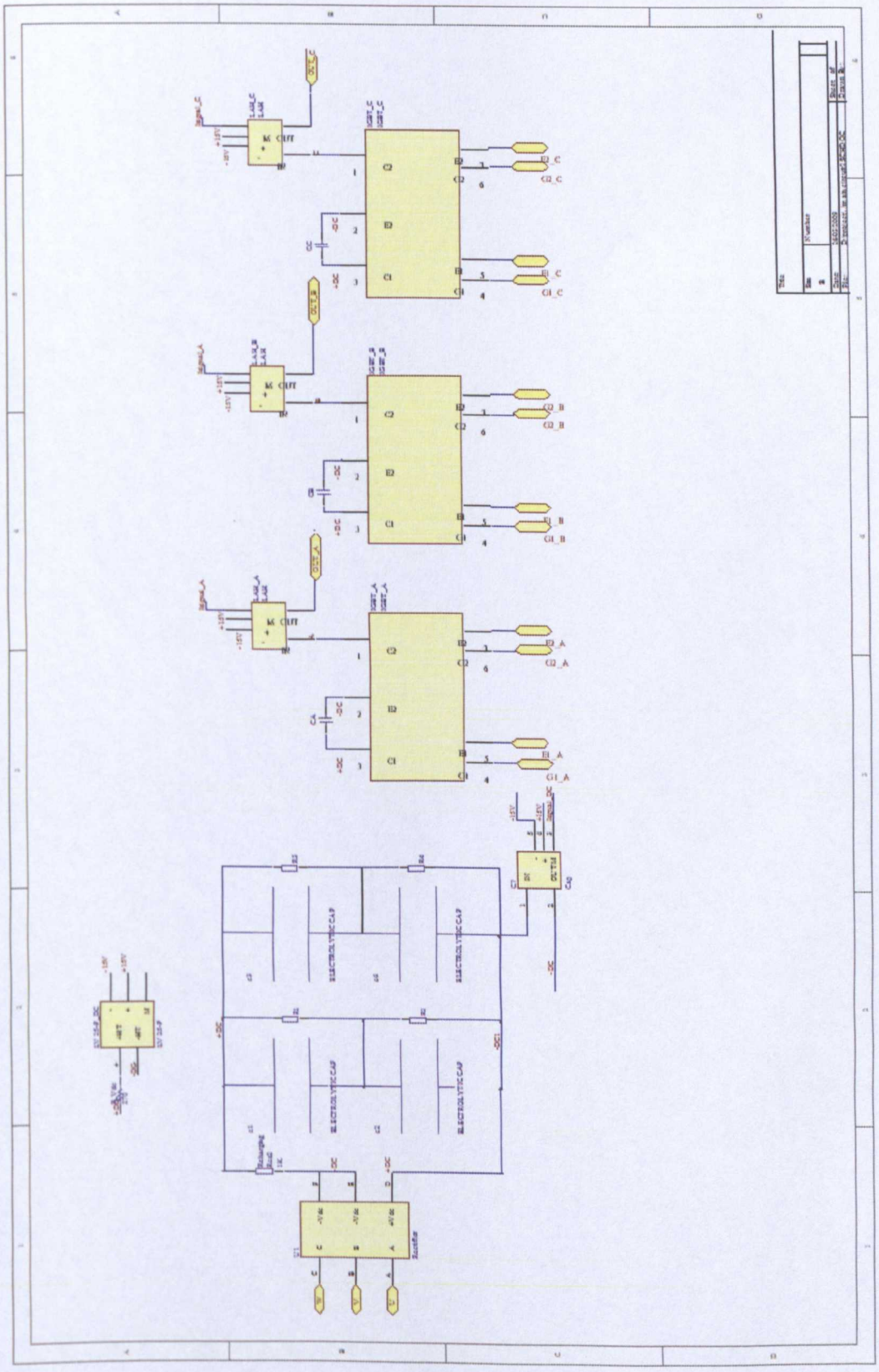

Fig B2 main power circuit schematics

B3. Gate Drive Circuit

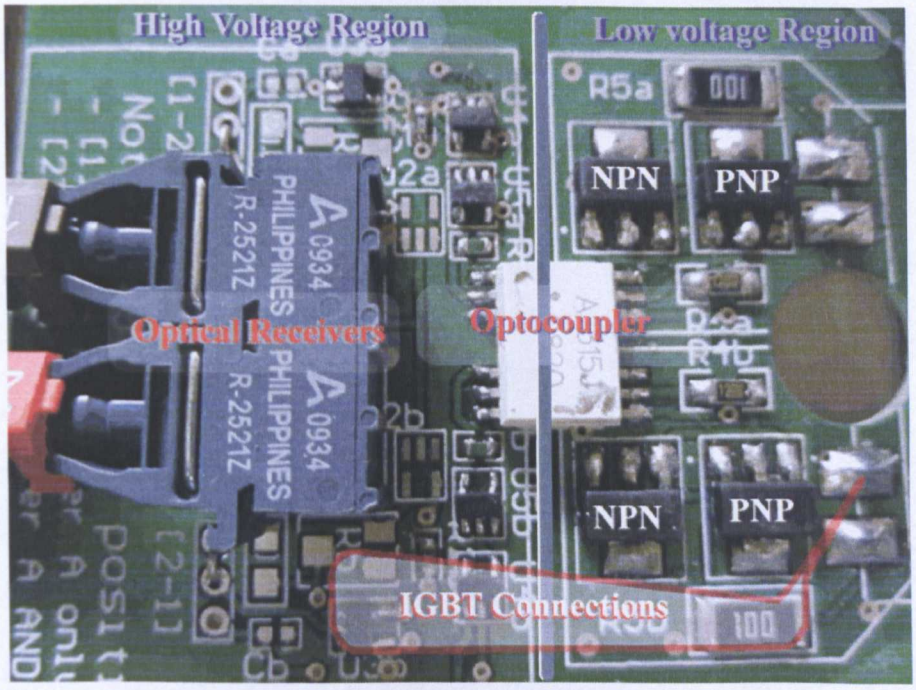

Fig B3 the photo of gate drive circuit board

B4. DC machine and PMSM

Fig B4 the DC machine and the PMSM

B5. Gate Drive Circuit Schematics

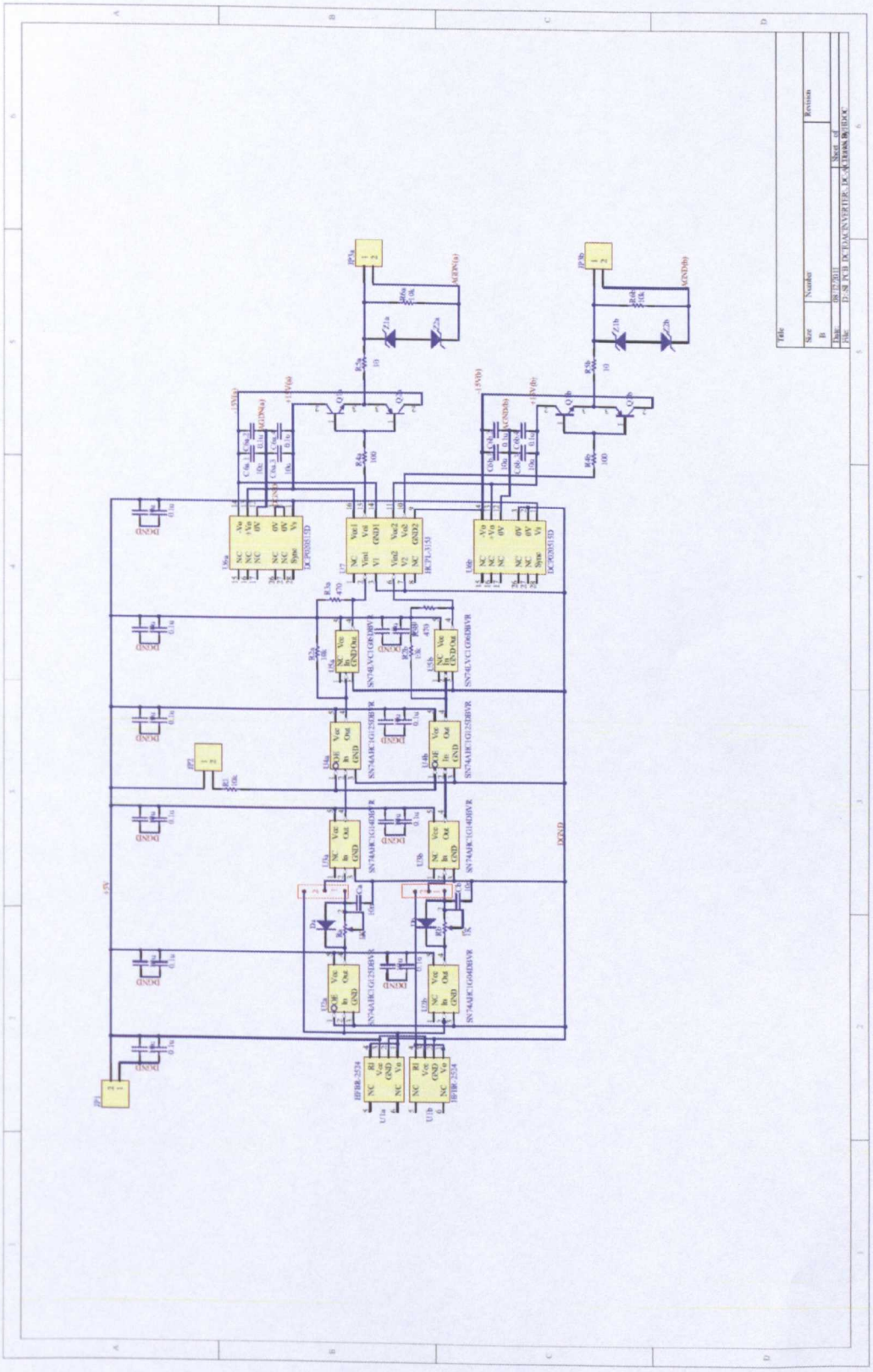

Fig B5 the circuit schematics of the IGBT gate driver

Appendix C

C MEX S-Function

a. Define and Include

```
#define S_FUNCTION_NAME  Tony
#define S_FUNCTION_LEVEL 2
#define INPUT_NUM 2
#define OUTPUT_NUM 1
```

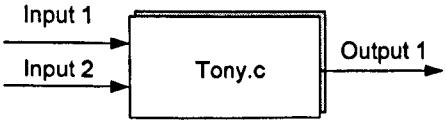

As above in the first line, the *S-function* defines the MEX-file's name as "Tony", which is shown in the functional block after compiling the S-function. The second programme line defines the version of *S-function* used. The third line defines the input numbers of the functional block. The last line also defines the output numbers of functional block. The explanations for *S-function* in details are next.

#include <math.h>

#include "simstruc.h"

The "simstruc.h" file defines a data structure, which is to maintain information about the *S-function*. The "math.h" file defines the maths functions that are used in the *S-function* - MEX-file. [56]

b. Input and Output Setting

The input and output setting presents the width of ports, number of ports, and feed directions of the ports. The numbers represent the size of the data and it is easy to understand from these commands.

Input Port Setting

ssSetNumInputPorts(S, 1)

ssSetInputPortWidth(S, 0, 1);

ssSetInputPortRequiredContiguous(S, 0, true);

ssSetInputPortDirectFeedThrough(S, 0, 1);

Output Port Setting

ssSetNumOutputPorts(S, 1)

ssSetOutputPortWidth(S, 0, 1);

In Table C1, the stages of the simulation are interpreted into the *S-function* routine [56] and each command represents the *MEX-file* to produce the desired results.

Simulation Stage	*S-Function Routine*
Initialization	mdlInitializeSizes
Sampling Time Setting	mdlInitializeSampleTimes
Input port setting	ssSetNumInputPorts
Output port setting	ssSetNumOutputPorts
Get input port signal	ssGetInputPortSignal
Generate output port signal	ssGetOutputPortSignal
Get the Simulation Time	ssGetT
End of simulation tasks	mdlTerminate

Table C1 translations of *S-function* routine

c. Set the Numbers of Working Elements

ssSetNumSampleTimes(S, 1); Set how many sample time uses

ssSetNumRWork(S, 0); Set how many Real numbers

ssSetNumIWork(S, 0); Set how many Integral numbers

ssSetNumPWork(S, 0); Set how many Proportional numbers

ssSetNumModes(S, 0); Set the size of block's mode vector

ssSetNumNonsampledZCs(S, 0); Set how many non sampled zero-crossing

ssSetOptions(S, 0); Specify the *S-function* Options

d. Simulation Loop Setting

Initialize the sample and offset time of the simulation.

```
static void mdlInitializeSampleTimes(SimStruct *S)
{
  ssSetSampleTime(S, 0, 0.0000002);
  ssSetOffsetTime(S, 0, 0.0);                    }
```

Function here represents the relationship between the input and output.

```
static void mdlOutputs(SimStruct *S, int_T tid){
    real_T *x = (const real_T*) ssGetInputPortSignal(S,0);
    real_T *y = (const real_T*) ssGetOutputPortSignal(S,0);
    }
```

Perform any actions that are necessary at the termination of a simulation.

```
static void mdlTerminate(SimStruct *S)
{
}
```

The simulation for sensorless control of the PM machine using current measurement is shown in Fig C1. S-function is implemented to achieve the digital sensorless control in a PM machine. Each S-function block realized each task for this simulation work such as speed/current control, position estimation, etc and the simulation results have been shown in chapter 3.

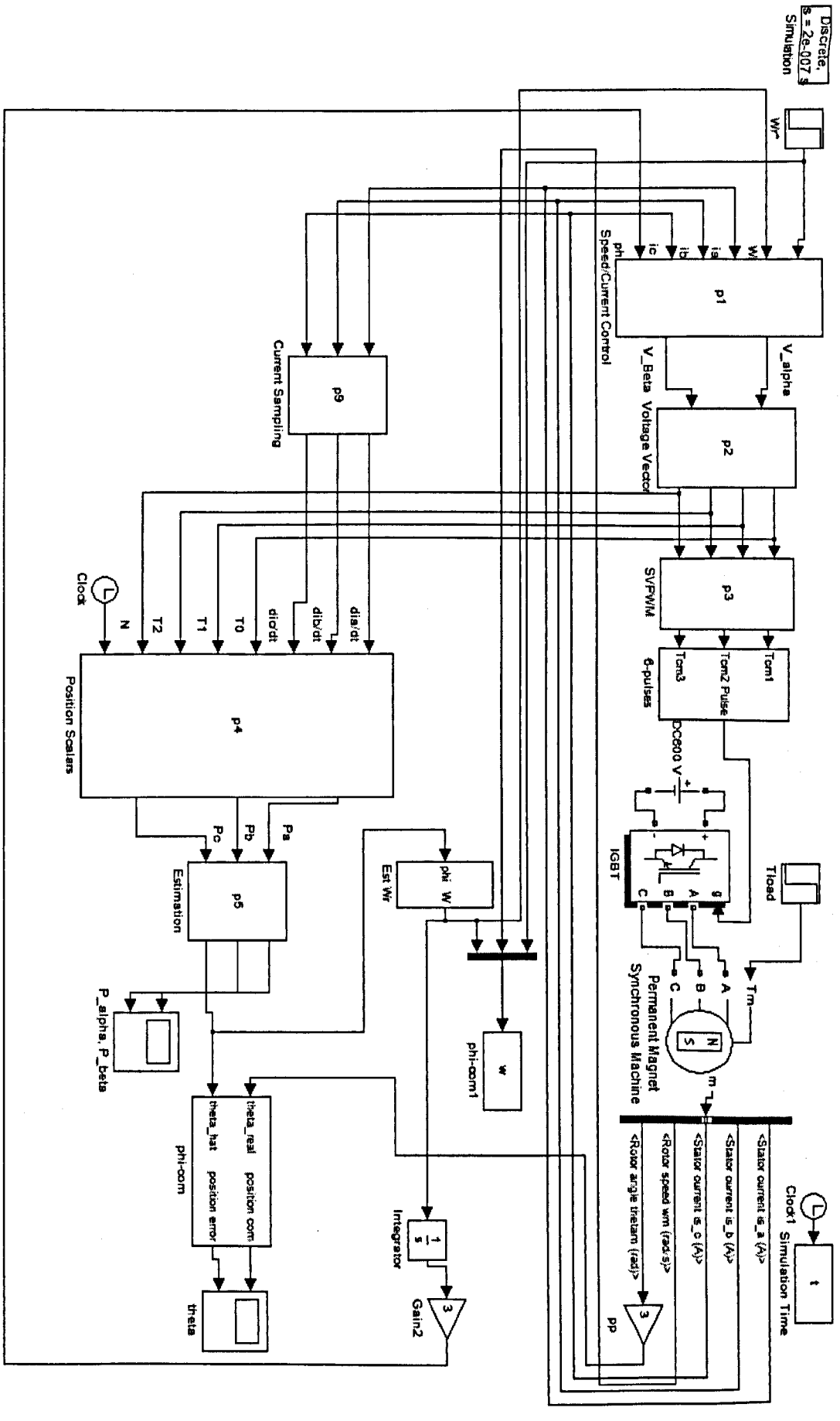

Fig C1 sensorless control simulation of PM machine using current measurement

Appendix D

Publications

Yu Duan; Paul Tucker. Idealized Cooling System for further uses of Computer, in International Conference on Computer, Communication and Control Technologies: CCCT '03, JUL 2003. ORLANDO, FL, USA

Yu Duan; Peng Dong. Improvement of Voice Qualities and Network Coverage for GSM Handsets, QOS, IET Telecommunication Conference, 2-3 Mar 2004, London Savoy place, UK

Yu Duan; Jeyraj Selvaraj. Computer Cooling System for CPU under the Certain Thermal Ranges, in International Conference on Computer, Communication and Control Technologies: CCCT '05, May 2005 in Austin, Texas, USA.

Yu Duan. Idealized Thermal Control of Computer Cooling System, 1st UK Chinese Academic PhD Forum CSSA-UK, Cambridge Journal, 30th, May, 2009, Nottingham University, UK

Yu Duan; Mark Sumner, A Novel Current Derivative Measurement Using Recursive Least Square Algorithms for Sensorless Control of Permanent Magnet Synchronous Machine, International Power Electronics and Motion Control (IPEMC-ECCE Asia), 2nd – 5th June 2012, Harbin, China P.R

Bibliography

[1] Blaschke F., Burgt J and Vandenput, "Sensorless Direct Field Orientation at Zero Flux Frequency", IEEE IAS Annual Meeting, October 1996, pp.189-196

[2] Literature Number: BPRA073, Field Oriented Control of 3-Phase AC-Motors, Texas Instruments Europe, February 1998.

[3] Calin Capitan, Torque Control in Field Weakening Mode, Master Thesis, 2009.

[4] Gao Qiang, Asher G M, Sumner M and Makys, P, Position Estimation of AC Machines over a Wide Frequency Range Based on Space Vector PWM Excitation, IEEE Transactions on Industry Applications, Vol. 43, No. 4, 2007.

[5] Hua Yahan, Sensorless Control of Surface Mounted Permanent Magnet Machine Using Fundamental PWM Excitation, PhD Thesis, 2009.

[6] Cesar Armando Silva, Sensorless Vector Control of Surface Mounted Permanent Magnet Machines Without Restriction of Zero Frequency, PhD Thesis, 2003.

[7] J.-I. Ha and S.-K. Sul, "Sensorless Field Orientation Control of an Induction Machine by High Frequency Signal Injection," presented at IEEE-IAS Annual Meeting, New Orleans, Lousiana, 1997.

[8] Ji-Hoon Jang, Jung-Ik Ha, Motomichi Ohto, Kozo Ide, Seung-Ki Sul, Analysis of Permanent-Magnet Machine for Sensorless Control Based on High-Frequency Signal Injection, IEEE Transactions on Industry Applications by the Industrial Drives Committee of IEEE Industry Application Society, 2003.

[9] Marco Linke, Ralph Kennel, Joachim Holtz, Sensorless Control of Permanent Magnet Synchronous Machines without Limitation at Zero Speed, IECON 02 Industrial Electronics Society, IEEE 2002 28th Annual Conference.

[10] Asher G, Review of INDUCTION MOTORS and PWM DRIVES, MSc Module H54IMD Induction Motor Drives Course Handouts, 2003.

[11] J. Holtz, Sensorless Control of Induction Machines with or without Signal Injection, IEEE Transactions on Industrial Electronics, 53(1):7–30, Feb 2006.

[12] Kazuhiro Ohyama, Comparative Analysis of Experimental Performance and Stability of Sensorless Induction Motor Drives, IEEE transactions on industrial Electronics, Vol.53, No 1, 2006.

[13] A. Larabi, M.S.Boucherit, Speed Sensorless Control of Induction Motor using Model Reference Adaptive System, International Conference on Electrical and Electronics Engineering, ELECO, Nov, 2009.

[14] MarKo Hinkkanen, Analysis and Design of Full-Order Flux Observers for Sensorless Induction Motors, IEEE transactions on industrial Electronics, Vol.51, No 5, 2004.

[15] Colin Schauder. Adaptive Speed Identification for Vector Control of Induction Motors without Rotational Transducers. IEEE Transactions on Industry Applications, 28:5, Sept/Oct 1992.

[16] C.Ilas; A.Bettini; L.Ferraris; G.Griva and F.Profumo. Comparison of Different Schemes Without Shaft Sensor for Field Oriented Control Drives. In Proceedings of IEEE Industrial Electronics Society, pages 1579–1588, Bologna, Italy, 1994.

[17] Eleonora Darie, The model of Permanent Magnet Synchronous Machines, Annals of the University of Craiova, Electrical Engineering series, No 30, 2006.

[18] Shanshan Wu, Yongdong Li, Zedong Zheng, Speed Sensorless Vector Control of Induction Motor Based on Full-Order Flux Observer, Power Electronics and Motion Control Conference, CES/IEEE 5th International Conference, IPEMC 2006.

[19] Cristian Lascu, Ion Boldea, Comparative Study of Adaptive and Inherently Sensorless Observers for Variable-Speed Induction-Motor Drives, IEEE transactions on industrial Electronics, Vol.53, No 1, 2006.

[20] C DeWit Canudas, A Youssef, J P Barbot, P Martin, F Malrait, Observability Conditions of Induction Motors at Low Frequencies, In IEEE Thirty-ninth Conference on Decission and Control, volume 3, pages 2044–2049, Sydney, NSW, Dec 2000.

[21] Shanshan Wu, Yongdong Li, Zedong Zheng, Speed Sensorless Vector Control of Induction Motor Based on Full-Order Flux ObserverPower Electronics and Motion Control Conference, IPEMC 2006.

[22] Hisao Kubota, Kouki Matsuse and Takayoshi Nakano, "DSP based Speed Adaptive Flux Observer of Induction Motor," IEEE Transactions on Industry Applications, Mar/Apr 1993.

[23] Somboon Sangwongwanich, Surapong Suwankawin, Sakorn Po-ngam, Suratsavadee Koonlaboon, A Unified Speed Estimation Design Framework for Sensorless AC Motor Drives Based on Positive-Real Property, Power Conversion Conference, Nagoya, 2007, PCC' 07.

[24] Zhang Bingyi, Chen Xiangjun, Sun Guanggui, Feng Guihong. A Position Sensorless Vector-control System Based on MRAS for Low Speed and High Torque PMSM Drive, Electrical Machines and Systems Conference, ICEMS 2005.

[25] Fang Zheng Peng, Fukao, T, Robust speed identification for speed sensorless vector control of induction motors, Industry Applications Society Annual Meeting, 1993, Conference Record of the 1993 IEEE.

[26] Greg Welch, Gary Bishop, An Introduction to the Kalman Filter, July, 2004

[27] G.Henneberger,B.J.Brunsbach, Th.Klepsch. Field Oriented Control of Synchronous and Asynchronous Drives without Mechanical Sensors using a Kalman Filter. In EPE91, pages 664–671, Florence, Italy, 1991.

[28] Y.R.Kim, S.K.Sul and M.H.Park. Speed Sensorless Vector Control of Induction Motor Using Extended Kalman Filter. IEEE Transactions on Industry Applications, 30(5):1225–1233, 1994.

[29] T. Wolbank, J. Machl, Anisotropy in Induction Machine Lamination and its Influence on Mechanical Sensorless Control and Conditioning Monitoring, EPE, Toulouse, vol. 10, no. 2, 2003.

[30] M. J. Corley, Rotor position and velocity estimation for a salient-pole permanent magnet synchronous machine at standstill and high speeds, IEEE Trans, vol. 34, no. 4, 1998, pp. 784- 789.

[31] T. Sawa, S. Sull, Sensorless position control and initial position estimation of an interior permanent magnet motor, IEEE Conference, vol. 1, no. 1, 2001.

[32] D Sativeri, A Arias, G Asyher, M Sumner, P Wheeler, L Empringham, C Silva, Sensorless Control of Surface Mounted Permanent Magnet Synchronous Motors Using Matrix Converter, Electrical Power Quality and Utilisation, Journal Vol X, No.1, 2006.

[33] Jacek F. Gieras and Mitchell Wing. Permanent Magnet Motor Technology: Design and Applications. Electrical and Computer Engineering. Marcel Dekker Inc, New York Basel, 3rd Edition, 2010.

[34] Schroedl, M, Sensorless control of AC machines at low speed and standstill based on the "INFORM" method, Industry Applications Conference, Thirty-First IAS Annual Meeting, IAS '1996.

[35] M.W.Degner, R.D.Lorenz. Using Multiple Saliencies for the Estimation of Flux, Position and Velocity in AC Machines. IEEE Transaction of Industry Applications, 34:1097–1104, Sept/Oct 1998.

[36] P. L. Jansen and R. D. Lorenz, "Transducerless Position and Velocity Estimation in Induction and Salient AC Machines," *IEEE Transactions on Industry Applications*, vol. 31, pp. 240-247, 1995.

[37] F. Blaschke, J. v. d. Burgt, and A. Vandenput, "Sensorless Direct Field Orientation at Zero Flux Frequency," presented at IEEE-IAS Annual Meeting, 1996.

[38] M. Corley and R. D. Lorenz, "Rotor Position and Velocity Estimation for a Salient-Pole Permanent Magnet Synchronous Machine at Standstill and High Speeds," *IEEE Transactions on Industry Applications*, vol. 34, pp. 784-789, 1998.

[39] J.I. Ha and S.K. Sul, "Sensorless field orientation of an induction machine by high frequency signal injection," IEEE IAS Annual Meeting, 1997, pp. 426–432.

[40] Jung-Ik Ha, Ide, K Sawa, T.Seung-Ki Sul, Sensorless rotor position estimation of an interior permanent-magnet motor from initial states, IEEE Transactions on industry applications, by the Industrial Drives Committee of the IEEE Industry Applications Society, 2003.

[41] Paul P. Acarnley and John F. Watson, Review of position-sensorless opeartion of brushless permanent-magnet machines, IEEE transactions on industrial electronics, vol. 53, no. 2, April 2006.

[42] Campbell, P, Al-Murshid, S, A model of anisotropic alnico magnets for field computation, IEEE Transactions on magnetic, vol. mag-18, no. 3, May 1982.

[43] Y.-D. Yoon and S.-K Sul, Sensorless Control for induction machines using square-wave voltage injection, in Energy conversion congress and exposition(ECCE), 2010 IEEE, pp. 3174-3152.

[44] Reigosa. D, Garcia. P, Briz, F, Raca, D, Lorenz, R.D, Modelling and adaptive decoupling of transient resistance and temperature effects in carrier-based sensorless control of PM synchronous machines, IEEE transactions on industry applications, vol. 46, no. 1, January/February 2010.

[45] H. Polinder, M. J. Hoeijmakers, Eddy Current Losses in the Permanent Magnets of a PM Machine, in Proc. Int. Conf. EMD, Sep. 1997, pp. 138–142.

[46] Jiabin Wang, K. Atallah, R. Chin, W. M.Arshad, and H. lendenmann, Rotor Eddy-Current Loss in Permanent-Magnet Brushless AC Machines, IEEE Transactions on Magnetics, Vol. 46, No7, July, 2010.

[47] Jianggang Hu, Jingbo Liu, and Longya Xu, Eddy Current Effects on Rotor Position Estimation and Magnetic Pole Identification of PMSM at Zero and Low Speeds, IEEE Transactions on power Electronics, Vol. 23, NO. 5, September 2008.

[48] Mats Leksell, Lennart Harnefors, Hans-Peter Nee, Machine Design Considerations for Sensorless Control of PM Motors.

[49] Y-D Yoon, S-K Sul, S Morimoto, K Ide, High-Bandwidth Sensorless Algorithm for AC Machines Based on Square-wave-Type Voltage Injection, IEEE Transaction on Industry Applications, Vol. 47. No3. May/June 2011.

[50] Qiang Gao, Greg M. Asher, Mark Sumner, and Pavol Makyš, Position Estimation of AC Machines over a Wide Frequency Range Based on Space Vector PWM Excitation, IEEE Transactions on Industry Applications, Vol. 43, No. 4, July/August 2007.

[51] C.Carusna, G.M.Asher, J.C.Clare. Sensorless Flux Position Estimation at Low and Zero Frequency by Measuring Zero Sequence Current in Delta Connected Cage Induction Machines. IEEE Transaction of Industry Applications, 41:609– 617, Mar/April 2005.

[52] E.Robeischl and M.Schroedl. Direct Axis Current Utilization for Intelligent Sensorless Permanent Magnet Synchronous Drives. In industrial Applications Conference 36th IAS Annual Meeting, volume 1, pages 475–481. IEEE, 2001.

[53] E.Robeischl and M. Schroedl. Optimized INFORM Measurement Sequence for Sensorless PM Synchronous Motor Drives with Respect to Minimum Current Distortion. IEEE Transaction of Industry Applications, 40:591–598, Mar/April 2004.

[54] T.M.Wolbank, H.Giuliani, R.Woehrnschimmel, J.L.Machl. Sensorless Control of Induction Machines by Combining Fundamental Wave Models with Transient Excitation Technique. In IEEE International Conference on Electric Machines and Drives, pages 1379–1384, May 2005.

[55] Qiang Gao, Asher, G, and Sumner, M. Wide-speed range **sensorless** control of an AC PM motor using the PWM waveform of a matrix converter and without di/dt sensors, Industrial Electronics, IECON '09. 35th Annual Conference of IEEE, pp 1389 – 1394, 2009

[56] The Math Works Inc, Simulink-Dynamic system simulation for Matlab, version 3, 1997.

[57] G F Franklin, J D Powell, M L Workman, Digital Control of Dynamic Systems, 2nd Edition, 1990.

[58] H.W.Broeck, H.C.Skudelny, and G.V.Stanke, Analysis and Realization of a Pulsewidth Modulator based on Voltage. IEEE Transaction of Industry Applications, 24:142–150, Jan-Feb 1988.

[59] Eric R. Motto, Hybrid Circuits Simplify IGBT Module Gate Drive, Powerex Inc., Youngwood, Pennsylvania, USA, PCIM, 1999.

[60] R.Heinz, Intelligent Interfaces between Power and Control. Siemens Components Magazine, 1(3):8–11, 1996.

[61] G.Terzulli, B.W.Peace. Film Technology to Replace Electrolytic Technology. www.avx.com.

[62] A.M.R.Amaral, A.J.M.Cardoso. An Experimental Technique for Estimating the Aluminum Electrolytic Capacitor Equivalent Circuit at High Frequencies. In IEEE International Conference on Industrial Technology ICIT, pages 86–91, 2005.

[63] M.Bramoulle. Electrolytic or Film Capacitor? In IEEE Industry Application Conference Thirty-third IAS Annual Meeting, volume 2, pages 1138–1141, St.Louis, MO, Oct 1998.

[64] LEM Components, www.lem.com. Current Transducer LAH 100P Datasheet.

[65] LEM Components, www.lem.com. Voltage Transducer LV 25P Datasheet.

[66] Fuji Electric Device Technology Co., Ltd, Japan. Fuji IGBT Modules Application Manual, Feb 2004.

[67] Horowitz & Hill, Paul & Winfield (1989). The Art of Electronics, 2nd Ed, Cambridge University. pp. 53.

[68] Spectrum Digital Inc. TMS320C6713 DSK Technical Reference, May 2003.

[69] Host Port Interface Daughter card for the Texas Instruments TMS320C6713/6416T Digital Signal Processing (DSP) Starter Kits, Board revisions 1.3a/b Firmware revision 1.0.1.0, Educational DSP, LLC, www.educationaldsp.com.

[70] George C. Verghese, Seth R. Sanders. Observers for Flux Estimation in Induction Machines, IEEE Transactions on Industry Electronics, 35(1): 85–94, Feb 1988.

[71] Daniel R. McMahill, and Charles G. Sodini. Automatic Calibration of Modulated Frequency Synthesizers. IEEE transactions on circuits and systems—ii: Analogue and Digital signal processing, Vol. 49, no. 5, May 2002.

[72] Shih-Chin Yang and Robert D. Lorenz, Surface permanent magnet synchronous machine self-sensing position estimation at low speed using eddy current reflected asymmetric resistance, EPE 2011, ISBN: 9789075815153, P1-P10.

[73] Reigosa, D., Briz, F., Degner, M.W., Garcia, P. and Guerrero, J.M.: Temperature issues in saliency tracking based sensorless methods for PM synchronous machines. Energy Conversion Congress and Exposition (ECCE), 2010 IEEE, pp. 3123-31302010.

[74] Sungmin Kim, and Seung-Ki Sul, High Performance Position Sensorless Control Using Rotating Voltage Signal Injection in IPMSM, EPE 2011, ISBN: 9789075815153

[75] Forest M Hoffman, An introduction to Fourier theory, 1997, P1-P10.

[76] J.-H. Jang, J.-I. Ha, and S.-K. Sul, Vector Control of Surface Mounted Permanent Magnet Motor without any Rotational Transducer, presented at IEEE-APEC Annual Meeting, 2001.

[77] J.-K. Ha and S.-K. Sul, Sensorless Field-Orientation Control of an Induction Machine by High-Frequency Signal Injection, *IEEE Transactions Industry Appplications*, vol. 35, pp. 45-51, 1999.

[78] Yahan Hua, Asher, G.M, Sumner, M, Qiang Gao, Sensorless Control of Surface Mounted Permanent Magnetic Machine Using the Standard Space Vector PWM, Industry Applications Conference, 2007. 42nd IAS Annual Meeting, IEEE Conference.

[79] Yu Duan, Optimization of Sensorless Control by Using Applications of Advanced Signal Processing, first year of PhD report, 2008.

[80] Spectrum Digital, INC, "TMS320C6713 DSK Technical Reference", Nov, 2003

[81] Dang Huy Quoc Si. A new implementation of high frequency, high voltage Direct Power Converter, PhD Thesis, 2006

[82] M. E. Haque, L. Zhong and M. F. Rahman, Initial rotor position estimation of interior permanent magnet synchronous motor without a mechanical sensor, AUPEC conference, 2000.

[83] Dumitru Daniel Popa, Liviu Mario Kreindler, Raducu Giuclea, Aurelian Sarca, A novel method for PM synchronous machine rotor position detection, Power Electronics and Applications, 2007 European Conference, 2-5 Sept. 2007.

[84] Duro Basic, Francois Malrait, and Pierre Rouchon, Initial Rotor Position Detection in PMSM based on Low Frequency Harmonic Current Injection 14th International Power Electronics and Motion Control Conference, EPE-PEMC 2010.

[85] Joachim Holtz, Initial Rotor Polarity Detection and Sensorless Control of PM Synchronous Machines, 41st IAS Annual Meeting, Applications Conference, 2006.

[86] Y.-S. Jeong, R. D. Lorenz, T. M, Jahns and S.-K. Sul, Initial Rotor Position Estimation of an Interior Permanent Magnet Synchronous Machine using Carrier-Frequency Injection Methods, *IEEE Intern. Electric Machines a. Drives Conf. IEMDC,* Madison, WI, June 1-4, 2003, pp. 1218–1223; later in *IEEE Trans. Industry Appl.*, Vol. 41, No. 1, Jan./Feb. 2005, pp. 38-45.

[87] Kuo, Benjamin C & Golnaraghi M.F. Automatic control systems (Eighth edition 2003). NY: Wiley. pp. 236–237. ISBN 0471134767.

[88] Tay, Teng-Tiow; Iven Mareels, John B. Moore, High performance control. Birkhäuser, 1997, pp93, ISBN 0817640045.

[89] Ping Zheng, Peter Thelin, Anyuan Chen, and Erik Nordlund, Influence of Saturation and Saliency on the Inductance of a Four-Quadrant Transducer Prototype Machine, IEEE Transactions on Magnetics, vol. 42, no. 4, April 2006.

[90] H. Johnson & W. Harrison, inventor; 1979 Apr. 22, the permanent magnet motor, United States patent US 4,151,431.

[91] Lecroy Wavesurfer 424 200MHz Oscilloscope, www.lecroy.com

[92] Arbiter systems, inc, Calibrating meters and transducers with the model 1040c panel meter calibrator, PD0010800A 9-92, 1992

[93] Andrew Nicholas; Edward Crellier . Rogowski coil, 2000.